UNIVERSITY OF MANITOBA

Frequency Domain System Identification of Fixed-Wing Unmanned Aerial Vehicles

By
KAIWEN XU
8/14/2014

A Thesis

Submitted to the Faculty of Graduate Studies of the University of Manitoba

In Partial Fulfillment of the Requirements of the Degree of

MASTER OF SCIENCE

Department of Mechanical Engineering

The University of Manitoba

Winnipeg, Manitoba

Abstract

The goal of this thesis is to identify airplanes' reduced order transfer functions, and aerodynamic derivatives in the longitudinal channel. The outcome of the research will benefit aircraft systems' controller design, modeling and simulation. Aircraft under study are a conventional fixed wing airplane called Cropcam, and a nonconventional delta-wing aircraft. To identify the system transfer functions and aerodynamic derivatives, direct and indirect frequency domain identification methods are applied. For the direct method, the Equation Error (EE) method is adopted to process the Cropcam's input-output data pairs and identify the aerodynamic derivatives from the flight data directly. The indirect approach is called the Transfer Function (TF) method. For this method, a commercially available system identification tool kit called CIFER is utilized to identify the longitudinal transfer function of the aircraft first. Then the aerodynamic derivatives are extracted from the identified transfer function. The derivatives identified by the EE method and transfer function method are compared with the ones computed from a Vortex Lattice based program called AVL. The identification results are further verified by comparing computer simulation outputs with flight test responses. Issues such as input excitation design, data gathering, data reliability analysis and result verification are also investigated in this thesis.

Table of Contents

Acknowledgements

First, I would like to thank my supervisor Dr. Nariman Sepehri and co-advisor Dr. Hamidreza Bolandhemmat, whose invaluable guidance and support has helped steer my work in the right direction over the past two years. I also thank the staffs from MicroPilot Inc., especially Howard Loewen (president of the company), Asadilan Indrabudi and Adam Toews for providing me technical support and fruitful suggestions. I thank my colleagues from the Fluid Power & Tele-Robotics Research Laboratory, especially Morgan May and Divyarajsinh Raol, for their kind help during this research. I also thank NSERC, MITACS and MicroPilot Inc., for sponsoring the research. Finally, sincere thanks go to Drs. W Kinsner and S Balakrishnan, for the examination of this thesis and their constructive comments.

List of Figures

List of Tables

Nomenclature

a	Acceleration
b	Wing span
c	Chord
$\bar{c}$	Standard mean chord
cg	Center of gravity
C_D	Drag force coefficient
C_l	Rolling moment coefficient
C_L	Lift force coefficient
C_m	Pitching moment coefficient
C_{m_α}	The coefficient of effect of α on pitching moment
C_n	Yawing moment coefficient
C_x	Axial force coefficient
C_y	Lateral force coefficient
C_z	Normal force coefficient
D	Drag force
e	Exponential function
f	Frequency (Hz)
F	Aerodynamic force
g	Acceleration of gravity
G	System transfer function
h	Height
i	Current sequence number
I_x	Moment of inertia in roll
I_y	Moment of inertia in pitch
I_z	Moment of inertia in yaw
I_{xy}	Product of inertia about *ox* and *oy* axes
I_{xz}	Product of inertia about *ox* and *oz* axes
I_{yz}	Product of inertia about *oy* and *oz* axes
j	Imaginary number ($j = \sqrt{-1}$)

k Stiffness coefficient of spring

k_u Axial velocity transfer function gain constant

k_q Pitch rate transfer function gain constant

k_w Normal velocity transfer function gain constant

L Lift; rolling moment

m Mass

M Pitch moment

N Yawing moment; white noise; total number of samples

o Origin of coordinates

p Roll rate perturbation

q Pitch rate perturbation

r Yaw rate perturbation; notation to denote autocorrelation or cross-correlation

R_0 Resistance

s Wing semi-span; Laplace operator

S Wing area; complex valued spectral density function

t Time

T Time constant

T_{θ_2} Incidence lag time constant

T_u Numerator zero in axial velocity transfer function

u Axial velocity perturbation; voltage

$\boldsymbol{u}$ Input vector

U Total axial velocity

U_e Axial steady state velocity

v Lateral velocity perturbation

v_i Discrete measurement noise vector

V Total (lateral) velocity

V_e Lateral steady state velocity

V_0 Steady equilibrium velocity

w Normal velocity perturbation

W Total normal velocity

W_e Normal component of steady state velocity

x *ox* axis in coordinate system

$\boldsymbol{x}$ State vector

X Axial force component

y *oy* axis in coordinate system

y Output vector

Y Lateral force component

z *oz* axis in coordinate system

z_i Measured output vector at ith sample

Z Normal force component

α Angle of Attack

α_e Equilibrium incidence

β Sideslip angle perturbation

β_e Equilibrium sideslip angle

γ Flight path angle perturbation

γ_e Equilibrium flight path angle

δ Control angle

δ_e, δ_η Elevator angle increment

δ_a Aileron increment

δ_r Rudder angle

ξ Damping ratio

ξ_p Phugoid damping ratio

ξ_s Short-period pitching oscillation damping ratio

η Elevator control angle perturbation

θ Pitch angle perturbation; *p*-dimensional parameter vector

θ_e Equilibrium pitch angle

ρ Air density

φ Roll angle perturbation

ϕ Notation to denote power spectral density

ψ Yaw angle perturbation

ω Angular velocity (rad/s)

ω_n Natural frequency

ω_p Phugoid natural frequency

ω_s Short-period pitching oscillation natural frequency

Symbols and Notations

x_u Shorthand notation to denote concise derivative, it is equal to dimensional derivative divided by appropriate mass or inertia parameters

X_u American shorthand notation to denote American normalised dimensional derivative $\frac{\mathring{\mathrm{X}}_u}{m}$

C_{x_u} American shorthand notation to denote American dimensionless derivative

X_u British shorthand notation to denote dimensionless derivative $\frac{\partial \hat{X}}{\partial \hat{u}}$

$\mathring{X}_u$ British shorthand notation to denote dimensional derivative $\frac{\partial \mathrm{X}}{\partial \mathrm{u}}$

$N_u^y(t)$ Shorthand notation to denote transfer function of output response *y* to input *u*

$\hat{u}$ Shorthand notation to denote non-dimensionalised *u*

Δ Characteristic polynomial; transfer function denominator

(^{o}) Symbol to denote dimensional derivatives in British notation

($\hat{}$) Symbol to denote dimensionless parameter; estimate

(^{T}) Superscript to denote transpose of a matrix

(†) Superscript to denote complex conjugate transpose of matrix

($^{-1}$) Superscript to denote matrix inverse

($\tilde{}$) Superscript denotes Fourier transform

($_{i}$) Subscript to denote value at the i^{th} sample

Re Real part

A, **B**, **C**, **D** System matrices

$E\{\ \}$ Expectation operator

1 Introduction

1.1 Motivation

Unmanned Aerial Vehicles (UAVs) are being used extensively in applications such as surveillance, search and rescue missions, remote sensing and geographic studies (Ryan *et al*., 2004; Fahimi, 2009; Nonami *et al*., 2010). Compared to piloted aerial vehicles, the control of UAVs is more challenging – because all flight control, navigation and guidance operations must be carried out by an onboard computer. Usually, the design and tuning of the control systems are done by trial-and-error on actual prototype aircrafts. This method is time-consuming and costly. In some cases, the tests do not cover the entire flight envelope, leading to unsatisfactory performance during unseen real world scenarios. As a result, it is a common practice to develop time-domain computer simulation models of UAVs that resemble the actual behaviour of aircraft in flight. The autopilot control systems used on UAVs are then designed and tested using the simulation program first, before being deployed on real platforms. This approach, if implemented well, reduces the need for extensive tuning and validation. However, one problem which often plagues this approach is that the computer simulation results may not match the actual responses obtained from the actual flight. This discrepancy is mainly caused by inaccuracies of the time-domain model structure, the magnitudes of its parameters, or the manner in which it is numerically simulated. These issues reduce the reliability of any design based on the available simulation software. Therefore, obtaining accurate models of UAVs is critical for the development of algorithms or software tools that can be used to design and analyze the UAV autopilot control systems under different flight conditions. System identification techniques

allow the derivation of reliable analytical models which can be used, not only in simulations of different flight scenarios, but also for the development of more advanced controllers for the UAVs.

1.2 Objectives

One major challenge in composing an analytical model of an aircraft is to accurately characterize its aerodynamic behavior by a set of coefficients known as aerodynamic derivatives. These derivatives relate the host aircraft motion variables to the aerodynamic forces and moments. Since autopilots are commonly designed to fly a wide variety of airframes, identifying the aerodynamic characteristics of the platform, either on-line or off-line, could significantly ease the control system design process. The conventional method for finding these derivative values involves conducting wind tunnel experiments on a scaled vehicle. While this method is effective, it is expensive, often preventing civilian UAV manufacturers from adopting it. Also, some of the dynamic aerodynamic derivatives are not calculated accurately by this method. The computational program Athena Vortex Lattice (AVL) program, produces estimates of the aerodynamic derivatives given the aircraft geometry; however, AVL does not take into account the viscous effects of aerodynamic and, thus, cannot produce accurate results for small UAVs flying at low speeds. Recently, off-line or on-line system identification techniques have been adopted by aircraft manufacturers and industry researchers to build mathematical models for UAVs by using measurements of input-output data pairs. These techniques process certain inputs excited aircraft frequency (Theodore *et al.*, 2004; Tischler and Remple, 2006; Debusk *et al.*,

2011; Dorobantu *et al*., 2013; Lee and Park, 2009; Morelli, 1999) or time domain (Klein and Morelli, 2006; Jategaonkar, 2006; Chowdhary and Jategaonkar, 2006) responses.

The objective of this research is to find an effective tool that can process flight data, and either extract the aerodynamic derivatives directly or obtain them indirectly from the platform transfer functions, given minimum flight test data and limited sensory information. The outcome of this research will provide a technology that improves the reliability of UAVs computer simulation software and, as a result, enhances fidelity of the designed control system. Also, the optimal design of the autopilot control system without excessive flight tests will reduce manufacturing costs.

Input-output data pairs of two UAVs, including a nonconventional delta-wing aircraft and a conventional fixed wing aircraft, are available to be processed in this thesis. It is expected that the system transfer functions in the longitudinal channel, as well as the related aerodynamic derivatives will be identified.

1.3 Methodology

Two frequency domain system identification techniques are implemented in this research. The first approach is the Transfer Function (TF) method. This method uses spectral densities of the measured input-output signals to obtain system transfer function (Tischler *et al*., 2006; Dorobantu *et al*., 2011). For this method, an empirical estimate of the system frequency response is calculated by using auto Power Spectral Density (PSD) of the input and cross Power Spectral Density of the input and the output signals. The main challenge here is how to calculate PSD

functions accurately. The main source of errors are inaccuracies in sensor measurements and insufficient frequency resolution for identifying lightly damped modes of the aircraft.

The second approach is the Equation Error method, which is also called the recursive Fourier Transform Regression (FTR) method (Klein *et al.*, 2006; Tischler *et al.*, 2006; DeBusk *et al.*, 2009). The advantage of the FTR method is that the DC gains and zero biases can be removed from the measured data by omitting the zero frequency from the frequencies over which the Fourier Transform is calculated. Also, the higher frequency components of the measured data, which are usually due to noise or external disturbances, can be removed.

The research is built and expanded upon an in-house simulation model, as well as a commercially available identification software tool called CIFER (Tischler *et al.*, 2006). CIFER is short for Comprehensive Identification from FrEquency Responses. Appropriate tools are adopted and further developed for extracting the aerodynamic derivatives used by the model. It was jointly developed by the U.S. Army and the University of California, Santa Cruz (UARC). The most significant feature of CIFER is that it can extract high-quality frequency responses from multi-input/multi-output time domain data. Its advanced Chirp-transform and composite optimal window techniques allow it to extract significantly higher quality frequency responses compared to standard Fast Fourier Transforms (FFTs).

After the simulation model system identification is done, both the TF and EE methods are initially will be applied on the platform called Cropcam. As the research unfolds, it will be expanded to a nonconventional delta-wing UAV. Identification of longitudinal aerodynamic derivatives during cruise flight mode is investigated first, followed by the derivation of

appropriate frequency-domain models (transfer functions) of the aircrafts. The following issues are commonly addressed in the context of UAVs' system identification (Morelli, 2009):

i. which states should be measured, and how they are measured;

ii. which states cannot be measured and need to be determined post flight;

iii. what kind of filter(s) and/or post processing procedure(s) are required to eliminate undesired and unnecessary components from the measured data;

iv. how should the aircraft be excited effectively to assure that the measured data is sufficiently rich for system identification purposes in the frequency domain;

v. what is the required sampling rate to guarantee that the fastest mode of the aircraft model can be reconstructed;

vi. how high should the input excitation amplitude be without violating the small perturbation criteria, while providing a sufficiently large signal-to-noise ratio;

vii. how should the input excitation be implemented: in the Pilot in Control (PIC) or Computer in Control (CIC) mode.

In this research, the following questions are investigated:

i. How can the aerodynamic derivatives be obtained from the transfer functions in UAVs using frequency domain method?

ii. What method (transfer function/equation error identification, or AVL estimation) is more accurate in obtaining the aerodynamic derivatives?

Figure 1.1 shows the procedure by what the frequency-response system identification method is applied in this research (Tischler and Remple, 2012).

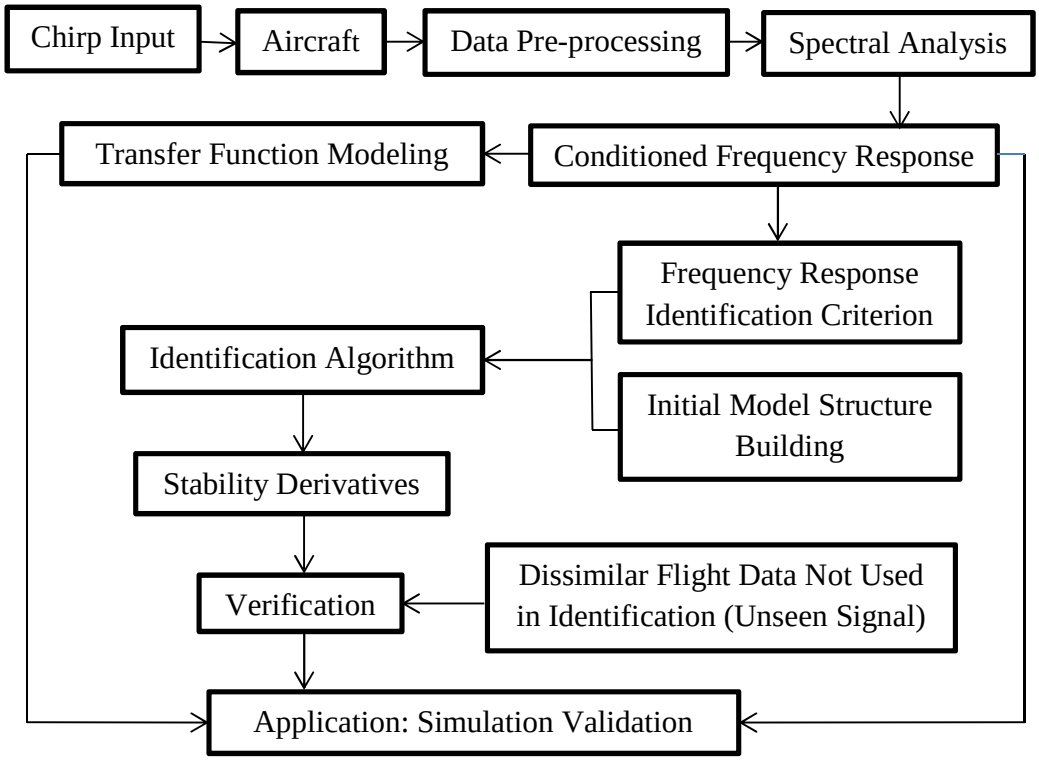

Figure 1.1 Frequency-response system identification procedure

Chirp input is designed first as input excitation for the UAV under investigation. Then, the aircraft responses are measured and processed. Once the data are processed, the identification methods can be applied to identify the system transfer functions and/or the aerodynamic derivatives. The identification results need to be verified before applying to enhance the performance of simulation model.

1.4 Thesis outline

In Chapter 2, the theoretical background of system identification will be introduced. In order to discuss aerodynamic characteristics of UAVs, basic aerodynamic theory needs to be studied as

well. Therefore, Chapter 3 gives an introduction to basic aerodynamic theory. It starts by introducing the coordinate systems that are used to describe aircraft motion both in the body and wind axes, as well as the axes transformations.

In Chapter 4, the general aircraft equations of motion are derived, and the effect of aerodynamic forces and moments on the motion variables are discussed. In addition, the complete dynamic equations are decoupled for the convenience of system identification. In Chapter 5, the frequency domain system identification input excitations requirements are discussed, and the computer-based method for generating the Chirp signal is introduced.

Chapter 6 presents the two system identification methods used in the thesis, namely the transfer function method and the equation error method. In Chapter 7, the system identification techniques are applied to the flight test data of the two fixed-wing UAVs. For Cropcam, the transfer function method is implemented to obtain its longitudinal channel transfer functions first; and then the related aerodynamic derivatives are extracted from the identified transfer functions. Next, the equation error method is applied to identify the longitudinal aerodynamic derivatives. For the second aircraft, the delta-wing, first the longitudinal system transfer function is identified, and then some aerodynamic derivatives are extracted from the identified transfer function. Chapter 8 summarizes the contributions made in this thesis and potential future research is also discussed.

In Appendix 1, the aerodynamic derivatives' conversion between different notations is tabulated. In Appendix 2, first the aircraft simulation model is discussed; then the transfer function method is applied to identify the simulation model's longitudinal channel transfer functions, and some aerodynamic derivatives by using the simulation responses; next, the equation error method is

applied to identify the longitudinal aerodynamic derivatives. At the end of the appendix, the longitudinal channel derivatives calculated by the equation error method, the transfer function method and AVL are compared, to examine and verify their accuracy.

2 Background

This chapter comprised of two parts. The first part gives a brief introduction of UAV and its state of development. In this part, the UAV's application is introduced first, its development prospect is discussed next. In the second part, the concept of system identification and system modeling are introduced first. Typical system identification methods are discussed and compared followed by a literature review.

2.1 Preliminary remark

For two decades, UAVs have been utilised for military purposes, such as geographical study and national security. More recently, several applications have been introduced for UAVs in the civilian sector. UAVs are now employed for search and rescue missions, facility and infrastructure inspections, and environmental studies. Other UAV applications include: "*i*) wildfire detection and management; *ii*) pollution monitoring; *iii*) event security; *iv*) traffic monitoring; *v*) disaster relief; *vi*) fisheries management; *vii*) pipeline & oil and gas security monitoring; *viii*) meteorology - storm tracking; *ix*) remote aerial mapping; *x*) transmission line inspection" (Hon *et al.*, 2013).

The UAVs' market will continue to expand and the world's spending on UAVs is expected to double in the coming decade. The annual expenditure on UAVs will increase from 5.2 billion dollars to 11.6 billion dollars, representing a total of about 89 billion dollars (Zaloga *et al.*, 2011). The predictions about world UAV expenditure suggest that UAVs will have a booming development in the near future.

2.2 System identification

Presently, computer simulation is largely used to support control design and validation. Normally, modeling of a system can be visually classified as three types: white-box modeling, grey-box modeling and black-box modeling (Khan and Khan, 2012).

The white-box modeling approach is based on a grasp of axioms or postulates, or some foundational propositions or assumptions that cannot be deduced from any other proposition or assumption. The white-box model is almost a full description which describes the details of the physical system. Most of the time, white-box modeling is either difficult or else it may take an unreasonable length of time due to the high complexity of the identified system or process.

In grey-box modeling, the incipient model can be constructed on the basis of the insight gleaned from the system or experimentally measured data. However, the prior built model is incomplete, because some of the model parameters or coefficients of the system are unknown. In this case, system identification is required to find the unknown parameters.

In black-box modeling, as its name implies, the system is an unknown unit. There is no prior model available to use or to refer to. In practice, the common method used for grey-box and black-box modeling is “system identification”. System identification is a general term referring to mathematical tools and algorithms which are used to determine dynamical models’ characteristics from measured data (Pintelon and Schoukens, 2012). It is widely used in the fields of Mechanical Engineering, Chemical Engineering and Electrical Engineering, for prediction, control, physical interpretation and design of mechanical and electrical systems (Pintelon and Schoukens, 2012). System identification is based on an analysis of the system experimental data and insight into the system.

System identification methods can be classified in two categories: time domain system identification methods and frequency domain system identification methods. The time domain methods are straightforward to implement, but two main issues commonly plague accurate system identification: noise and data information content (Morelli, 1999). In the context of aircraft system identification, if the signal-to-noise-ratio (SNR) is too low, the time domain identification method usually fails to provide reliable estimates of the unknown parameters. Also, most of the time domain identification studies placed no limitations on computational power, which is rather restrictive for low-cost on-board processors of UAV autopilots.

Two optimization algorithms, Least Mean Square (LMS) and the Maximum Likelihood (ML, Klein and Morelli, 2006; Crassidis and Junkins, 2004; Simon, 2006) are commonly used for the time domain system identification. The LMS technique attempts to identify the unknown parameters by minimizing the sum of the squares of the estimation error. Estimation results are validated using the available statistical metrics such as the Cramer-Rao band, or the residual auto-correlation sequence. The major problem when using the LMS method is not robust in deal with data collinearity. This may result in inaccurate or fail estimates. The ML method (Crassidis and Junkins, 2001; Simon, 2006) offers estimates for the unknown parameters so that the probability of obtaining the measured set of data is maximized. This technique allows the estimation results to become minimum variance unbiased as the number of measured samples increases. However, as the dimension of the identification problem grows, increasing computational complexity of the ML algorithm becomes problematic. Furthermore, in practice, the ML cost function is barely quadratic having multiple minima which makes finding the global minimum rather difficult.

Compared to the time domain methods, frequency domain system identification techniques are more robust in coping with noise and inaccuracies in the measurements (Morelli, 1999). In addition, they require a smaller number of data points for identification, and can process signal components at different frequency ranges separately. They usually provide more physical characteristics over the entire frequency content, compared to the time domain approaches (Morelli, 1999). Frequency domain system identification techniques have been proved to be efficient in determining a UAV's aerodynamic model, control system tuning and validation (Theodore *et al*., 2004).

In this thesis, two frequency domain system identification methods are discussed. For the TF method, it uses CIFER to obtain the system Bode plot and transfer function first. CIFER uses power spectra method to estimate the system transfer functions. The approach is based on the lower-order equivalent system (LOES) concept. This concept was initially presented by Hodgkinson et al. (1976), and was used by Bischoff and Palmer (1982), Bischoff (1983) and Hodgkinson (1998). Once the transfer function is obtained, the aircraft aerodynamic derivatives are then extracted from the system transfer function. Much research was done to get the transfer function using this method and for using in controller design. To name a few, CIFER was first used to identify the system transfer function from flight test data by Tischler et al. (1983, 1987) and Tischler (1987b). Dorobantu *et al* (2011, 2013) and Carnduff (2008) also used CIFER for identifying the aircraft system transfer function. While, many institutes have used CIFER for doing frequency response system identification, to the best of the author's knowledge, nobody applied the identified system transfer function to extract the aerodynamic derivatives. In this thesis, the method of using the identified transfer function to calculate aerodynamic derivatives

will be investigated. The calculated derivatives will be examined and verified, and they will be compared with the ones computed by the other methods or sources.

The second method used in this thesis is the Equation Error (EE) method. This method, which is regression identification type, has proven effective for frequency domain system identification. This method was used by many researchers and for various aircraft. For example, NASA Langley used this method for the fighter F-18 High Alpha Research Vehicle's system identification (Klein *et al*, 1990). Science Applications International/Naval used it for F/A-18E's system identification (Paris and Bonner, 2004). NASA Langley also applied EE method for identification of aerodynamic derivatives of a Tu-144LL aircraft (Morelli, 2003b). Boeing used it for B717, B737, B747, B757, B767 and B777's system identification (Hodgkinson, 1998). The method have also it is also largely in the UAV system identification. For example, NASA Langley/Dryden used it for the X-43A's (Hyper-X) UAV system identification (Chowdhary, 2006). Stanford University applied the method for the DragonFly UAV aerodynamic coefficient identification (Jang, 2003). In this research, both TF and EE methods will be used to identify the Cropcam's system aerodynamic derivatives; the results will be compared for verifying reliability of each method.

3 Basic Aerodynamic Theory

In this chapter, the aircraft coordinate systems (earth and aircraft body-fixed) will be discussed first. Next, aircraft motion variables will be defined and explained based on the coordinate systems discussed. Then the transformations among different coordinate systems are derived. Finally, typical aircraft geometry and control surfaces parameters are introduced.

3.1 Coordinate axes

Aircraft motion has six degrees of freedom and it is quite complex. Describing aircraft's motion needs several notations and nomenclatures, and the notations should correspond to suitable coordinate frames. Commonly used frames are earth axes and body-fixed axes coordinate systems.

3.1.1 Earth axes

In cases where only normal atmospheric flights are considered, the aircraft motion is described with respect to the earth-fixed coordinate frame (Cook, 2012). For defining a coordinate frame, the reference point needs to be determined first. For the purpose of study, the reference point o_0 is defined on the earth surface, and o_0 is the origin of a right-handed orthogonal coordinate system ($o_0x_0y_0z_0$), which is shown in Figure 3.1. Plane ($x_0o_0y_0$) is tangential to the earth surface, which is defined as horizontal plane. Axes o_0x_0 and o_0y_0 always point north and east, respectively. The direction of axis o_0z_0 coincides with the direction of gravity. This coordinate system is also called North-East-Down (NED) reference frame.

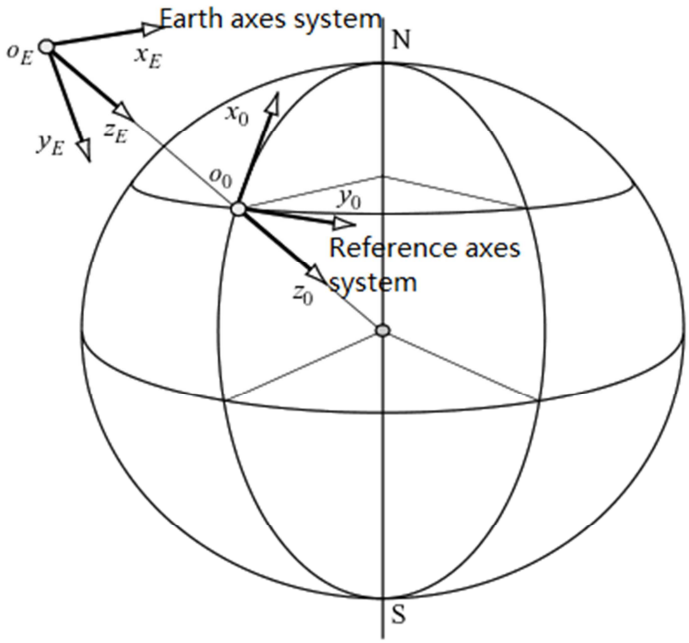

Figure 3.1 Earth axes (adapted from Cook, 2012)

Since the earth is approximately round, and the flight happen in normal atmosphere, the flight path is trans-global, and the aircraft is actually flying in a spherical path. In this case, the angular velocity of the earth needs to be considered. Therefore it is necessary to define a spherical coordinate frame ($o_Ex_Ey_Ez_E$), which is a fixed spatial axes system, to offset this natural angular velocity effect. Referring to Figure 3.1, plane ($o_Ex_Ey_E$) is defined as a horizontal plane, which is parallel to ($x_0o_0y_0$) plane. For short-range UAV application, the earth under the flight path can be assumed as a level and straight plane, which is described by plane ($o_0x_0y_0$). For the coordinate frame ($o_Ex_Ey_Ez_E$), the origin point o_E coincides with the aircraft body-fixed coordinate system's origin. Point o_E is usually put in the atmosphere at the most convenient place. Axis ox_E can point in any direction of the aircraft flight rather than just to the north, while axis oz_E points in the same direction as gravity.

3.1.2 Aircraft body-fixed axes

The body-fixed axes system is a commonly used coordinate system. Since only small perturbation is analysed, only generalised body axes and wind (or stability) axes are discussed.

Body axes

Figure 3.2 shows a typical body axis system ($ox_by_bz_b$). Since the body axis system is always constrained to move with the aircraft fuselage, the axes direction is changing with the motion of the aircraft. The origin of the axis system is usually defined by the aircraft gravity center. In Figure 3.2, the (ox_bz_b) plane is determined by the symmetry plane of the aircraft in which axis ox_b points to the forward direction, axis oy_b directs to the starboard of the aircraft (in the direction of the right wing), and axis oz_b is downward.

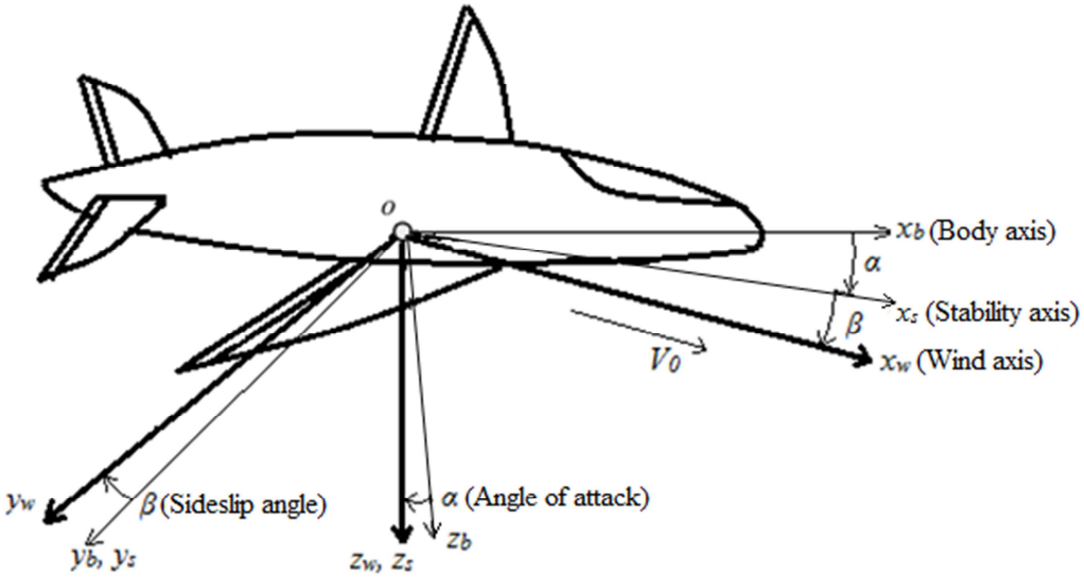

Figure 3.2 General aircraft coordinate system

Wind axes

Sometimes, it is more convenient to describe the aircraft's motion in a coordinate system which is defined with respect to the relative wind (or air) direction. As shown in Figure 3.2, the wind axes coordinate system is defined by ($ox_w y_w z_w$). When the aircraft sideslip angle is zero, wind axes is also known as aerodynamic or stability axes. The direction of the ox_w axis is set parallel to the total velocity V_0 of the aircraft; ($ox_b z_b$) is the symmetry plane of the aircraft. The angle α between axes ox_b and ox_w is called the aircraft angle of attack. When aircraft are flying under a steady state condition, $\alpha = \alpha_e$, where α_e is called equilibrium angle. The value of α_e is different under different flight conditions. β is called the sideslip angle. It is the angle between the aircraft total velocity and the symmetry plane. Therefore, the body axes system is always fixed to the aircraft body, and the wind axes orientation always changes under different flight conditions.

3.2 Definition of variables

The aircraft motion can be generalised by quantities in terms of force, moment, linear and angular velocities of the aircraft. In this thesis, all these variables are defined in body-fixed coordinate system for convenience. In order to depict the perturbed states of aircraft, the trimmed equilibrium state is defined. Trimmed equilibrium is the state in which the aircraft is flying under a steady state condition. When the aircraft is flying under an trimmed equilibrium condition, the forces and moments are in balance and sum to zero; therefore, there is no linear acceleration and the angular velocities are all equal to zero.

When the aircraft is excited with an external input or disturbance, the force and moment balance is broken and the aircraft deviates from the equilibrium state. The perturbation variables are shown in Figure 3.3 below.

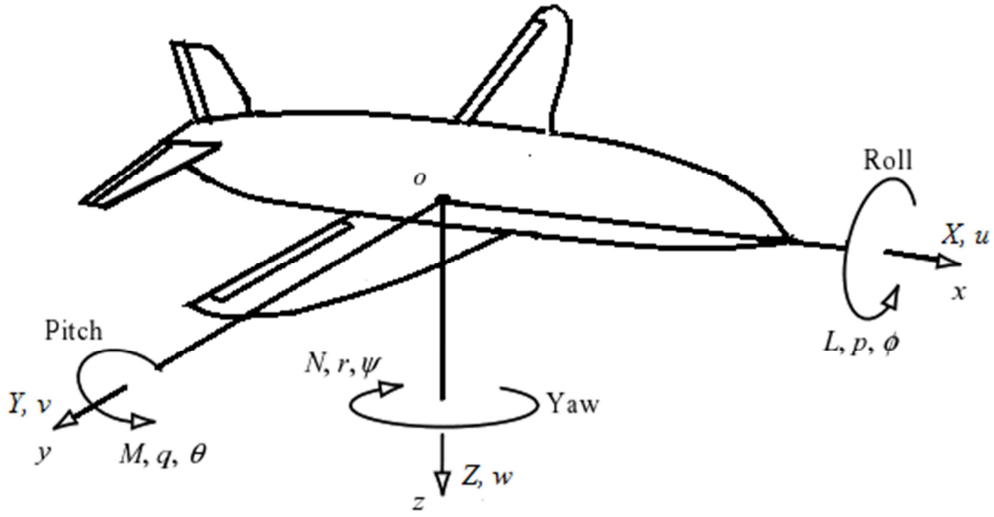

Figure 3.3 Aircraft motion variables

Table 3.1 Motion variables' notation (Cook, 2012)

	Trimmed equilibrium state			Perturbed state		
Orientation	*ox*	*oy*	*oz*	*ox*	*oy*	*oz*
Force	*0*	*0*	*0*	*X*	*Y*	*Z*
Moment	*0*	*0*	*0*	*L*	*M*	*N*
Linear velocity	U_e	V_e	W_e	$U=U_e+u$	$V=V_e+v$	$W=W_e+w$
Angular velocity	*0*	*0*	*0*	*p*	*q*	*r*
Attitude	*0*	θ_e	*0*	φ	θ	ψ

X, *Y*, *Z* — Axial, side and lift force

L, *M*, *N* — Rolling, pitching and yawing moment

U_e, V_e, W_e — Axial, lateral and normal component of steady equilibrium velocity

U, *V*, *W* — Axial, lateral and normal velocity, total linear velocity of gravity center (*cg*)

u, *v*, *w* — Axial, lateral and normal velocity perturbation

p, *q*, *r* — Roll, pitch and yaw rate

φ, θ, ψ — Roll, pitch and yaw angle with respect to *ox*, *oy* and *oz* axes, respectively

θ_e— Equilibrium pitch angle

In Figure 3.3, the signs of the variables are defined by the right-handed axes system. All the components of rotary quantity, moment, velocity and attitude are defined as positive based on the right-handed axes system. A positive roll occurs when the right wing goes down; positive pitch is defined when the aircraft's nose goes up; and positive yaw is achieved when the aircraft turns right. An alternate way of describing the variables' sign is: positive roll is axis *oy* going toward axis *oz*, positive pitch is axis *oz* going toward axis *ox*, and positive yaw is axis *ox* moving toward axis *oy*. The notations of motion variables in trimmed state and disturbed state are tabulated in Table 3.1.

Figure 3.4 shows the moment, angle and force components for longitudinal channel flight situation.

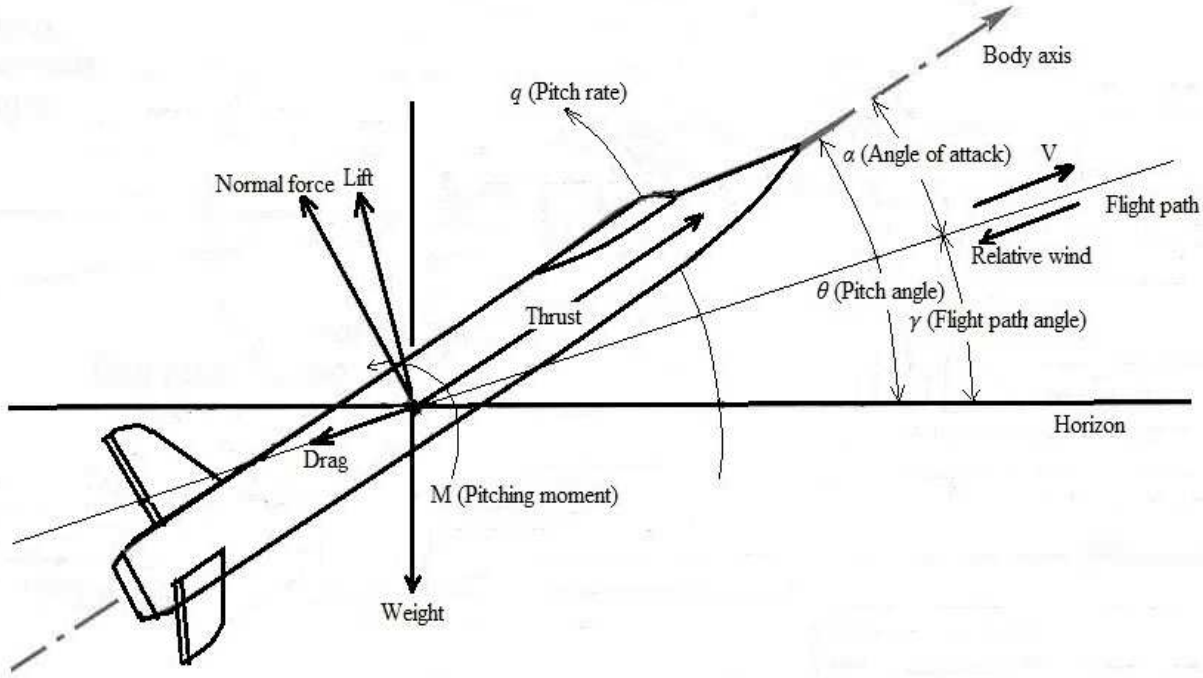

Figure 3.4 Longitudinal channel terms for typical aircraft climbing

When the aircraft is flying under a symmetric situation in which there is no lateral perturbation, the angle and velocity quantities can be simply depicted by Figure 3.5.

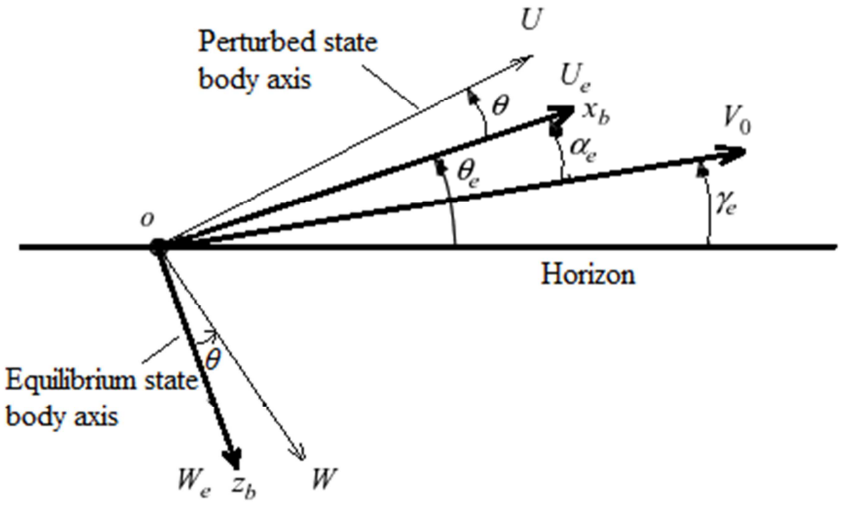

Figure 3.5 Quantities in body axes under symmetric flight (adapted from Cook, 2012)

In Figure 3.5, the angles and velocities have the following relation:

$$\theta_e = \alpha_e + \gamma_e \tag{3.1}$$

$$tan(\alpha_e + \theta) = \frac{W}{U} = \frac{W_e + w}{U_e + u} \tag{3.2}$$

When the aircraft body-fixed axes coincide with the wind axes, α_e = 0. For the specific case, in which the aircraft is flying in a level situation, and accounting for the flight in wind axes coordinate system, the following relation holds:

$$\alpha_e = \theta_e = 0 \tag{3.3}$$

3.3 Axes transformations

3.3.1 Linear acceleration, velocity and displacement transformation

The body attitude angles φ, θ, ψ are known as Euler angles. These angles are defined in the body-fixed axes system. Since the commutative law is inapplicable to angles, the order of the rotation is very important. Figure 3.6 shows a general example of the coordinate system rotation. ($ox_0y_0z_0$) is the reference axes frame, and ($ox_3y_3z_3$) is the body-fixed axes frame. The transformation order shown in Figure 3.6 is: first, rotate the body-fixed axes about axis ox_3 with an angle of φ. Thus the body-fixed axes are brought to ($ox_2y_2z_2$); next, rotate the frame about oy_2 axis by an angle of θ. The body-fixed axes are brought to ($ox_1y_1z_1$); last, rotate the current axes system about oz_1 axis by a yaw angle of ψ. Thus, the ($ox_3y_3z_3$) coordinate system is brought to the new coordinate system ($ox_0y_0z_0$).

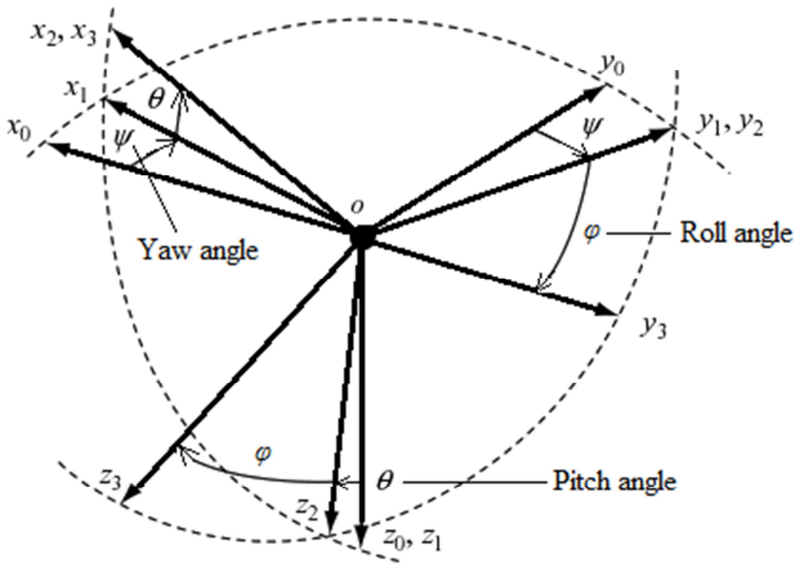

Figure 3.6 Axes transformation (adapted from Cook, 2012)

Let (ox_3, oy_3, oz_3) represents the linear quantity components in the ($ox_3y_3z_3$) axes system, and (ox_0, oy_0, oz_0) represents the linear quantity components in the ($ox_0y_0z_0$) axes system. The linear quantities can be velocity, displacement or acceleration. The transformation of quantities in different axes systems can be described by the following equations (Cook, 2012):

For the first step, rotating about ox_3 by a roll angle of φ,

$$ox_3 = ox_2 \tag{3.4}$$

$$oy_3 = oy_2 cos\varphi + oz_2 sin\varphi \tag{3.5}$$

$$oz_3 = -oy_2 sin\varphi + oz_2 cos\varphi \tag{3.6}$$

Equations (3.4) to (3.6) can be written in matrix equation form as:

$$\begin{bmatrix} ox_3 \\ oy_3 \\ oz_3 \end{bmatrix} = \begin{bmatrix} 1 & 0 & 0 \\ 0 & cos\varphi & sin\varphi \\ 0 & -sin\varphi & cos\varphi \end{bmatrix} \begin{bmatrix} ox_2 \\ oy_2 \\ oz_2 \end{bmatrix} \tag{3.7}$$

The second step is similar to step one, but this time rotate the coordinate system about axis oy_2 by a pitch angle of θ. The following relation holds:

$$\begin{bmatrix} ox_2 \\ oy_2 \\ oz_2 \end{bmatrix} = \begin{bmatrix} cos\theta & 0 & -sin\theta \\ 0 & 1 & 0 \\ sin\theta & 0 & cos\theta \end{bmatrix} \begin{bmatrix} ox_1 \\ oy_1 \\ oz_1 \end{bmatrix} \tag{3.8}$$

Similarly, for the last step, yawing about the axis oz_1 with a yaw angle of ψ, the following have:

$$\begin{bmatrix} ox_1 \\ oy_1 \\ oz_1 \end{bmatrix} = \begin{bmatrix} cos\psi & sin\psi & 0 \\ -sin\psi & cos\psi & 0 \\ 0 & 0 & 1 \end{bmatrix} \begin{bmatrix} ox_0 \\ oy_0 \\ oz_0 \end{bmatrix} \tag{3.9}$$

According to Equations (3.7), (3.8) and (3.9), (ox_3, oy_3, oz_3) can be combined with (ox_0, oy_0, oz_0) as:

$$\begin{bmatrix} ox_3 \\ oy_3 \\ oz_3 \end{bmatrix} = \begin{bmatrix} 1 & 0 & 0 \\ 0 & cos\varphi & sin\varphi \\ 0 & -sin\varphi & cos\varphi \end{bmatrix} \begin{bmatrix} cos\theta & 0 & -sin\theta \\ 0 & 1 & 0 \\ sin\theta & 0 & cos\theta \end{bmatrix} \begin{bmatrix} cos\psi & sin\psi & 0 \\ -sin\psi & cos\psi & 0 \\ 0 & 0 & 1 \end{bmatrix} \begin{bmatrix} ox_0 \\ oy_0 \\ oz_0 \end{bmatrix} \quad (3.10)$$

Equation (3.10) can be expressed in the concise notation as:

$$\begin{bmatrix} ox_3 \\ oy_3 \\ oz_3 \end{bmatrix} = D \begin{bmatrix} ox_0 \\ oy_0 \\ oz_0 \end{bmatrix} \quad (3.11)$$

where, D is a matrix given by:

$$D = \begin{bmatrix} cos\theta cos\psi & cos\theta sin\psi & -sin\theta \\ sin\varphi sin\theta cos\psi - cos\varphi sin\psi & sin\varphi sin\theta sin\psi + cos\varphi cos\psi & sin\varphi cos\theta \\ cos\varphi sin\theta cos\psi + sin\varphi sin\psi & cos\varphi sin\theta sin\psi - sin\varphi cos\psi & cos\varphi cos\theta \end{bmatrix} \quad (3.12)$$

The reverse transformation, from ($ox_3y_3z_3$) to ($ox_0y_0z_0$) is written as follows:

$$\begin{bmatrix} ox_0 \\ oy_0 \\ oz_0 \end{bmatrix} = D^{-1} \begin{bmatrix} ox_3 \\ oy_3 \\ oz_3 \end{bmatrix} \quad (3.13)$$

where,

$$D^{-1} = \begin{bmatrix} cos\theta cos\psi & sin\varphi sin\theta cos\psi - cos\varphi sin\psi & cos\varphi sin\theta cos\psi + sin\varphi sin\psi \\ cos\theta sin\psi & sin\varphi sin\theta sin\psi + cos\varphi cos\psi & cos\varphi sin\theta sin\psi - sin\varphi cos\psi \\ -sin\theta & sin\varphi cos\theta & cos\varphi cos\theta \end{bmatrix} \quad (3.14)$$

Next, the transformation matrix given by Equation (3.14) is used to determine the relevance of the body axes system components U, V, W with the wind axes system components V_0, α, β. Figure 3.7 shows the resolution of the velocity vector through incidence and sideslip angles to the body coordinate system.

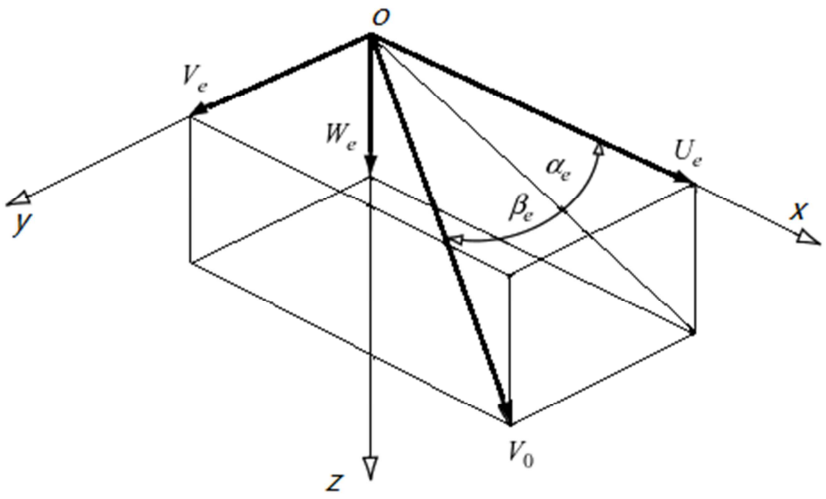

Figure 3.7 Transformation of velocities through incidence and sideslip angles (Cook, 2012)

In the earth axes coordinate system ($ox_0y_0z_0$), the motion vector can be written as:

$$(ox_0, oy_0, oz_0) = (V_0, 0, 0) \tag{3.15}$$

$$\text{and, } (ox_3, oy_3, oz_3) = (U_e, V_e, W_e) \tag{3.16}$$

For the case shown in Figure 3.7, the roll angle is 0, pitch angle is α_e, and yaw angle is β_e. Therefore for the attitude quantities, the following holds:

$$(\varphi, \theta, \psi) = (0, \alpha_e, \beta_e) \tag{3.17}$$

Thus, the transformation of quantities from earth axes to body axes for the specific case of Equation (3.17) can be described as:

$$\begin{bmatrix} U_e \\ V_e \\ W_e \end{bmatrix} = \begin{bmatrix} cos\alpha_e cos\beta_e & -cos\alpha_e sin\beta_e & -sin\alpha_e \\ sin\beta_e & cos\beta_e & 0 \\ sin\alpha_e cos\beta_e & -sin\alpha_e sin\beta_e & cos\alpha_e \end{bmatrix} \begin{bmatrix} V_0 \\ 0 \\ 0 \end{bmatrix} \tag{3.18}$$

which can be further written in the following form:

$$U_e = V_0\, cos\alpha_e cos\beta_e \tag{3.19}$$

$$V_e = V_0 \sin\beta_e \tag{3.20}$$

$$W_e = V_0\, \sin\alpha_e \cos\beta_e \tag{3.21}$$

The *D* matrix in Equation (3.12) is not only applicable for the trimming flight condition, but also can be applied by relating the perturbed velocity vector to the trim velocity vector:

$$\begin{bmatrix} U_e \\ V_e \\ W_e \end{bmatrix} = D^{-1} \begin{bmatrix} U \\ V \\ W \end{bmatrix}$$

$$= \begin{bmatrix} cos\theta cos\psi & sin\varphi sin\theta cos\psi - cos\varphi sin\psi & cos\varphi sin\theta cos\psi + sin\varphi sin\psi \\ cos\theta sin\psi & sin\varphi sin\theta sin\psi + cos\varphi cos\psi & cos\varphi sin\theta sin\psi - sin\varphi cos\psi \\ -sin\theta & sin\varphi cos\theta & cos\varphi cos\theta \end{bmatrix} \begin{bmatrix} U \\ V \\ W \end{bmatrix} \quad (3.22)$$

Since the flight height h in earth axes is defined as positive in the upward direction, and the positive W_e is defined as downward, therefore the following holds:

$$\dot{h} = -W_e \quad (3.23)$$

According to Equations (3.22) and (3.23), the following can be derived:

$$\dot{h} = Usin\theta - Vcos\theta sin\varphi - Wcos\theta cos\varphi \quad (3.24)$$

3.3.2 Angular velocities transformation

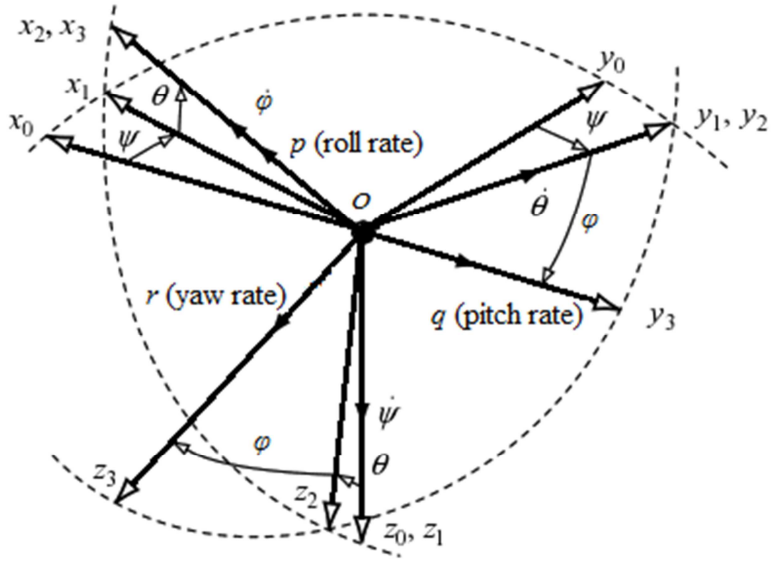

Figure 3.8 Transformation of angular velocity (adapted from Cook, 2012)

The body angular rates are expressed as p, q and r, which are shown in ($ox_3y_3z_3$) coordinate system in Figure 3.8. Similar to linear quantities transformation, the order of angular velocities' transformation is very important. In Figure 3.8, the transformation order can be described as the following: *i*) roll about axis ox_3 by angle of φ, with angular velocity of $\dot{\varphi}$; *ii*) pitch angle of θ about axis oy_2, with rotating velocity of $\dot{\theta}$; *iii*) yaw angle of ψ with respect to axis oz_1, by rotating velocity of $\dot{\psi}$. In this way, the body axes system variables are transformed into the variables referring to the earth axes. The transformation equations corresponding to each step are:

First, roll about ox_3 by φ, the roll rate p is a combined action of the components $\dot{\varphi}$, $\dot{\theta}$ and $\dot{\psi}$ which resolved along ox_3,

$$p = \dot{\varphi} - \dot{\psi} sin\theta \tag{3.25}$$

Second, pitch about oy_2 by θ, pitch rate q is a combined action of the components $\dot{\varphi}$, $\dot{\theta}$ and $\dot{\psi}$ which resolved along oy_3,

$$q = \dot{\theta}cos\varphi + \dot{\psi}sin\varphi cos\theta \tag{3.26}$$

Third, yaw about oz_1 by ψ, yaw rate r is a combined action of the components $\dot{\varphi}$, $\dot{\theta}$ and $\dot{\psi}$ which resolved along oz_3,

$$r = \dot{\psi}cos\varphi cos\theta - \dot{\theta}sin\varphi \tag{3.27}$$

The transformation equations (3.25) to (3.27) can be combined and expressed in concise matrix expression as:

$$\begin{bmatrix} p \\ q \\ r \end{bmatrix} = \begin{bmatrix} 1 & 0 & -sin\theta \\ 0 & cos\varphi & sin\varphi cos\theta \\ 0 & -sin\varphi & cos\varphi cos\theta \end{bmatrix} \begin{bmatrix} \dot{\varphi} \\ \dot{\theta} \\ \dot{\psi} \end{bmatrix} \tag{3.28}$$

Equation (3.28) shows the transformation from Euler rates to the angular velocities in the body coordinate system. The inverse transformation which shows how angular velocities transformed to attitude rates is given below:

$$\begin{bmatrix} \dot{\varphi} \\ \dot{\theta} \\ \dot{\psi} \end{bmatrix} = \begin{bmatrix} 1 & sin\varphi tan\theta & cos\varphi tan\theta \\ 0 & cos\varphi & -sin\varphi \\ 0 & sin\varphi sec\theta & \cos\varphi\sec\theta \end{bmatrix} \begin{bmatrix} p \\ q \\ r \end{bmatrix} \tag{3.29}$$

When the aircraft is undergoing very little perturbations in which φ, θ and ψ are all very small. Equation (3.28) can be simplified and written approximately as:

$$p = \dot{\varphi} \tag{3.30}$$

$$q = \dot{\theta} \tag{3.31}$$

$$r = \dot{\psi} \tag{3.32}$$

Equations (3.30) to (3.32) are commonly used equalities in aircraft flight data processing and system identification.

3.4 Aircraft reference geometry and control surfaces

3.4.1 Reference geometry

Measurement of aircraft geometry is very important for both aircraft modeling and simulations. Figure 3.9 shows a typical way to define aircraft geometric parameters. With reference to Figure 3.9, *b* stands for wing span, *s* denotes wing semi-span, $\bar{c}$ is the standard mean chord of the wing, and *cg* is short for the centre of gravity.

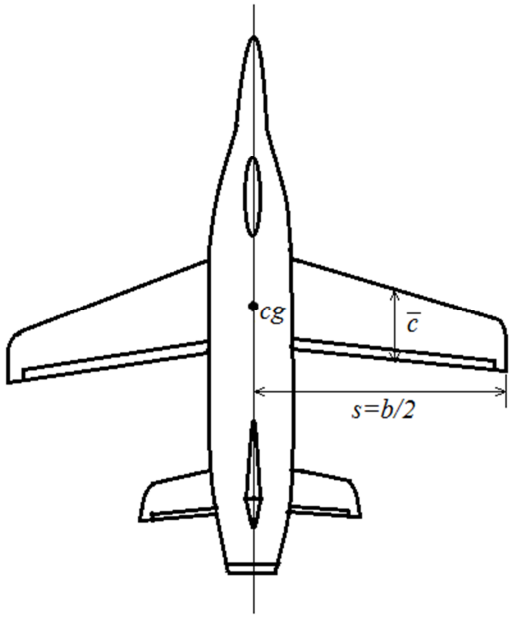

Figure 3.9 Reference geometry

Usually S is used to denote the reference area of the wing as:

$$S = b\bar{c} \tag{3.33}$$

3.4.2 Aircraft control surfaces

The most conventional control surfaces for aircrafts are aileron, elevator and rudder, which control the rolling, pitching and yawing motion of the aircraft, respectively. Figure 3.10 illustrates the aircraft control surfaces and directions of their positive deflections.

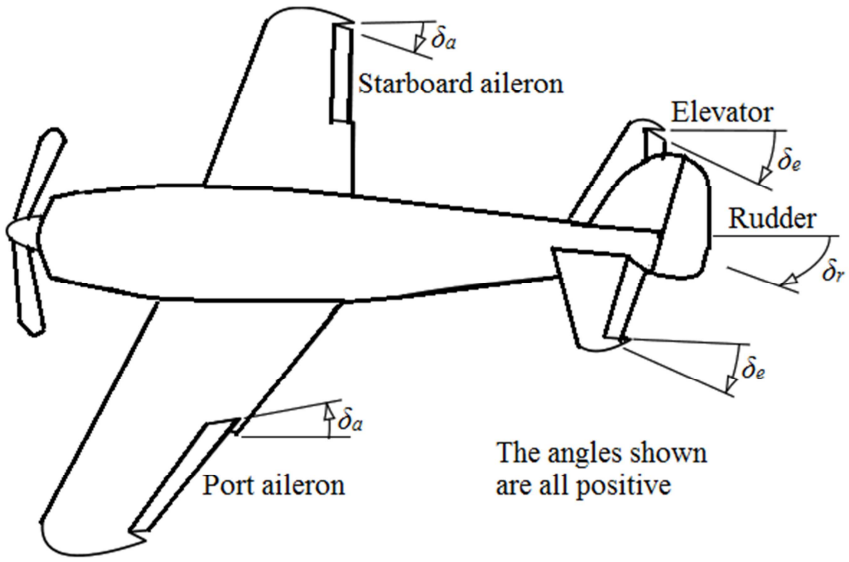

Figure 3.10 Aircraft control surfaces (adapted from Cook, 2012)

As shown by Figure 3.10, positive deflection for the control surfaces is defined as direction causing the aircraft to generate a negative rotation response. For the positive aileron input, it is defined as left aileron going up and right aileron going down. This positive aileron input causes the aircraft right aerofoil trailing edge to go up and the left wing trailing edge to go down. This is called a negative aircraft rolling response. For positive elevator input, the elevator trailing edge

goes up. And the aircraft nose goes up accordingly. For positive rudder input, the rudder trailing edge turns to the left and the aircraft nose turns left.

Usually δ_a, δ_e and δ_r are used to denote aileron, elevator and rudder angles, respectively. And the perturbation angles (angular displacement) of the aileron, elevator and rudder are denoted by ξ, η and ζ, respectively.

3.5 Summary

In this chapter, the aircraft coordinate systems (earth and body-fixed) were discussed first. Next, the aircraft motion variables were defined and explained on the basis of the coordinate systems discussed. The manner the parameters can be transformed from one coordinate system to another was described. Finally, typical aircraft geometry and control surfaces parameters were defined.

4 Aircraft Motion Equations

For system identification of an aircraft, grey box aircraft motion modeling is required. The aircraft analytical model describes an aircraft's behavioural characteristics in a mathematical way, which is developed on the basis of physical and mathematical laws. In this chapter, equations describing the motion of aircraft are derived.

4.1 General equations of motion

For aircraft analytical modeling, the airplane is commonly assumed to be rigid and symmetric. The rigid body assumption implies that effects like aircraft structure deformation, the control surface motion effect on *cg* and the fuel slosh are all omitted (Klein and Morelli, 2006). The generalisation of Newton's second law and Euler's law are the basis for aircraft modeling:

$$\boldsymbol{F} = \frac{d}{dt}(m\boldsymbol{V}) = m \times \boldsymbol{a} \tag{4.1}$$

$$\boldsymbol{M} = \frac{d}{dt}(\boldsymbol{I\omega}) = \boldsymbol{I} \times \dot{\boldsymbol{\omega}} \tag{4.2}$$

where $\boldsymbol{F}$ is the force applied, $\boldsymbol{V}$ is translational velocity, $m\boldsymbol{V}$ is linear momentum and $\boldsymbol{M}$ is applied moment about the centre of gravity. $\boldsymbol{I\omega}$ is angular momentum about the centre of gravity. $\boldsymbol{\omega}$ is angular velocity, and $\boldsymbol{I}$ is the inertia matrix.

$$\boldsymbol{F} = \begin{bmatrix} F_x \\ F_y \\ F_z \end{bmatrix} \tag{4.3}$$

$$\boldsymbol{V} = \begin{bmatrix} U \\ V \\ W \end{bmatrix} \tag{4.4}$$

$$\boldsymbol{M} = \begin{bmatrix} M_x \\ M_y \\ M_z \end{bmatrix} \tag{4.5}$$

$$\boldsymbol{\omega} = \begin{bmatrix} p \\ q \\ r \end{bmatrix} \tag{4.6}$$

$$\boldsymbol{I} = \begin{bmatrix} I_x & -I_{xy} & -I_{xz} \\ -I_{yx} & I_y & -I_{yz} \\ -I_{zx} & -I_{xy} & I_z \end{bmatrix} \tag{4.7}$$

where

$$I_x = \int x^2 dm \tag{4.8}$$

$$I_y = \int y^2 dm \tag{4.9}$$

$$I_z = \int z^2 dm \tag{4.10}$$

$$I_{xy} = \int xy dm = I_{yx} \tag{4.11}$$

$$I_{yz} = \int yz dm = I_{zy} \tag{4.12}$$

$$I_{xz} = \int xz dm = I_{zx} \tag{4.13}$$

Since the aircraft is rigid and symmetric about the (*oxz*) plane, the inertia matrix is symmetric and,

$$I_{xy} = I_{yx} = I_{yz} = I_{zy} = 0 \tag{4.14}$$

As a result, the inertia matrix can be simplified as:

$$\boldsymbol{I} = \begin{bmatrix} I_x & 0 & -I_{xz} \\ 0 & I_y & 0 \\ -I_{zx} & 0 & I_z \end{bmatrix} \tag{4.15}$$

Thus,

$$\boldsymbol{I\omega} = \begin{bmatrix} I_x p - I_{xz} r \\ I_y q \\ -I_{xz} p + I_z r \end{bmatrix} \tag{4.16}$$

For the rotating axes system, the derivative operator applied to vectors has two parts: one is the rate of change of the vector components expressed in the rotating system; another one is the effect of the axes system rotation of the rotating system with respect to a fixed frame. Therefore the operator can be written as:

$$\frac{d}{dt}(\,) = \frac{\delta}{\delta t}(\,) + \boldsymbol{\omega} \times (\,) \tag{4.17}$$

Equations (4.1) and (4.2) are then written as,

$$\boldsymbol{F} = m\dot{\boldsymbol{V}} + \boldsymbol{\omega} \times m\boldsymbol{V} \tag{4.18}$$

$$\boldsymbol{M} = \boldsymbol{I}\dot{\boldsymbol{\omega}} + \boldsymbol{\omega} \times \boldsymbol{I\omega} \tag{4.19}$$

Combining Equations (4.3) and (4.18), the force equations can be written as (Cook, 2013):

$$F_x = m(\dot{U} + qW - rV) \tag{4.20}$$

$$F_y = m(\dot{V} + rU - pW) \tag{4.21}$$

$$F_z = m(\dot{W} + pV - qU) \tag{4.22}$$

Similarly, combining Equations (4.5) and (4.19), moment equations can be written as:

$$M_x = \dot{p}I_x - \dot{r}I_{xz} + qr(I_z - I_y) - qpI_{xz} \tag{4.23}$$

$$M_y = \dot{q}I_y + pr(I_x - I_z) - (p^2 - r^2)I_{xz} \tag{4.24}$$

$$M_z = \dot{r}I_z - \dot{p}I_{xz} + pq(I_y - I_x) - qrI_{xz} \tag{4.25}$$

The total force and moment acting on the aircraft are the combined effects of aerodynamic ($\boldsymbol{F}_A$, $\boldsymbol{M}_A$), gravity ($\boldsymbol{F}_G$) and propulsion ($\boldsymbol{F}_T$, $\boldsymbol{M}_T$). Therefore total force and moment can be denoted as:

$$\boldsymbol{F} = \boldsymbol{F}_A + \boldsymbol{F}_T + \boldsymbol{F}_G \tag{4.26}$$

$$\boldsymbol{M} = \boldsymbol{M}_A + \boldsymbol{M}_T \tag{4.27}$$

Since the moment equation is written with respect to the centre of gravity, the moment due to the gravity is omitted in Equation (4.27). For the aerodynamic forces, the following holds,

$$\boldsymbol{F}_A = \begin{bmatrix} X \\ Y \\ Z \end{bmatrix} = \bar{q}S \begin{bmatrix} C_X \\ C_Y \\ C_Z \end{bmatrix} \tag{4.28}$$

where, C_X, C_Y and C_Z are non-dimensional aerodynamic force coefficients in the body-axes, $\bar{q}$ is the dynamic pressure, and S denotes the aircraft reference area. Dynamic pressure $\bar{q}$ is a function of the air density ρ which is given by:

$$\bar{q} = \frac{1}{2}\rho(U^2 + V^2 + W^2) = \frac{1}{2}\rho V^2 \tag{4.29}$$

In Equation (4.26), the thrust force F_T is given by:

$$\boldsymbol{F}_T = \begin{bmatrix} T_X \\ T_Y \\ T_Z \end{bmatrix} \tag{4.30}$$

where, T_X, T_Y and T_Z are the engine trust components in the body frame. The gravity force F_G is given by:

$$\boldsymbol{F}_G = m\boldsymbol{g} \tag{4.31}$$

where, $\boldsymbol{g}$ is the gravitational acceleration vector expressed in the body frame,

$$\boldsymbol{g} = \begin{bmatrix} g_x \\ g_y \\ g_z \end{bmatrix} = \begin{bmatrix} 1 & 0 & 0 \\ 0 & cos\varphi & sin\varphi \\ 0 & -sin\varphi & cos\varphi \end{bmatrix} \begin{bmatrix} cos\theta & 0 & -sin\theta \\ 0 & 1 & 0 \\ sin\theta & 0 & cos\theta \end{bmatrix} \begin{bmatrix} cos\psi & sin\psi & 0 \\ -sin\psi & cos\psi & 0 \\ 0 & 0 & 1 \end{bmatrix} \begin{bmatrix} 0 \\ 0 \\ g \end{bmatrix} \tag{4.32}$$

$\boldsymbol{g}$ can be simplified as:

$$\boldsymbol{g} = \begin{bmatrix} g_x \\ g_y \\ g_z \end{bmatrix} = \begin{bmatrix} -gsin\theta \\ gsin\varphi cos\theta \\ gcos\varphi cos\theta \end{bmatrix} \tag{4.33}$$

Therefore,

$$\boldsymbol{F}_G = m\begin{bmatrix} g_x \\ g_y \\ g_z \end{bmatrix} = \begin{bmatrix} -mgsin\theta \\ mgsin\varphi cos\theta \\ mgcos\varphi cos\theta \end{bmatrix} \tag{4.34}$$

By combining Equations (4.20) to (4.22), (4.26), (4.28) and (4.34), the followings can be derived:

$$F_x = m\left(\dot{U} + qW - rV\right) = T_X + \bar{q}SC_X - mgsin\theta \tag{4.35}$$

$$F_y = m\left(\dot{V} + rU - pW\right) = T_Y + \bar{q}SC_Y + mgsin\varphi cos\theta \tag{4.36}$$

$$F_z = m\left(\dot{W} + pV - qU\right) = T_Z + \bar{q}SC_Z + mgcos\varphi cos\theta \tag{4.37}$$

where *u*, *v* and *w* are linear velocity (air-speed) components; *p*, *q* and *r* are angular velocity components (measured by the gyroscopes onboard) in the aircraft body frame; φ and θ are the roll and pitch attitude of the aircraft, which describe the aircraft body orientation with respect to the inertial reference frame.

The right hand side of Equations (4.35), (4.36) and (4.37) can be written in terms of wind axes components (drag, lift and side force) as the following:

$$F_x = m\left(\dot{U} + qW - rV\right) = T_X - Dcos\alpha + Lsin\alpha - mgsin\theta \tag{4.38}$$

$$F_y = m\left(\dot{V} + rU - pW\right) = T_Y + Y + mgsin\varphi cos\theta \tag{4.39}$$

$$F_z = m\left(\dot{W} + pV - qU\right) = T_Z - Dsin\alpha - Lcos\alpha + mgcos\varphi cos\theta \tag{4.40}$$

where *D*, *Y* and *L* are drag, sideslip and lift forces, respectively:

$$\begin{bmatrix} D \\ Y \\ L \end{bmatrix} = \bar{q}S \begin{bmatrix} C_D \\ C_Y \\ C_L \end{bmatrix} \tag{4.41}$$

where C_D, C_Y and C_L in Equation (4.41) are dimensionless drag, sideslip and lift force coefficients, respectively. For the specific situation in which the sideslip angle β=0, the body axes force coefficients are related to the wind axes force coefficients by angle of attack α as:

$$C_L = -C_Z cos\alpha + C_X sin\alpha \tag{4.42}$$

$$C_D = -C_X cos\alpha - C_Z sin\alpha \tag{4.43}$$

Next, the moment equations are derived in the components form expressed in the body coordinate system. For the moment components in Equation (4.27), the following relation holds:

$$\boldsymbol{M}_A = \begin{bmatrix} l \\ m \\ n \end{bmatrix} = \bar{q}S \begin{bmatrix} bC_l \\ \bar{c}C_m \\ bC_n \end{bmatrix} \tag{4.44}$$

where C_l, C_m and C_n are dimensionless rolling, pitching and yawing moment coefficients, respectively.

$$\boldsymbol{M}_T = \begin{bmatrix} M_{T_x} \\ M_{T_y} \\ M_{T_z} \end{bmatrix} = \begin{bmatrix} 0 \\ I_p \Omega_p r \\ -I_p \Omega_p q \end{bmatrix} \tag{4.45}$$

where I_p is the inertia of the rotating mass, such as the propeller, and Ω_p is its angular velocity, q and r are the pitch and yaw rate of the aircraft body. By combining Equations (4.23), (4.24), (4.25), (4.27), (4.44) and (4.45), the following are derived:

$$M_x = I_{xx}\dot{p} - I_{xz}\dot{r} - I_{xz}pq + \left(I_{zz} - I_{yy}\right)qr = \bar{q}SbC_l + M_{T_x} \tag{4.46}$$

$$M_y = I_{yy}\dot{q} + (I_{xx} - I_{zz})pr + I_{xz}(p^2 - r^2) = \bar{q}S\bar{c}C_m + M_{T_y} \tag{4.47}$$

$$M_z = I_{zz}\dot{r} - I_{xz}\dot{p} + I_{xz}qr + \left(I_{yy} - I_{xx}\right)pq = \bar{q}SbC_n + M_{T_z} \tag{4.48}$$

The equations of motion discussed above can be summarized as four parts: force, moment, kinematics and navigation equations. They are described in Sections 4.1.1 to 4.1.4.

4.1.1 Force equations

The force equations in the body axes coordinate system are given by Equations (4.35) to (4.37), which can be rewritten as:

$$\dot{U} = rV - qW + \frac{T}{m} + \frac{\bar{q}SC_X}{m} - gsin\theta \tag{4.49}$$

$$\dot{V} = pW - rU + \frac{\bar{q}SC_Y}{m} + gcos\theta sin\varphi \tag{4.50}$$

$$\dot{W} = qU - pV + \frac{\bar{q}SC_Z}{m} + gcos\theta \cos\varphi \tag{4.51}$$

They can also be given with respect to wind-axes coordinate system as:

$$\dot{V} = -\frac{\bar{q}S}{m}C_{D_w} + \frac{T}{m}cos\alpha cos\beta + g(cos\varphi cos\theta sin\alpha cos\beta + sin\varphi cos\theta sin\beta - sin\theta cos\alpha cos\beta) \tag{4.52}$$

$$\dot{\alpha} = -\frac{\bar{q}S}{mVcos\beta}C_L + q - tan\beta(pcos\alpha + rsin\alpha) + \frac{g}{Vcos\beta}(cos\varphi cos\theta cos\alpha + sin\theta sin\alpha) - \frac{Tsin\alpha}{mVcos\beta} \tag{4.53}$$

$$\dot{\beta} = \frac{\bar{q}S}{mV}C_{Y_w} + psin\alpha - rcos\alpha + \frac{g}{V}cos\beta sin\varphi cos\theta + \frac{sin\beta}{V}(gcos\alpha sin\theta - gsin\alpha cos\varphi cos\theta + \frac{Tcos\alpha}{m}) \tag{4.54}$$

where,

$$C_{D_w} = -C_X cos\alpha cos\beta - C_Y sin\beta - C_Z sin\alpha cos\beta = C_D cos\beta - C_Y sin\beta \tag{4.55}$$

$$C_{Y_w} = -C_X cos\alpha sin\beta + C_Y cos\beta - C_Z sin\alpha sin\beta = C_Y cos\beta - C_D sin\beta \tag{4.56}$$

$$V = \sqrt{U^2 + {V_L}^2 + W^2} \tag{4.57}$$

$$\alpha = tan^{-1}(\frac{W}{U}) \tag{4.58}$$

$$\beta = sin^{-1}(\frac{V_L}{V}) \tag{4.59}$$

V_L in Equations (4.57) and (4.59) is the total velocity component in a lateral direction. V is the total velocity while α and β are incidence and sideslip angles respectively. Positive directions of the lift force coefficient C_L and the drag force coefficient C_D are along the $-z_s$ and $-x_s$ stability axes (referring to Figure 3.2), whereas positive directions of wind-axes drag coefficient C_{Dw} and side force coefficient C_{Yw} are along $-x_w$ and $+y_w$ axes, respectively.

The onboard accelerometers can sense all the specific forces except those from gravity. Therefore, the general equation of the translational acceleration can be written as:

$$\boldsymbol{a} = \dot{\boldsymbol{V}} + \boldsymbol{\omega} \times \boldsymbol{V} - \frac{\boldsymbol{F}_G}{m} = \frac{1}{m}(\boldsymbol{F}_A + \boldsymbol{F}_T) \tag{4.60}$$

which can be rewritten in the extended form as,

$$a_x = \dot{U} - rV + qW + gsin\theta = \frac{1}{m}(\bar{q}SC_X + T) \tag{4.61}$$

$$a_y = \dot{V} - pW + rU - gcos\theta sin\varphi = \frac{1}{m}(\bar{q}SC_Y) \tag{4.62}$$

$$a_z = \dot{W} - qU + pV - gcos\theta cos\varphi = \frac{1}{m}(\bar{q}SC_Z) \tag{4.63}$$

and,

$$C_X = \frac{ma_x - T}{\bar{q}S} \tag{4.64}$$

$$C_Y = \frac{ma_y}{\bar{q}S} \tag{4.65}$$

$$C_Z = \frac{ma_z}{\bar{q}S} \tag{4.66}$$

In Equations (4.64) to (4.66), all the quantities are measurable or computable for system identification, by using flight test data. For aircraft modeling, however, the acceleration components are all unknowns; thus, they need to be described using the aerodynamic equations which will be discussed in Sections 4.2 and 4.4. For using the aerodynamic equations, the aerodynamic derivatives need to be identified in advance. This is another motivation for carrying out system identification for UAVs.

4.1.2 Moment equations

Referring to Equations (4.46) to (4.48), the moment equations can be rewritten as:

$$\dot{p} = \frac{I_{xz}}{I_x}\dot{r} + \frac{\bar{q}Sb}{I_x}C_l - \frac{I_z - I_y}{I_x}qr + \frac{I_{xz}}{I_x}qp \tag{4.67}$$

$$\dot{q} = \frac{\bar{q}S\bar{c}}{I_y}C_m - \frac{I_x - I_z}{I_y}pr - \frac{I_{xz}}{I_y}(p^2 - r^2) + \frac{I_p}{I_y}\Omega_p r \tag{4.68}$$

$$\dot{r} = \frac{I_{xz}}{I_z}\dot{p} + \frac{\bar{q}Sb}{I_z}C_n - \frac{I_y - I_x}{I_z}pq - \frac{I_{xz}}{I_z}qr - \frac{I_p}{I_z}\Omega_p q \tag{4.69}$$

where Ω_p is the propeller angular rate.

4.1.3 Kinematics equations

Kinematics equations describe the attitudes of the aircraft. Equations (4.70) to (4.72) give the roll, pitch and yaw angular rates as functions of the angular rates in the body coordinate system:

$$\dot{\varphi} = p + tan\theta(qsin\varphi + rcos\varphi) \tag{4.70}$$

$$\dot{\theta} = qcos\varphi - rsin\varphi \tag{4.71}$$

$$\dot{\psi} = \frac{qsin\varphi + rcos\varphi}{cos\theta} \tag{4.72}$$

4.1.4 Navigation equations

Navigation equations depict the aircraft's position with respect to the earth axes coordinate system, which are shown as:

$$\dot{x}_E = Vcos\alpha cos\beta cos\psi cos\theta + Vsin\beta(cos\psi sin\theta sin\varphi - sin\psi cos\varphi) + Vsin\alpha cos\beta(cos\psi sin\theta cos\varphi + sin\psi sin\varphi) \tag{4.73}$$

$$\dot{y}_E = Vcos\alpha cos\beta sin\psi cos\theta + Vsin\beta(sin\psi sin\theta sin\varphi + cos\psi cos\varphi) + Vsin\alpha cos\beta(sin\psi sin\theta sin\varphi - cos\psi sin\varphi) \tag{4.74}$$

$$\dot{h} = Vcos\alpha cos\beta sin\theta - Vsin\beta cos\theta sin\varphi - Vsin\alpha cos\beta cos\theta cos\varphi \tag{4.75}$$

The force, moment, kinematics and navigation equations described above are developed under the following assumptions (Klein and Morelli, 2006):

i. the aircraft body is rigid;

ii. the earth surface is flat;

iii. the aircraft mass and its distribution are constants;

iv. the aircraft's mass and geometry is symmetrical about its plane of symmetry;

v. direction thrust is along the *ox* body axis and through the center of gravity;

vi. the earth is fixed in inertial space.

The aircraft motion equations can further be expressed in general form by a set of first order nonlinear differential equations:

$$\dot{\boldsymbol{x}} = f(\boldsymbol{x}, \boldsymbol{u}) \tag{4.76}$$

where $\boldsymbol{x}$ is a vector of state variables: $\boldsymbol{x} = [u, v, w, p, q, r, \varphi, \theta, \psi, x_E, y_E, h]^T$ in body axes coordinate system (except for x_E, y_E, h); $\boldsymbol{x} = [V, \alpha, \beta, p, q, r, \varphi, \theta, \psi, x_E, y_E, h]^T$ with respect to wind axes coordinate system (except for x_E, y_E, h). $\boldsymbol{u} = [\delta_{th}, \delta_a, \delta_e, \delta_r]^T$ is a vector of inputs, which is composed of throttle position and control surfaces such as elevator, aileron and rudder deflections. The input variables are not shown in the force and moment equations above, but they are included implicitly, since they influence the motion of aircraft.

Output variables of the aircraft mathematical model are measured aircraft responses: $\boldsymbol{y} = [V, \alpha, \beta, p, q, r, \varphi, \theta, \psi, h, a_x, a_y, a_z, \dot{p}, \dot{q}, \dot{r}]^T$. The quantities x_E and y_E are not included, since they are not related to the aircraft dynamics. Position variable h is included, because it has effect on the air density and air pressure (Klein and Morelli, 2006). The output equations show the dependency of the output variables, to the aircraft states, state derivatives and control inputs. The output equations can be written in a general form as,

$$\boldsymbol{y} = h(\boldsymbol{x}, \dot{\boldsymbol{x}}, \boldsymbol{u}) \tag{4.77}$$

Quantities V, α, β, p, q, r, φ, θ and ψ are both states and outputs (referring to Equations (4.49) to (4.51), and (4.67) to (4.75)).

4.2 Aerodynamic terms

When the aircraft is excited by an input from autopilot command or wind/gust disturbances, it deviates from its equilibrium state and the balance of the aircraft is broken. In this research, it is assumed that aerodynamic force and the moment terms are only dependent on the disturbed motion variables. The aerodynamic force and the moment can be expressed mathematically as the sum of a number of Taylor series which is shown as (Cook, 2013):

$$
\begin{aligned}
X_a = X_{a_e} &+ \left(\frac{\partial X}{\partial u}u + \frac{\partial^2 X}{\partial u^2}\frac{u^2}{2!} + \frac{\partial^3 X}{\partial u^3}\frac{u^3}{3!} + \frac{\partial^4 X}{\partial u^4}\frac{u^4}{4!} + \cdots\right) \\
&+ \left(\frac{\partial \mathrm{X}}{\partial \mathrm{v}}\mathrm{v} + \frac{\partial^2 \mathrm{X}}{\partial \mathrm{v}^2}\frac{\mathrm{v}^2}{2!} + \frac{\partial^3 \mathrm{X}}{\partial \mathrm{v}^3}\frac{\mathrm{v}^3}{3!} + \frac{\partial^4 \mathrm{X}}{\partial \mathrm{v}^4}\frac{\mathrm{v}^4}{4!} + \cdots\right) \\
&+ \left(\frac{\partial X}{\partial w}w + \frac{\partial^2 X}{\partial w^2}\frac{w^2}{2!} + \frac{\partial^3 X}{\partial w^3}\frac{w^3}{3!} + \frac{\partial^4 X}{\partial w^4}\frac{w^4}{4!} + \cdots\right) \\
&+ \left(\frac{\partial X}{\partial p}p + \frac{\partial^2 X}{\partial p^2}\frac{p^2}{2!} + \frac{\partial^3 X}{\partial p^3}\frac{p}{3!} + \frac{\partial^4 X}{\partial p^4}\frac{p^4}{4!} + \cdots\right) \\
&+ \left(\frac{\partial X}{\partial q}q + \frac{\partial^2 X}{\partial q^2}\frac{q^2}{2!} + \frac{\partial^3 X}{\partial q^3}\frac{q^3}{3!} + \frac{\partial^4 X}{\partial q^4}\frac{q^4}{4!} + \cdots\right) \\
&+ \left(\frac{\partial X}{\partial r}r + \frac{\partial^2 X}{\partial r^2}\frac{r^2}{2!} + \frac{\partial^3 X}{\partial r^3}\frac{r^3}{3!} + \frac{\partial^4 X}{\partial r^4}\frac{r^4}{4!} + \cdots\right) \\
&+ \left(\frac{\partial X}{\partial \dot{u}}\dot{u} + \frac{\partial^2 X}{\partial \dot{u}^2}\frac{\dot{u}^2}{2!} + \frac{\partial^3 X}{\partial \dot{u}^3}\frac{\dot{u}^3}{3!} + \frac{\partial^4 X}{\partial \dot{u}^4}\frac{\dot{u}^4}{4!} + \cdots\right)
\end{aligned}
\tag{4.78}
$$

$$+\left(\frac{\partial X}{\partial \dot{v}}\dot{v}+\frac{\partial^2 X}{\partial \dot{v}^2}\frac{\dot{v}^2}{2!}+\frac{\partial^3 X}{\partial \dot{v}^3}\frac{\dot{v}^3}{3!}+\frac{\partial^4 X}{\partial \dot{v}^4}\frac{\dot{v}^4}{4!}+\cdots\right)$$

$$+series\ terms\ in\ \dot{w},\dot{p},\dot{q},\dot{r}$$

$$+series\ terms\ in\ higher\ order\ derivatives$$

where, X_{a_e} is a constant term. For small perturbations, only the first term of each series is significant. Further, for higher order derivative terms, only terms that involve $\dot{w}$ are significant. Therefore, Equation (4.78) can be truncated and simplified in linear format as (Cook, 2013):

$$X_a = X_{a_e}+\frac{\partial X}{\partial u}u+\frac{\partial X}{\partial v}v+\frac{\partial X}{\partial w}w+\frac{\partial X}{\partial p}p+\frac{\partial X}{\partial q}q+\frac{\partial X}{\partial r}r+\frac{\partial X}{\partial \dot{w}}\dot{w} \tag{4.79}$$

By defining $\mathring{\mathrm{X}}_u = \frac{\partial X}{\partial u}$ and extending this manner to other terms, Equation (4.79) can be rewritten with the shorthand notations as:

$$\mathrm{X}_a = \mathrm{X}_{a_e}+\mathring{\mathrm{X}}_u u+\mathring{\mathrm{X}}_v v+\mathring{\mathrm{X}}_w w+\mathring{\mathrm{X}}_p p+\mathring{\mathrm{X}}_q q+\mathring{\mathrm{X}}_{\mathrm{r}} r+\mathring{\mathrm{X}}_{\dot{w}}\dot{w} \tag{4.80}$$

where, coefficients $\mathring{\mathrm{X}}_u$, $\mathring{\mathrm{X}}_v$, $\mathring{\mathrm{X}}_w$, $\mathring{\mathrm{X}}_p$, $\mathring{\mathrm{X}}_q$, $\mathring{\mathrm{X}}_{\mathrm{r}}$ and $\mathring{\mathrm{X}}_{\dot{w}}$ are known as aerodynamic stability derivatives. The dressing " ° " denotes that they are dimensional. Equation (4.80) can also be written in dimensionless form as (Klein and Morelli, 2006):

$$C_{X_a} = C_{X_{a_e}}+C_{X_u}\hat{u}++C_{X_v}\hat{v}+C_{X_w}\hat{w}+C_{X_p}\hat{p}+C_{X_q}\hat{q}+C_{X_r}\hat{r}+C_{X_{\dot{w}}}\hat{\dot{w}} \tag{4.81}$$

where, $\hat{u}$, $\hat{v}$, $\hat{w}$, $\hat{p}$, $\hat{q}$, $\hat{r}$ and $\hat{\dot{w}}$ are non-dimensionalized u, v, w, p, q, r and $\dot{w}$, respectively. The conversions between dimensional and non-dimensional variables are expressed as (Klein and Morelli, 2006):

$$\hat{V} = \frac{V}{V_0} \quad \hat{p} = \frac{pb}{2V} \quad \hat{q} = \frac{q\bar{c}}{2V} \quad \hat{r} = \frac{rb}{2V} \quad \hat{\dot{\alpha}} = \frac{\dot{\alpha}\bar{c}}{2V} \quad \hat{\dot{\beta}} = \frac{\dot{\beta}\bar{c}}{2V} \tag{4.82}$$

Equation (4.81) can be further expressed as:

$$C_i = C_i(\frac{u}{V_0}, \frac{v}{V_0}, \frac{w}{V_0}, \frac{pb}{2V}, \frac{q\bar{c}}{2V}, \frac{rb}{2V}, \frac{\dot{w}\bar{c}}{2V}, \delta) \tag{4.83}$$

where, $i = D, Y, L, l, m, n$. V_0 is the airspeed at the equilibrium condition also known as trim, δ stands for the control inputs, which can be elevator, aileron or rudder deflection.

4.3 Equations of motion for small perturbations

When the aircraft is perturbed from the steady state flight, the aircraft will have a perturbation, which is a response to the input excitation. The full aircraft motion equations are comprised of aerodynamic force, gravitational, aerodynamic control and thrust terms. The equations can be written by combining Equations (4.35) to (4.37), (4.46) to (4.48), and (4.78). Since the aircraft is assumed to be initially flying in trimming state, the roll, yaw and sideslip angles are all zeroes, and the angular rates are all zeroes or negligibly small. Because the sideslip angle is 0, therefore V_e=0. According to definition, quantities u, v, w, p, q and r are small; therefore, the terms involving their products and squares can be ignored. Also by removing the higher order terms of the motion variables, Equations (4.84) to (4.89) are obtained (Cook, 2013):

$$m(\dot{u} + qW_e) = \mathrm{X}_{a_e} + \mathring{\mathrm{X}}_u u + \mathring{\mathrm{X}}_v v + \mathring{\mathrm{X}}_w w + \mathring{\mathrm{X}}_p p + \mathring{\mathrm{X}}_q q + \mathring{\mathrm{X}}_r r + \mathring{\mathrm{X}}_{\dot{w}} \dot{w} - mgsin\theta_e$$
$$-mg\theta cos\theta_e + \mathring{\mathrm{X}}_\xi \xi + \mathring{\mathrm{X}}_\eta \eta + \mathring{\mathrm{X}}_\zeta \zeta + \mathring{\mathrm{X}}_\tau \tau \tag{4.84}$$

$$m(\dot{v} - pW_e + rU_e) = \mathrm{Y}_{a_e} + \mathring{\mathrm{Y}}_u u + \mathring{\mathrm{Y}}_v v + \mathring{\mathrm{Y}}_w w + \mathring{\mathrm{Y}}_p p + \mathring{\mathrm{Y}}_q q + \mathring{\mathrm{Y}}_r r + \mathring{\mathrm{Y}}_{\dot{w}} \dot{w} + mg\psi sin\theta_e + mg\varphi cos\theta_e + \mathring{\mathrm{Y}}_\xi \xi + \mathring{\mathrm{Y}}_\eta \eta + \mathring{\mathrm{Y}}_\zeta \zeta + \mathring{\mathrm{Y}}_\tau \tau \quad (4.85)$$

$$m(\dot{w} - qU_e) = \mathrm{Z}_{a_e} + \mathring{\mathrm{Z}}_u u + \mathring{\mathrm{Z}}_v v + \mathring{\mathrm{Z}}_w w + \mathring{\mathrm{Z}}_p p + \mathring{\mathrm{Z}}_q q + \mathring{\mathrm{Z}}_r r + \mathring{\mathrm{Z}}_{\dot{w}} \dot{w} + mgcos\theta_e - mg\theta sin\theta_e + \mathring{\mathrm{Z}}_\xi \xi + \mathring{\mathrm{Z}}_\eta \eta + \mathring{\mathrm{Z}}_\zeta \zeta + \mathring{\mathrm{Z}}_\tau \tau \quad (4.86)$$

$$I_x \dot{p} - I_{xz} \dot{r} = \mathrm{L}_{a_e} + \mathring{\mathrm{L}}_u u + \mathring{\mathrm{L}}_v v + \mathring{\mathrm{L}}_w w + \mathring{\mathrm{L}}_p p + \mathring{\mathrm{L}}_q q + \mathring{\mathrm{L}}_r r + \mathring{\mathrm{L}}_{\dot{w}} \dot{w} + \mathring{\mathrm{L}}_\xi \xi + \mathring{\mathrm{L}}_\eta \eta + \mathring{\mathrm{L}}_\zeta \zeta + \mathring{\mathrm{L}}_\tau \tau \quad (4.87)$$

$$I_y \dot{q} = \mathrm{M}_{a_e} + \mathring{\mathrm{M}}_u u + \mathring{\mathrm{M}}_v v + \mathring{\mathrm{M}}_w w + \mathring{\mathrm{M}}_p p + \mathring{\mathrm{M}}_q q + \mathring{\mathrm{M}}_r r + \mathring{\mathrm{M}}_{\dot{w}} \dot{w} + \mathring{\mathrm{M}}_\xi \xi + \mathring{\mathrm{M}}_\eta \eta + \mathring{\mathrm{M}}_\zeta \zeta + \mathring{\mathrm{M}}_\tau \tau \quad (4.88)$$

$$I_z \dot{r} - I_{xz} \dot{p} = \mathrm{N}_{a_e} + \mathrm{N}_u u + \mathrm{N}_v v + \mathrm{N}_w w + \mathrm{N}_p p + \mathrm{N}_q q + \mathrm{N}_r r + \mathrm{N}_{\dot{w}} \dot{w} + \mathrm{N}_\xi \xi + \mathrm{N}_\eta \eta + \mathrm{N}_\zeta \zeta + \mathrm{N}_\tau \tau \quad (4.89)$$

In Equation (4.86), $(-mgsin\theta_e - mg\theta cos\theta_e)$ is the gravitational effect, $(\mathring{\mathrm{X}}_\xi \xi + \mathring{\mathrm{X}}_\eta \eta + \mathring{\mathrm{X}}_\zeta \zeta)$ is the aerodynamic control term, $\mathring{\mathrm{X}}_\tau \tau$ is the thrust term, and the other terms are aerodynamic terms. These definitions are applicable for the other equations above. At steady state, there is no perturbation. Therefore, some of the terms in Equations (4.84) to (4.89) are reduced to the following equalities for the magnitudes of the aerodynamic forces and moments at the trim condition:

$$\mathrm{X}_{a_e} = mgsin\theta_e \quad (4.90)$$

$$\mathrm{Y}_{a_e} = 0 \quad (4.91)$$

$$\mathrm{Z}_{a_e} = -mgcos\theta_e \quad (4.92)$$

$$\mathrm{L}_{a_e} = 0 \quad (4.93)$$

$$M_{a_e} = 0 \tag{4.94}$$

$$N_{a_e} = 0 \tag{4.95}$$

By substituting Equations (4.90) to (4.95) into Equations (4.84) to (4.89), the aircraft's perturbed equations of motion can be written as (Cook, 2013):

$$m(\dot{u} + qW_e) = \mathring{X}_u u + \mathring{X}_v v + \mathring{X}_w w + \mathring{X}_p p + \mathring{X}_q q + \mathring{X}_r r + \mathring{X}_{\dot{w}} \dot{w} - mg\theta cos\theta_e + \mathring{X}_\xi \xi + \mathring{X}_\eta \eta + \mathring{X}_\zeta \zeta + \mathring{X}_\tau \tau \tag{4.96}$$

$$m(\dot{v} - pW_e + rU_e) = \mathring{Y}_u u + \mathring{Y}_v v + \mathring{Y}_w w + \mathring{Y}_p p + \mathring{Y}_q q + \mathring{Y}_r r + \mathring{Y}_{\dot{w}} \dot{w} + mg\psi sin\theta_e + mg\varphi cos\theta_e + \mathring{Y}_\xi \xi + \mathring{Y}_\eta \eta + \mathring{Y}_\zeta \zeta + \mathring{Y}_\tau \tau \tag{4.97}$$

$$m(\dot{w} - qU_e) = \mathring{Z}_u u + \mathring{Z}_v v + \mathring{Z}_w w + \mathring{Z}_p p + \mathring{Z}_q q + \mathring{Z}_r r + \mathring{Z}_{\dot{w}} \dot{w} - mg\theta sin\theta_e + \mathring{Z}_\xi \xi + \mathring{Z}_\eta \eta + \mathring{Z}_\zeta \zeta + \mathring{Z}_\tau \tau \tag{4.98}$$

$$I_x \dot{p} - I_{xz} \dot{r} = \mathring{L}_u u + \mathring{L}_v v + \mathring{L}_w w + \mathring{L}_p p + \mathring{L}_q q + \mathring{L}_r r + \mathring{L}_{\dot{w}} \dot{w} + \mathring{L}_\xi \xi + \mathring{L}_\eta \eta + \mathring{L}_\zeta \zeta + \mathring{L}_\tau \tau \tag{4.99}$$

$$I_y \dot{q} = \mathring{M}_u u + \mathring{M}_v v + \mathring{M}_w w + \mathring{M}_p p + \mathring{M}_q q + \mathring{M}_r r + \mathring{M}_{\dot{w}} \dot{w} + \mathring{M}_\xi \xi + \mathring{M}_\eta \eta + \mathring{M}_\zeta \zeta + \mathring{M}_\tau \tau \tag{4.100}$$

$$I_z \dot{r} - I_{xz} \dot{p} = \mathring{N}_u u + \mathring{N}_v v + \mathring{N}_w w + \mathring{N}_p p + \mathring{N}_q q + \mathring{N}_r r + \mathring{N}_{\dot{w}} \dot{w} + \mathring{N}_\xi \xi + \mathring{N}_\eta \eta + \mathring{N}_\zeta \zeta + \mathring{N}_\tau \tau \tag{4.101}$$

4.4 Decoupled motion equations

4.4.1 Longitudinal motion equations

The motion equations (4.96) to (4.101) can be further decoupled and simplified. By keeping only the longitudinal channel related input and states, and setting the lateral channel related inputs and states to zero, decoupled longitudinal channel equations can be obtained. In this case, the aileron

and rudder perturbations, states, *v*, *p* and *r* are all zeroes. Therefore Equations (4.96), (4.98) and (4.100) can be simplified as (Cook, 2013):

$$m\dot{u} - \mathring{\mathrm{X}}_{\mathrm{u}}u - \mathring{\mathrm{X}}_{\mathrm{w}}w - \mathring{\mathrm{X}}_{\dot{\mathrm{w}}}\dot{w} - \left(\mathring{\mathrm{X}}_{\mathrm{q}} - mW_e\right)q + mg\theta cos\theta_e = \mathring{\mathrm{X}}_{\eta}\eta + \mathring{\mathrm{X}}_{\boldsymbol{\tau}}\tau \tag{4.102}$$

$$-\mathring{\mathrm{Z}}_{\mathrm{u}}u + (m - \mathring{\mathrm{Z}}_{\dot{\mathrm{w}}})\dot{w} - \mathring{\mathrm{Z}}_{\mathrm{w}}w - (\mathring{\mathrm{Z}}_{\mathrm{q}} + mU_e)q + mg\theta sin\theta_e = \mathring{\mathrm{Z}}_{\eta}\eta + \mathring{\mathrm{Z}}_{\boldsymbol{\tau}}\tau \tag{4.103}$$

$$I_y\dot{q} - \mathring{\mathrm{M}}_{\mathrm{u}}u - \mathring{\mathrm{M}}_{\mathrm{w}}w - \mathring{\mathrm{M}}_{\mathrm{q}}q - \mathring{\mathrm{M}}_{\dot{\mathrm{w}}}\dot{w} = \mathring{\mathrm{M}}_{\eta}\eta + \mathring{\mathrm{M}}_{\boldsymbol{\tau}}\tau \tag{4.104}$$

Equations (4.102) to (4.104) can be further written as,

$$\dot{u} = \frac{\mathring{\mathrm{X}}_{\mathrm{u}}}{m}u + \frac{\mathring{\mathrm{X}}_{\mathrm{w}}}{m}w + \frac{\mathring{\mathrm{X}}_{\dot{\mathrm{w}}}}{m}\dot{w} + \left(\frac{\mathring{\mathrm{X}}_{\mathrm{q}}}{m} - W_e\right)q - g\theta cos\theta_e + \mathring{\mathrm{X}}_{\eta}\eta + \mathring{\mathrm{X}}_{\tau}\tau \tag{4.105}$$

$$\dot{w} = \frac{\mathring{\mathrm{Z}}_{\mathrm{u}}}{m}u + \frac{\mathring{\mathrm{Z}}_{\dot{\mathrm{w}}}}{m}\dot{w} + \frac{\mathring{\mathrm{Z}}_{\mathrm{w}}}{m}w + \left(\frac{\mathring{\mathrm{Z}}_{\mathrm{q}}}{m} + U_e\right)q - g\theta sin\theta_e + \mathring{\mathrm{Z}}_{\eta}\eta + \mathring{\mathrm{Z}}_{\tau}\tau \tag{4.106}$$

$$\dot{q} = \frac{\mathring{\mathrm{M}}_{\mathrm{u}}}{I_y}u + \frac{\mathring{\mathrm{M}}_{\mathrm{w}}}{I_y}w + \frac{\mathring{\mathrm{M}}_{\mathrm{q}}}{I_y}q + \frac{\mathring{\mathrm{M}}_{\dot{\mathrm{w}}}}{I_y}\dot{w} + \frac{\mathring{\mathrm{M}}_{\eta}}{I_y}\eta + \frac{\mathring{\mathrm{M}}_{\boldsymbol{\tau}}}{I_y}\tau \tag{4.107}$$

The aerodynamic derivatives with "$^{\circ}$" dressing in above equations are dimensional derivatives in British notation. In this thesis, North American notations are used, Equations (4.105) to (4.107) can then be rewritten by using North American notations as:

$$\dot{u} = \mathrm{X}_u u + \mathrm{X}_w w + \mathrm{X}_{\dot{w}}\dot{w} + \left(\mathrm{X}_q - W_e\right)q - g\theta cos\theta_e + \mathrm{X}_{\delta_e}\delta_e + \mathrm{X}_{\delta_{th}}\delta_{th} \tag{4.108}$$

$$\dot{w} = \mathrm{Z}_u u + \mathrm{Z}_w w + \mathrm{Z}_{\dot{w}}\dot{w} + \left(\mathrm{Z}_q + U_e\right)q - g\theta sin\theta_e + \mathrm{Z}_{\delta_e}\delta_e + \mathrm{Z}_{\delta_{th}}\delta_{th} \tag{4.109}$$

$$\dot{q} = \mathrm{M}_u u + \mathrm{M}_w w + \mathrm{M}_{\dot{w}}\dot{w} + \mathrm{M}_q q + \mathrm{M}_{\delta_e}\delta_e + \mathrm{M}_{\delta_{th}}\delta_{th} \tag{4.110}$$

Where, δ_e and δ_{th} stand for elevator and propeller thrust perturbations in American notation, which correspond to η and τ in British notation. The aerodynamic derivatives used in Equations

(4.108) to (4.110) are the ones needed to be identified through system identification, which is the main objective of this research. Usually propeller thrust is constant; thus, propeller thrust perturbation can be set to zero. The reduced order model of the aircraft given by Equations (4.108) to (4.110) can also be written in the following matrix form (Cook, 2013):

$$\begin{bmatrix} 1 & -\mathrm{X}_{\dot{w}} & 0 & 0 \\ 0 & 1-\mathrm{Z}_{\dot{w}} & 0 & 0 \\ 0 & -\mathrm{M}_{\dot{w}} & 1 & 0 \\ 0 & 0 & 0 & 1 \end{bmatrix} \begin{bmatrix} \dot{u} \\ \dot{w} \\ \dot{q} \\ \dot{\theta} \end{bmatrix} = \begin{bmatrix} \mathrm{X}_u & \mathrm{X}_w & \mathrm{X}_q - W_e & -g\cos\theta_e \\ \mathrm{Z}_u & \mathrm{Z}_w & \mathrm{Z}_q + U_e & -g\sin\theta_e \\ \mathrm{M}_u & \mathrm{M}_w & \mathrm{M}_q & 0 \\ 0 & 0 & 1 & 0 \end{bmatrix} \begin{bmatrix} u \\ w \\ q \\ \theta \end{bmatrix} + \begin{bmatrix} \mathrm{X}_{\delta_e} \\ \mathrm{Z}_{\delta_e} \\ \mathrm{M}_{\delta_e} \\ 0 \end{bmatrix} \delta_e \qquad (4.111)$$

Equation (4.111) can be written as,

$$\boldsymbol{M}\dot{\boldsymbol{x}}(t) = \boldsymbol{A}'\boldsymbol{x}(t) + \boldsymbol{B}'\boldsymbol{u}(t) \qquad (4.112)$$

which can also be further rewritten as,

$$\dot{\boldsymbol{x}}(t) = \boldsymbol{M}^{-1}\boldsymbol{A}'\boldsymbol{x}(t) + \boldsymbol{M}^{-1}\boldsymbol{B}'\boldsymbol{u}(t) \qquad (4.113)$$

Therefore the reduced order longitudinal state equation can be derived from Equations (4.111) and (4.113) as,

$$\begin{bmatrix} \dot{u} \\ \dot{w} \\ \dot{q} \\ \dot{\theta} \end{bmatrix} = \begin{bmatrix} x_u & x_w & x_q & x_\theta \\ z_u & z_w & z_q & z_\theta \\ m_u & m_w & m_q & m_\theta \\ 0 & 0 & 1 & 0 \end{bmatrix} \begin{bmatrix} u \\ w \\ q \\ \theta \end{bmatrix} + \begin{bmatrix} x_\eta \\ z_\eta \\ m_\eta \\ 0 \end{bmatrix} \eta \qquad (4.114)$$

The conversion between x_u and X_u is shown in Appendix 1, and the other coefficients' conversions are also shown in Appendix 1. Equation (4.114) can be expressed in general equation as,

$$\dot{\boldsymbol{x}}(t) = \mathbf{A}\boldsymbol{x}(t) + \mathbf{B}\boldsymbol{u}(t) \qquad (4.115)$$

where $\boldsymbol{x}$ is called state vector, $\boldsymbol{u}$ is input vector, **A** is state matrix, and **B** is input matrix. The coefficients in matrix **A** and **B** are the aerodynamic derivatives needed to be identified in this research. Usually the output equation is written as,

$$\boldsymbol{y}(t) = \mathbf{C}\boldsymbol{x}(t) + \mathbf{D}\boldsymbol{u}(t) \tag{4.116}$$

which is usually combined with Equation (4.115) to describe the full aircraft motion. Commonly the aircraft output vector is the same as the state vector. In this case **C** is an identity matrix and **D** is a zero matrix.

In aircraft system identification, sometimes it is more convenient to use dimensionless aerodynamic parameters like C_D, C_X, C_L or C_Z, C_Y, C_l, C_m, C_n than dimensional derivatives. Since dimensionless derivatives remove the known dependence on the airspeed and air density (dynamic pressure), they are normalised partial derivatives. The aerodynamic equations (4.108) to (4.110) can be written as general dimensionless format as:

$$C_a = C_a(u, w, \dot{w}, q, \delta) \text{ , for } a=D, L, m \tag{4.117}$$

which is short for,

$$C_a = C_{a_0} + C_{a_u}\frac{u}{V_0} + C_{a_w}w + C_{a_{\dot{w}}}\frac{\dot{w}\bar{c}}{2V_0} + C_{a_q}\frac{q\bar{c}}{2V_0} + C_{a_\delta}\Delta\delta, \text{ for } a = L, D, m \tag{4.118}$$

where, the dimensionless coefficients are defined as:

$$C_{a_u} = V_0\frac{\partial C_a}{\partial u}|_o \tag{4.119}$$

$$C_{a_w} = \frac{\partial C_a}{\partial w}|_o \tag{4.120}$$

$$C_{a_{\dot{w}}} = \frac{2V_0}{\bar{c}} \frac{\partial C_a}{\partial \dot{w}}|_o \tag{4.121}$$

$$C_{a_q} = \frac{2V_0}{\bar{c}} \frac{\partial C_a}{\partial q}|_o \tag{4.122}$$

$$C_{a_\delta} = \frac{\partial C_a}{\partial \delta}|_o \text{ for } a = D, L, m \tag{4.123}$$

C_{a_δ} — Control derivatives.

C_{a_u} — Static stability derivatives (derivatives associated with the air-relative velocity quantities such as (*u, v, w, V, α, β*)).

C_{a_q} — Dynamic stability derivatives (derivatives associated with angular rates (*p, q, r*)).

$C_{a_{\dot{w}}}$ — Unsteady derivatives (derivatives associated with unsteady aerodynamics ($\dot{\alpha}$, $\dot{w}$)).

An example showing how to use the equations on drag force is:

$$C_D = C_{D_0} + C_{D_u} \frac{u}{V_0} + C_{D_w} w + C_{D_{\dot{w}}} \frac{\dot{w}\bar{c}}{2V_0} + C_{D_q} \frac{q\bar{c}}{2V_0} + C_{D_\delta} \Delta\delta \tag{4.124}$$

4.4.2 Lateral motion equations

Lateral motion equations can be written in concise format as (Cook, 2013):

$$m\dot{v} - \mathring{Y}_v v - \left(\mathring{Y}_p + mW_e\right)p - \left(\mathring{Y}_r - mU_e\right)r - mg\psi sin\theta_e - mg\varphi cos\theta_e = \mathring{Y}_\xi \xi + \mathring{Y}_\zeta \zeta \tag{4.125}$$

$$-\mathring{L}_v v + I_x \dot{p} - \mathring{L}_p p - I_{xz}\dot{r} - \mathring{L}_r r = \mathring{L}_\xi \xi + \mathring{L}_\zeta \zeta \tag{4.126}$$

$$-\mathring{N}_v v - I_{xz}\dot{p} - \mathring{N}_p p + I_z \dot{r} - \mathring{N}_r r = \mathring{N}_\xi \xi + \mathring{N}_\zeta \zeta \tag{4.127}$$

Recalling Equations (4.39), (4.46) and (4.48), Equations (4.125) to (4.127) can be rewritten as:

$$\mathrm{Y} = \mathring{\mathrm{Y}}_{\mathrm{v}} v + \mathring{\mathrm{Y}}_{\mathrm{p}} p + \mathring{\mathrm{Y}}_{\mathrm{r}} r + mg\psi sin\theta_e + mg\varphi cos\theta_e + \mathring{\mathrm{Y}}_{\xi}\xi + \mathring{\mathrm{Y}}_{\zeta}\zeta \tag{4.128}$$

$$\mathrm{L} = \mathring{\mathrm{L}}_{\mathrm{v}} v + \mathring{\mathrm{L}}_{\mathrm{p}} p + \mathring{\mathrm{L}}_{\mathrm{r}} r + \mathring{\mathrm{L}}_{\xi}\xi + \mathring{\mathrm{L}}_{\zeta}\zeta \tag{4.129}$$

$$\mathrm{N} = \mathring{\mathrm{N}}_{\mathrm{v}} v + \mathring{\mathrm{N}}_{\mathrm{p}} p + \mathring{\mathrm{N}}_{\mathrm{r}} r + \mathring{\mathrm{N}}_{\xi}\xi + \mathring{\mathrm{N}}_{\zeta}\zeta \tag{4.130}$$

where Y, L and N denote lateral force, rolling and yawing moment, respectively. Equations (4.128) to (4.130) can be written in general dimensionless format as:

$$C_a = C_{a_0} + C_{a_\beta}\Delta\beta + C_{a_p}\frac{pb}{2V_0} + C_{a_r}\frac{rb}{2V_0} + C_{a_\delta}\Delta\delta \quad \text{for } a = Y, l, n \tag{4.131}$$

where,

$$C_{a_\beta} = \frac{\partial C_a}{\partial \beta}|_o \tag{4.132}$$

$$C_{a_p} = \frac{2V_0}{b}\frac{\partial C_a}{\partial p}|_o \tag{4.133}$$

$$C_{a_r} = \frac{2V_0}{b}\frac{\partial C_a}{\partial r}|_o \tag{4.134}$$

$$C_{a_\delta} = \frac{\partial C_a}{\partial \delta}|_o, \text{for } a = Y, l, n \tag{4.135}$$

The decoupled equations of motion discussed above are usually the basis for system modeling and identification. The structures presented here are essential for system identification algorithm used in this thesis.

4.5 Summary

This chapter discussed the mathematical model of the aircraft system. Section 4.1 focused on equations of motion for the aircraft. The aircraft motion was described by force equations, moment equations, kinematic equations and navigation equations. Section 4.2 discussed the aircraft motion from the aerodynamic view point. In Section 4.3, the aircraft motion with respect to small perturbations was studied. It was also shown how the dynamic equations can be decoupled into longitudinal mode motion and lateral mode motion, which facilitated the reseach conducted in thus thesis.

5 Input Excitation

The quality of the system identification results is highly dependent on two points (Tischler and Remple, 2012): *i*) a properly designed and executed flight test; *ii*) an accurate system characteristics analysis. This chapter will focus on the proper input design. The recommended input excitation for frequency domain system identification is a frequency sweep signal called "Chirp". Chirp is a signal which can provide a fairly uniform spectral excitation over the frequency range of interest for high quality frequency response identification (Tischler and Remple, 2012). The topics to be covered in this chapter are: *i*) general data requirements for system identification; *ii*) optimal excitation design; *iii*) frequency sweep excitation generation.

5.1 Input excitation requirements of system identification

For system identification, the desired aircraft characteristics need to be captured in the flight tests. Thus, an eligible input excitation should be capable of exciting those characteristics of the aircraft that need to be captured. The requirements of input excitation include frequency range, excitation length and signal amplitude. Besides the requirements of input signal, the flight test condition is also essential for gathering data for system identification.

5.1.1 Frequency range

The desired frequency range of input for system identification depends on an aircraft's characteristics. The primary requirement on the frequency range is that it should include the natural frequencies. In another words, the signal's upper frequency bound should cover the

aircraft's natural frequencies. As a result, before designing the input excitation, a rough estimation of the aircraft's natural frequency needs to be made. The requirement for the high frequency part of the input excitation is also partly determined by the sampling frequency of the data recording device. For example, given a data sampling rate of 30 Hz, the frequency over the Nyquist frequency of 15 Hz cannot be recorded accurately (Dorobantu *et al.*, 2011). The fastest mode of an aircraft flight is its short period mode. Short period mode is a damped oscillation motion in pitch about the *oy* axis. For Cropcam and the delta-wing aircraft, their short period mode natural frequencies are estimated to be lower than 4 Hz; thus, a 7 Hz input frequency which includes 4 Hz frequency components is high enough to excite the aircraft characteristics.

Aircraft input excitation's low frequency part is also very important. The selection of the low frequency bound is usually depends on the aircraft's level flight time competency. For example, if an aircraft can achieve 20 seconds level flight, considering the requirements of trimming after each turn, a 10 second data window is realistic. Therefore, the signal frequency lower than 0.1 Hz cannot be identified (Dorobantu *et al.*, 2011). By trial and error, a reference input frequency range of 0.05 ~ 6 Hz is proven appropriate for the delta-wing and Cropcam aircrafts' system identification.

In data processing, the coherence distribution can be used to guide the frequency range selection. Coherence quantifies the linear correlation between input and output (Dorobantu *et al.*, 2011). The coherence function is given by:

$$\gamma_{u,y}^2(\omega) = \frac{|S_{y,u}(\omega)|^2}{S_{u,u}(\omega)S_{y,y}(\omega)} \tag{5.1}$$

where, γ^2 is coherence function, *S* represents a complex valued spectral density function, *u* is the input to the system, and *y* is the system output signal.

Coherence is an indication of the frequency response linearity. Its variation interval is 0 to 1. A high coherence indicates that there is a good linear correlation between the input and output, while a low coherence means the output was not excited by the control input (Lawler *et al*., 2006). A coherence value of zero implies that there is no correlation between input and output. A coherence value of one signifies a perfect linear correlation between input and output signals. The presence of low coherence may be caused by the nonlinearity or low signal-to-noise ratio (SNR) of the signal. It may also be cause by the power spectral density of the input-output signals which have not been estimated correctly. A frequency range with coherence over 0.6 is considered acceptable for frequency domain system identification, and the coherence above 0.8 indicates that the data's linearity is very good for system identification (Tischler and Remple, 2012). When selecting the proper frequency components for system identification, the low coherence frequency part is truncated and dropped.

5.1.2 Length of input excitation

The length of data must be consistent with the periods of interest (Dorobantu *et al*, 2013). Roughly, an individual sweep record length should have at least two or ideally four or five times the maximum dynamic period of interest. A full aircraft dynamic period includes both a short period and a phugoid mode. That is because, although in theory an individual mode can be identified from one dynamic period, the practical issues such as presence of measurement noise, multiple closely spaced modes, atmospheric turbulence and model structure uncertainty, all drive the need for a longer record length.

For the sake of safety, the aircraft needs to be flying in the line of sight all the time. Therefore the maximum level flight time of Cropcam is limited to 10 seconds. Considering the trimming requirement after each turn, the ideal experiment data window is limited to 5 seconds. However, 5 seconds is too short for system identification. Therefore a trade-off is made by setting the input excitation length to 8 seconds. As a result, the trimming requirement may not be met ideally, but that is the physical limitation of the experiment. In fact, the identification results demonstrate that this setting works.

5.1.3 Amplitude of input signal

In order to achieve a sufficiently high signal-to-noise ratio (SNR), it is desirable that the amplitudes of output angular rates are over 6 deg/s, and linear accelerations are beyond 1.5 m/s^2 (Dorobantu *et al.*, 2013). However, if the amplitudes of input are too high, outputs of the aircraft will deviate far from the nominal condition and will not remain in the linear region anymore. Preliminary simulation and experiments showed that an output amplitude of 20 deg/s is large enough for the angular rate to distinguish dynamical response from noise while maintaining the nominal flight characteristics. Typical effective input (elevator deflection) and output (body pitch rate) pair plots are shown in Figure 5.1 and Figure 5.2.

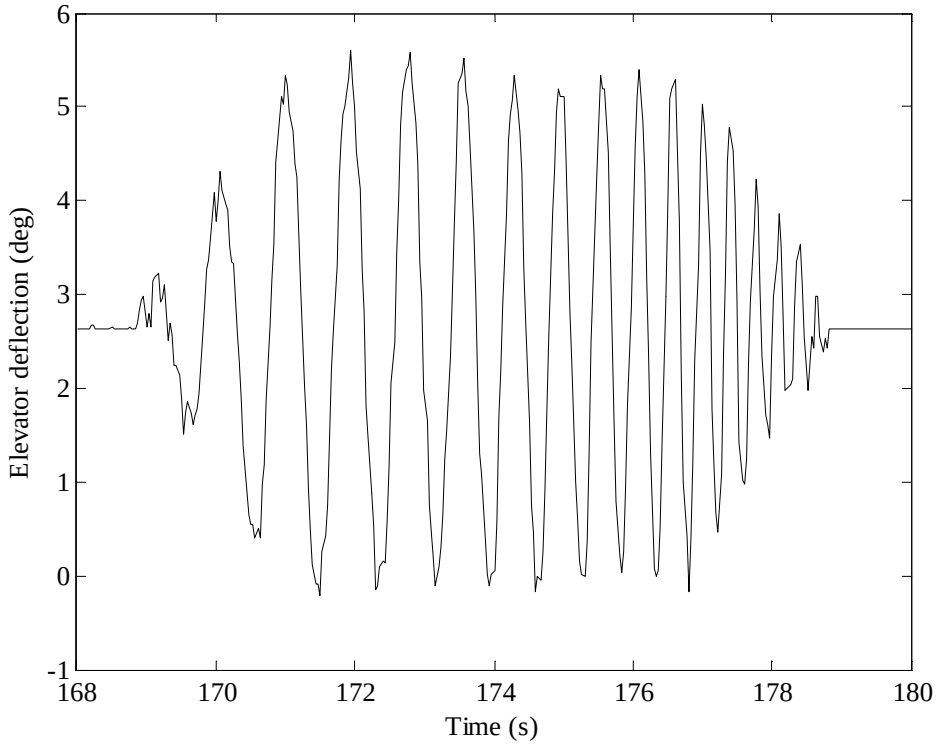

Figure 5.1 Elevator deflection

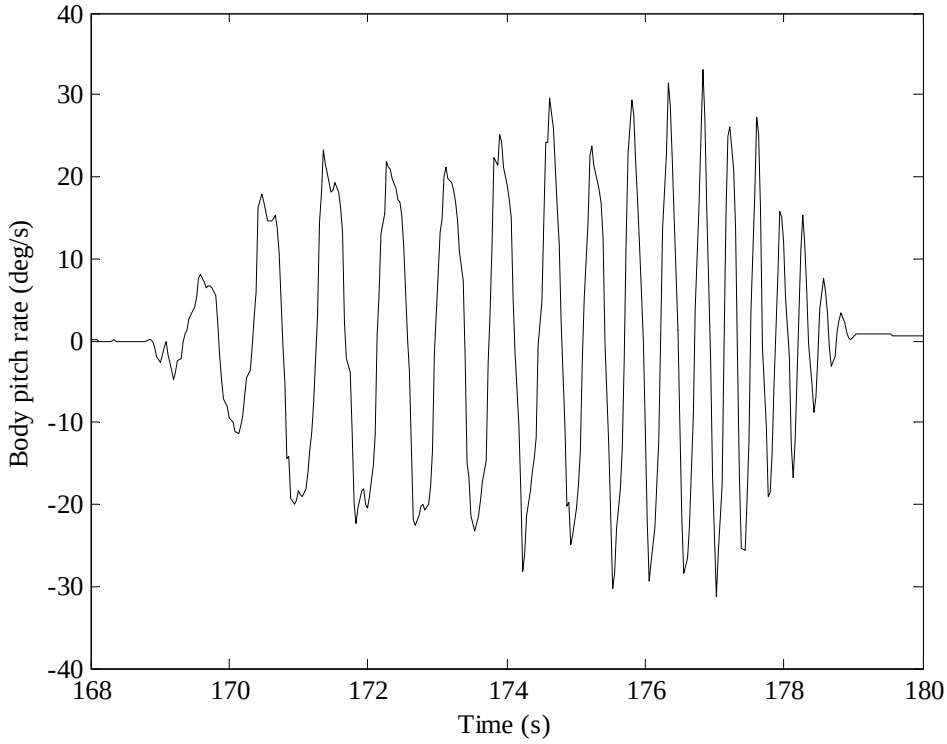

Figure 5.2 Body pitch rate

From Figure 5.2, it is seen that the amplitude of body pitch rate follows the output requirements exactly. This demonstrated that the input excitation is designed properly.

5.1.4 Flight test conditions

The important flight conditions include wind speed, air pressure, air humidity and the trimming condition. The flight condition requirements are determined by the purpose under investigation. For instance, in order to obtain the aircraft's aerodynamic model in the cruise, the aircraft must be trimmed in a steady state level flight at a constant altitude before deploying the input excitations. For this particular case, air pressure and humidity mostly remain constant. Therefore, wind speed and trimming condition are the factors that matter the most. It is desirable that the flight experiments are executed under a low-wind weather condition to avoid the effect of a large external disturbance. Besides, in order to avoid interference from disturbance, the input excitation must be executed only when the aircraft is flying at level condition. In other words, the aircraft should be flying at a steady speed, stable height and an almost zero angular rate before deploying the input excitation.

To make sure that the data quality is high, the experiments should to be repeated. For the flight test in this research, several frequency sweep input commands are executed by the control stick. Also a few doublets are executed to ensure that at least one is free of large disturbance and the results are consistent. A typical doublet input signal and its corresponding response body pitch rate are shown in Figure 5.3 and Figure 5.4 (simulated by Horizon software which developed by MicroPilot).

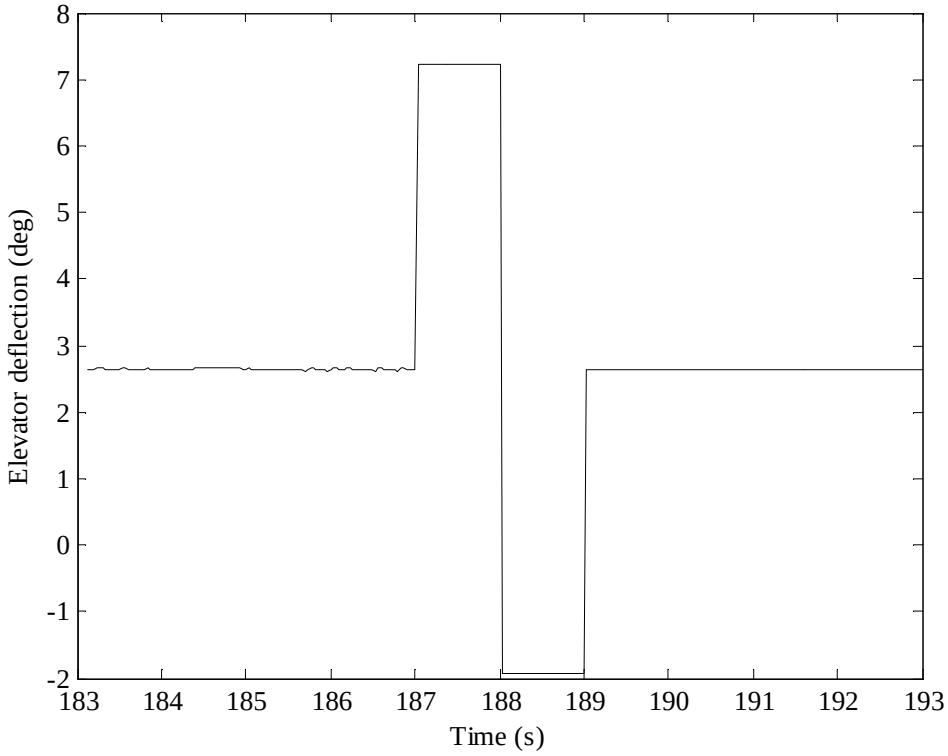

Figure 5.3 Doublet input excitation

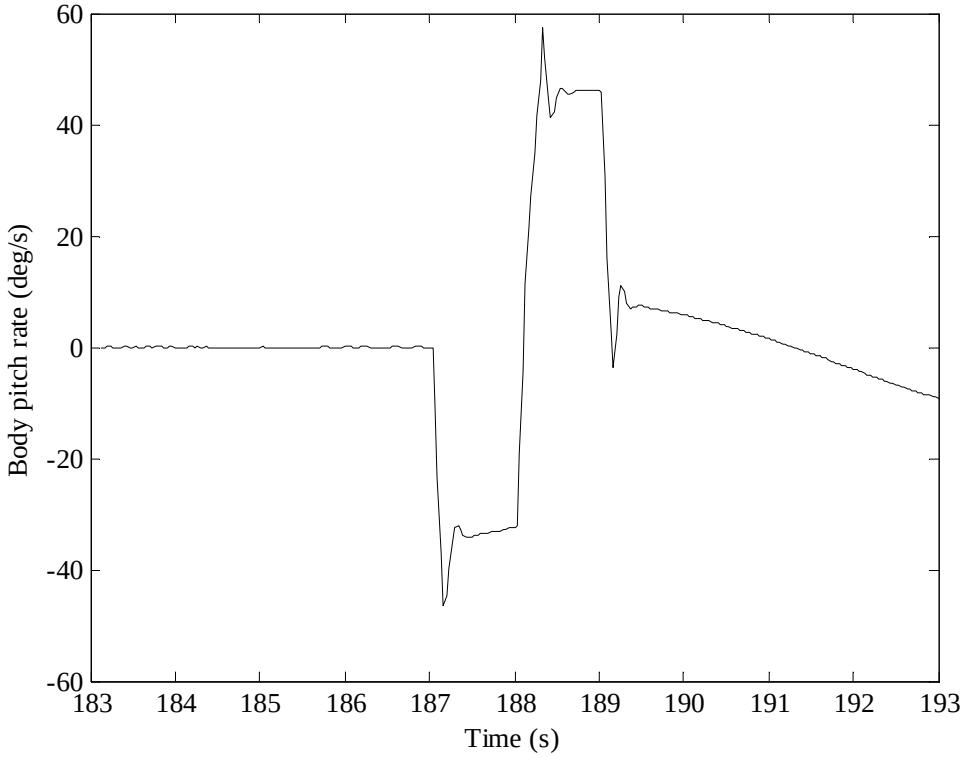

Figure 5.4 Body pitch rate

From Figure 5.3 it is seen that the elevator position starts and ends at trim state, and the input amplitude is symmetric about the trim value.

5.2 Optimal input design

Design of input excitation has been widely studied. A lot of literature on optimal input design has been published (Hamel, 1991; Chen, 1975; Mehra and Gupta, 1975; Morelli, 1997; Tischler and Remple, 2012). A good excitation should be capable of using minimum maneuver time and minimum peak response to obtain maximum information content (*e.g.* power spectral density). In other words, an input signal can excite a good flight effect with low operation amplitude in short time length. The input excitation design is based on the prior knowledge of model structure and dynamical response characteristics. But usually, before doing system identification, the model structure and dynamical characteristics are unknown in advance. Therefore the initial design is mainly dependent on prior experience and rough estimation (Tischler and Remple, 2012).

Different input excitation modes are required for different ways of system identification. In time domain system identification, multistep inputs are proven to be effective. Popular inputs like doublet and 3-2-1-1 are categorized within the multi-step inputs. The 3-2-1-1 test input was developed by researchers in the German DLR Research Laboratory (Marchand and Koehler, 1974). Doublet and 3-2-1-1 test signals and their variants have been demonstrated to be able to excite the aircraft modes of interest in conjunction with time-domain system identification techniques such as the widely used maximum likelihood (ML) method (Jategaonkar and Monnich, 1997). Morelli (1993, 1997) used optimal input design based on multistep inputs for a high performance aircraft application. Figure 5.5 is a typical 3-2-1-1 signal.

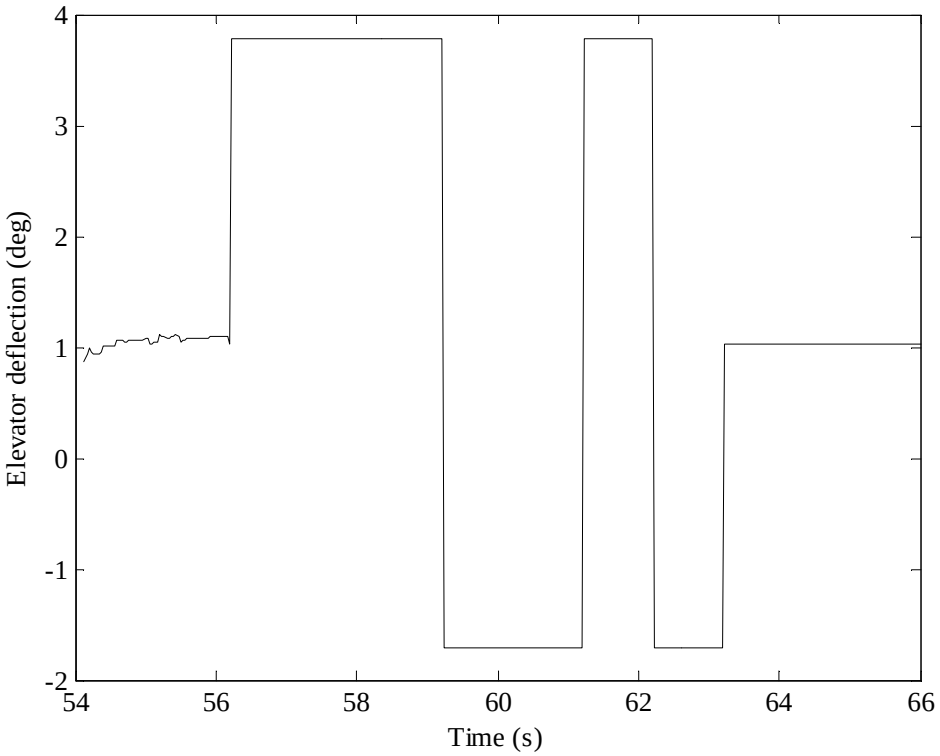

Figure 5.5 Typical 3-2-1-1 signal

A well-established input for frequency domain system identification is the Schroeder-phase signal (Tischler and Remple, 2012). The Schroeder-phase signal is a multi-frequency signal which is composed of a large number of harmonics at equally spaced frequencies. Young (1989) and Young and Patton (1990) demonstrated that the Schroeder-phase design minimizes the peak excitation amplitude and can result in a flat power spectral density, which makes it ideal for frequency domain system identification methods. Based on the Schroeder-phase signal, Morelli (2003) designed an optimal input with minimum peak which is designed for real time parameter estimation in the frequency domain. The above designs minimized the flight test duration and proved to be suitable for frequency domain system identification.

The input excitation used for system identification in this research is a frequency sweep signal called “Chirp”. It is a multi-frequency and amplitude variation wave. Frequency sweep was first

used for frequency response identification by System Technology Inc. (Hoh *et al*., 1981) in applications to fixed-wing aircraft.

The reasons for using Chirp signal for frequency response identification are (Tischler and Remple, 2012):

i. Chirp's spectral content (also called power spectral density, PSD) is fairly rich and the excitation has a uniform distribution across the desired frequency range. This characteristic guarantees that input and output have a persistent high level of frequency response accuracy across the frequency range of interest;

ii. time history of Chirp magnitude is roughly symmetric. This means that deviations in the input are generally symmetric with respect to trim (reference) state;

iii. the frequency range can be strictly controlled during the test. The input start frequency and end frequency are all predefined, and the frequency is smoothly changing with time.

Figure 5.6 shows a typical frequency sweep input.

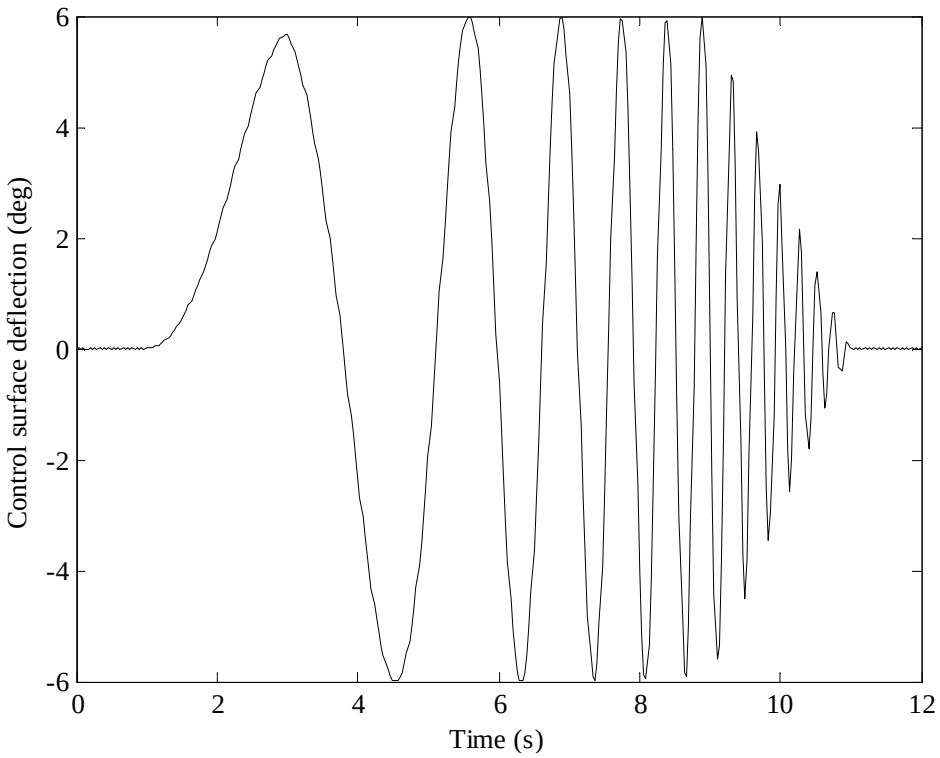

Figure 5.6 Frequency sweep input excitation

When using frequency-sweep signal, some important points need to be considered (Tischler and Remple, 2012):

i. sweeps should start and end with at least 3 seconds of trim state in the test record;

ii. after the initial trim period, execute two complete Chirps;

iii. make sure the input frequency increases smoothly, without rushing through mid-frequencies;

iv. adjust the input to make sure its amplitude is symmetric with respect to the control surface trim value;

v. the required frequency range should be determined before the flight test.

Other points also considered:

i. constant input amplitude is unnecessary;

ii. exact sinusoidal input shape is unnecessary, and actually not desirable;

iii. exact frequency progression is unnecessary;

iv. exact repeatability is unnecessary and not desirable;

v. high frequency input is not needed;

vi. increase input amplitude at high frequency is not needed.

Computer generated frequency sweep input is has been proven to be time efficient and effective for flight test. Tischler (2012) developed an automated frequency sweep testing method for frequency domain system identification. The signal is composed of exponential sweep and white noise. The advantage of exponential sweep is that it takes a longer time at low frequencies where most of the aircraft modes and characteristics lie, while it takes a shorter time at higher frequencies. Figure 5.7 shows the increasing trend of the sweep frequency.

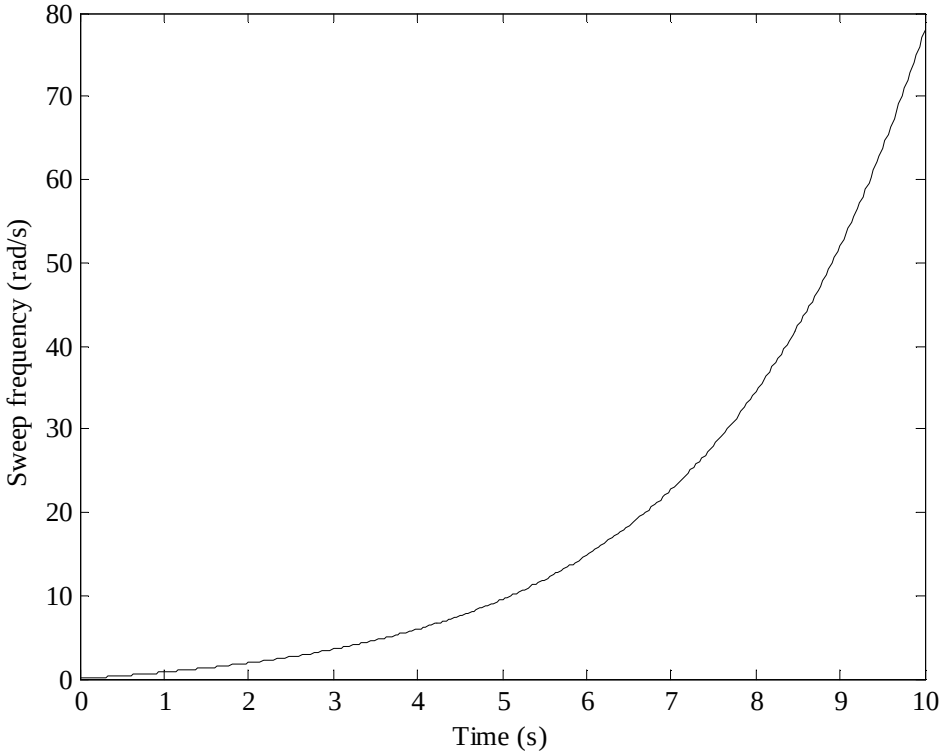

Figure 5.7 Increasing trend of sweep frequency

A frequency sweep generating equation is (Tischler and Remple, 2012),

$$\delta_{sweep} = Asin[\theta(t)] \tag{5.2}$$

where, A is the amplitude of the sweep signal, and it is 10% of the control surface deflection limit. $\theta(t)$ is defined as:

$$\theta(t) = \int_0^{T_{rec}} \omega(t)dt \tag{5.3}$$

where T_{rec} is the sweep time duration, and $\omega(t)$ is given as,

$$\omega(t) = \omega_{min} + K(t)(\omega_{max} - \omega_{min}) \tag{5.4}$$

In Equation (5.4), $K(t)$ is given as:

$$K(t) = C_2[exp\left(\frac{C_1 t}{T_{rec}}\right) - 1] \tag{5.5}$$

The requirement of Chirp frequency range is: at $t = 0$, the frequency $\omega = \omega_{min}$; and at $t = T_{rec}$, $\omega = \omega_{max}$. Therefore, C_1 can be set arbitrarily, while C_2 needs to be set accordingly to satisfy the above requirement. A typical setting pair, $C_1 = 4$, and $C_2 = 0.0187$, have been proven suitable for a wide range of applications (Tischler and Remple, 2012).

Combining Equations (5.2) to (5.5), the following holds,

$$\delta_{sweep} = Asin \int_0^{T_{rec}} [\omega_{min} + C_2 \left(e^{\frac{C_1 t}{T_{rec}}} - 1\right)(\omega_{max} - \omega_{min})]dt \tag{5.6}$$

In the implementation of the input excitation, some features are recommended to add to the signal (Tischler and Remple, 2012):

i. zero starts and zero ends, to ensure a steady-state condition;

ii. constant ω_{min} for one full period, to ensure sufficient spectral content at the starting frequency;

iii. White Gaussian Noise (*WGN*) should be added to the excitation, to enrich the excitation spectral content. Because the computer-generated sine sweeps alone may not have sufficient spectral content due to it having no irregularities in signal shape;

iv. amplitude fade in and fade out, to avoid sharp start and end;

v. the excitation should be low pass filtered, to suppress high frequency content in the excitation.

Given the above requirements, the final input excitation can be expressed mathematically as:

$$\delta_{excitaion} = \delta_{sweep} + \delta_{white\ noise} \tag{5.7}$$

where, typical noise signal level is set as:

$$\delta_{white\ noise}: \sigma = 0.1A \tag{5.8}$$

Figure 5.8 shows a typical final sweep input excitation.

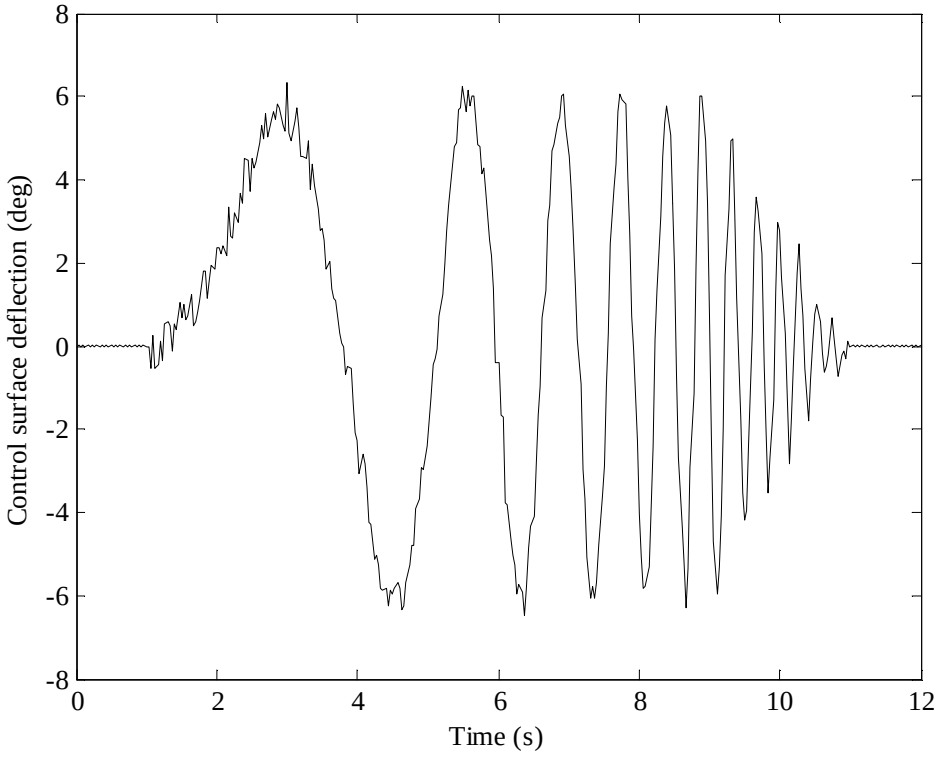

Figure 5.8 Typical Chirp input excitation

Figure 5.9 is the finite Fourier transform plot of the input excitation shown in Figure 5.8. It displays the frequency range of the implemented Chirp input excitation, which is in the range of 0.5 to 5 Hz.

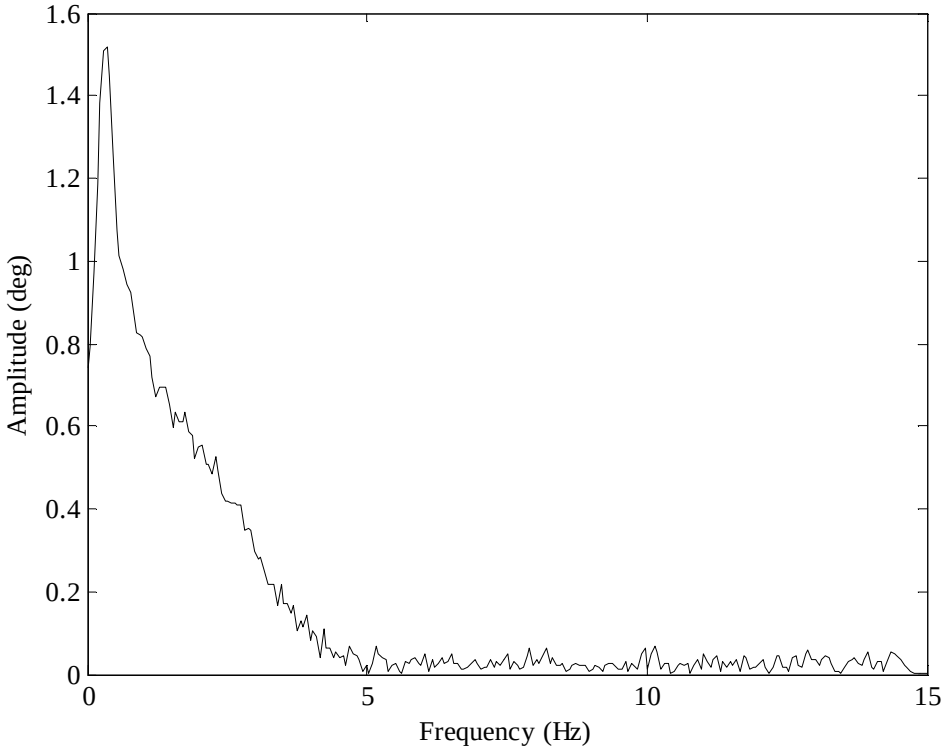

Figure 5.9 Finite Fourier transform of input signal

A computer generated frequency sweep signal can provide the needed excitation content over the frequency range of interest. It has been demonstrated to be fairly effective for frequency domain system identification. And, it has wide support as a successful application in the development of aircraft system modeling.

5.3 Summary

As discussed before, the quality of system identification is highly dependent on the quality of flight test, and in turn, the input excitation. Hence in the Section 5.1, the optimum input excitation was discussed, and the key points in designing the input excitation were highlighted and clarified. In Section 5.2, different excitation signals were introduced and compared. Among

them, the “Chirp” signal was determined as a good candidate for the flight test in this research due to its rich frequency components property. A Chirp generating algorithm was introduced that effectively determines the optimum input excitation.

6 Estimation of Aerodynamic Derivatives

In system identification, two issues influence the accurate parameter estimation: one is noise, another one is low information content. It is difficult to design a parameter estimation technique which can perfectly distinguish the response from the noise while still responding rapidly to sudden changes in the system dynamics (Morelli, 1999). This is because distinguishing the system response from noise requires long term data. In time domain, this problem is solved by using recursive least squares and a "forgetting factor" (Bodson, 1995), or by using sequential batch least squares with short data records and including cost function (Chandler *et al*, 1995; Ward *et al*, 1996). In frequency domain, it is dealt with by using correlation and spectrum algorithms. The transfer function method has a property of immunity to noise. If an extended Kalman Filter approach is applied, the signal can be distinguished from noise more clearly.

A lack of data information content is a universal problem in system identification. Time domain methods are more sensitive to the lack of data information content (Morelli, 1999). Another known problem associated with the data information content is the data co-linearity. In a flight test, several control surfaces frequently move at the same time, or else the control surfaces move in proportional to state variables with a tiny time delay. When the states and controls move proportional to one another, it is hard to identify the individual stability derivatives from the response (Morelli, 1999). The effects of these problems can be relieved in frequency domain calculation.

There are a couple of algorithms for identification of unknown aerodynamic derivatives. However, the field is narrowed if only the real-time methods are considered (Tischler and

Remple, 2012). The current task is to examine a single-step frequency domain method for real-time longitudinal channel aerodynamic parameters identification.

In this thesis, two frequency domain system identification approaches are implemented and tested to extract the unmanned aircraft aerodynamic derivatives from flight data. The first one, transfer function method, is more appropriate for off-line calculations. For this method the aircraft transfer functions corresponding to the mode of interest are developed first. The aerodynamic derivatives are then calculated from the transfer function parameters. The second method, Equation Error method (complex linear regressionmethod), is more suitable for real-time parameter estimations. Both methods assume that the aircraft remains in the linear region during the flight test. An important requirement for implementing these two identification approaches is that the dynamic model should have a linear structure with time-varying parameters to account for the changes in the flight condition or the aircraft configuration.

6.1 Transfer function method

Before applying any system identification techniques, a general understanding of the aircraft dynamics is required. In this section, ways of obtaining the transfer function are discussed. Section 6.1.1 explains how to derive it empirically from the measured input-output data pairs. Section 6.1.2 discusses how to derive it analytically based on theory.

6.1.1 Obtaining transfer function empirically

There are several methods to acquire transfer functions of a dynamical system from experimental data. In this section the Empirical Transfer-Function Estimate (ETFE) method and Power Spectra method are discussed.

1. Empirical transfer-function estimate (Keesman, 2011)

Recalling that $Y(s) = G(s)U(s)$, by substitution of $s = j\omega$, the following can be obtained,

$$Y(j\omega) = G(j\omega)U(j\omega) \tag{6.1}$$

Therefore for a given input $u(t)$, and output $y(t)$, by doing finite Fourier transform, the transfer function referring to input and output can be obtained and expressed as,

$$G(j\omega) = \frac{Y(j\omega)}{U(j\omega)} \tag{6.2}$$

For each of the frequency components contained in the input and output, the relationship (6.2) holds. This allows the construction of both magnitude and phase response of the signal for a number of frequencies.

2. Transfer-function estimate using power spectra (Keesman, 2011)

The Empirical Transfer-Function Estimate is simple to use, however, the disadvantage is that it uses the raw input-output data, which means that this approach is sensitive to noise. Therefore, another algorithm called “power spectra method” is developed to offer robustness to the measurement of noise. In order to implement the power spectra method, autocorrelation and

cross-correlation of the input-output pairs needs to be calculated. The autocorrelation of the input signal $u(t)$ can be expressed as:

$$r_{uu}(\tau, t) = E[u(t)u(t+\tau)] \tag{6.3}$$

where τ is the time lag and the notation $E[\bullet]$ stands for the expectation operator. Equation (6.3) can be further rewritten as,

$$r_{uu}(\tau) = \lim_{T\to\infty} \frac{1}{2T} \int_{-T}^{T} u(t)u(t+\tau)dt \tag{6.4}$$

Since in practice, the input signal is measured in discrete data, a discrete time algorithm is needed to process the data, which is shown as:

$$r_{uu}(l) = \lim_{N\to\infty} \frac{1}{2N+1} \sum_{i=-N}^{N} u(i)u(i+l) \tag{6.5}$$

The cross-correlation of input-output can be expressed as:

$$r_{uy}(\tau, t) = E[u(t)y(t+\tau)] \tag{6.6}$$

which can be further written as,

$$r_{uy}(\tau) = \lim_{T\to\infty} \frac{1}{2T} \int_{-T}^{T} u(t)y(t+\tau)dt \tag{6.7}$$

For the discrete time case, Equation (6.7) is written as,

$$r_{uy}(l) = \lim_{N\to\infty} \frac{1}{2N+1} \sum_{i=-N}^{N} u(i)y(i+l) \tag{6.8}$$

Recalling the time domain input-output relevance $y(t) = \sum_{k=0}^{\infty} g(k)u(t-k)$, at the time instant of $t = i + 1$,

$$y(i+l) = \sum_{k=0}^{\infty} g(k)u(i+l-k) \tag{6.9}$$

Practically, $y(t) = \bar{y}(t) + v(t)$, where *v* is noise. Thus the cross-correlation of input *u*(*t*)- output *y*(*t*) is,

$$r_{uy}(l) = \lim_{N\to\infty} \frac{1}{2N+1} \sum_{i=-N}^{N} u(i) \left[\sum_{k=0}^{\infty} g(k)u(i+l-k) + v(i+l)\right] \tag{6.10}$$

Therefore, as long as *v* is unrelated to *u* and has a zero mean, the long-term average of *u*(*i*)*v*(*i*+*l*) is close to zero. This is the reason why the power spectra method is immune to noise. Equation (6.10) can be deduced as:

$$\begin{aligned} r_{uy}(l) &= \lim_{N\to\infty} \frac{1}{2N+1} \sum_{i=-N}^{N} u(i) \left[\sum_{k=0}^{\infty} g(k)u(i+l-k) + v(i+l)\right] \\ &= \sum_{k=0}^{\infty} g(k) \lim_{N\to\infty} \frac{1}{2N+1} \sum_{i=-N}^{N} u(i)\, u(i+l-k) \\ &= \sum_{k=0}^{\infty} g(k)\, r_{uu}(l-k) \end{aligned} \tag{6.11}$$

Equation (6.11) is called the Wiener-Hopf equation. The auto-spectrum and cross-spectrum of signals are obtained by taking the finite Fourier transform of the auto-correlation and cross-correlation of the signals. The auto-spectrum function is defined as:

$$\Phi_{uu}(\omega) = \sum_{l=-\infty}^{\infty} r_{uu}(l)e^{-j\omega l} \tag{6.12}$$

while cross-spectrum is:

$$\Phi_{uy}(\omega) = \sum_{l=-\infty}^{\infty} r_{uy}(l)e^{-j\omega l} \tag{6.13}$$

The relationship of $\Phi_{uy}(\omega)$ and $\Phi_{uu}(\omega)$ can be derived by substituting r_{uy} from Equation (6.11) into (6.13), which is:

$$\begin{aligned}
\Phi_{uy}(\omega) &= \sum_{l=-\infty}^{\infty} r_{uy}(l)e^{-j\omega l} \\
&= \sum_{l=-\infty}^{\infty}\sum_{k=0}^{\infty} g(k)r_{uu}(l-k)e^{-j\omega l} \\
&= \sum_{l=-\infty}^{\infty}\sum_{k=0}^{\infty} g(k)e^{-j\omega k}r_{uu}(l-k)e^{-j\omega(l-k)} \\
&= \sum_{k=0}^{\infty} g(k)e^{-j\omega k}\sum_{l=-\infty}^{\infty} r_{uu}(l-k)e^{-j\omega(l-k)} \\
&= \sum_{k=0}^{\infty} g(k)e^{-j\omega k}\sum_{\lambda=-\infty}^{\infty} r_{uu}(\lambda)e^{-j\omega\lambda} \\
&= G(e^{j\omega})\Phi_{uu}(\omega)
\end{aligned} \tag{6.14}$$

Thus, an alternative approach to ETFE is given as:

$$G(\omega) = \frac{\Phi_{uy}(\omega)}{\Phi_{uu}(\omega)} \tag{6.15}$$

Since the power spectra method is immune to noise compare to the ETFE method, it is widely used in practice. Some commercial software like MATLAB and CIFER are also using this method for system identification.

6.1.2 Obtaining transfer function analytically

Since aircraft motion can be decoupled into short period and phugoid modes, they can be explained separately.

Short - period mode response

Short-period mode is a typical damped oscillation in the pitch with respect to the *oy* axis. One of the features of the short-period mode response is, when the aircraft is disturbed from its pitch equilibrium state, the aircraft response quantities such as incidence angle α(or w), pitch rate q and pitch attitude θ change significantly. Since the short period mode is short, the effects of inertia and momentum on speed are negligible, the speed can be considered as approximately constant. Thus, axial velocity perturbation u=0. The short-period mode flight feature can be visually shown as Figure 6.1.

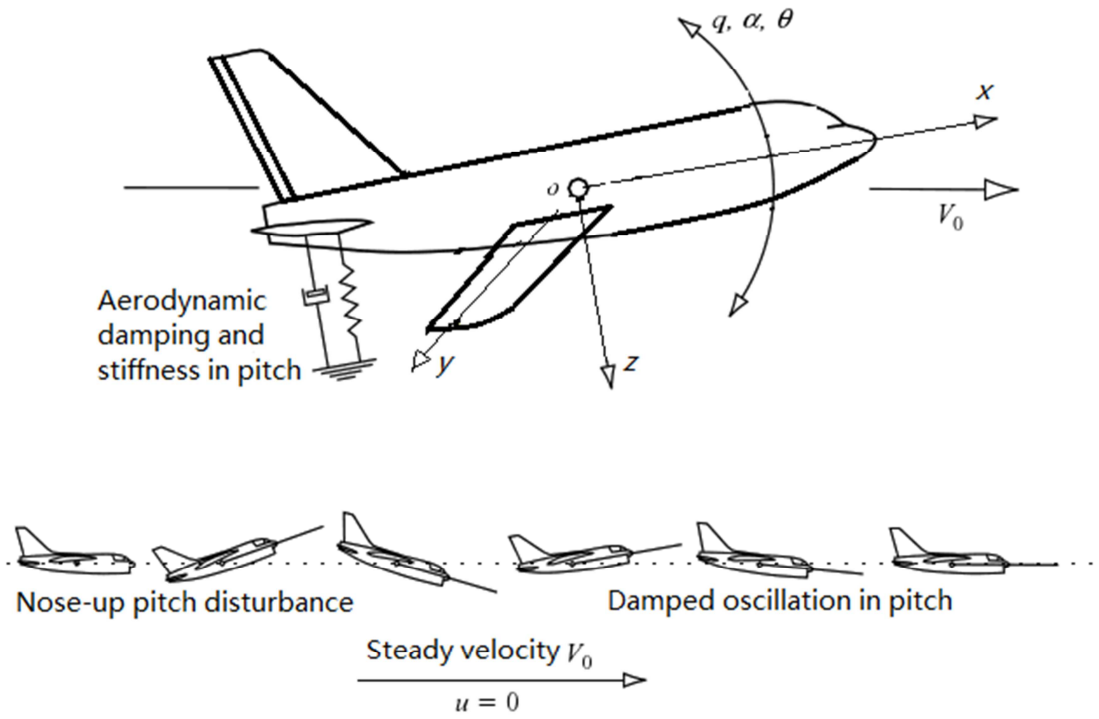

Figure 6.1 Short-period mode flight (adapt from Cook, 2012)

Phugoid mode response

Phugoid mode is a lightly damped low-frequency oscillation in speed *u*, which couples into pitch attitude θ and altitude *h*. One of the characteristics of the phugoid mode is that the incidence angle α remains constant when the aircraft is in the phugoid mode (Cook, 2012). The phugoid flight mode can be visually shown as Figure 6.2.

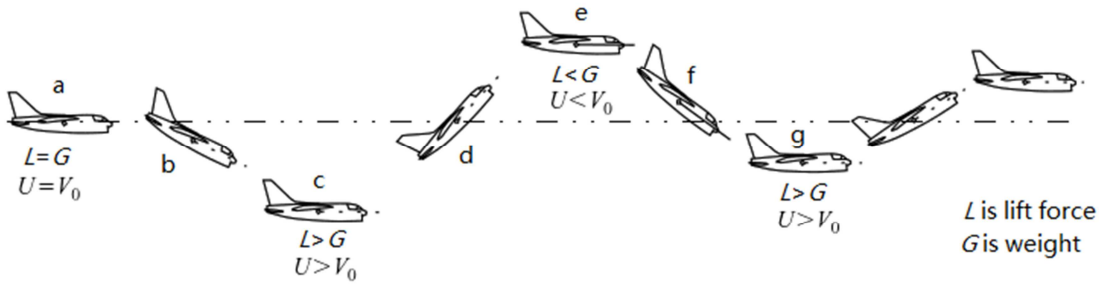

Figure 6.2 Phugoid mode flight (adapt from Cook, 2012)

When the aircraft is flying downhill, the potential energy is decreasing; thus, the kinetic energy is increasing and therefore the aircraft velocity increases accordingly. That is why, when the aircraft goes down, it is accelerating and when it goes up, it is decelerating.

Figure 6.3 and Figure 6.4 show typical longitudinal mode responses to a 1° elevator deflection step input.

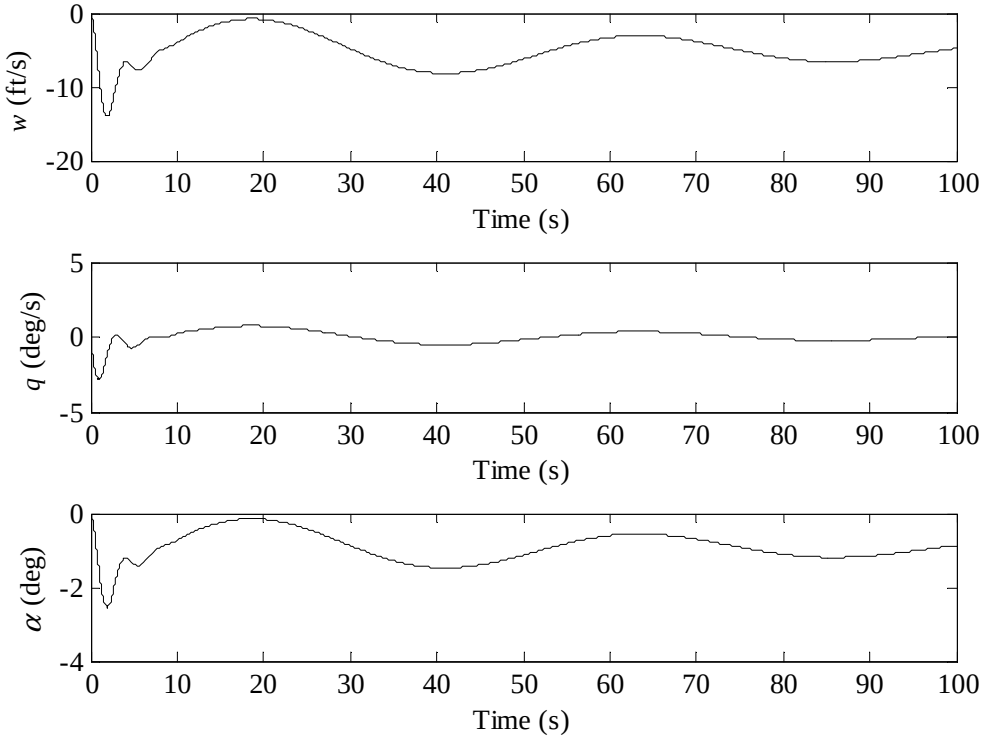

Figure 6.3 Aircraft responses (*w, q, α*) to a 1° elevator step input

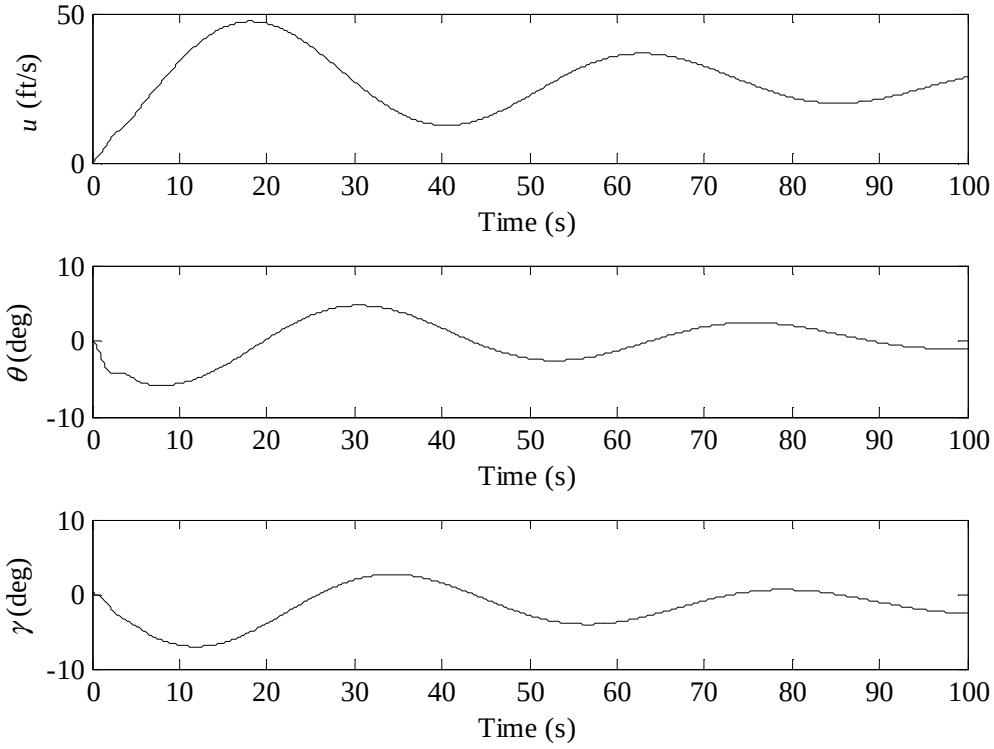

Figure 6.4 Aircraft responses (u, θ, γ) to a 1° elevator step input

From the figures, it is seen that the variables w, q and α are significant short period mode dominated variables, while variables u, θ and γ are less dominant in short period mode. The short period response characteristic of aircraft is essential. The short-period mode has a natural frequency close to the human pilot's natural frequency. Therefore, the probability of dynamic coupling with the pilot occurring under certain conditions is relatively higher than in the phugoid mode. This may lead to severe or catastrophic handling problems (Cook, 2012). On the other hand, the phugoid mode's natural frequency is much lower. Therefore, the phugoid mode is less influenced by the piloting task; the human pilot can easily control the aircraft even when the aircraft phugoid is mildly unstable.

Short-period mode approximation

The short-term response is dominated by the short-period mode. It is more convenient to obtain the reduced-order aircraft motion equations if the phugoid mode is suppressed or omitted. It is possible to simplify the longitudinal motion equations to a reduced-order set of equations, which describe only the short-period mode. Since the dominant quantities of short-period motion are *u*, *w*, *q* and θ, while *u* is essentially almost zero, Equation (4.114) can be further written as:

$$\begin{bmatrix} \dot{w} \\ \dot{q} \\ \dot{\theta} \end{bmatrix} = \begin{bmatrix} z_w & z_q & z_\theta \\ m_w & m_q & m_\theta \\ 0 & 1 & 0 \end{bmatrix} \begin{bmatrix} w \\ q \\ \theta \end{bmatrix} + \begin{bmatrix} z_\eta \\ m_\eta \\ 0 \end{bmatrix} \eta \tag{6.16}$$

Assuming that the motion equations are written with respect to the wind axes coordinate system, and the aircraft is initially in steady level flight, then the following holds,

$$\theta_e \equiv \alpha_e = 0 \text{ and } U_e = V_0 \tag{6.17}$$

further,

$$z_\theta = -\frac{mgsin\theta_e}{m - \mathring{Z}_{\dot{w}}} = 0 \tag{6.18}$$

$$m_\theta = -\frac{\mathring{M}_{\dot{w}} mgsin\theta_e}{I_y(m - \mathring{Z}_{\dot{w}})} = 0 \tag{6.19}$$

Therefore Equation (6.16) can be further reduced as:

$$\begin{bmatrix} \dot{w} \\ \dot{q} \end{bmatrix} = \begin{bmatrix} z_w & z_q \\ m_w & m_q \end{bmatrix} \begin{bmatrix} w \\ q \end{bmatrix} + \begin{bmatrix} z_\eta \\ m_\eta \end{bmatrix} \eta \tag{6.20}$$

The derivatives in equation (6.20) are given in the body axes system. The transfer functions can be derived from Equation (6.20) (Cook, 2012):

$$\frac{w(s)}{\eta(s)} = \frac{z_\eta \left(s + m_q + z_q \frac{m_\eta}{z_\eta}\right)}{s^2 - \left(m_q + z_w\right)s + \left(m_q z_w - m_w z_q\right)} \tag{6.21}$$

$$\frac{q(s)}{\eta(s)} = \frac{m_\eta (s + m_w \frac{z_\eta}{m_\eta} - z_w)}{s^2 - \left(m_q + z_w\right)s + \left(m_q z_w - m_w z_q\right)} \tag{6.22}$$

Since $z_q \frac{m_\eta}{z_\eta} \gg m_q$, $-z_w \gg m_w \frac{z_\eta}{m_\eta}$, and,

$$z_q = -\frac{\mathring{Z}_q + mU_e}{m - \mathring{Z}_{\dot{w}}} \cong U_e \tag{6.23}$$

also, $\mathring{Z}_q \ll mU_e$ and $m \gg \mathring{Z}_{\dot{w}}$.

Thus, the transfer functions can be decoupled and simplified as,

$$\frac{w(s)}{\eta(s)} = \frac{z_\eta (s + U_e \frac{m_\eta}{z_\eta})}{s^2 - \left(m_q + z_w\right)s + \left(m_q z_w - m_w U_e\right)} \equiv \frac{k_w (s + 1/T_\alpha)}{s^2 + 2\xi_s \omega_s s + \omega_s^2} \tag{6.24}$$

$$\frac{q(s)}{\eta(s)} = \frac{m_\eta (s - z_w)}{s^2 - \left(m_q + z_w\right)s + \left(m_q z_w - m_w U_e\right)} \equiv \frac{k_q (s + 1/T_{\theta_2})}{s^2 + 2\xi_s \omega_s s + \omega_s^2} \tag{6.25}$$

The characteristic equation is,

$$\Delta(s) = s^2 - \left(m_q + z_w\right)s + \left(m_q z_w - m_w U_e\right) = s^2 + 2\xi_s \omega_s s + \omega_s^2 \tag{6.26}$$

6.1.3 Applying the transfer function method

Once the numerical and parameter transfer functions are obtained, the TF method can be applied to extract the aerodynamic derivatives. By observing Equations (6.24) and (6.25), the following can be deduced:

$$-\left(m_q + z_w\right) = 2\xi_s\omega_s \tag{6.27}$$

$$m_q z_w - m_w U_e = \omega_s^2 \tag{6.28}$$

The above equations can also be rewritten using the dimensional derivatives as:

$$2\xi_s\omega_s = -\left(\frac{\mathring{M}_q}{I_y} + \frac{\mathring{Z}_w}{m} + \frac{\mathring{M}_{\dot{w}} U_e}{I_y}\right) \tag{6.29}$$

$$\omega_s = \sqrt{\frac{\mathring{M}_q}{I_y}\frac{\mathring{Z}_w}{m} - \frac{\mathring{M}_w U_e}{I_y}} \tag{6.30}$$

For a typical aeroplane, the aerodynamic derivatives can be written as a crude approximation (Cook, 2012):

$$2\xi_s\omega_s = -\frac{\mathring{M}_q}{I_y} \tag{6.31}$$

$$\omega_s = \sqrt{-\frac{\mathring{M}_w U_e}{I_y}} \tag{6.32}$$

Normally, $\mathring{Z}_w$ is dependent on the lift curve slope of the wing, $\mathring{M}_q$ is largely determined by the viscous "paddle" damping properties of the tailplane, and they are both negative. $\mathring{M}_w$ is a measure of aerodynamic stiffness in pitch and is also dominated by the aerodynamics of the tailplane. Its sign depends on the position of the *cg*. When the *cg* moves forward, it becomes increasingly negative. Therefore the short-period mode is stable if the *cg* is far enough forward on the airframe (Cook, 2012). These three aerodynamic derivatives are the most important derivatives in longitudinal channel aircraft modeling.

By observing Equations (6.24) and (6.25), the following equalities can be set,

$$\begin{cases} z_\eta = k_w \\ m_\eta = k_q \\ -z_w = 1/T_{\theta_2} \\ -(m_q + z_w) = 2\xi_s\omega_s \\ m_q z_w - m_w U_e = \omega_s^2 \end{cases} \tag{6.33}$$

Since k_w, T_α, $T_{\theta 2}$, ξ_s, ω_s and U_e are all known from the identified transfer function, the aerodynamic parameters z_η, m_η, z_w, m_q and m_w can be calculated easily. It should be noticed that z_η, m_η, z_w, m_q and m_w are neither dimensional nor dimensionless parameters. They are shorthand notations denoting concise derivatives, which are equal to their dimensional derivatives divided by the appropriate mass or inertia parameters. The conversions are shown in Appendix 1.

In this research, the aircraft's input-output data pairs are fed to the CIFER to obtain the corresponding frequency responses and the transfer functions. An advantage of the transfer function method is that it requires less data quantities compared to other methods. For example, for longitudinal channel parameters' estimation, the aircraft's input and outputs that need to be known are only elevator deflection η, vertical velocity w and pitch rate q. These are readily available from the aircraft onboard autopilot.

Although the transfer function method is simple to implement, its identification result is not as accurate as the ones given by the direct methods, such as the Equation Error method which will be discussed in the next section. The TF method is less accurate because several simplifying approximations are made: *i*) the longitudinal mode state space model is decoupled from the full aerodynamic state space equation; *ii*) the transfer functions used are a reduced order of the decoupled state space mode; *iii*) phugoid mode related aerodynamic derivatives are omitted; *iv*) some extra terms are further simplified, while extracting the aerodynamic derivatives from transfer functions(*e.g*. Equation (6.23)); *v*) some approximations were made, when converting

the derivatives from the concise format to their corresponding dimensional or dimensionless format derivatives(see the Appendix 1).

Since the transfer function method is considered an approximate method for identifying aerodynamic derivatives, an alternative way needs to be developed for identifying the derivatives more accurately. The equation error method, which will be introduced in Section 6.2, is chosen as the main method for identifying aerodynamic derivatives in this research.

6.2 Equation error method

Since it is assumed that the dynamic model has a linear structure in the given period of flight, the airplane dynamics can be described by the following linear state space model (referring to Equations (4.115) and (4.116)):

$$\dot{\boldsymbol{x}}(t) = \mathbf{A}\boldsymbol{x}(t) + \mathbf{B}\boldsymbol{u}(t) \tag{6.34}$$

$$\boldsymbol{y}(t) = \mathbf{C}\boldsymbol{x}(t) + \mathbf{D}\boldsymbol{u}(t) \tag{6.35}$$

$$\boldsymbol{z}_i = \boldsymbol{y}_i + \boldsymbol{v}_i \qquad i = 1, 2, \ldots, N \tag{6.36}$$

Matrices **A**, **B**, **C** and **D** contain the aerodynamic stability and control derivatives (refer to Equation (4.111)) of the aircraft, which are all assumed to be constants. $\boldsymbol{u}(t)$ is the input which contains quantities of the control surfaces' deflection δ_e, δ_a and δ_r. Matrix $\boldsymbol{x}$ is comprised of the states of the system, such as linear body velocities u, v and w; the angular body velocities p, q and r; or Euler angles φ, θ and ψ. Here the output quantities are also states of the system. $\boldsymbol{y}$ is the

output vector and it is usually the same as $\boldsymbol{x}$. $\boldsymbol{z}$ is the measured output vector and $\boldsymbol{v}$ denotes measurement error.

6.2.1 Data transformation

The Fourier transform is necessary for frequency domain data processing, to map the time domain data into frequency domain. The Fourier transform algorithm for converting a time domain continuous vector $\boldsymbol{x}(t)$ to a frequency domain vector $\tilde{\boldsymbol{x}}(\omega)$ is:

$$F[\boldsymbol{x}(t)] = \tilde{\boldsymbol{x}}(\omega) = \int_{-\infty}^{\infty} \boldsymbol{x}(t) e^{-j\omega t} dt \tag{6.37}$$

where $j = \sqrt{-1}$, ω is the angular frequency which its unit is rad/s. By applying the inverse Fourier transform, frequency domain data can also be converted into time domain. The inverse Fourier transform algorithm is:

$$\boldsymbol{x}(t) = \frac{1}{2\pi} \int_{-\infty}^{\infty} \tilde{\boldsymbol{x}}(\omega) e^{j\omega t} d\omega \tag{6.38}$$

The Fourier transform of a continuous time function $\boldsymbol{x}(t)$ on a finite time interval [0, T] is called the finite Fourier transform (Klein and Morelli, 2006), which is defined as,

$$\tilde{\boldsymbol{x}}(\omega) = \int_{0}^{T} \boldsymbol{x}(t) e^{-j\omega t} dt \tag{6.39}$$

or,

$$\tilde{\boldsymbol{x}}(f) = \int_{0}^{T} \boldsymbol{x}(t) e^{-j2\pi f t} dt \tag{6.40}$$

where, $\omega = 2\pi f$, f is frequency with a unit of Hz.

Since the continuous time domain data $\boldsymbol{x}(t)$ is sampled at discrete sample in the physical world, the sampling time is evenly distributed by Δt (dt), therefore Equation (6.40) can be approximated written as:

$$\tilde{\boldsymbol{x}}(\omega) = \Delta t \sum_{i=0}^{N-1} \boldsymbol{x}_i e^{-j\omega t_i} \tag{6.41}$$

where $\boldsymbol{x}_i$ is the sampled signal magnitude at time t_i, and $t_i = i\Delta t$. The discrete Fourier transform (DFT) is then defined as:

$$\boldsymbol{X}(\omega) = \sum_{i=0}^{N-1} \boldsymbol{x}_i e^{-j\omega t_i} \tag{6.42}$$

Thus for recursive calculation of the DFT of the signal $\boldsymbol{x}$, given frequency ω, the discrete Fourier transform at sample point i can be related to the sample point $i - 1$ as:

$$\boldsymbol{X}_i(\omega) = \boldsymbol{X}_{i-1}(\omega) + \boldsymbol{x}_i e^{-j\omega i\Delta t} \tag{6.43}$$

where,

$$e^{-j\omega i\Delta t} = e^{-j\omega\Delta t} e^{-j\omega(i-1)\Delta t} \tag{6.44}$$

and term $e^{-j\omega\Delta t}$ is constant for the given frequency and sampling time.

6.2.2 Equation error method in frequency domain

By writing Equations (6.34) and (6.35) in frequency domain format, the following have:

$$j\omega\tilde{\boldsymbol{x}}(\omega) = \mathbf{A}\tilde{\boldsymbol{x}}(\omega) + \mathbf{B}\tilde{\boldsymbol{u}}(\omega) \tag{6.45}$$

$$\tilde{\boldsymbol{y}}(\omega) = \mathbf{C}\tilde{\boldsymbol{x}}(\omega) + \mathbf{D}\tilde{\boldsymbol{u}}(\omega) \tag{6.46}$$

The basis of the Equation Error method (also known as Complex Linear Regression method) is the cost function which is derived from Equation (6.45) and shown as:

$$J_k = \frac{1}{2}\sum_{n=1}^{m} |j\omega_n \tilde{\boldsymbol{x}}_k(n) - \boldsymbol{A}_k \tilde{\boldsymbol{x}}(n) - \boldsymbol{B}_k \tilde{\boldsymbol{u}}(n)|^2 \tag{6.47}$$

where, J_k is the cost function of k^{th} state equation, $\boldsymbol{A}_k$ and $\boldsymbol{B}_k$ are the k^{th} row of matrices **A** and **B** respectively. Notation "~" is a symbol of frequency domain data; $\tilde{\boldsymbol{x}}(n)$ and $\tilde{\boldsymbol{u}}(n)$ are the Fourier transformed states and inputs data vector at frequency ω_n; $\tilde{x}_k(n)$ is the k^{th} element of vector $\tilde{\boldsymbol{x}}$ at frequency ω_n. There are m terms in the summation, which correspond to m frequency components:

$$\omega_n = 2\pi f_n = 2\pi \frac{n}{N\Delta t}, \quad n = 0, 1, 2, \ldots, N-1 \tag{6.48}$$

where N is the total number of the time domain data points. If denoting the unknown parameters in matrices **A** and **B** by a matrix $\boldsymbol{\theta}$, Equations (6.45) and (6.46) can be further written in compact form as,

$$\boldsymbol{Y} = \boldsymbol{X}\boldsymbol{\theta} + \boldsymbol{v} \tag{6.49}$$

where,

$$\boldsymbol{Y} = \begin{bmatrix} j\omega_1 \tilde{\boldsymbol{x}}_k(1) \\ j\omega_2 \tilde{\boldsymbol{x}}_k(2) \\ \cdot \\ \cdot \\ \cdot \\ j\omega_m \tilde{\boldsymbol{x}}_k(m) \end{bmatrix} \tag{6.50}$$

$$\boldsymbol{X} = \begin{bmatrix} \tilde{\boldsymbol{x}}^T(1) & \tilde{\boldsymbol{u}}^T(1) \\ \tilde{\boldsymbol{x}}^T(2) & \tilde{\boldsymbol{u}}^T(2) \\ \cdot & \cdot \\ \cdot & \cdot \\ \cdot & \cdot \\ \tilde{\boldsymbol{x}}^T(m) & \tilde{\boldsymbol{u}}^T(m) \end{bmatrix} \tag{6.51}$$

And $\boldsymbol{v}$ is the complex equation error or the fit error in the frequency domain. The least squares cost function (6.47) can also be written in standard quadratic form as,

$$J = \frac{1}{2}(\boldsymbol{Y} - \boldsymbol{X\theta})^{\dagger}(\boldsymbol{Y} - \boldsymbol{X\theta}) \tag{6.52}$$

which is essentially identical to Equation (6.47), where the dressing "†" stands for "complex conjugate transpose". In order to acquire the minimum cost, the value of $\boldsymbol{\theta}$ at which the derivative of the cost function J must be found by setting:

$$\frac{\partial J}{\partial \boldsymbol{\theta}} = 0 \tag{6.53}$$

Since,

$$J = \frac{1}{2}(\boldsymbol{Y} - \boldsymbol{X\theta})^{\dagger}(\boldsymbol{Y} - \boldsymbol{X\theta})$$

$$= \frac{1}{2}(\boldsymbol{Y}^{\dagger}\boldsymbol{Y} - \boldsymbol{Y}^{\dagger}\boldsymbol{X\theta} - \boldsymbol{\theta}^{\dagger}\boldsymbol{X}^{\dagger}\boldsymbol{Y} + \boldsymbol{\theta}^{\dagger}\boldsymbol{X}^{\dagger}\boldsymbol{X\theta}) \tag{6.54}$$

therefore,

$$\frac{\partial J}{\partial \boldsymbol{\theta}} = \frac{1}{2}(-\boldsymbol{Y}^{\dagger}\boldsymbol{X} + \boldsymbol{\theta}^{\dagger}\boldsymbol{X}^{\dagger}\boldsymbol{X}) = 0 \tag{6.55}$$

thus,

$$\boldsymbol{\theta}^{\dagger} = \boldsymbol{Y}^{\dagger}\boldsymbol{X}(\boldsymbol{X}^{\dagger}\boldsymbol{X})^{-1} \tag{6.56}$$

as a result,

$$\begin{aligned} \boldsymbol{\theta} &= [\boldsymbol{Y}^{\dagger}\boldsymbol{X}(\boldsymbol{X}^{\dagger}\boldsymbol{X})^{-1}]^{\dagger} \\ &= [(\boldsymbol{X}^{\dagger}\boldsymbol{X})^{-1}]^{\dagger}\boldsymbol{X}^{\dagger}\boldsymbol{Y} \\ &= [(\boldsymbol{X}^{\dagger}\boldsymbol{X})^{\dagger}]^{-1}\boldsymbol{X}^{\dagger}\boldsymbol{Y} \\ &= (\boldsymbol{X}^{\dagger}\boldsymbol{X})^{-1}\boldsymbol{X}^{\dagger}\boldsymbol{Y} \end{aligned} \tag{6.57}$$

By picking the real part of Equation (6.57), the parameter matrix can be solved by:

$$\widehat{\boldsymbol{\theta}} = Re[(\boldsymbol{X}^{\dagger}\boldsymbol{X})]^{-1}Re(\boldsymbol{X}^{\dagger}\boldsymbol{Y}) \tag{6.58}$$

where, $\widehat{\boldsymbol{\theta}}$ is a row vector which is comprised of the identified derivatives.

In order to know how accurate the identified derivatives are, a parameter standard error algorithm is developed for examining identified parameters' accuracy based on the identification error covariance matrix. The identification error covariance matrix is defined as:

$$\begin{aligned} cov(\widehat{\boldsymbol{\theta}}) &\equiv E\{(\widehat{\boldsymbol{\theta}} - \boldsymbol{\theta})(\widehat{\boldsymbol{\theta}} - \boldsymbol{\theta})^{T}\} \\ &= E[(\boldsymbol{X}^{\dagger}\boldsymbol{X})^{-1}\boldsymbol{X}^{\dagger}(\boldsymbol{Z} - \boldsymbol{Y})(\boldsymbol{Z} - \boldsymbol{Y})^{\dagger}\boldsymbol{X}(\boldsymbol{X}^{\dagger}\boldsymbol{X})^{-1}] \\ &= (\boldsymbol{X}^{\dagger}\boldsymbol{X})^{-1}\boldsymbol{X}^{\dagger}E(\boldsymbol{V}\boldsymbol{V}^{\dagger})\boldsymbol{X}(\boldsymbol{X}^{\dagger}\boldsymbol{X})^{-1}] \\ &= \sigma^{2}(\boldsymbol{X}^{\dagger}\boldsymbol{X})^{-1} \end{aligned} \tag{6.59}$$

where, $\boldsymbol{Z} = \boldsymbol{X}\boldsymbol{\theta}$, $\boldsymbol{V}$ is the Fourier transformed complex equation error $\boldsymbol{v}$ (the fit error).

$$E(\boldsymbol{V}\boldsymbol{V}^{\dagger}) = \sigma^2 \boldsymbol{I} \tag{6.60}$$

σ^2 is equation error covariance, which can be estimated from the residuals and calculated as,

$$\hat{\sigma}^2 = \frac{1}{m-p}[(\boldsymbol{Y} - \boldsymbol{X}\hat{\boldsymbol{\theta}})^{\dagger}(\boldsymbol{Y} - \boldsymbol{X}\hat{\boldsymbol{\theta}})] \tag{6.61}$$

where p is the number of elements of parameter vector $\boldsymbol{\theta}$. σ^2 is a real number representing the squared magnitude of the complex residuals vector. The parameter standard error corresponding to each identified derivative is then computed as the square root of the diagonal elements of the matrix $cov(\hat{\boldsymbol{\theta}})$.

So far, the EE method in frequency domain has been introduced. A linear regression based algorithm is derived to compute the unknown parameter vector from the states and inputs measurement vectors. The advantage of the EE method is that it requires low computational power to identify the aerodynamic derivatives, and therefore it is very suitable for the real-time parameter estimations.

6.3 Summary

In this chapter, the two frequency domain system identification methods were introduced. The first method is transfer function method, which is so-called indirect method. The second method is the equation error method, namely the direct method. Section 6.1 discussed the principle of using transfer function (TF) method. In this method, the system transfer function needs to be obtained both analytically and experimentally. The transfer functions were derived first based on the physical and mathematical laws. The software CIFER could then be used in experiment for

getting the system transfer functions. It was also shown how the unknown aerodynamic derivatives can be calculated from the obtained transfer functions. Section 6.2 discussed the implementation of equation error (EE) method. A method for transforming time domain data to frequency domain data was introduced. The manner in which the transformed data determine the aerodynamic derivatives was explained.

7 Experimental Results

In this chapter, the transfer function and equation error methods will be applied to identify the transfer functions and aerodynamic derivatives of a conventional fixed-wing UAV called-Cropcam. First, the Cropcam's longitudinal channel transfer functions are identified using CIFER, and some aerodynamic derivatives are extracted from the identified transfer functions. Then, the equation error method is implemented to identify the longitudinal channel aerodynamic derivatives. Lastly, the derivatives which are computed in different ways are compared to verify the accuracy of the identification results and the applicability of the identification methods. After the applicability of the transfer function method is validated, it is used to identify a delta-wing UAV's longitudinal channel transfer function and its related aerodynamic derivatives. For the flight test, Pilot in Control (PIC) mode is used to execute the target input excitation. And MicroPilot's autopilot "MP2128 Heli" is used to execute the Computer in Control (CIC) mode flight and record sensors' data. The flight test was executed and the data were gathered by MicroPilot Inc.

7.1 Identification of Cropcam UAV

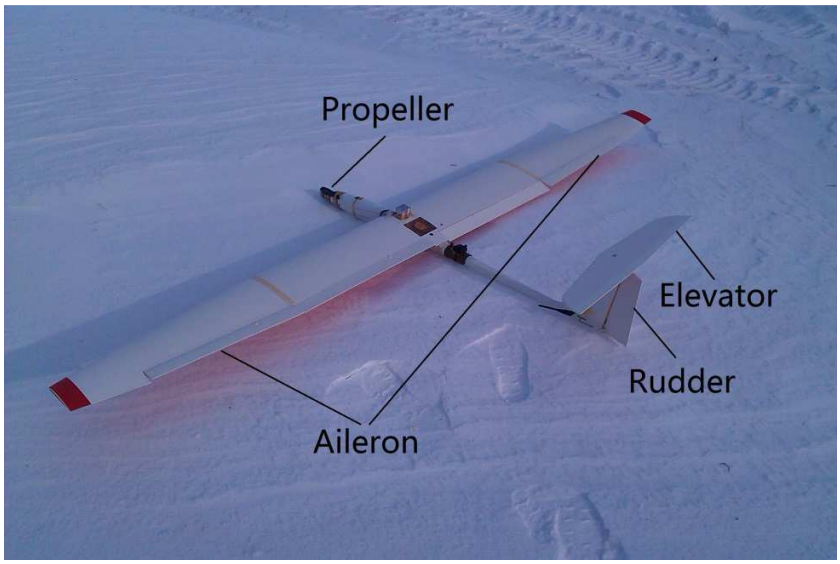

Figure 7.1 Cropcam aircraft

Figure 7.1 is a picture of the Cropcam aircraft. For longitudinal channel system identification, the required variables are linear body velocities u and w, body pitch rate q, and elevator deflection δ_e. There is a Kalman filter onboard the autopilot which combines the sensors, including the inertial sensors (gyro, accelerometers), GPS, barometric sensor, and the magnetic compass. The onboard Kalman filter removes the measuring Gaussian noise and calculates accurate estimates of velocity and attitude of the aircraft which are used in the system identification algorithm. Also, the gyro and accelerometer sensor bias errors are estimated by the Kalman filter and therefore used to compensate for the inertial sensor measurement errors. Based on the onboard measurements, the Kalman filter estimates the aircraft velocities in the North-East-Down (NED) frame. The NED velocities are then converted to the body velocities. For translating NED velocity components into body-axes velocities, the attitude angles φ, θ, ψ are needed. These are calculated by integrating the angular velocities p, q, and r. The angular

velocity measurements from the onboard gyros are calculated after correction of the bias errors by the Kalman filter. The aircraft position estimates as well as its altitude are also provided by the onboard Kalman filter. The sampling frequency of the autopilot is 30 Hz. the Nyquist frequency (15 Hz) is much higher than the frequency of the signals that need to be measured (usually less than 7 Hz). Therefore, 30 Hz sampling frequency is adequate for recording the flight response of Cropcam. The ways of obtaining the data and the data accuracy are listed in Table 7.1.

Table 7.1 Data measuring

Variables	Methods of obtaining	Sensor accuracy	Post-filter accuracy
GPS velocities $\dot{x}$ and $\dot{y}$	Measured by GPS	0.5 m/s	N/A
Altitude z	Measured by Barometric sensor	0.5 m	N/A
Angular velocities p, q and r	Measured by Gyros	0.25 deg/s	0.05 deg/s
Accelerations a_x, a_y and a_z	Measured by Accelerometers	0.15 m/s^2	0.02 m/s^2
Heading angle	Measured by magnetic compass	1 deg	N/A
Attitude angles φ, θ, ψ	Integrated from angular velocities p, q, and r by Kalman filter	N/A	0.5 deg
Linear velocities u, v and w	Calculated from GPS velocities and attitude angles by Kalman filter	N/A	0.3 m/s

The input excitation used for Cropcam's longitudinal channel system identification is shown in Figure 7.2, which is a manually generated Chirp signal.

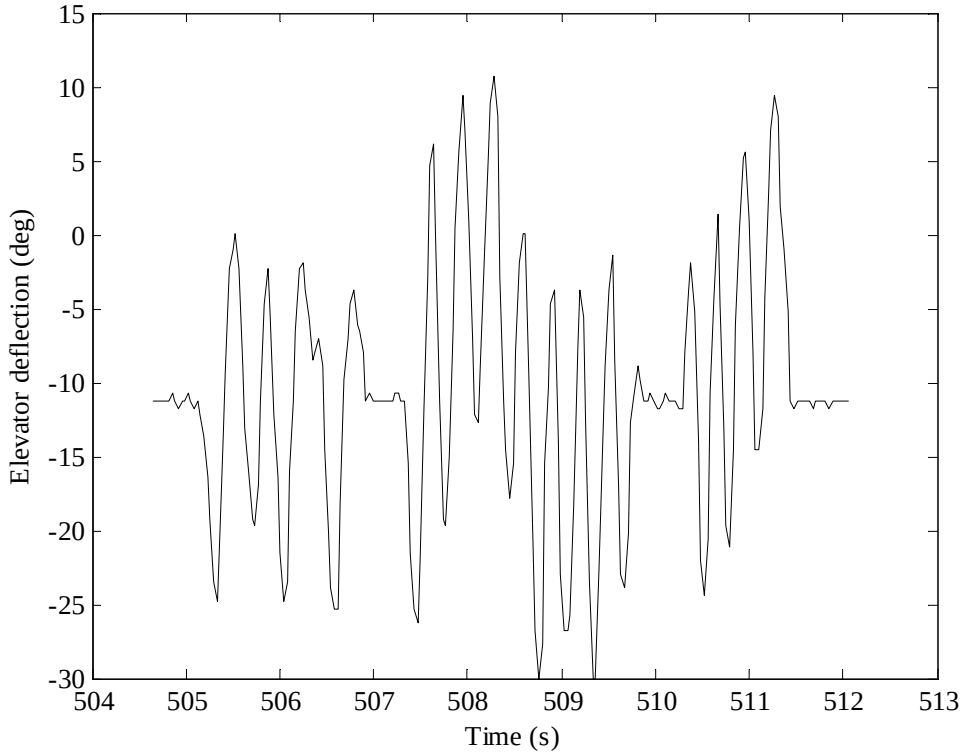

Figure 7.2 Manually generated Chirp input excitation

Figure 7.3 shows the FFT plot of the input excitation which display the frequency range of the input signal.

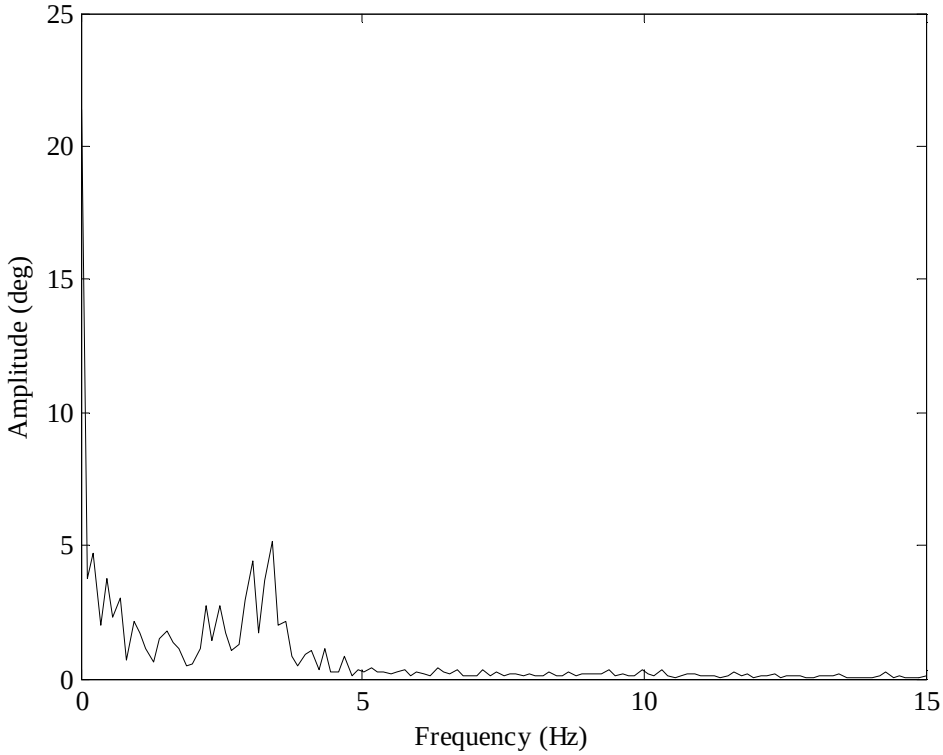

Figure 7.3 FFT of input signal

From the FFT graph, it can be seen that the input excitation's frequency range is 0.3 ~ 5 Hz, which is reasonably appropriate for the current system identification application. Also, from Figure 7.3, it can be seen that the frequency component of the input signal is fairly rich for system identification. The system output responses corresponding to the input are shown in Figure 7.4 to Figure 7.13. *U*, *V* and *W* are the components of total velocity in axial, lateral and vertical direction, respectively; *p*, *q* and *r* are the aircraft body roll, pitch and yaw rate, respectively; φ, θ and ψ are the aircraft attitude angles, which represent aircraft body roll, pitch and yaw angles, respectively; where *z* is the aircraft altitude.

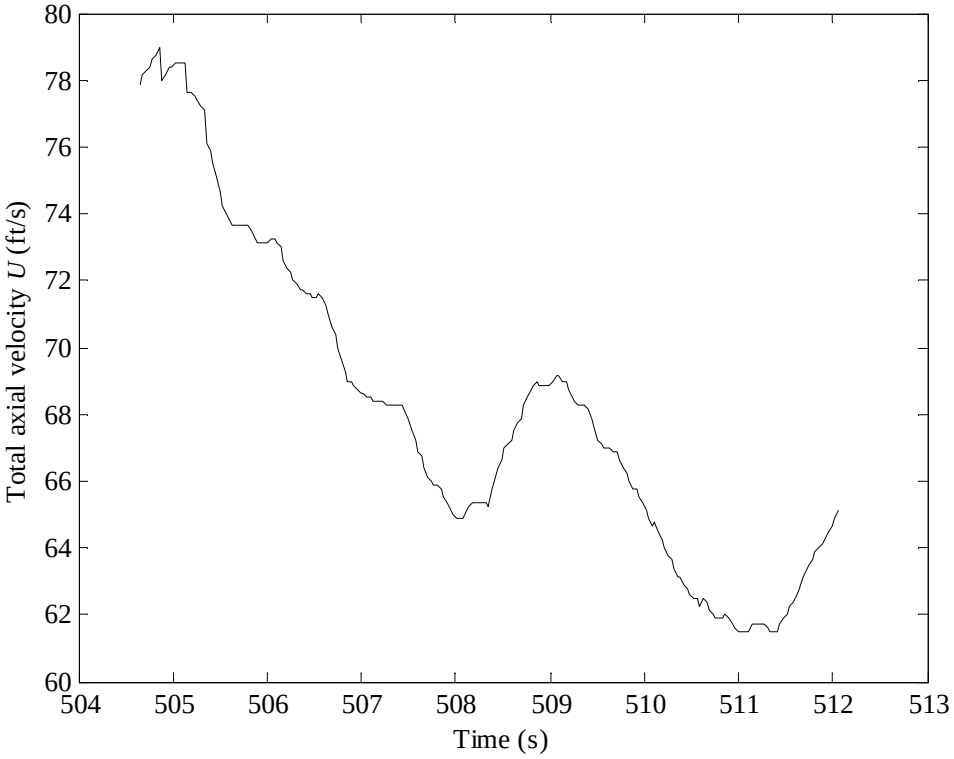

Figure 7.4 Total axial velocity *U*

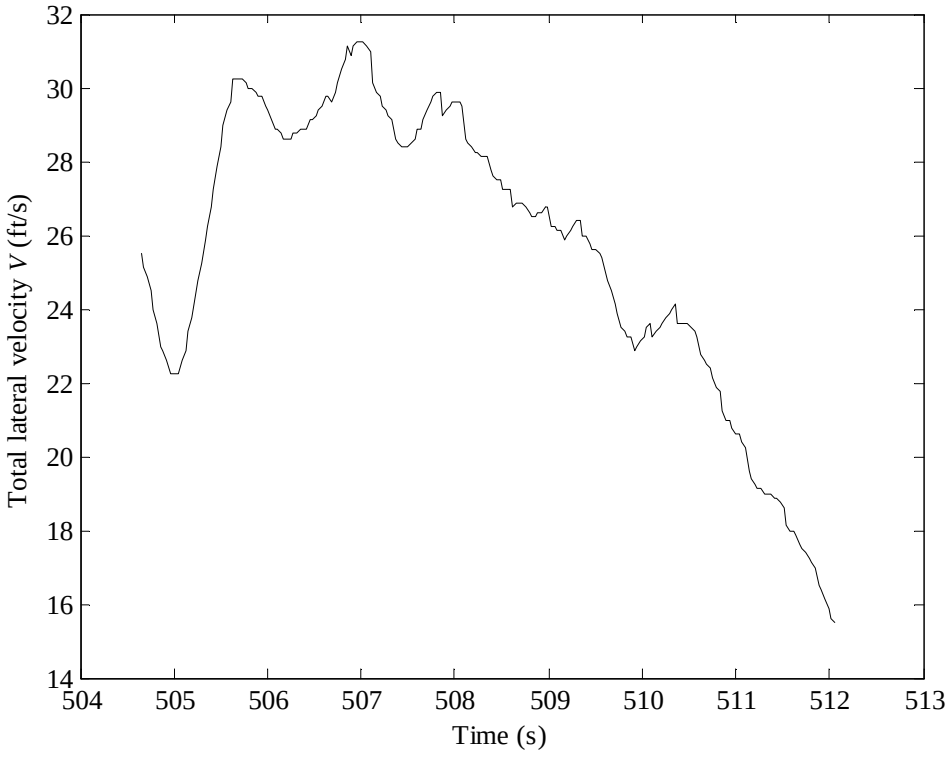

Figure 7.5 Total lateral velocity *V*

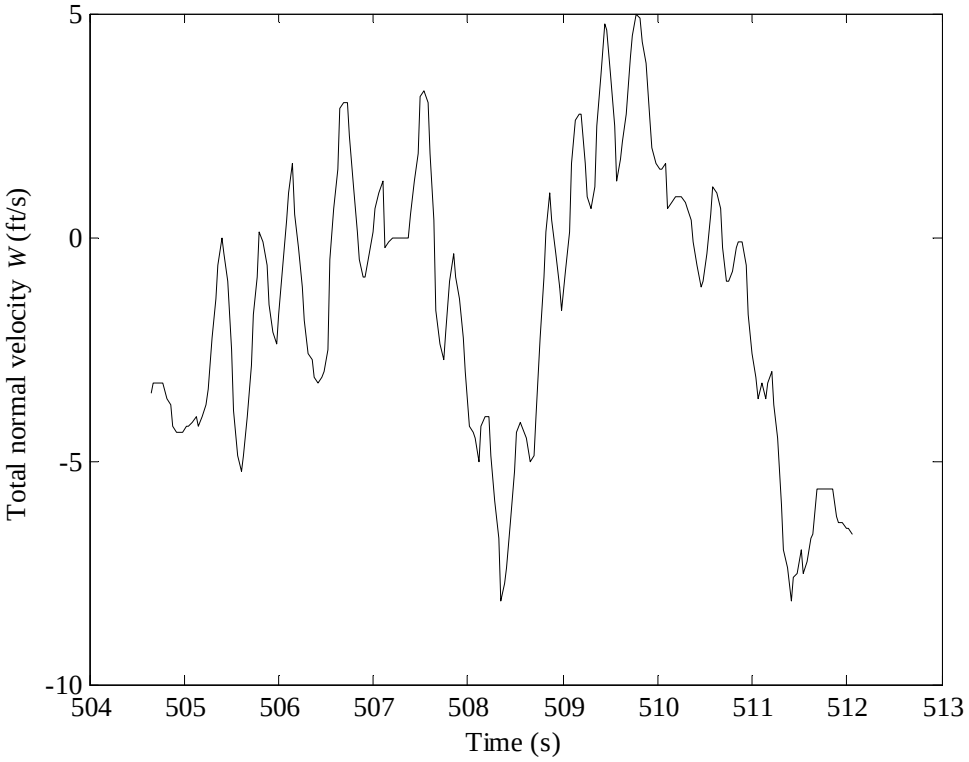

Figure 7.6 Total normal velocity *W*

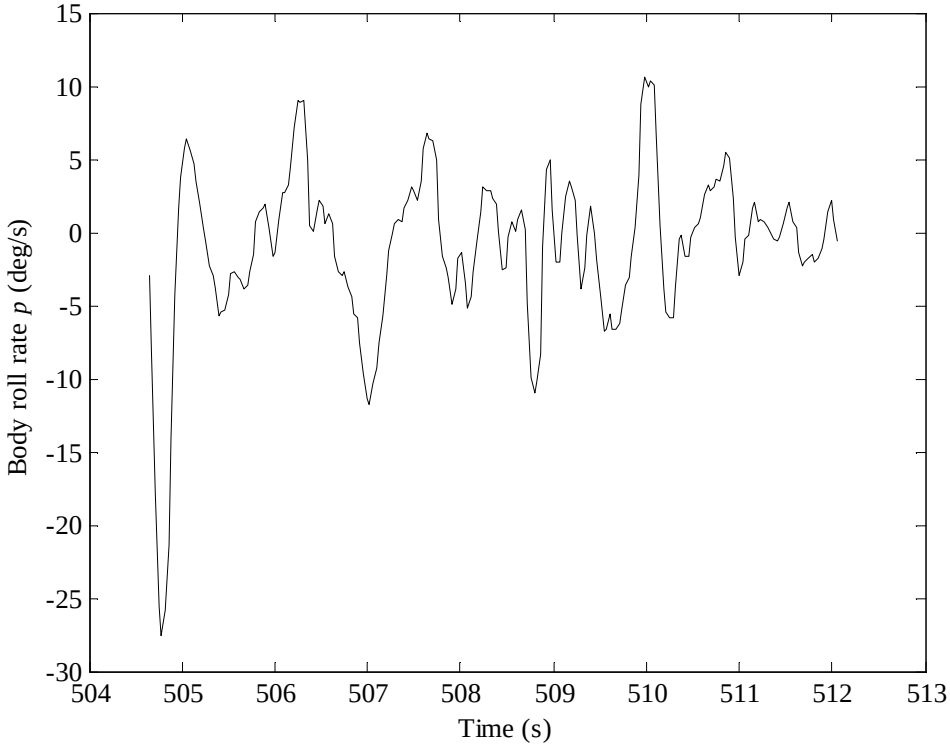

Figure 7.7 Body roll rate *p*

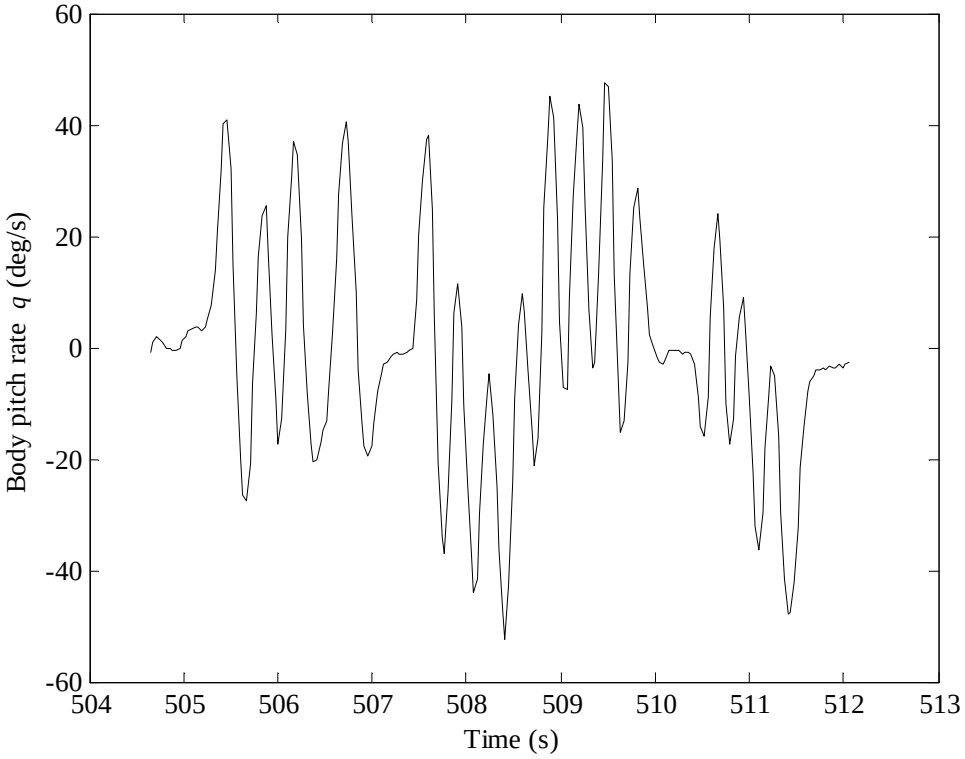

Figure 7.8 Body pitch rate *q*

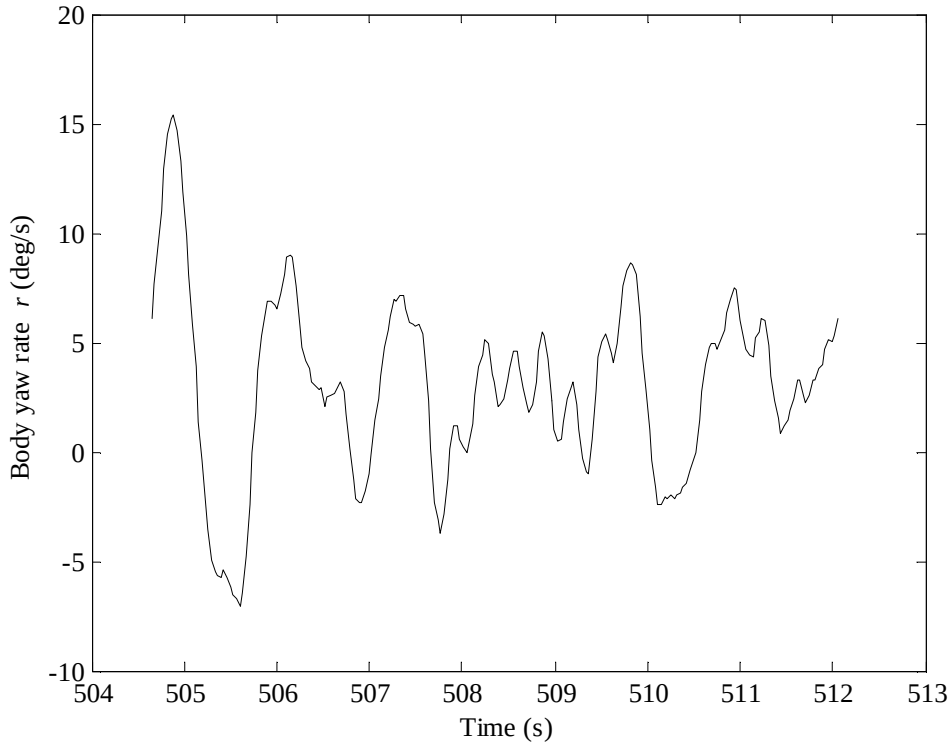

Figure 7.9 Body yaw rate *r*

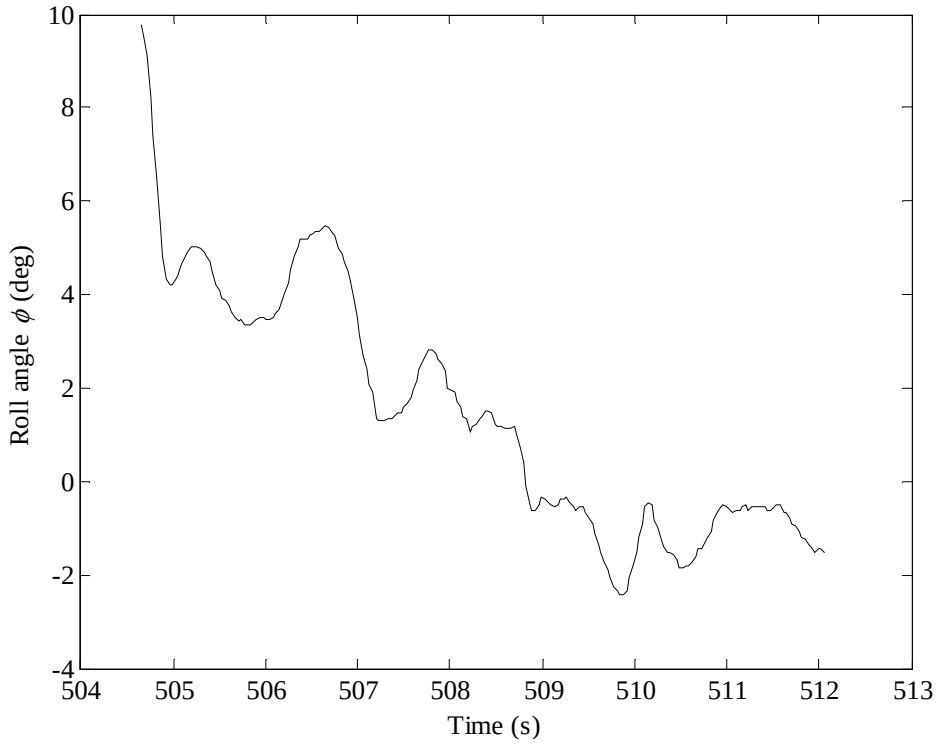

Figure 7.10 Roll angle φ

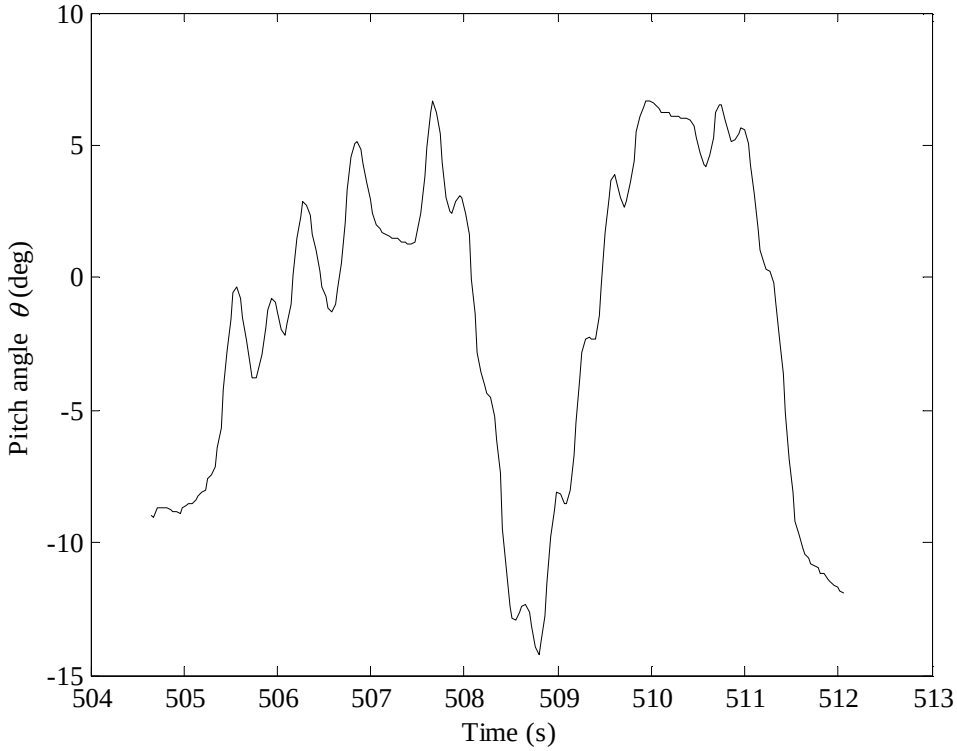

Figure 7.11 Pitch angle θ

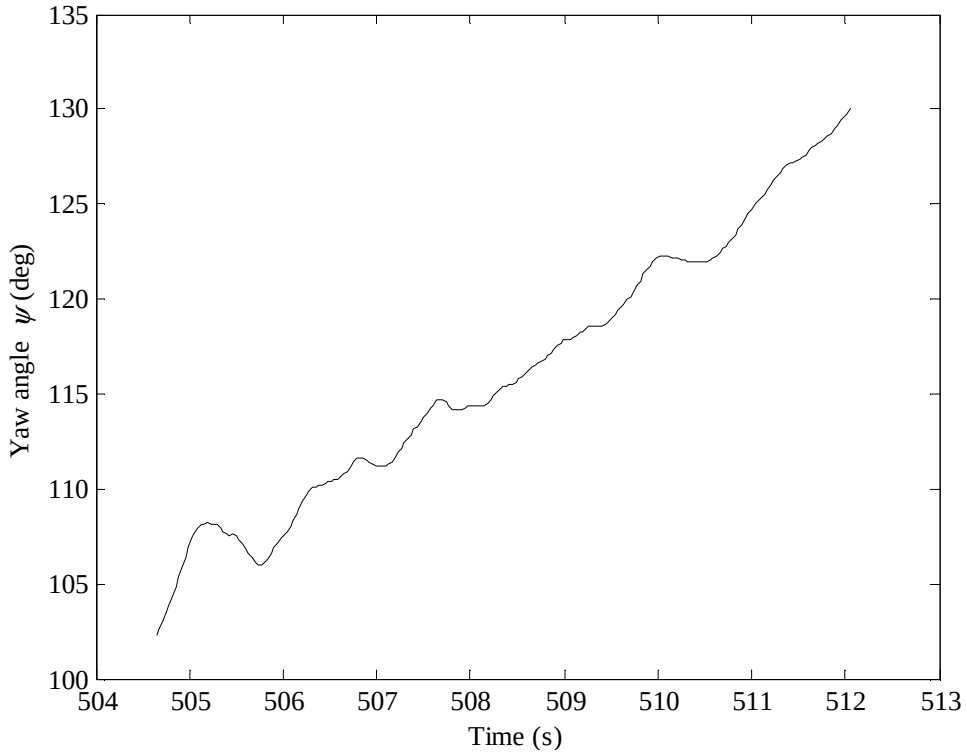

Figure 7.12 Yaw angle ψ

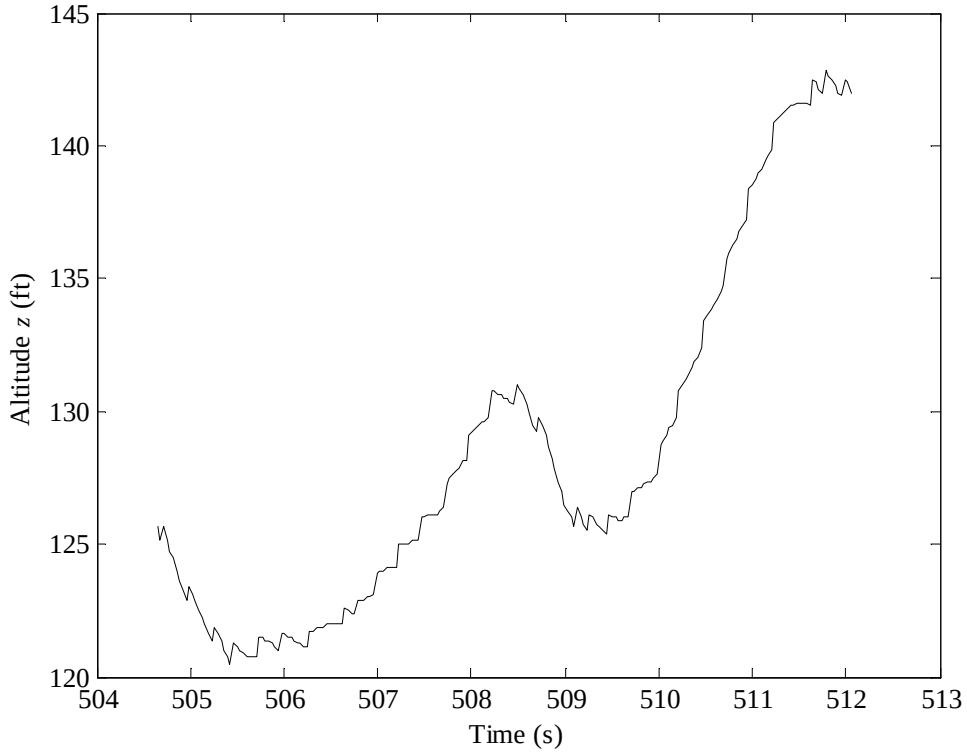

Figure 7.13 Altitude *z*

In this section 7.1, the EE method will be used as the main approach to identify the Cropcam's aerodynamic derivatives. The transfer function method will be applied to identify the longitudinal channel transfer functions, and it is also chosen as an auxiliary way of identifying derivatives. The derivatives extracted from identified transfer functions will be compared to the ones identified by the EE method for verification. Finally, various approaches will be applied for verifying the identification results.

7.1.1 Transfer function method

The utilized input and outputs are shown as Figure 7.14 and Figure 7.15. Theoretically, the output body pitch rate q should have a negative correlation with respect to input elevator deflection δ_e (when elevator rear-end moves up for a pitch up command, the body pitch rate sign goes positive, and vice versa). However by observing Figure 7.14, it can be seen that for most of the time, the input and output keep a positive correlation. This is due to the existence of delay between the commanded elevator signal and the recorded pitch rate measurement.

The total delay is comprised of servo delay, signal gathering delay, as well as the delay inherently associated with the dynamical system response in the longitudinal channel. The servo delay is due to the dynamics of the motors. The signal gathering delay is caused by the sampling time inconsistency. The dynamical system response delay is due to the UAV nature; every dynamical system has response delay.

The same problem exists in the linear velocity data as well. Figure 7.15 shows that the delay exists in the vertical velocity signal w. Since CIFER can deal with the delay automatically, its existence can be ignored when processing the data, and using the transfer function method. The Bode plots of δ_e-w and δ_e-q are shown as Figure 7.16 and Figure 7.17, respectively.

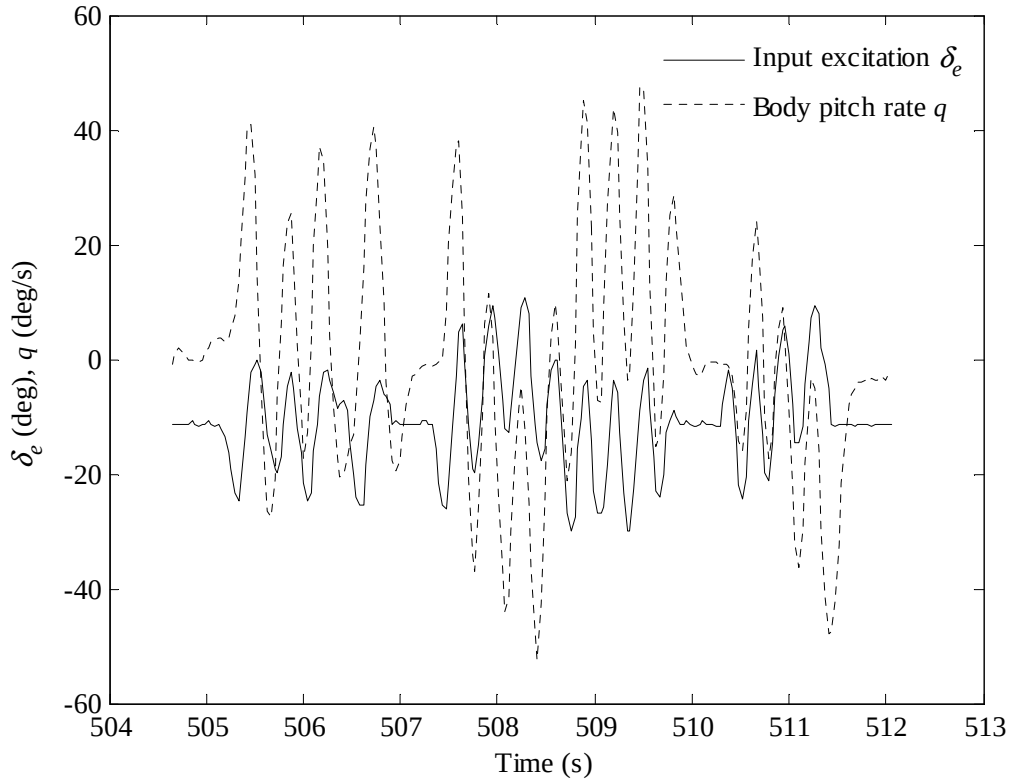

Figure 7.14 δ_e-q data pair

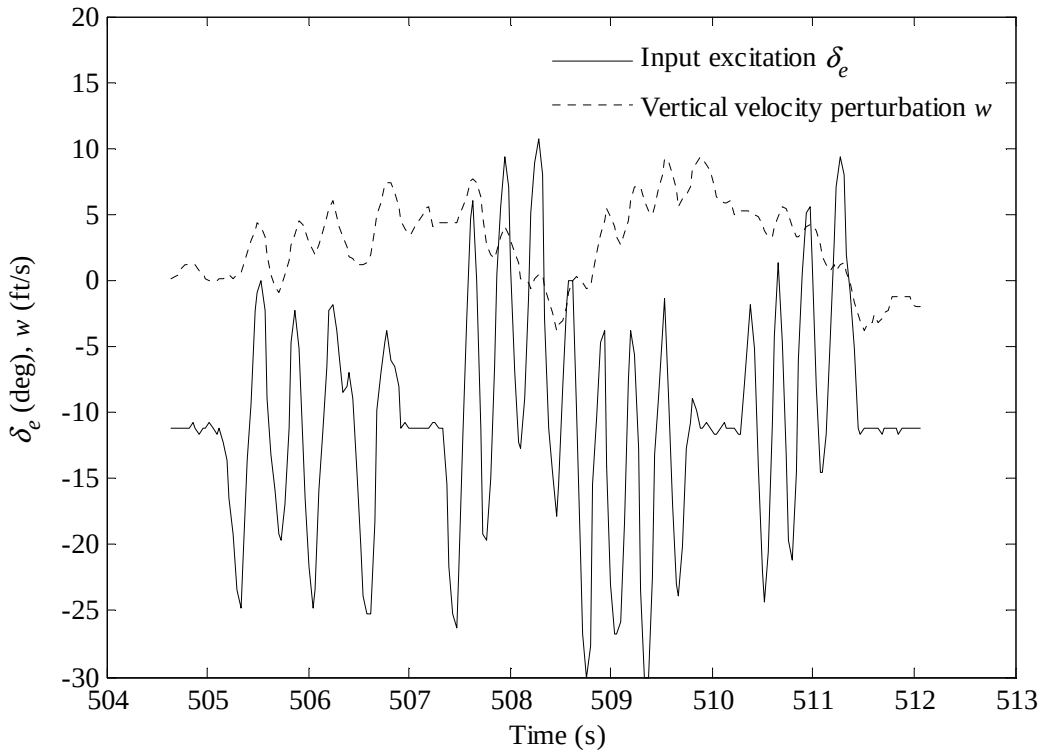

Figure 7.15 δ_e-w data pair

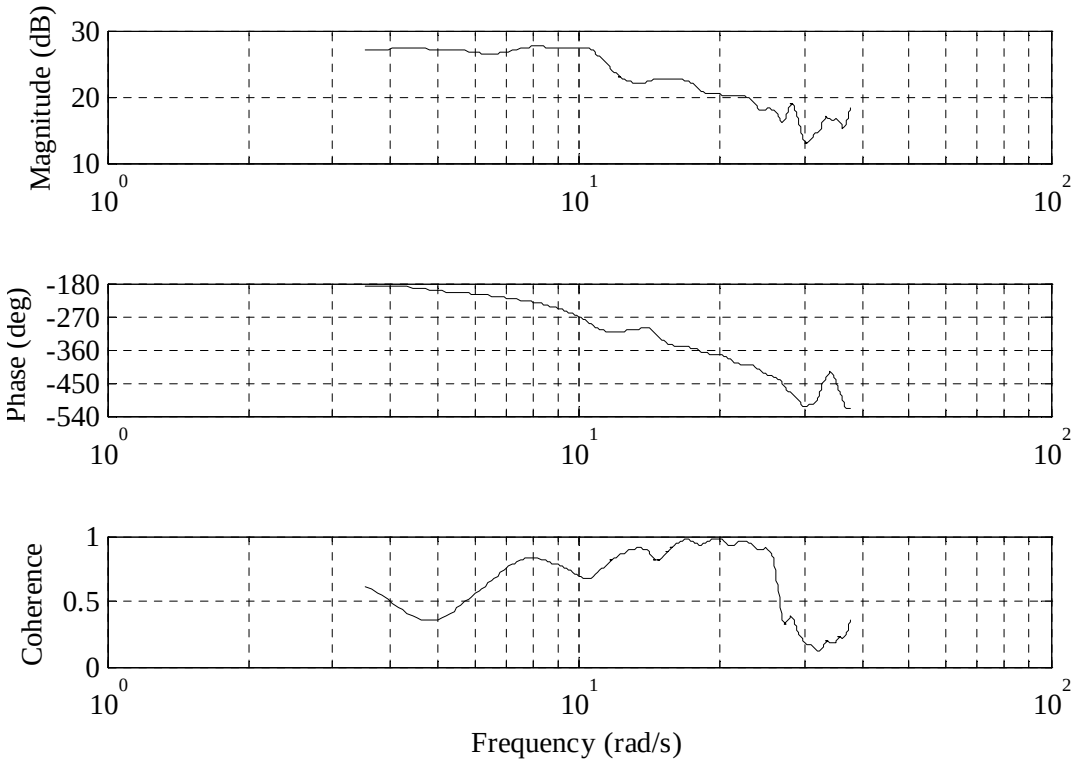

Figure 7.16 Bode plot of δ_e-w

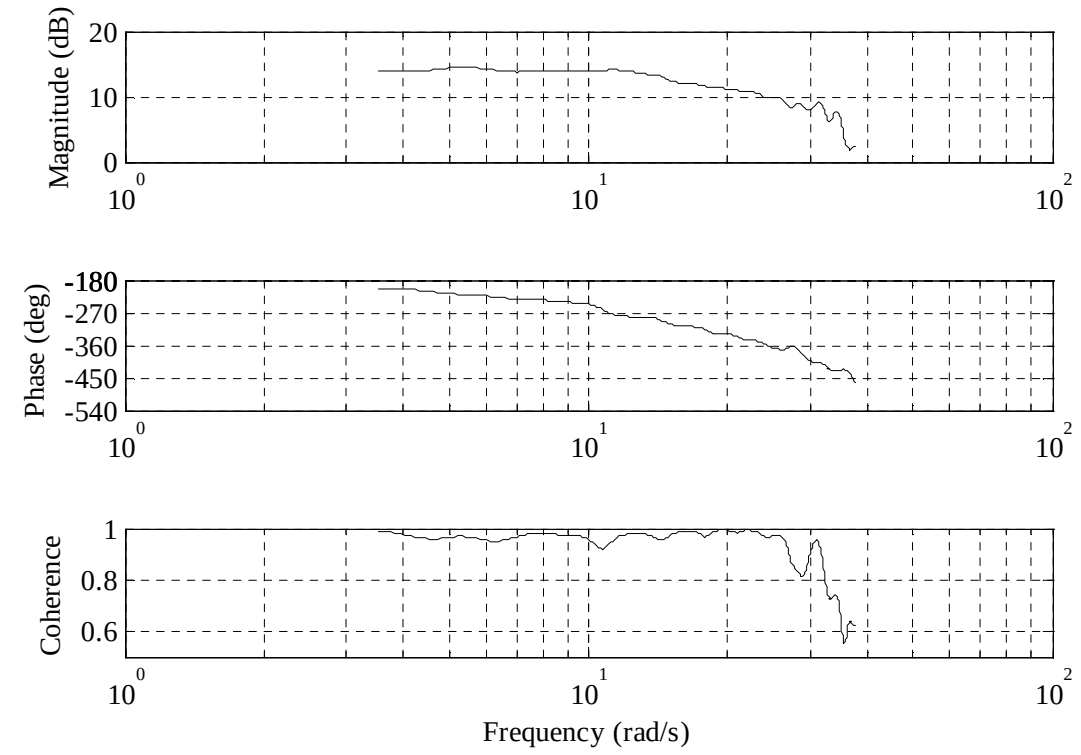

Figure 7.17 Bode plot of δ_e-q

From Figure 7.17, it is seen that the phase curve starts at -200 degrees. Theoretically saying, it should starts at -180 degrees. However, the phase shifted due to the existence of delay. By observing the coherence range, the applicable frequency range for identifying transfer functions can be selected as: 6.7 ~ 26 rad/s for δ_e-w; and 3.54 ~ 34 rad/s for δ_e-q. By utilizing CIFER, these transfer functions are obtained:

$$\frac{w(s)}{\delta_e(s)} = \frac{-17.3(s + 235.44)e^{-0.075s}}{s^2 + 16.92s + 223.33} \tag{7.1}$$

$$\frac{q(s)}{\delta_e(s)} = \frac{-82.37(s + 9.03)e^{-0.0867s}}{s^2 + 21.52s + 158.19} \tag{7.2}$$

The costs of these two transfer functions are 81.45 and 9.04 respectively, which are all under the acceptable cost guideline of 100. Cost (Tischler and Remple, 2012) is an indication of the consistency between the transfer function's frequency response and the flight data's frequency response. The cost function is given by (Tischler and Remple, 2012):

$$J = \frac{20}{n}\sum_{\omega_1}^{\omega_n} W_\gamma[W_g(|T_{data}| - |T_{model}|)^2 + W_p(\angle T_{data} - \angle T_{model})^2] \tag{7.3}$$

where, n is number of frequency points (default value is 20); ω_1 and ω_n are starting and ending frequencies of fit; W_γ is coherence weighting to emphasize most reliable data, which equals $1.58(1.0 - e^{-\gamma_{xy}})$; W_g is weighting on gain error (default value is 1.0) and W_p is weighting on phase error (default value is 0.01745).

The low cost preliminarily proved that the identified transfer functions' accuracies are acceptable, but further verification is still required. The fittings of transfer functions and flight frequency responses are shown in Figure 7.18 to Figure 7.21.

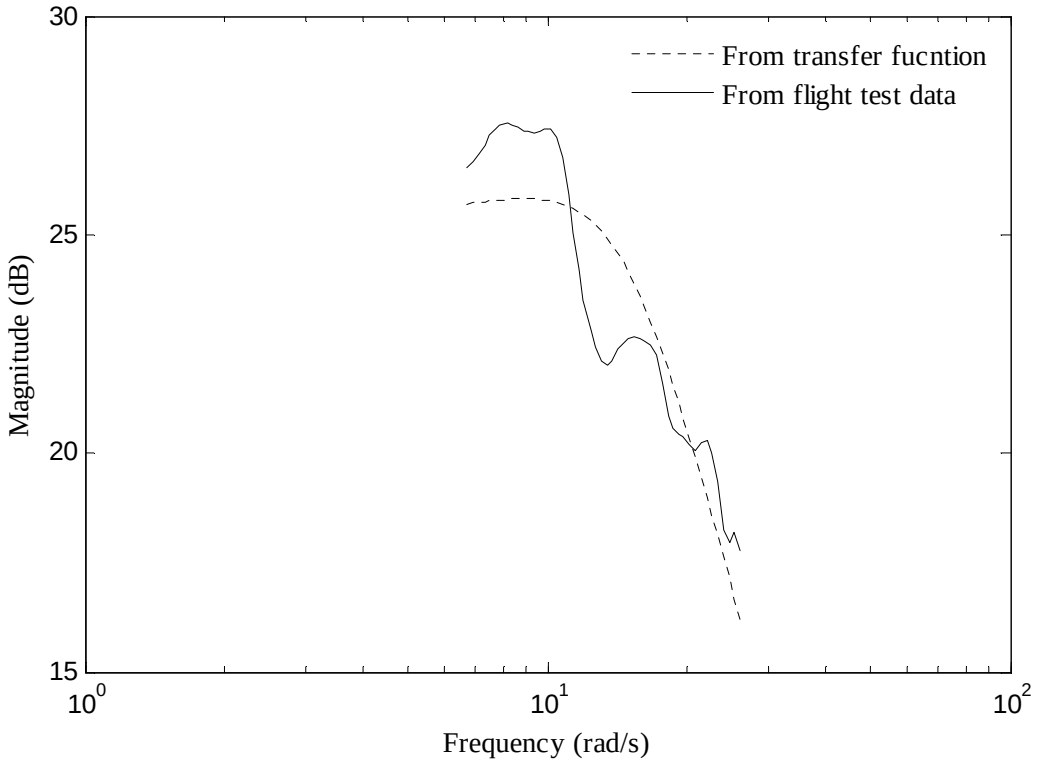

Figure 7.18 Verification of magnitude of δ_e-w

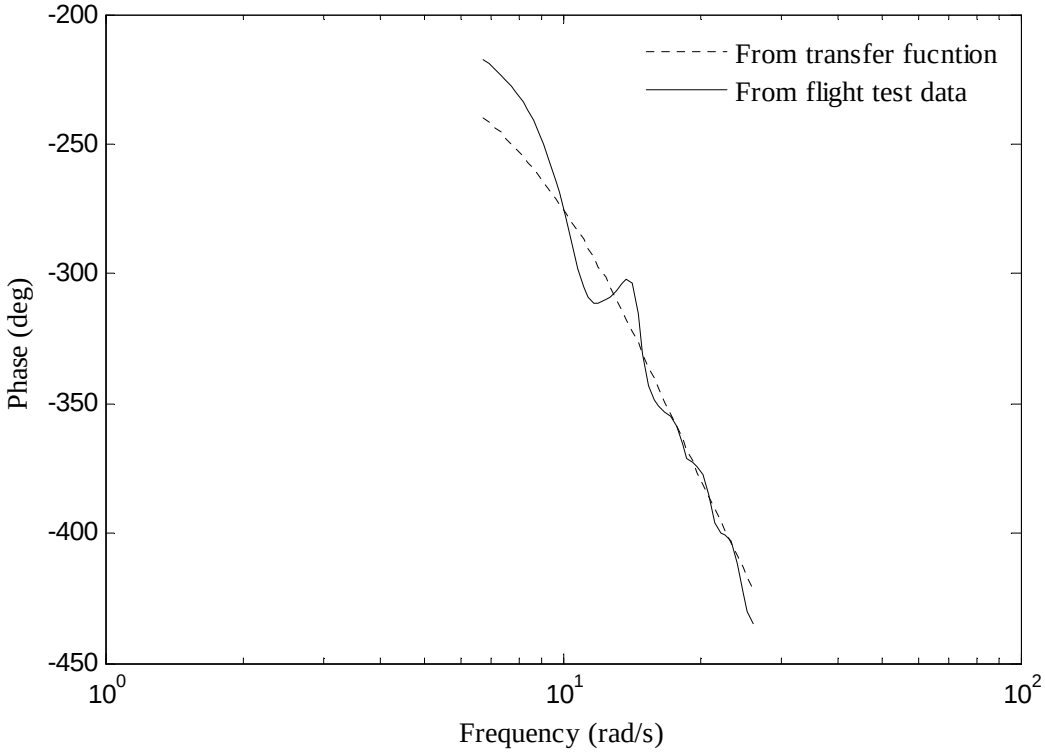

Figure 7.19 Verification of phase of δ_e-w

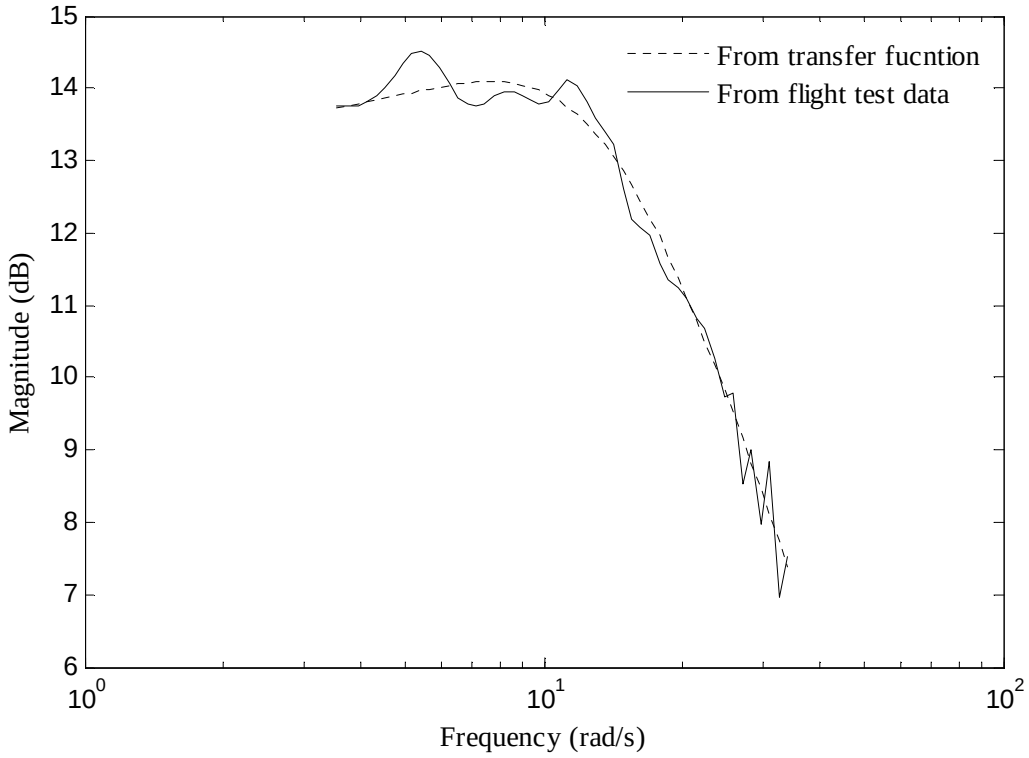

Figure 7.20 Verification of magnitude of δ_e-q

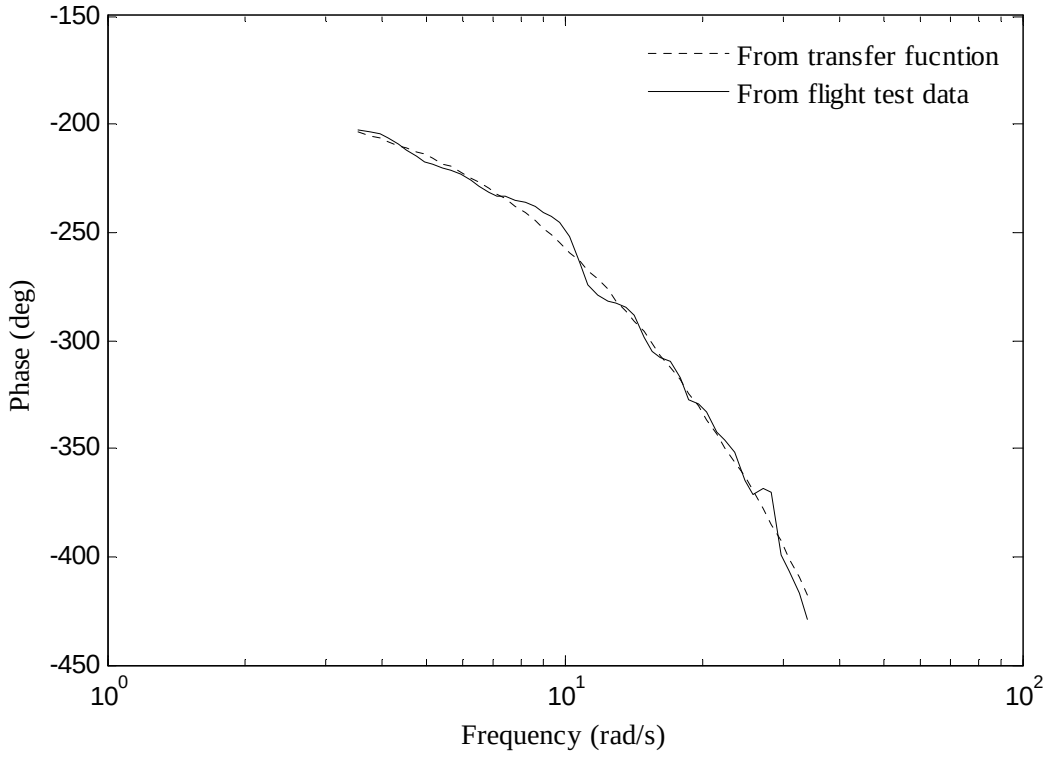

Figure 7.21 Verification of phase of δ_e-q

From the graphs it is seen that the curves match reasonably well. This means that the identified transfer functions are fairly accurate. So far, the frequency domain verification method has been applied and the accuracy of transfer functions has been demonstrated. However, the most convincing way to verify the accuracy of transfer functions is time domain verification. For time domain verification, the flight test input excitation is fed to the identified transfer functions to simulate the time domain responses. The simulated responses are compared with the flight measurements. Figure 7.22 shows the comparison between simulated *w* and the measured *w*. Figure 7.23 shows the comparison between the simulated *q* and the measured *q*.

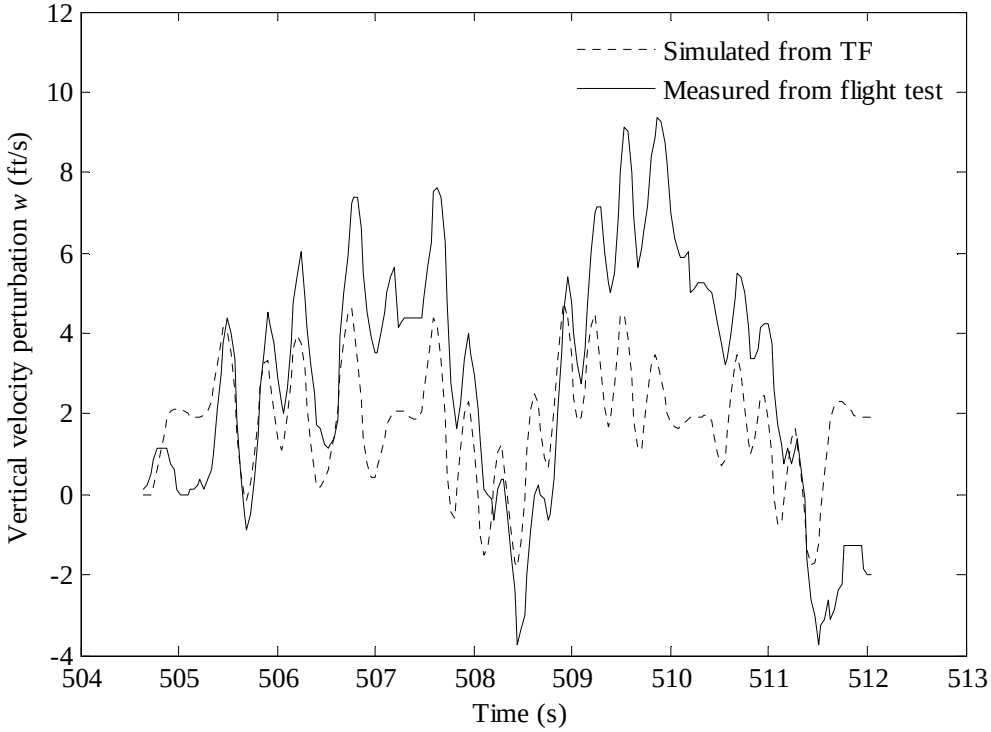

Figure 7.22 Comparison of simulated *w* and measured *w*

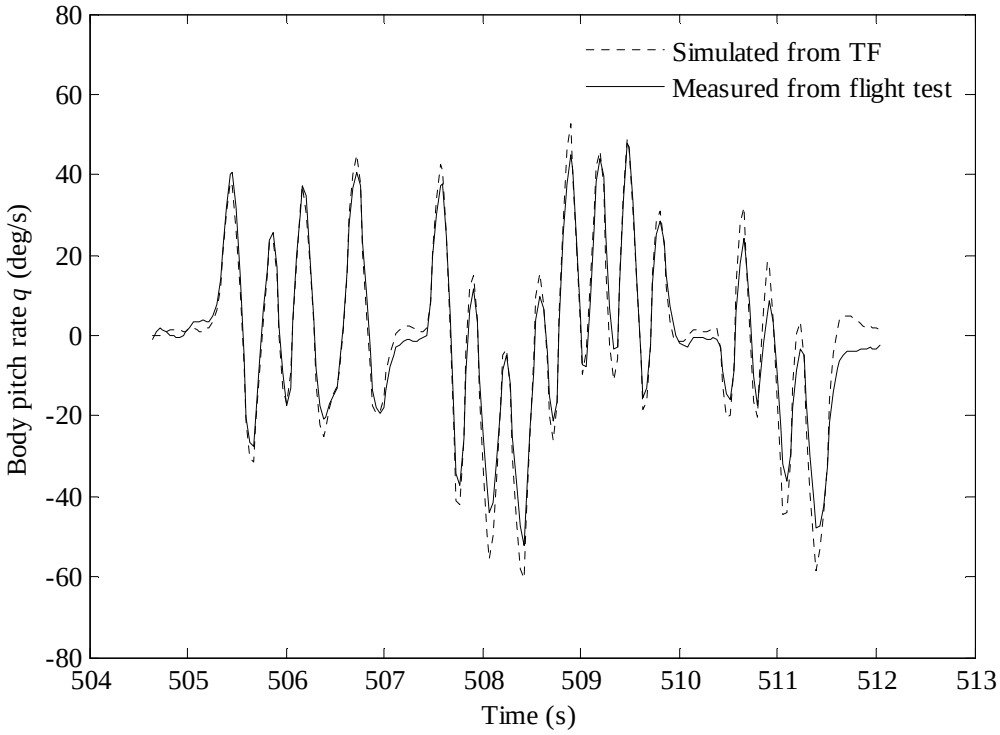

Figure 7.23 Comparison of simulated *q* and measured *q*

The comparison shown in Figure 7.23 demonstrated that the transfer function simulated body pitch rate *q*, and the flight test measured *q* are matching quite well. For the vertical velocity *w*, the simulated one is also quite similar to the measured one, the largest difference gap between the simulate *w* and flight test measured *w* occurred at the less oscillation part (the part oscillates mildly, which is also low frequency part). Because the difference is not large, the matching is still acceptable. Actually the appearance of difference matches to the coherence plot shown in Figure 7.16. In the coherence graph, the coherence is quite low at low frequency. Low coherence indicates low accuracy; therefore, it is reasonable that the matching is not that accurate at the low frequency part. Low coherence is caused by some nonlinearities involved in the input-output model. Therefore, the linear transfer function cannot perfectly match the nonlinear behaviour.

To further validate the identified transfer functions, Equations (7.1) and (7.2) were tested with the unseen Doublet signal. The unseen Doublet signal is shown in Figure 7.24. Figure 7.25 and Figure 7.26 show the comparisons between simulated *w*, *q* and measured *w*, *q*.

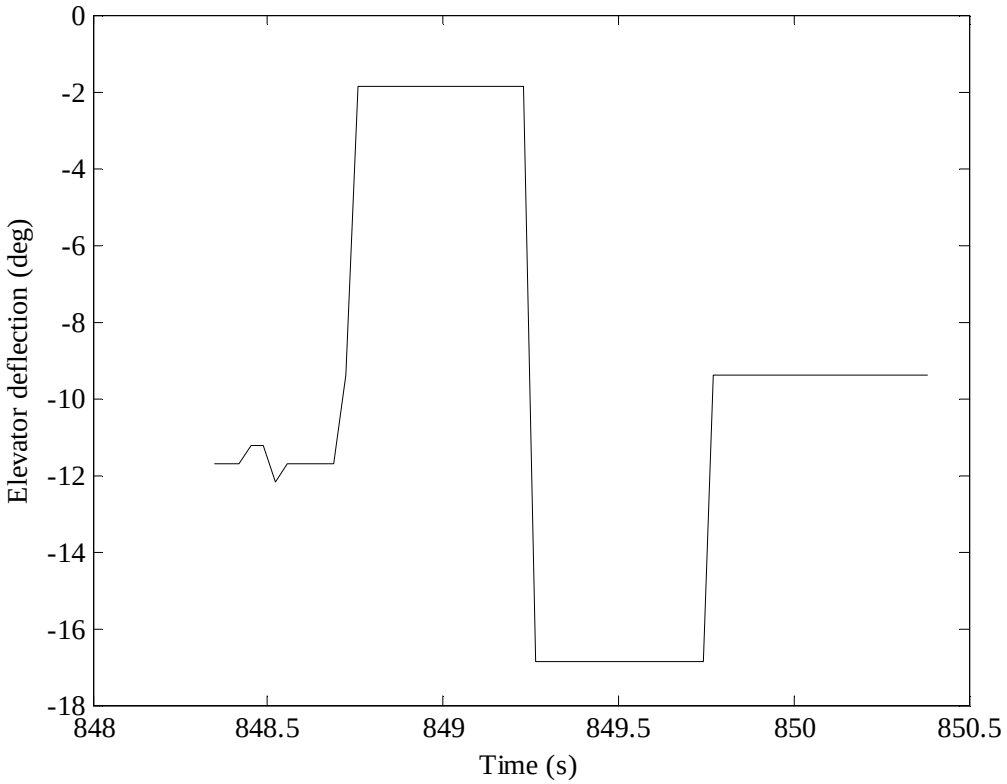

Figure 7.24 Unseen Doublet signal

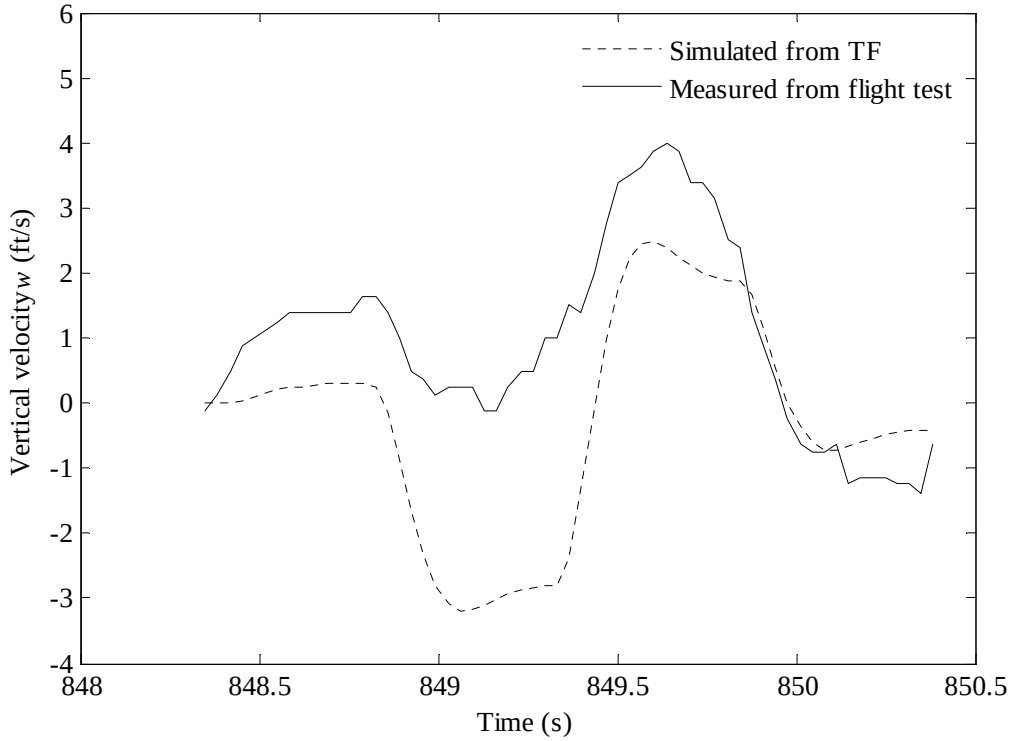

Figure 7.25 Comparison of simulated *w* and measured *w* with the unseen Doublet signal

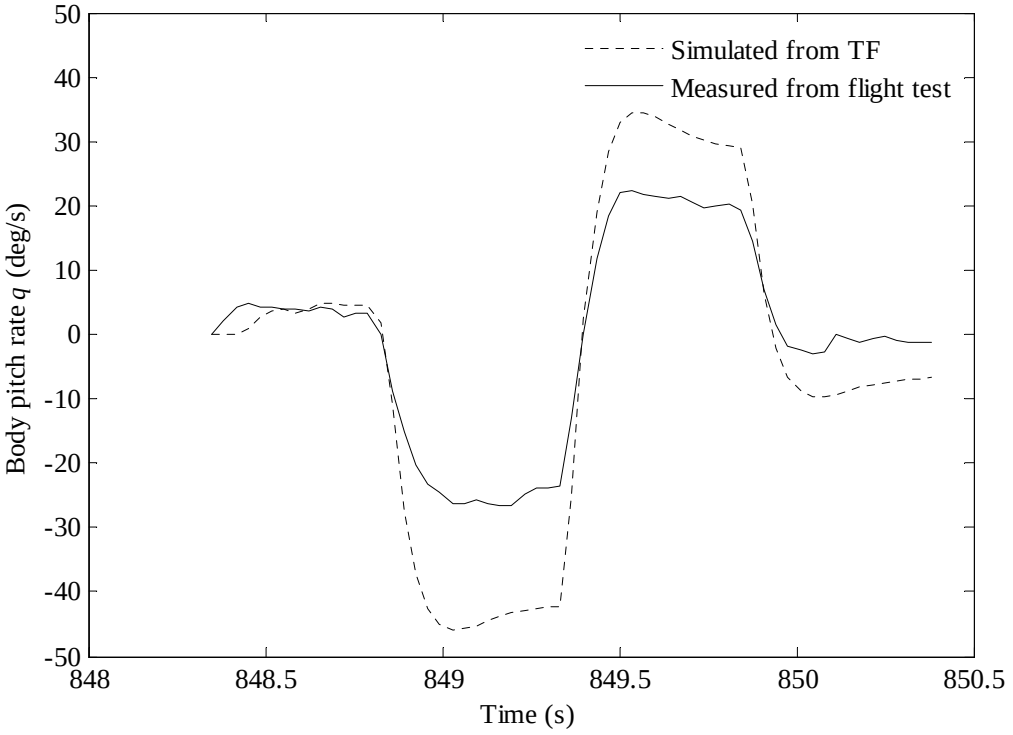

Figure 7.26 Comparison of simulated *q* and measured *q* with the unseen Doublet signal

In Figure 7.25 and Figure 7.26, it is seen that the phase of the simulated *w* and *q* match closely with flight test measured *w* and *q*. However, the magnitudes do not match well. This is because the model describing the system was linearized around an operating point, and the aerodynamic derivatives and transfer functions were identified at this operating point. Now this set of transfer functions are used for simulating the output around another operating point (the doublet input test). Therefore, it is reasonable that the simulated output cannot match well with the measured output. Also from the figures it is seen that the *q* plot matches slightly closer than the *w* plot. The reason was already explained when referring to the original signal verification. This further proves that the identified transfer functions are reliable.

Theoretically, the denominators of δ_e-*w* and δ_e-*q* transfer functions should be the same or very close, but due to some deficiencies in the data quality, the results are inconsistent. However, the difference is not large. Since verification shows that the transfer function of δ_e-*q* has a higher accuracy than δ_e-*w*, the transfer function of δ_e-*q* is used for extracting aerodynamic derivatives $C_{m_{\delta e}}$, C_{m_q}, C_{Z_w} and C_{m_w}. The transfer function of δ_e-*w* is only used to calculate $C_{Z_{\delta e}}$.

Applying the algorithm discussed in Section 6.1.2:

$$\frac{w(s)}{\delta_e(s)} = \frac{z_{\delta_e}(s + U_e \frac{m_{\delta_e}}{z_{\delta_e}})}{s^2 - (m_q + z_w)s + (m_q z_w - m_w U_e)} = \frac{-17.3(s + 235.44)}{s^2 + 16.92s + 223.33} \tag{7.4}$$

$$\frac{q(s)}{\delta_e(s)} = \frac{m_{\delta_e}(s - z_w)}{s^2 - (m_q + z_w)s + (m_q z_w - m_w U_e)} = \frac{-82.37(s + 9.03)}{s^2 + 21.52s + 158.19} \tag{7.5}$$

By extracting the equal terms from Equations (7.4) and (7.5), the following equalities hold,

$$\begin{cases} z_{\delta_e} = -17.3 \\ m_{\delta_e} = -82.37 \\ -z_w = 9.03 \\ -(m_q + z_w) = 21.52 \\ m_q z_w - m_w U_e = 158.19 \end{cases}$$

where U_e = 55 ft/s. By solving the above equations, the following concise notated derivatives are obtained,

$$\begin{cases} z_{\delta_e} = -17.3 \\ m_{\delta_e} = -82.37 \\ z_w = -9.03 \\ m_q = -12.49 \\ m_w = -0.83 \end{cases}$$

For convenience, the above derivatives are converted into North American dimensionless derivatives (refer to Appendix 1). The final results are listed in Table 7.2. Here is an example showing how to convert concise notated derivative m_q to North American dimensionless derivative C_{m_q}. Other derivatives conversion can be found in the Appendix 1.

i. Convert m_q to dimensional British format derivative $\mathring{\mathrm{M}}_q$:

$$\mathring{\mathrm{M}}_q = I_y \times m_q \tag{7.6}$$

ii. Convert $\mathring{\mathrm{M}}_q$ to dimensionless British derivative M_q:

$$M_q = \mathring{\mathrm{M}}_q / 0.5\rho V_0 S\bar{\bar{c}} \tag{7.7}$$

iii. Convert M_q to dimensionless North American derivative C_{m_q}:

$$C_{m_q} = 2M_q \tag{7.8}$$

Thus, dimensionless North American notation derivative C_{m_q} can be acquired. The conversion of dimensionless North American notation derivative C_{m_q} to dimensional North American notation derivative M_q is shown as,

$$M_q = C_{m_q} \times \rho V_0 S \bar{\bar{c}}^2 / 4 I_y \tag{7.9}$$

where ρ = 0.002286 slug/ft^3, S = 5.31 ft^2, $\bar{\bar{c}}$ = 0.77 ft, V_0 = 68.26 ft/s and I_y= 3.04 lb·ft^2. In this way, all the derivatives can be converted to dimensionless North American derivatives.

Table 7.2 Transfer function method identified aerodynamic derivatives

C_{Z_w}	-6.4492
$C_{Z_{\delta e}}$	-0.2246
C_{m_w}	-0.3036
C_{m_q}	-11.9227
$C_{m_{\delta e}}$	-0.5506

The accuracy of the derivatives will be examined together with the ones identified by the EE method in the coming section.

7.1.2 Equation error method

For applying the EE method, data analysis and pre-processing is essential. In this section, typical data analysis and pre-processing methods will be applied. As shown in Figure 7.14 and Figure 7.15, there are delays between the input and the outputs. Since the priori model (e.g. Equation (4.110)) utilised for the EE system identification method does not expect the physical delay, the delay in the input-output data pair must be removed first. Otherwise, the identification results will not be accurate. By analyzing and pre-processing the data, the delay is found to be approximately 100 ms. This is in agreement with the delay shown in the identified transfer

function (7.2). From Equation (7.2), it is seen that the delay between the input and the output is 86.7 ms. Therefore, the angular velocity responses are shifted ahead by 3 data points in time (equivalent to 100 ms in the 30 Hz data sampling). The linear velocities are found to have the same problem, and from the Equation (7.1), it is seen that the delay between input elevator deflection and output vertical velocity is 75 ms. Therefore the vertical velocity is shifted ahead by 3 data points as well. The shifted δ_e-q, δ_e-w and δ_e-u data pairs are shown in Figure 7.27 to Figure 7.29.

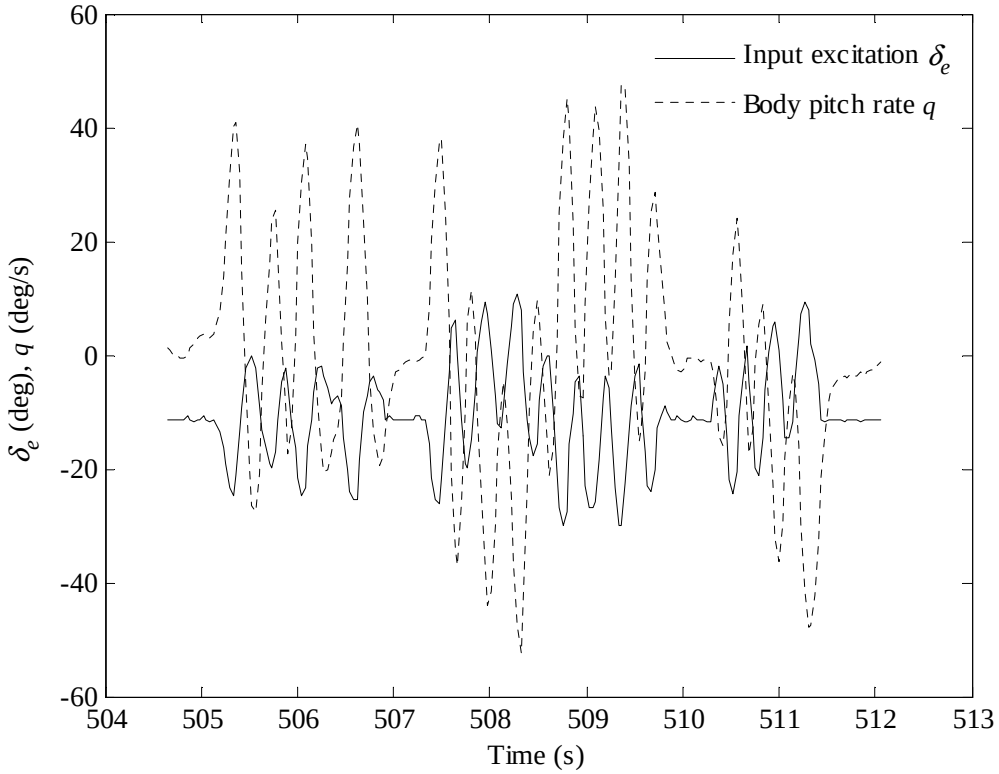

Figure 7.27 Delay removed δ_e-q data pair

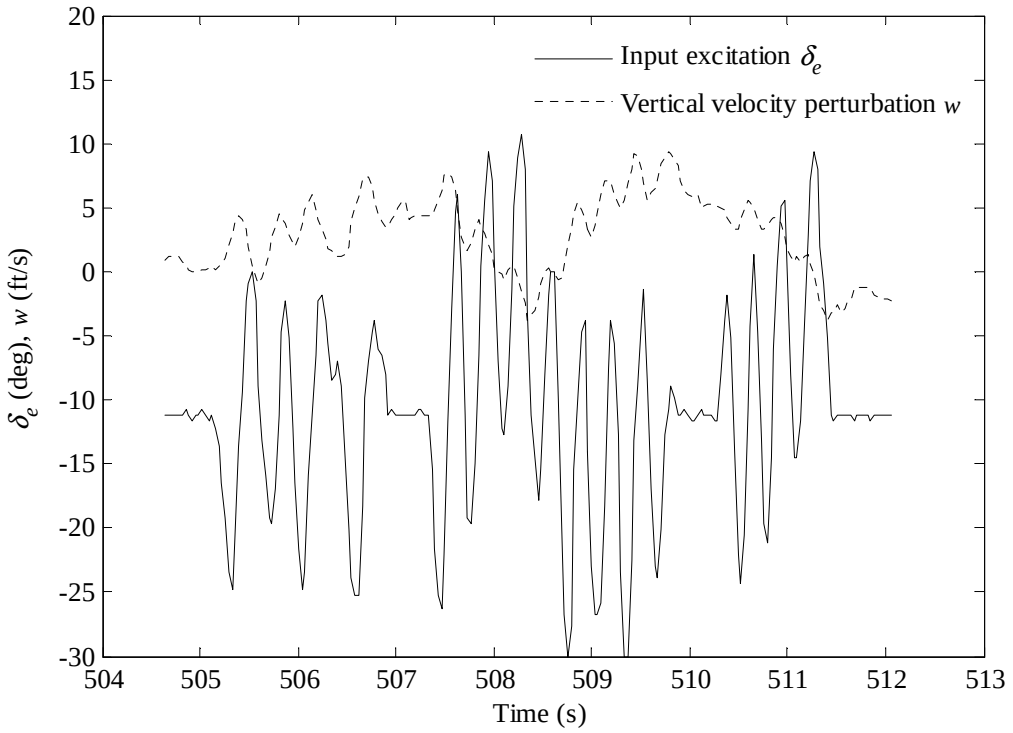

Figure 7.28 Delay removed δ_e-w data pair

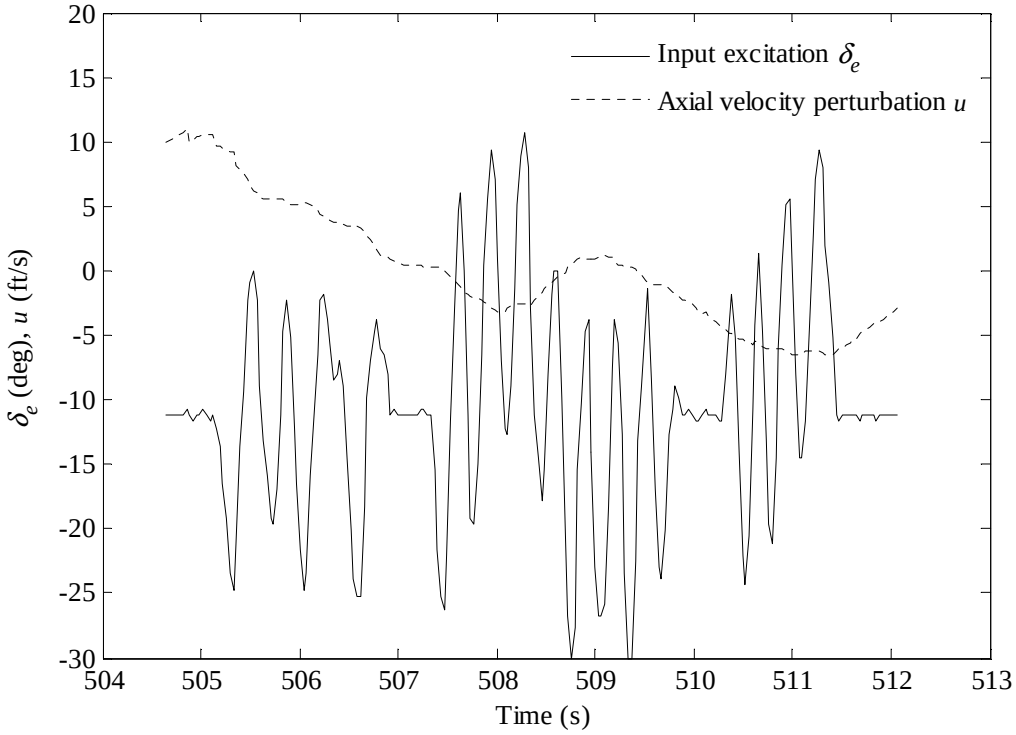

Figure 7.29 Delay removed δ_e-u data pair

From Figure 7.27 to Figure 7.29, it can be seen that there is a negative correlation between the shifted input-output data pairs. In addition to the problem of delay, sampling time inconsistency is another issue that needs to be addressed. The nominal sampling frequency of the autopilot data recording device is 30 Hz. Therefore, the sampling time is expected to be around 33.33 ms. However, in the real measurement, the actual sampling time is fluctuating near the average 33.33 ms. The actual sampling time of the gathered data is shown by Figure 7.30. The sampling time inconsistency problem is solved by interpolating and distributing the data evenly on the time axis.

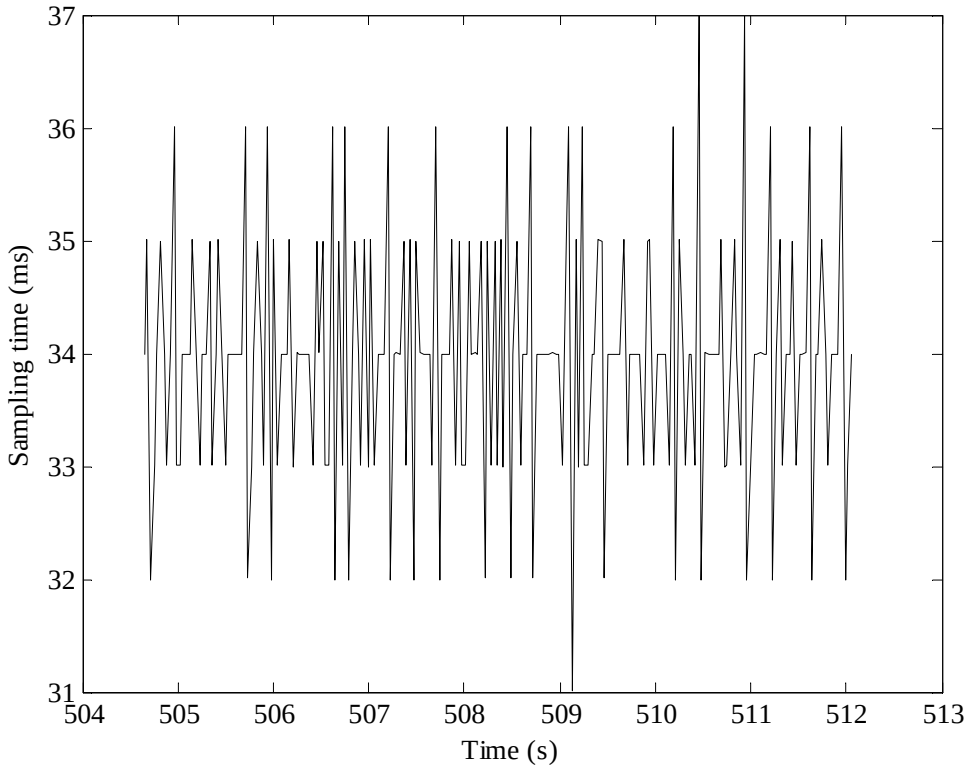

Figure 7.30 Original data sampling time

The sampling time of interpolated data is 33.9 ms. After pre-processing the flight data, the EE method is applied for derivatives identification.

Pitching moment related derivatives identification

Equation (7.10) derived from Equation (4.110) is the postulated aerodynamic model used for the pitching moment derivatives identification:

$$\dot{q} = \mathrm{M}_u u + \mathrm{M}_w w + \mathrm{M}_q q + \mathrm{M}_{\delta_e} \delta_e \tag{7.10}$$

The derivatives M_u, M_w, M_q and M_{δ_e} are all dimensional, therefore, the states u, w, q and input δ_e should also be dimensional. Thus, the following regression matrix is derived from Equation (6.51):

$$\boldsymbol{X} = \begin{bmatrix} \widetilde{\boldsymbol{u}}(1) & \widetilde{\boldsymbol{w}}(1) & \widetilde{\boldsymbol{q}}(1) & \widetilde{\boldsymbol{\delta_e}}(1) \\ \widetilde{\boldsymbol{u}}(2) & \widetilde{\boldsymbol{w}}(2) & \widetilde{\boldsymbol{q}}(2) & \widetilde{\boldsymbol{\delta_e}}(2) \\ \cdot & \cdot & \cdot & \cdot \\ \cdot & \cdot & \cdot & \cdot \\ \cdot & \cdot & \cdot & \cdot \\ \widetilde{\boldsymbol{u}}(m) & \widetilde{\boldsymbol{w}}(m) & \widetilde{\boldsymbol{q}}(m) & \widetilde{\boldsymbol{\delta_e}}(m) \end{bmatrix} \tag{7.11}$$

For the $\boldsymbol{Y}$ vector as shown in Equation (6.50), there are two ways to obtain it:

1) First calculate $\dot{\boldsymbol{q}}$ from $\boldsymbol{q}$ using 2-point regression,

$$\dot{\boldsymbol{q}}(m) \approx \frac{\boldsymbol{q}(m) - \boldsymbol{q}(m-1)}{dt} \tag{7.12}$$

Then perform the finite Fourier transform to $\dot{\boldsymbol{q}}$, therefore the following have,

$$\boldsymbol{Y} = \begin{bmatrix} \widetilde{\dot{\boldsymbol{q}}}(1) \\ \widetilde{\dot{\boldsymbol{q}}}(2) \\ \cdot \\ \cdot \\ \cdot \\ \widetilde{\dot{\boldsymbol{q}}}(m) \end{bmatrix} \tag{7.13}$$

This method requires that the flight data has a sufficiently high SNR. If the SNR is low, the calculated $\dot{q}$ will be extremely inaccurate because the 2-point regression differentiation of noise causes high magnitude spikes. Multiple-point regression differentiation is immune to signal noise. However, it introduces delay between input and output, which the EE method is sensitive to.

2) Perform finite Fourier transform on $\dot{\boldsymbol{q}}$ directly instead of calculating the time derivative of $\boldsymbol{q}$,

$$\boldsymbol{F}(\dot{q}) = s\tilde{\boldsymbol{q}} = j\omega\tilde{\boldsymbol{q}} \tag{7.14}$$

Therefore the following have,

$$\boldsymbol{Y} = \begin{bmatrix} j\omega_1\tilde{\boldsymbol{q}}(1) \\ j\omega_2\tilde{\boldsymbol{q}}(2) \\ . \\ . \\ . \\ j\omega_m\tilde{\boldsymbol{q}}(m) \end{bmatrix} \tag{7.15}$$

Next, the pitching moment aerodynamic derivatives can be calculated by using Equation (6.58). In order to compare the EE identified derivatives with the ones estimated by AVL, the two sets of derivatives are put together as shown in Table 7.3.

Table 7.3 Pitching moment related aerodynamic derivatives

	EE (use Equation (7.13))	Parameter Standard Error	EE (use Equation (7.15))	Parameter Standard Error	AVL
C_{m_u}	0.0009	0.0447	0.0414	0.0465	0
C_{m_w}	-0.0984	0.0607	-0.0485	0.0689	-0.64~0.018
C_{m_q}	-8.9382	0.8496	-13.3980	0.9515	-13.8
$C_{m_{\delta_e}}$	-0.3058	2.8735	-0.2295	1.9892	-1.772

In Table 7.3, the second column is the EE method identified dimensionless derivatives calculated by using Equation (7.13)'s $\boldsymbol{Y}$ vector. The third column is their corresponding parameter standard errors. Similarly the fourth column is the derivatives calculated using Equation (7.15)'s $\boldsymbol{Y}$ vector. The fifth column is their corresponding parameter standard errors. The last column shows the dimensionless derivatives estimated by AVL. In this thesis, all the AVL coefficients are calculated by MicroPilot Inc. and are used in their aircraft flight simulation and ground control station software called Horizon. By comparing the second and fourth column identified derivatives, it can be seen that these two methods identified derivatives are close. Comparing the identified derivatives with the ones calculated by AVL in the last column, C_{m_u} and C_{m_q} are found to be very close, but C_{m_w} and $C_{m_{\delta_e}}$ do not match very well. Therefore, it is necessary to examine which set of derivatives are more accurate. In order to examine the accuracy of the derivatives, the estimated body pitch rate $\hat{\dot{q}}$ is calculated using the identified derivatives and the priori model (referring to Equation (7.10)):

$$\hat{\dot{q}} = \mathrm{M}_u u + \mathrm{M}_w w + \mathrm{M}_q q + \mathrm{M}_{\delta_e} \delta_e \tag{7.16}$$

as well as the measured states u, w, q and δ_e from the flight test. The estimated body pitch rate $\hat{\dot{q}}$ is compared with the $\dot{q}$, which was calculated by taking the first time derivative of the measured q. This comparison helps to find out which set of derivatives can simulate the flight data $\dot{q}$ better.

By feeding the flight data of u, w, q and δ_e to model equation (7.16), the EE (Column 4 in Table 7.3) and AVL derivatives verification plot can be acquired, as shown by Figure 7.31 and Figure 7.32, respectively.

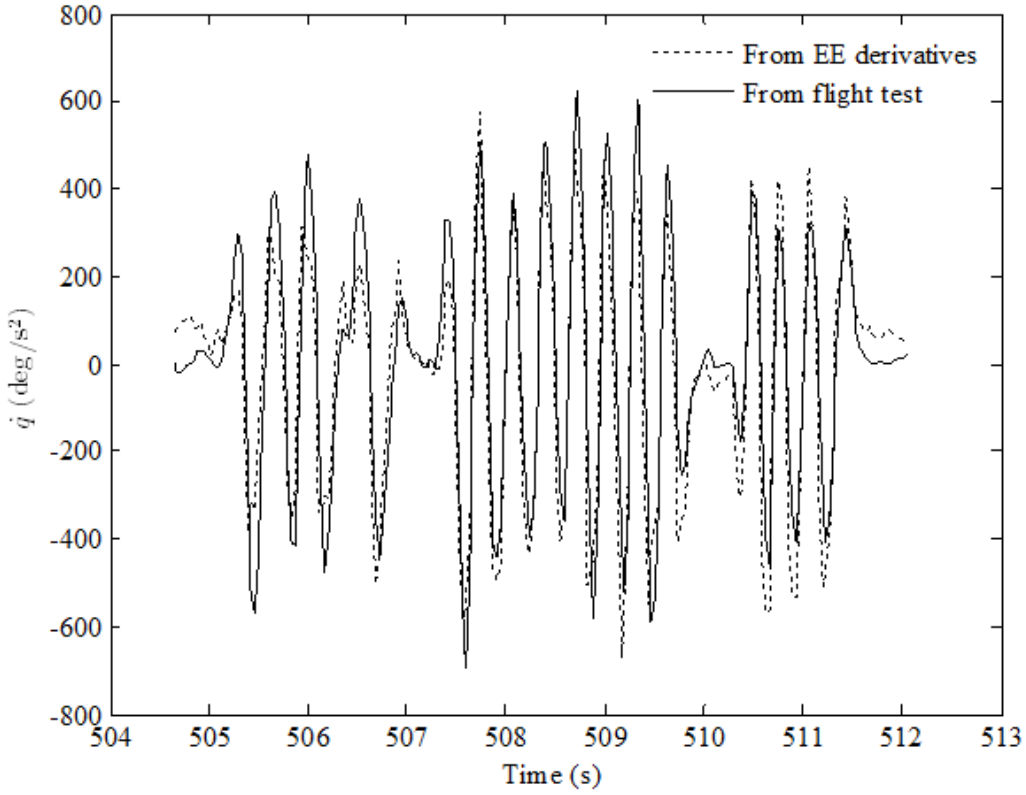

Figure 7.31 Verification of EE identified pitching moment related derivatives

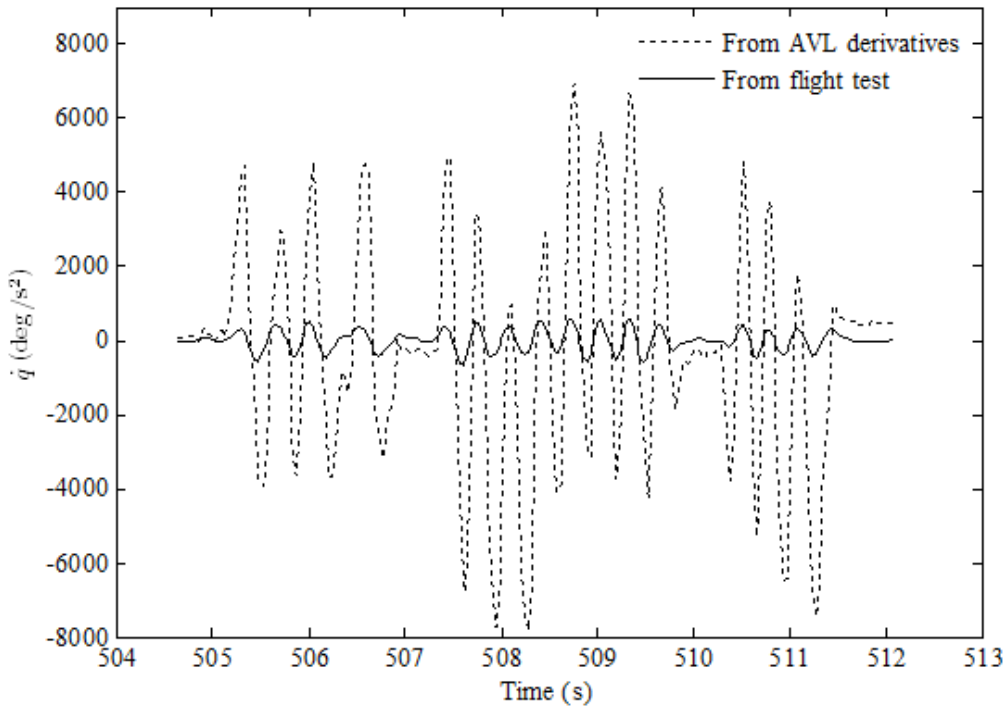

Figure 7.32 Verification of AVL estimated pitching moment related derivatives

From the plots, it can be seen that EE identified derivatives can track the flight test response more accurately than the AVL calculated ones. By calculating the Mean Square Error (MSE), it is seen that for EE derivatives' fitting, the $MSE_{(EE)}$ = 1.8; for AVL derivatives' fitting, the $MSE_{(AVL)}$ = 31.8. Therefore the MSE of EE identified derivatives' fitting is much lower than the AVL calculated derivatives' fitting. Note that MSE index cannot always quantify the accuracy of simulated data since it only quantifies magnitude and not phase. Nevertheless, from Figure 7.31 and Figure 7.32, it can be visually determined that the derivatives identified by EE method can track the flight response more accurately that the AVL estimated ones.

To validate the identification results, an unseen signal is now utilized to test the accuracy of the identified derivatives. The unseen signal used is shown in Figure 7.33 below. The unseen

random signal verification results of EE and AVL derivatives are shown in Figure 7.34 and Figure 7.35.

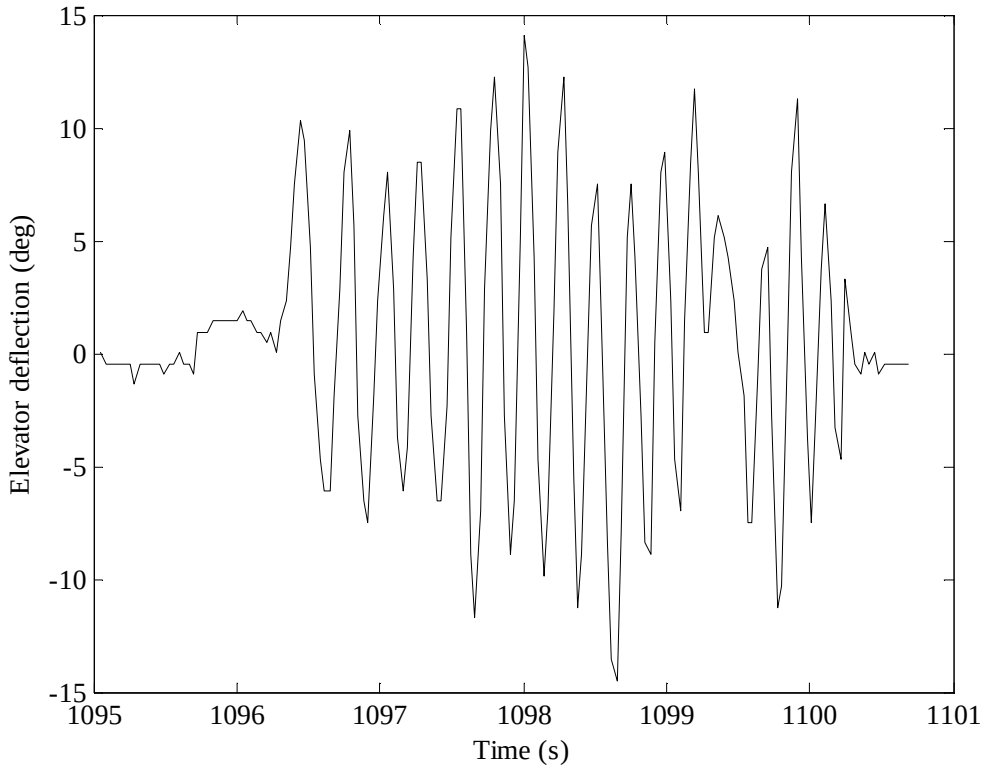

Figure 7.33 Unseen random signal used for verification

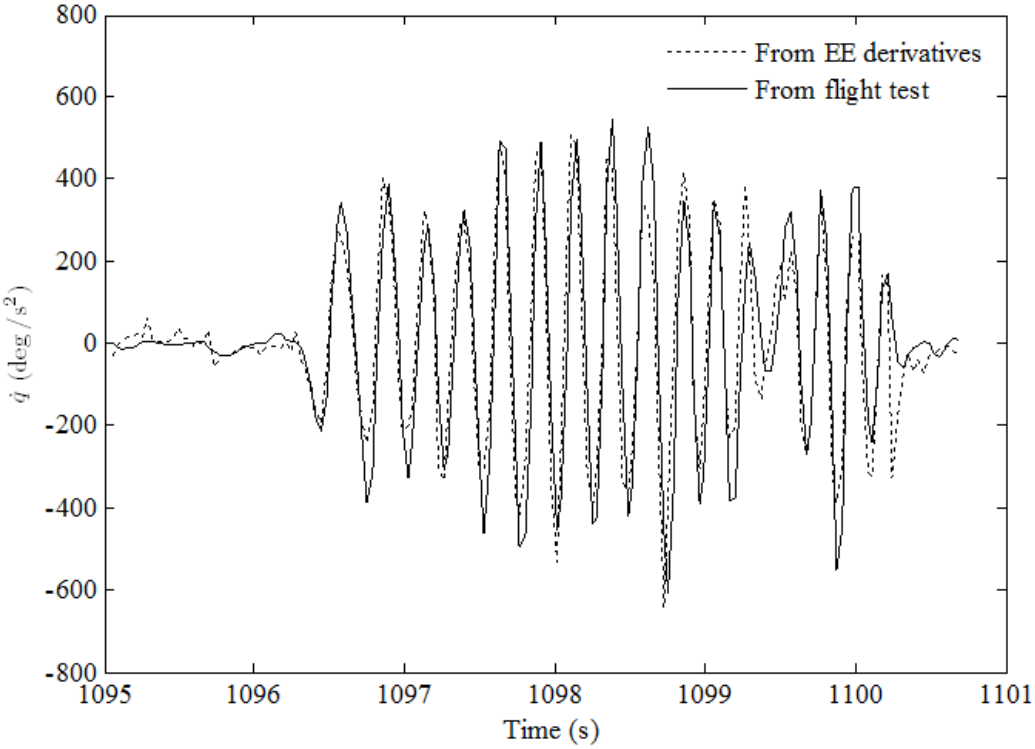

Figure 7.34 Verification of EE identified pitching moment related derivatives with unseen random signal

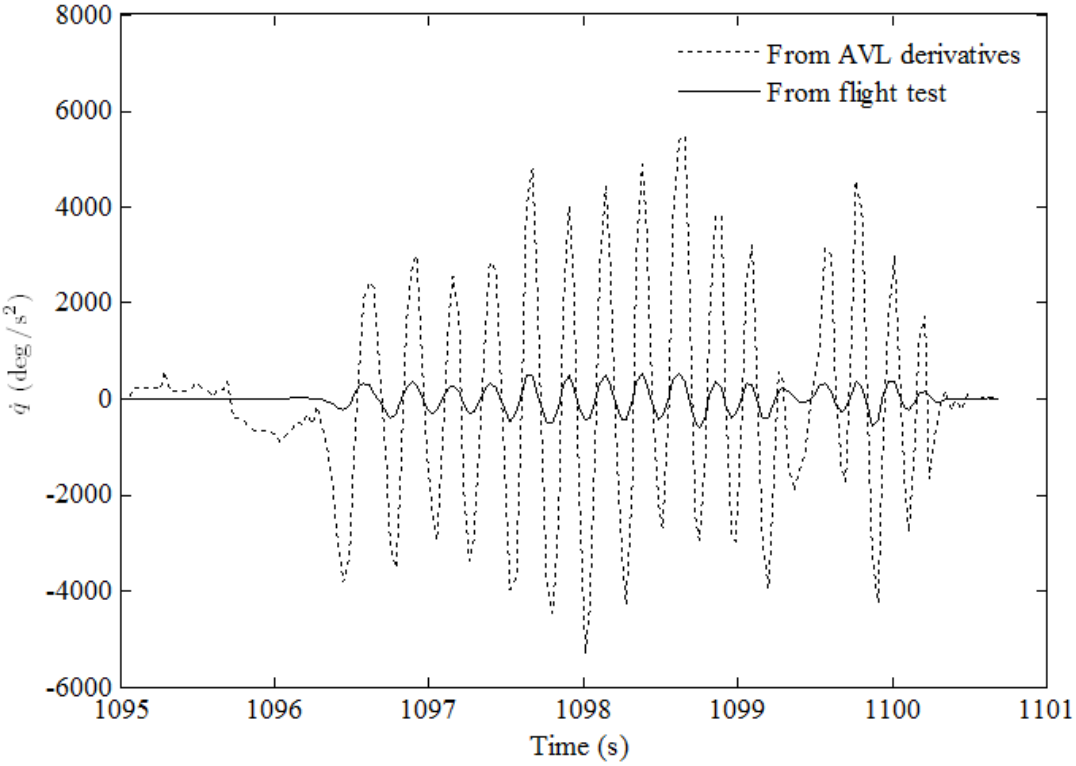

Figure 7.35 Verification of AVL computed pitching moment related derivatives with unseen random signal

From Figure 7.34 and Figure 7.35, it is seen that the EE-based identified aerodynamic derivatives can track the real flight response more accurate than the AVL estimated ones. The Mean Square Error of the simulation responses fitting using two sets of derivatives are: $MSE_{(EE)}$ = 1.5 and $MSE_{(AVL)}$ = 22.2. This is also indicates that the derivatives identified by the EE method can track the aircraft's actual response more accurately. To further verify the applicability of the identified derivatives, a Doublet signal is also applied as an unseen signal for verification. The Doublet truncated from the flight test is shown in Figure 7.36.

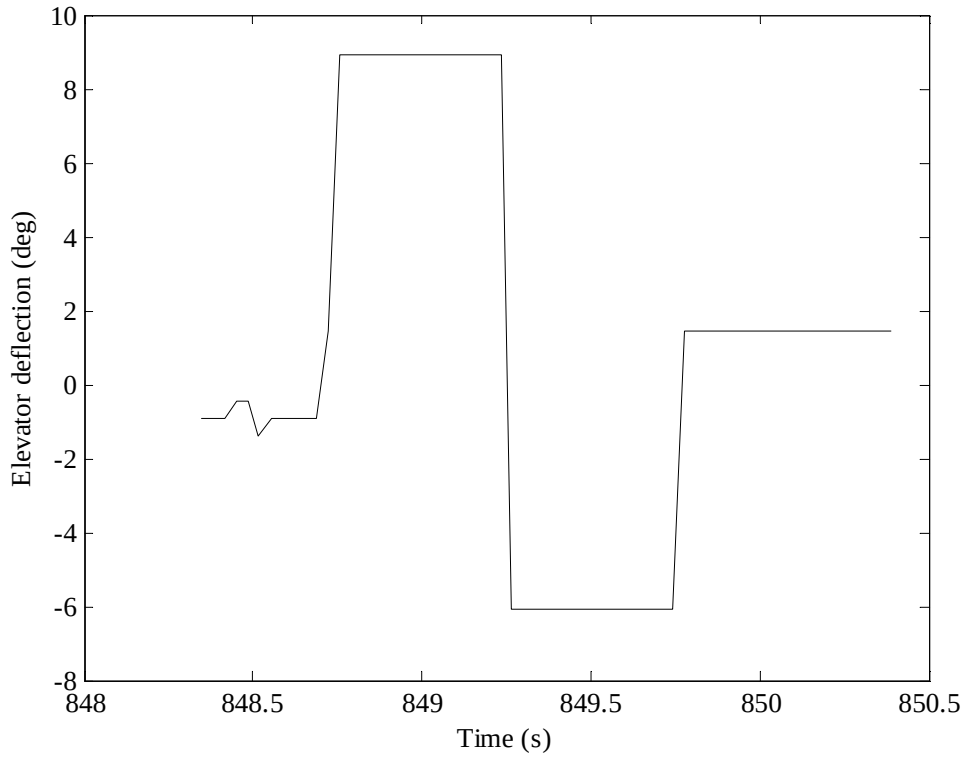

Figure 7.36 Unseen Doublet signal

By feeding the EE, AVL derivatives and the model with the unseen Doublet signal, the simulated output can be calculated. The verification results are shown by Figure 7.37 and Figure 7.38.

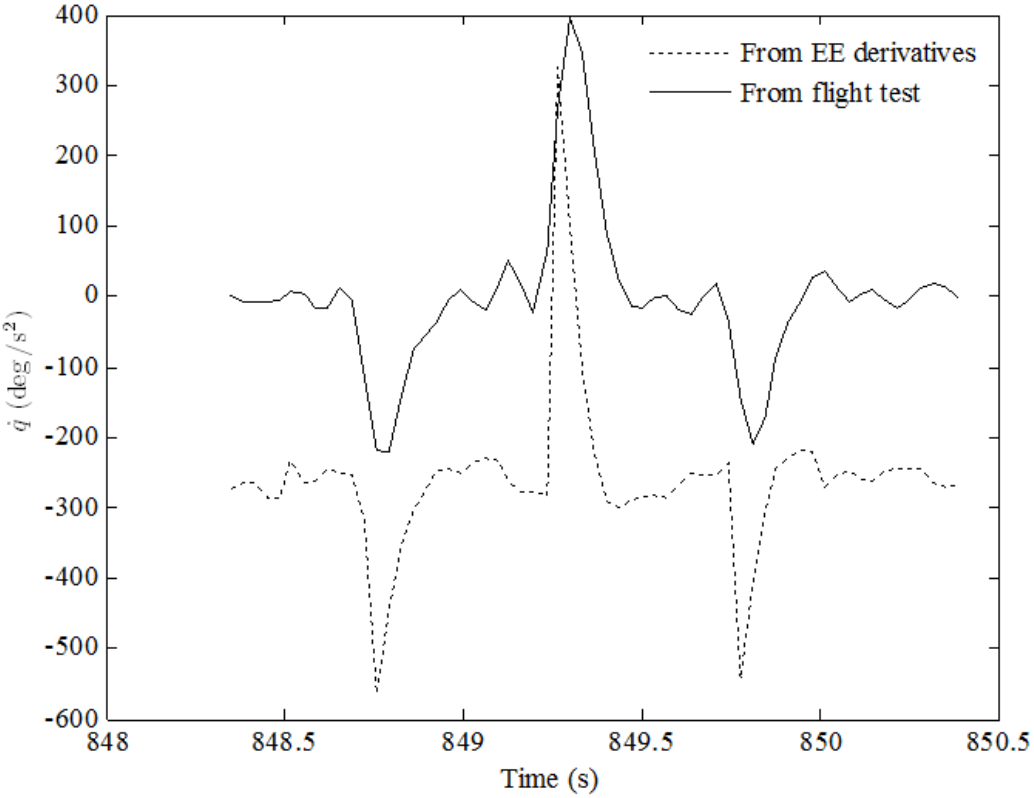

Figure 7.37 Verification of EE identified pitching moment related derivatives with unseen Doublet signal

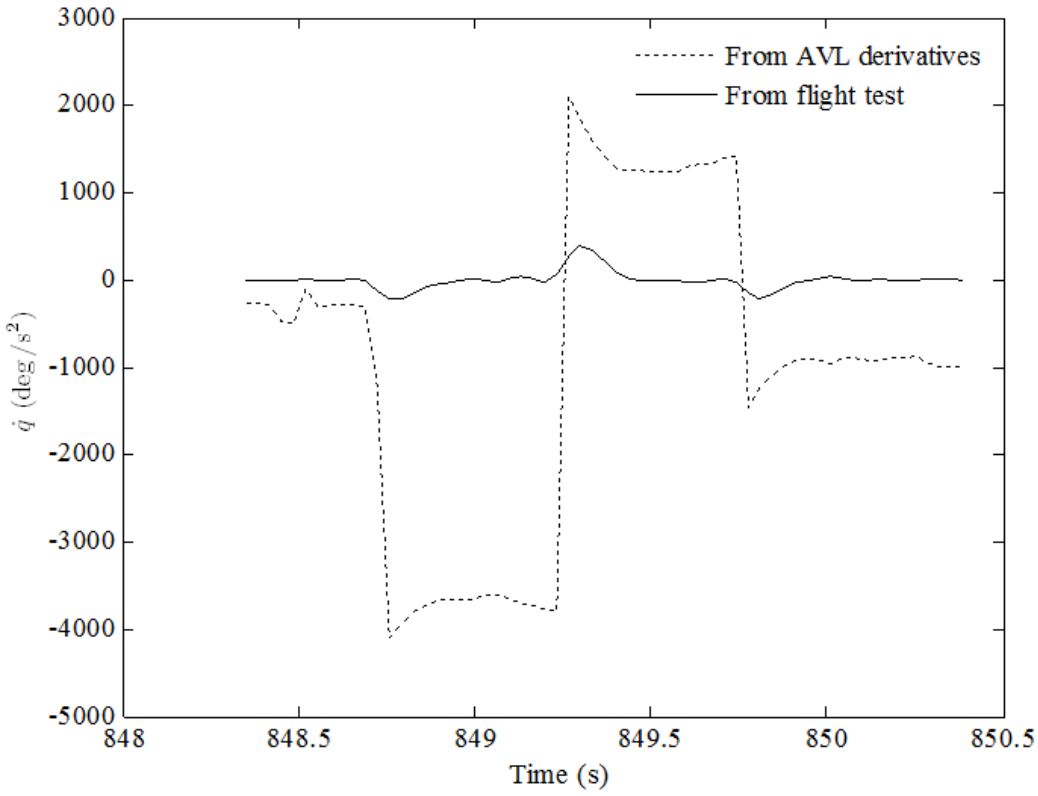

Figure 7.38 Verification of AVL computed pitching moment related derivatives with unseen Doublet signal

From Figure 7.37 and Figure 7.38, it is seen that the EE-based identified aerodynamic derivatives can track the real flight response more accurately than the AVL estimated ones. The phases shown in the figures are matching very well. However, the magnitudes do not match as well as the phases. The Mean Square Errors of EE and AVL derivatives fitting are: $MSE_{(EE)}$ = 4.7, and $MSE_{(AVL)}$ = 35.5. This once again indicates that the derivatives identified by EE method can track the real flight test response more accurately than the AVL estimated ones. Therefore, the EE method is more accurate than AVL in the calculation of pitch moment related derivatives.

Lift force related derivatives identification

The model used for lift force related derivatives identification is adapted from Equation (4.109):

$$\dot{w} - qU_e + g\theta sin\theta_e = \mathrm{Z}_u u + \mathrm{Z}_w w + \mathrm{Z}_q q + \mathrm{Z}_{\delta_e}\delta_e \tag{7.17}$$

The state matrix $\boldsymbol{X}$ is the same as the one used for identification of pitching moment related derivatives. However, the $\boldsymbol{Y}$ vector needs to be changed. The lift force divided by mass is:

$$\mathbf{Z} = \dot{w} - qU_e + g\theta sin\theta_e \tag{7.18}$$

Equation (7.18) is used to calculate the time domain **Z**. By performing finite Fourier transform to **Z**, frequency domain $\widetilde{\boldsymbol{Z}}$ is obtained, which comprises the $\boldsymbol{Y}$ matrix. Therefore,

$$\boldsymbol{Y} = \begin{bmatrix} \widetilde{\boldsymbol{Z}}(1) \\ \widetilde{\boldsymbol{Z}}(2) \\ \cdot \\ \cdot \\ \cdot \\ \widetilde{\boldsymbol{Z}}(m) \end{bmatrix} \tag{7.19}$$

By performing the EE algorithm to the information above, the lift force related aerodynamic derivatives are calculated. The results are shown in Table 7.4.

Table 7.4 EE method identified lift force related aerodynamic derivatives

EE value (dimensional)	EE value (dimensional)	Standard Error	AVL value (dimensionless)
Z_u= -0.5579	C_{Z_u}= -0.3210	0.4074	C_{Z_u}= 0
Z_w= -2.8831	C_{Z_w}= -1.6590	0.6038	C_{Z_w}= -4.12
Z_q= -30.5650	C_{Z_q}= -45.6833	8.3425	C_{Z_q}= -9.4
$\mathrm{Z}_{\delta e}$ = -57.6947	$C_{Z_{\delta e}}$= -0.4864	17.4406	$C_{Z_{\delta e}}$= -0.56

In Table 7.4, the first column is the EE identified dimensional derivatives, while the second column showing the non-dimensionalized derivatives. The third column is the corresponding

parameter standard errors. The last column is the dimensionless derivatives estimated by AVL. By comparing the dimensionless derivatives identified by EE and AVL methods, it is seen that most of the corresponding derivatives are close, except for C_{Z_q}. In the following context, different sets of derivatives will be checked to see which one is more accurate in tracking the real aircraft response. The verification method is the same as the one utilized for verifying the pitching moment derivatives. The verification begins with the original signal and the comparisons are shown as Figure 7.39 and Figure 7.40.

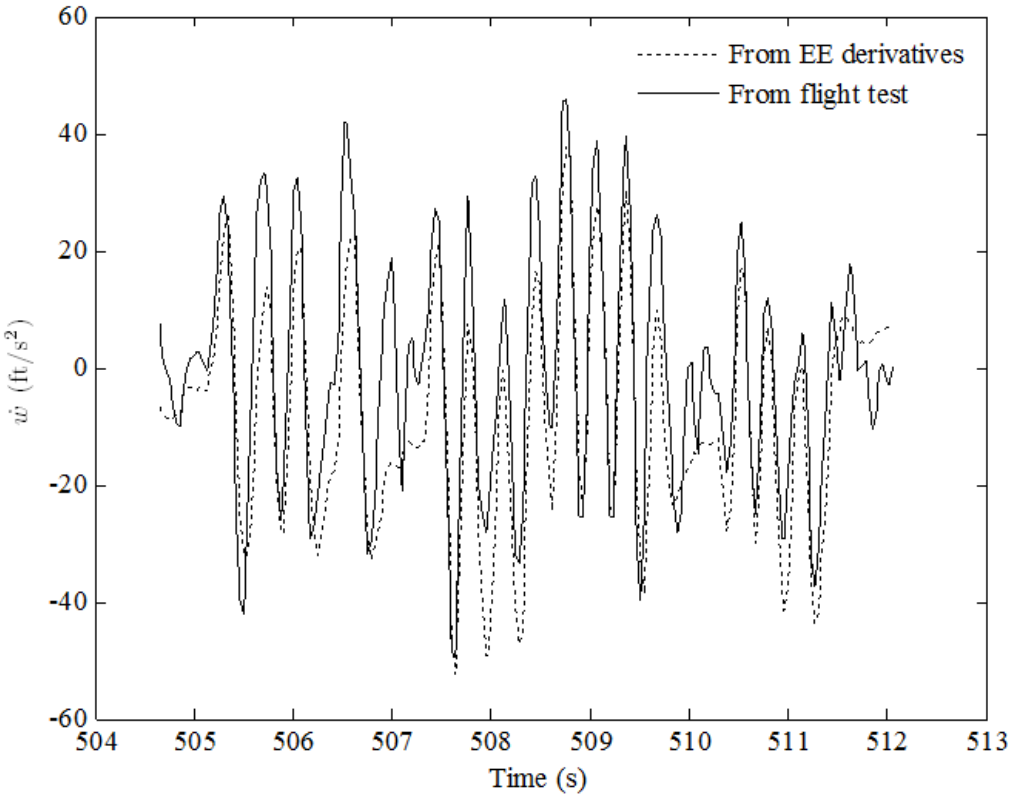

Figure 7.39 Verification of EE identified lift force related derivatives with original signal

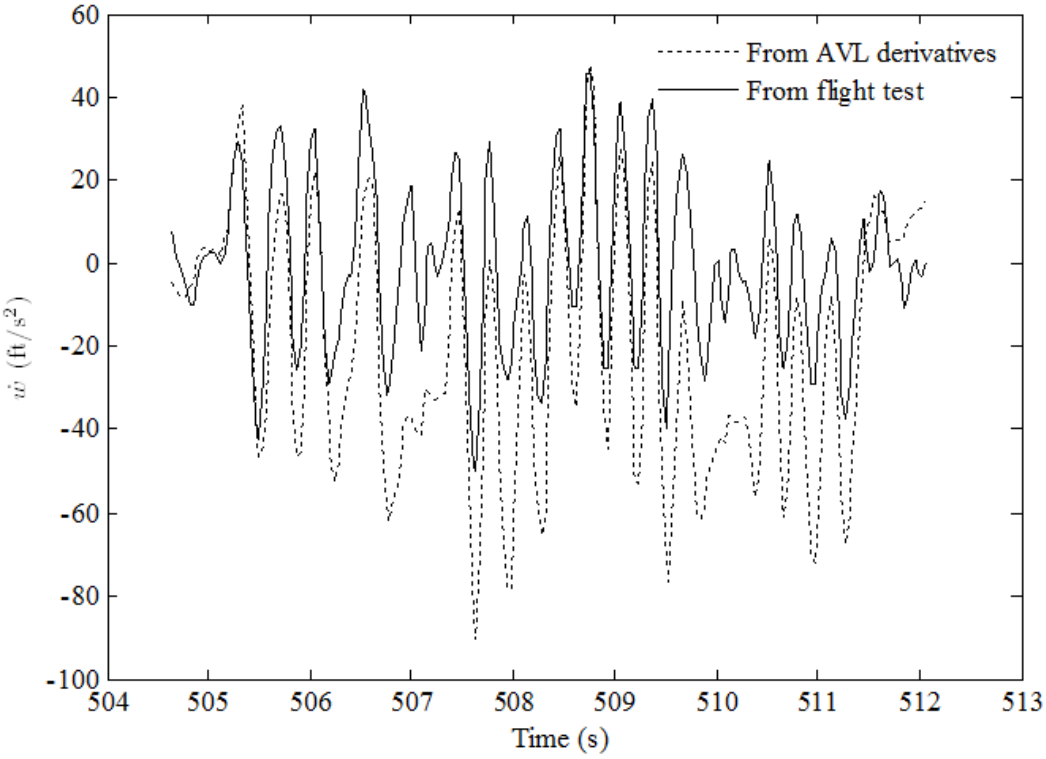

Figure 7.40 Verification of AVL computed lift force related derivatives with original signal

From Figure 7.37 and Figure 7.38, it is seen that the EE-based identified aerodynamic derivatives can track the real flight response more accurate than the AVL estimated ones. The Mean Square Error of the simulation responses fitting using two sets of derivatives are: $MSE_{(EE)}$ = 13.5, and $MSE_{(AVL)}$ = 27.9. Which also indicates that the EE identified derivatives are more capable of tracking aircraft flight responses than the AVL calculated ones. For validation of the identified derivatives and further examination of the general applicability of them, their accuracy can be tested with an unseen random signal. The unseen signal verification is shown by Figure 7.41 and Figure 7.42.

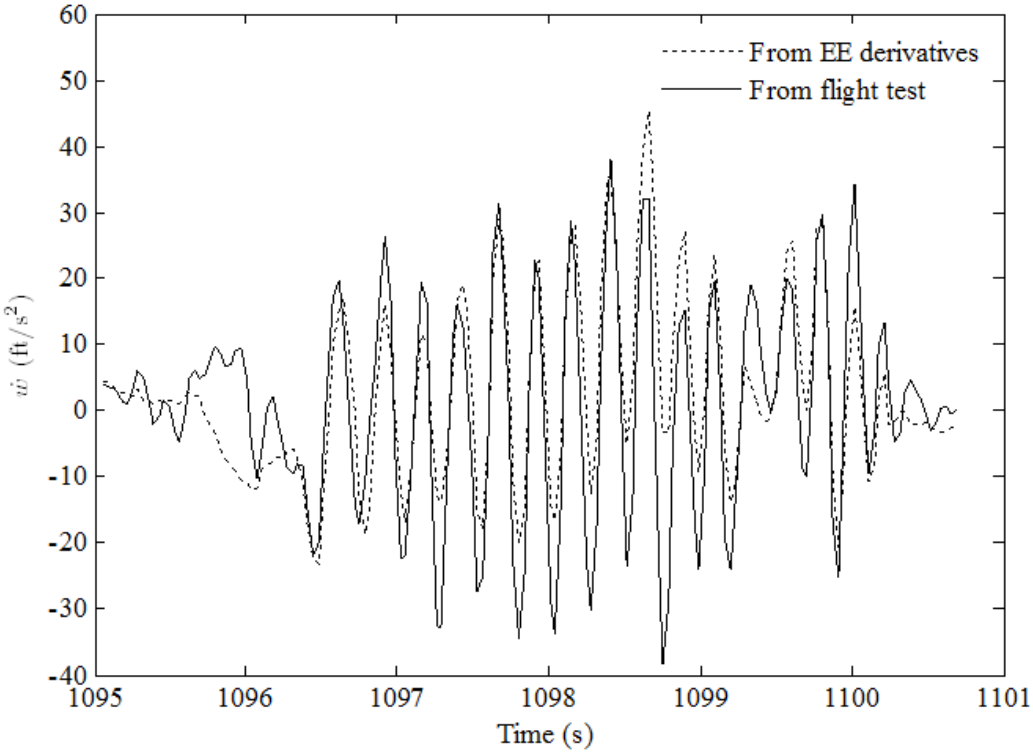

Figure 7.41 Verification of EE identified lift force related derivatives with unseen random signal

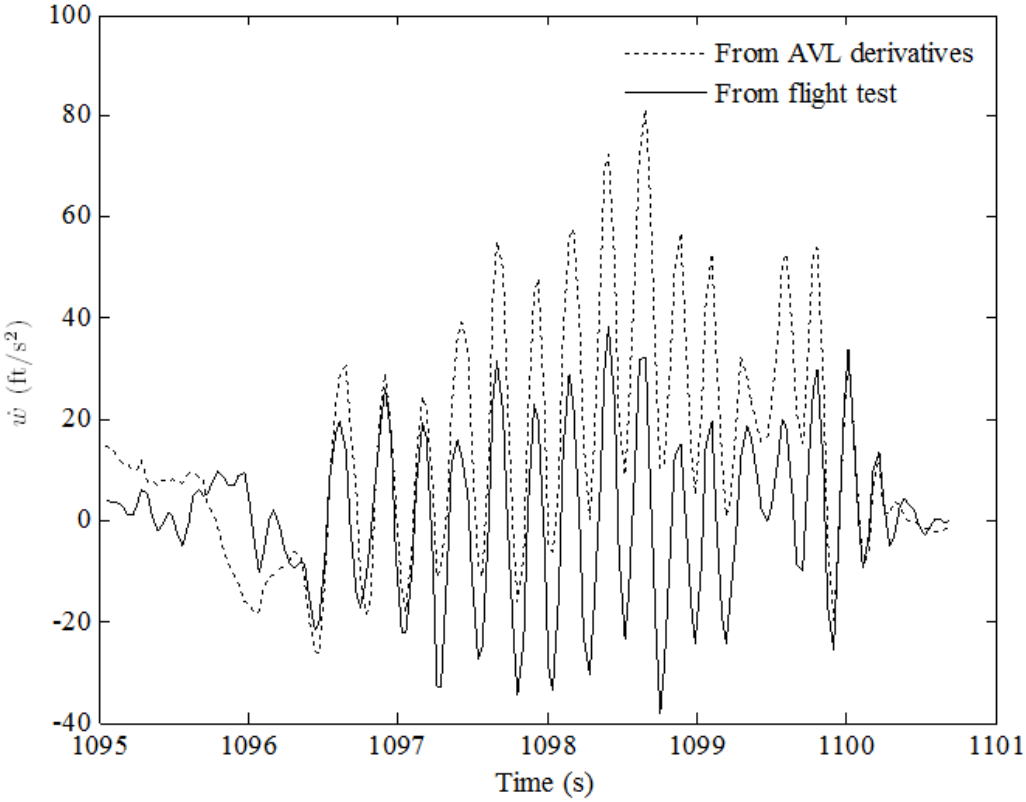

Figure 7.42 Verification of AVL computed lift force related derivatives with unseen random signal

By observing the comparison plots and calculating their Mean Square Error: $MSE_{(EE)}$ = 11.1, $MSE_{(AVL)}$ = 22.9. It can be seen that the EE's derivatives can track the flight test response more accurately. Like verification for pitching moment related derivatives, the Doublet signal can also be used for further verification. The verification result using the unseen Doublet input is shown in Figure 7.43 and Figure 7.44.

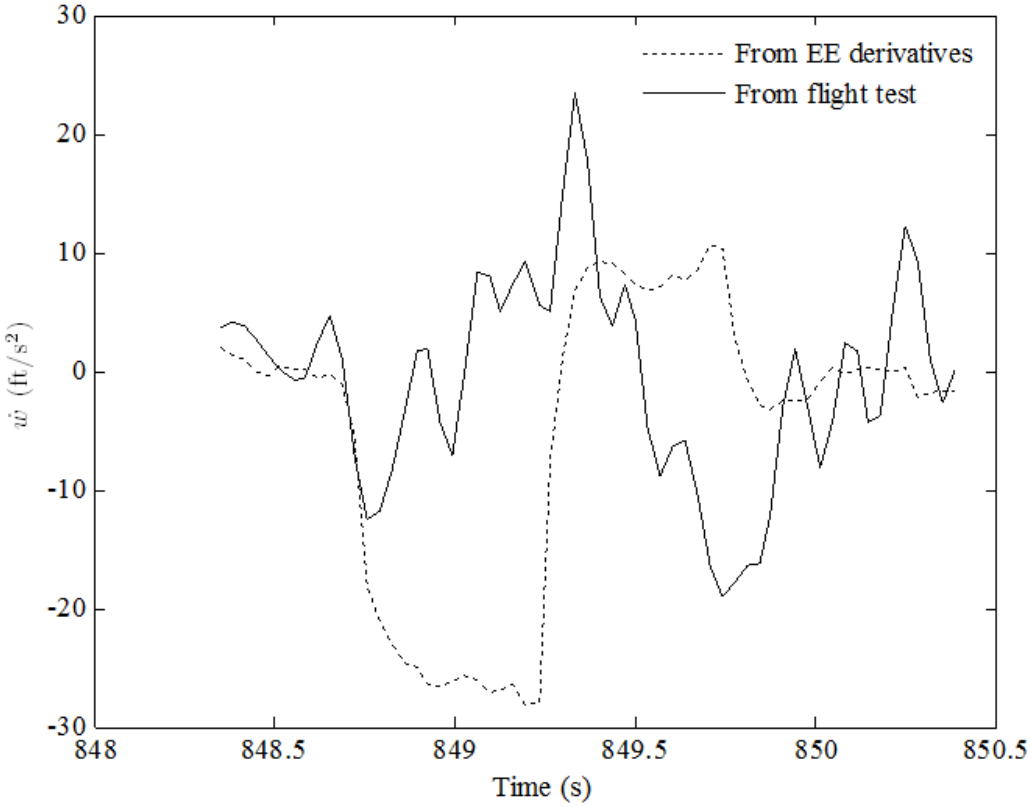

Figure 7.43 Verification of EE identified lift force related derivatives with unseen Doublet signal

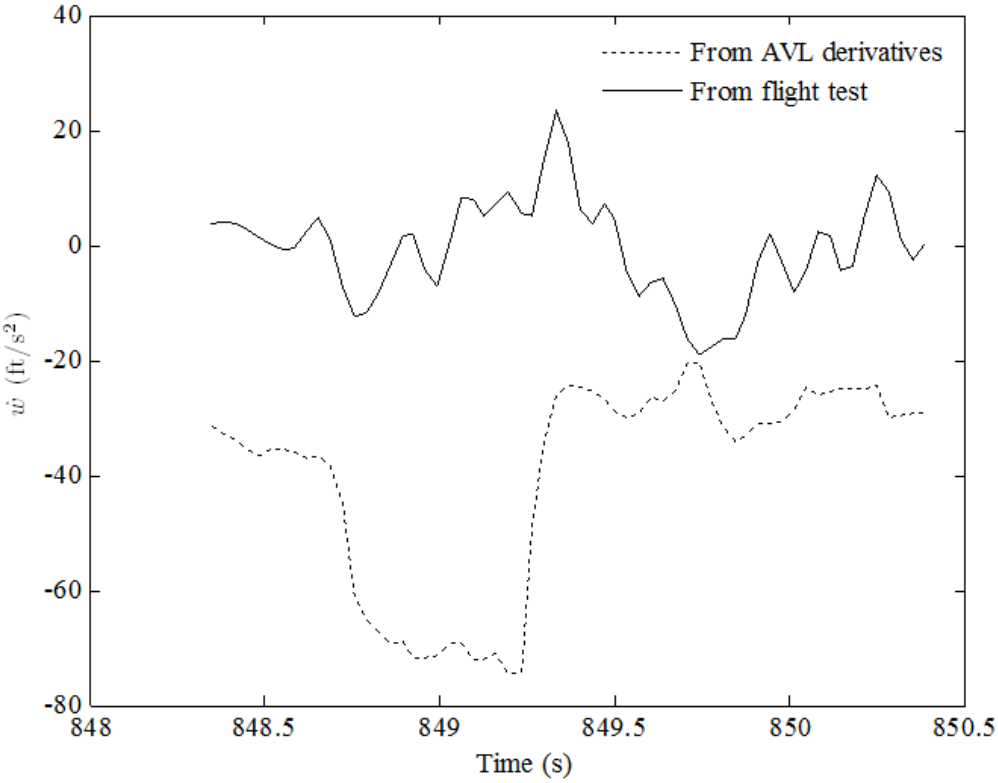

Figure 7.44 Verification of AVL computed lift force related derivatives with unseen Doublet signal

The Mean Square Error of EE and AVL derivatives fitting are 16.8 and 44.8, respectively. This also indicates that the derivatives calculated by EE can track the flight test response better.

Axial force related derivatives identification

The model used for axial force related aerodynamic derivatives identification is adapted from Equation (4.108):

$$\dot{u} + qW_e + g\theta cos\theta_e = \mathrm{X}_u u + \mathrm{X}_w w + \mathrm{X}_q q + \mathrm{X}_{\delta_e}\delta_e \tag{7.20}$$

By setting:

$$\mathbf{X} = \dot{u} + qW_e + g\theta cos\theta_e \tag{7.21}$$

Executing finite Fourier transform to the time domain **X**, the $\boldsymbol{Y}$ vector can be acquired, which is equal to the frequency domain $\widetilde{\boldsymbol{X}}$:

$$\boldsymbol{Y} = \begin{bmatrix} \widetilde{\boldsymbol{X}}(1) \\ \widetilde{\boldsymbol{X}}(2) \\ . \\ . \\ . \\ \widetilde{\boldsymbol{X}}(m) \end{bmatrix} \tag{7.22}$$

By performing EE algorithm to the above information, the axial force related aerodynamic derivatives can be identified as shown in Table 7.5.

Table 7.5 EE method identified axial force related aerodynamic derivatives

EE value (dimensional)	EE value (dimensionless)	Standard Error	AVL value (dimensionless)
X_u= -0.1796	C_{X_u}= -0.1034	0.6957	C_{X_u}= 0
X_w= -1.2083	C_{X_w}= -0.6953	1.0312	C_{X_w}= -0.44
X_q= -5.1463	C_{X_q}= -7.6918	14.2461	C_{X_q}= 0
$X_{\delta e}$ = -11.0759	$C_{X_{\delta_e}}$= -0.0934	29.7825	$C_{X_{\delta_e}}$= 0

In the table, the first column is the dimensional derivatives identified using the EE method. The second column is the dimensionless derivatives converted from the dimensional derivatives. The third column is their corresponding parameter standard errors, which quantify the accuracy of the identified derivatives. The last column shows the dimensionless derivatives estimated by AVL. In the last column, the derivatives C_{X_u}, C_{X_q} and $C_{X_{\delta_e}}$ are all shown as zeroes. This means that they exist, but are negligibly small, and AVL didn't calculate them. The original signal and the

unseen signal are used to examine the accuracy of axial force related derivatives. First start verifying with original signal, the verification results are shown as Figure 7.45 and Figure 7.46.

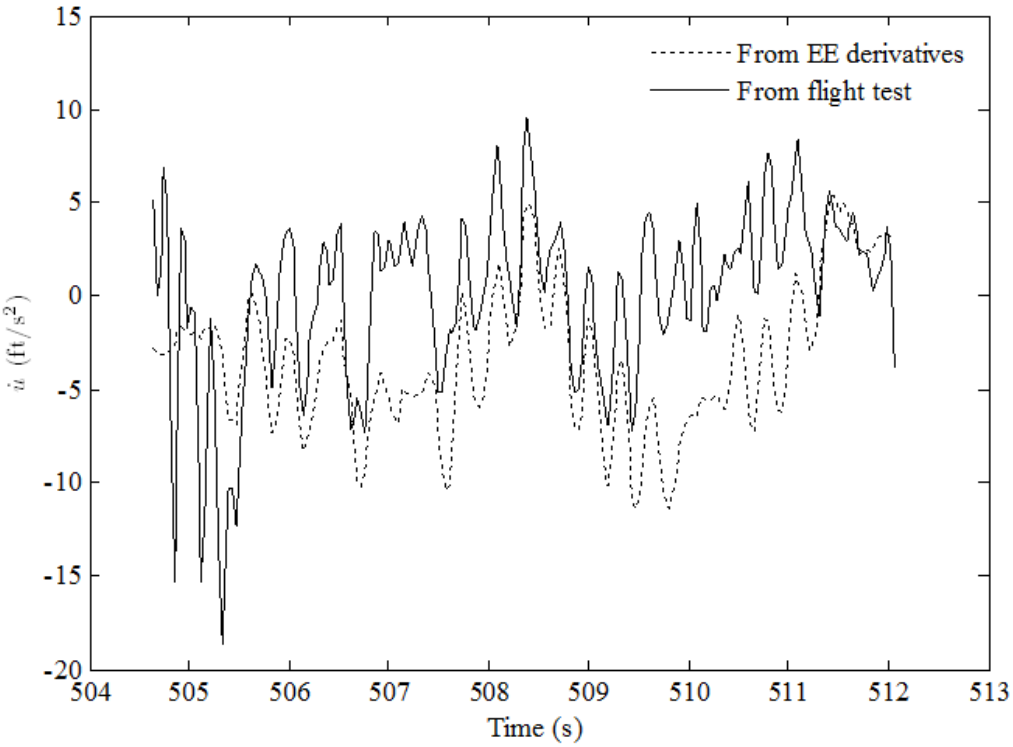

Figure 7.45 Verification of EE identified axial force related derivatives with original signal

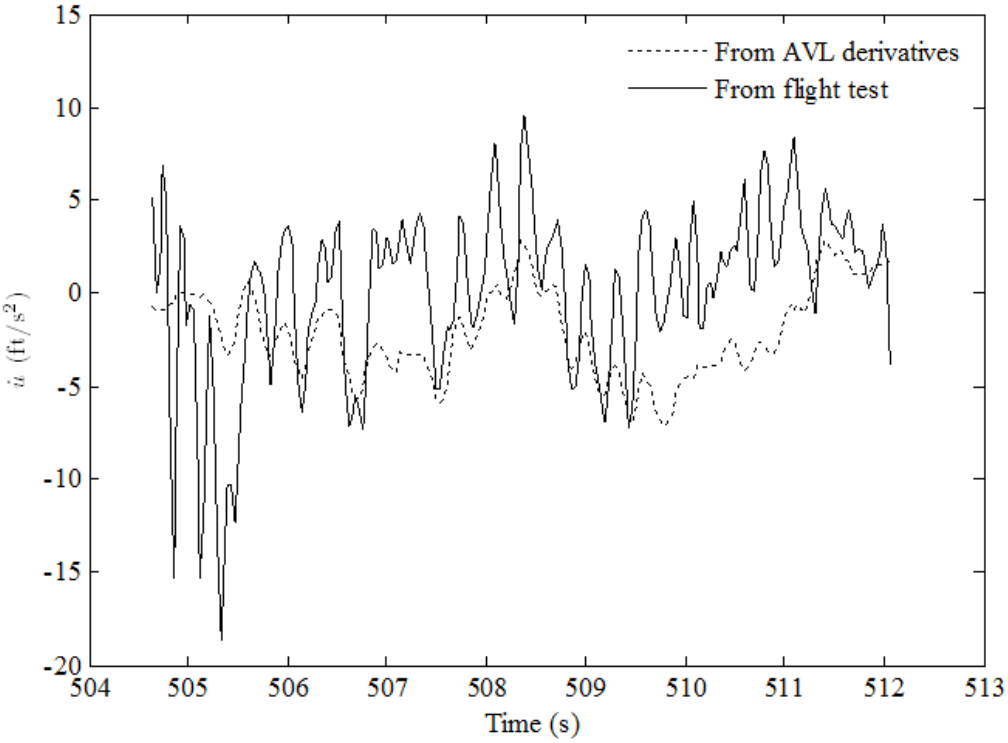

Figure 7.46 Verification of AVL computed axial force related derivatives with original signal

From Figure 7.45 and Figure 7.46, it is hard to determine which simulated output matches the flight output more closely. However, by calculating the Mean Square Error of the simulation responses fitting using two sets of derivatives: $MSE_{(EE)} = 4.8$, and $MSE_{(AVL)} = 6.1$, it can be seen that the derivatives calculated by the EE method are slightly more accurate in tracking the flight test response. In order to test the broad applicability of the identified derivatives, the derivatives are examined and tested with an unseen random signal as well. The unseen random signal verification is shown in Figure 7.47 and Figure 7.48.

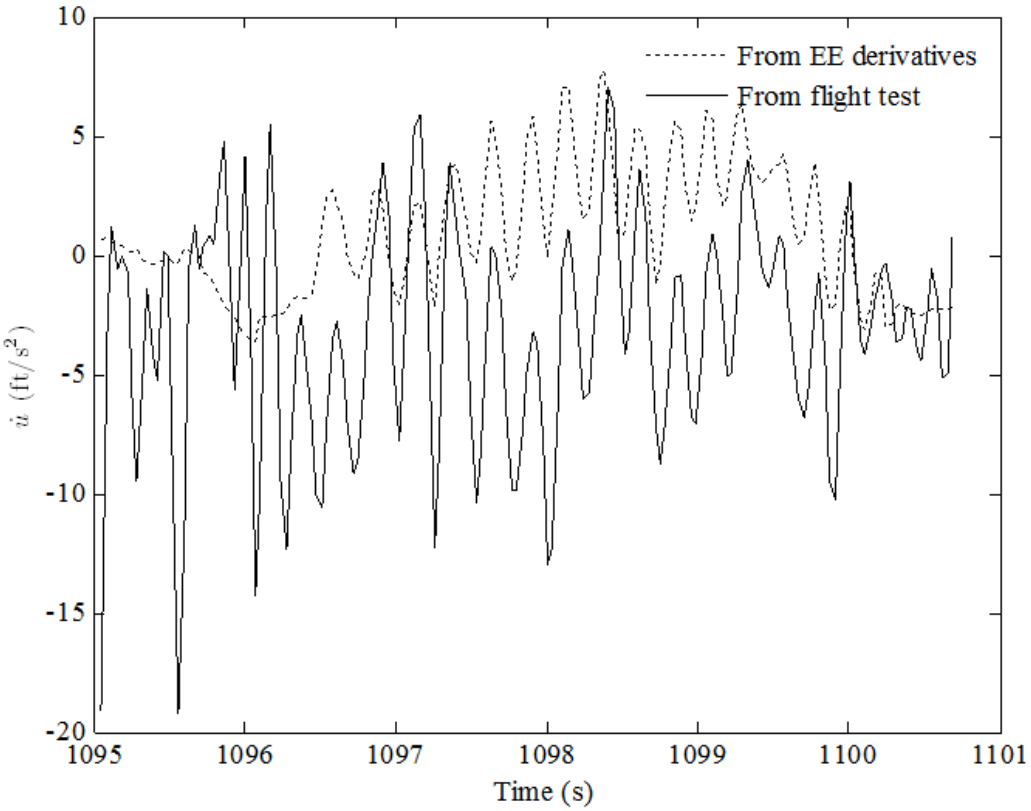

Figure 7.47 Verification of EE identified axial force related derivatives with unseen random signal

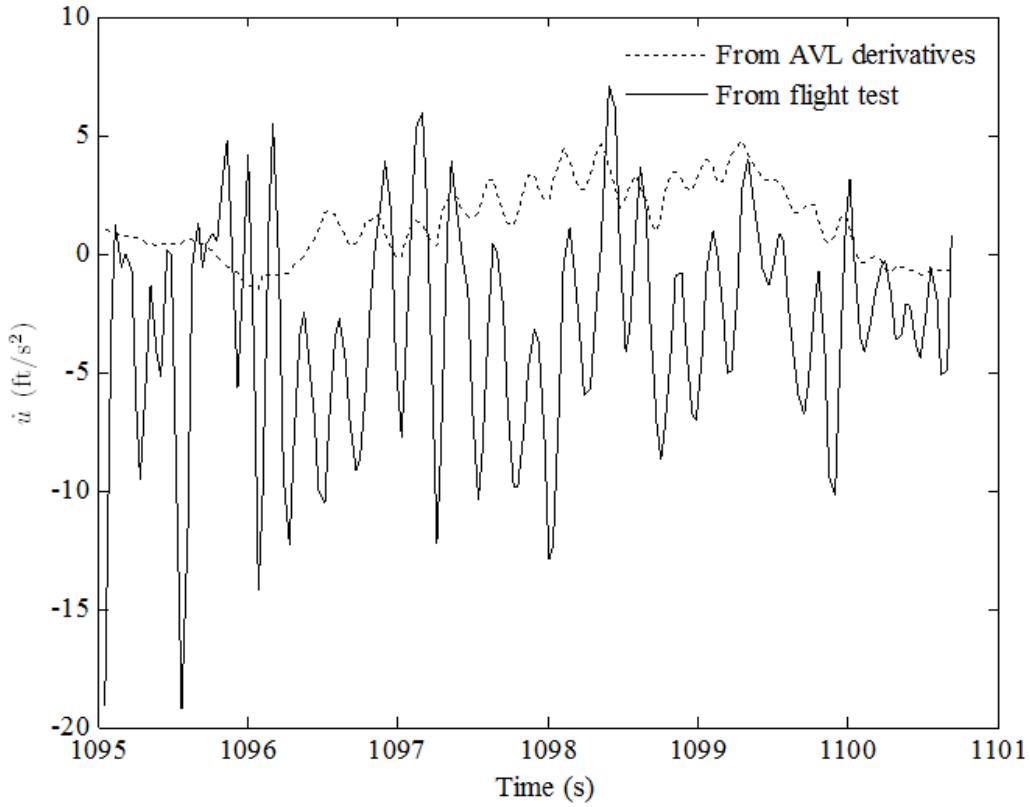

Figure 7.48 Verification of AVL computed axial force related derivatives with unseen random signal

The Mean Square Error of the above fittings are: $MSE_{(EE)}$ = 5.8, and $MSE_{(AVL)}$ = 7.2. It is seen that the EE method identified derivatives are a little bit more accurate in tracking flight response. As before, a Doublet signal is also used for further verifying the accuracy of the calculated derivatives. The unseen Doublet signal verification results are shown in Figure 7.49 and Figure 7.50.

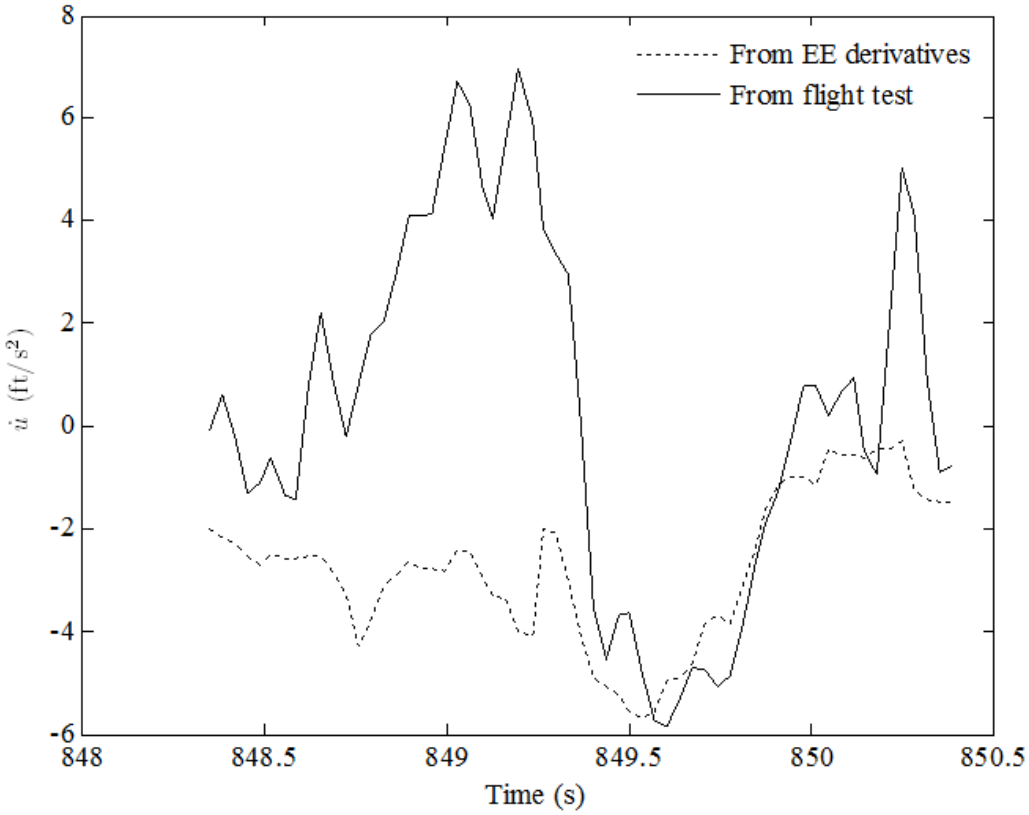

Figure 7.49 Verification of EE identified axial force related derivatives with unseen Doublet signal

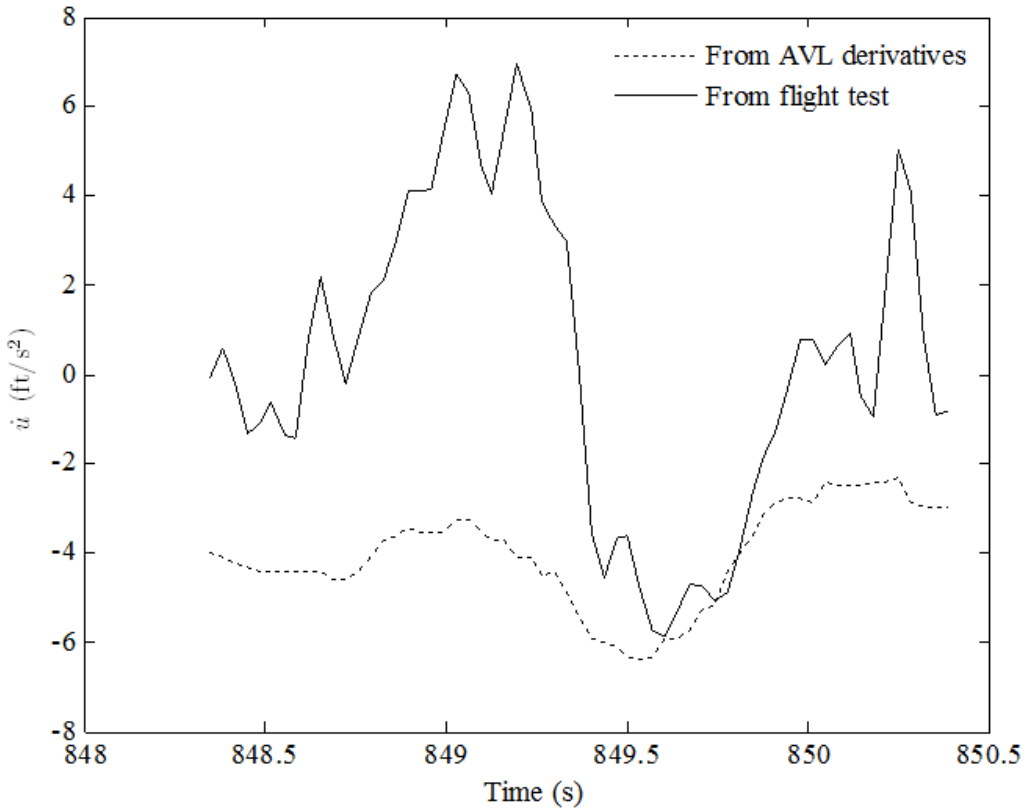

Figure 7.50 Verification of AVL computed axial force related derivatives with unseen Doublet signal

The Mean Square Error of the simulation responses fitting using two sets of derivatives are: $MSE_{(EE)}$ = 4.4, and $MSE_{(AVL)}$ = 5.3. This indicates that the derivatives estimated by the EE method are slightly more accurate in tracking the real flight test response. It is seen that the identified axial force related derivatives are not as accurate as the pitching moment and lift force related derivatives.

According to the above verification analysis, it is summarized that, for most cases, the EE identified derivatives can track the real flight test better than the AVL estimated ones, especially for pitching moment related derivatives C_{m_u}, C_{m_w}, C_{m_q} and $C_{m_{\delta_e}}$. Nevertheless, for some derivatives like axial force related derivatives, the accuracy of EE identified ones are not

significantly higher than the AVL computed ones for some scenarios. This is a point which requires further investigation.

For comparing and verifying the identification results obtained from different methods, all the identified or computed derivatives are put in one table as shown in Table 7.6 below.

Table 7.6 Different ways calculated Cropcam aerodynamic derivatives

	Dimensionless Coefficient	AVL Value	EE Value	TF Value
Axial force related	C_{X_u}	0	-0.1034	—
	C_{X_w}	-0.44~0.44	-0.6953	—
	C_{X_q}	0	-7.6918	—
	$C_{X_{\delta e}}$	0	-0.0934	—
Lift force related derivatives	C_{Z_u}	0	-0.3210	—
	$C_{Z_w}(-C_{L_\alpha})$	-4.12	-1.6590	-6.4492
	$C_{Z_q}(-C_{L_q})$	-9.4	-45.6833	—
	$C_{Z_{\delta e}}(-C_{L_{\delta e}})$	-0.56	-0.4864	-0.2246
Pitch moment related	C_{m_u}	0	0.0414	—
	C_{m_w}	-0.64~0.018	-0.0485	-0.3036
	C_{m_q}	-13.8	-13.3980	-11.9227
	$C_{m_{\delta e}}$	-1.772	-0.2295	-0.5506

From Table 7.6, it is seen that most of the derivatives identified and computed in different ways are close, except for C_{X_q} and C_{Z_q}. This could probably be due to the effect of coupling and nonlinearities which are not considered in the identification process. Or it may be because of the poor data content (e.g. δ_e and *w*), and this can be seen from the coherence plot which is shown on Figure 7.16.

Before executing the identification of Cropcam, the EE and TF methods were tested for the identification of the aircraft simulation model (a model built by students in Fluid Power and Telerobotics Research Laboratory, at the University of Manitoba). The simulation response and identification of model are presented in Appendix 2. The identification results of the simulation model show that the transfer function and equation error methods are accurate in identifying the aerodynamic derivatives (Refer to Table A 5). From Table A 5, it is seen that the values of the derivatives identified by the EE method are fairly close to the model using ones (the ones estimated by AVL), except for C_{X_q}. This explains why most of the identified Cropcam derivatives are reasonable, while C_{X_q} is a exception. In Table A 5, the transfer function method identified derivatives are a little bit different with the model using ones, but they are still close. This is because the transfer function method used some approximations in calculating the derivatives. Therefore, it is reasonable that the TF result shown in Table 7.6 is slightly different with the EE result.

The correctness of the derivatives can be further checked by comparing them with the ones estimated by AVL as shown in Table 7.7, and by comparing them to the typical aircrafts' aerodynamic derivatives as shown in Table 7.8.

Table 7.7 Comparison of two methods identified and AVL estimated derivatives

Dimensionless Derivative	AVL ($\alpha = -8^{\circ}$)	AVL ($\alpha = -4^{\circ}$)	AVL ($\alpha = 0°$)	AVL ($\alpha = 4^{\circ}$)	EE Result	TF Result
C_{X_u}	-0.100944	-0.069100	-0.036897	-0.004492	-0.1034	—
C_{X_w}	-0.939468	-0.244152	0.451359	1.143740	-0.6953	—
C_{X_q}	-1.224395	-0.683795	-0.146494	0.385232	-7.6918	—
$C_{X_{\delta e}}$	-0.001194	-0.000683	-0.000152	0.000389	-0.0934	—
C_{Z_u}	-0.437534	-0.825067	-1.206411	-1.579810	-0.3210	—
C_{Z_w}	-5.864017	-5.919652	-5.946587	-5.944692	-1.6590	-6.4492
C_{Z_q}	-9.434812	-9.408881	-9.340460	-9.229713	-45.6833	—
$C_{Z_{\delta e}}$	-0.009687	-0.009843	-0.009903	-0.009867	-0.4864	-0.2246
C_{m_u}	-0.027421	-0.038784	-0.042927	-0.040193	0.0414	—
C_{m_w}	-1.474770	-1.610013	-1.736625	-1.854029	-0.0485	-0.3036
C_{m_q}	-13.518798	-13.860711	-14.141084	-14.358251	-13.3980	-11.9227
$C_{m_{\delta e}}$	-0.030368	-0.031263	-0.031865	-0.032164	-0.2295	-0.5506

In Table 7.7, the AVL's derivatives are estimated at different angle of attacks.

Table 7.8 Aerodynamic derivatives of typical aircrafts

Dimensionless Derivative	NAVION	F104-A	A 4D	Jetstar	Convair 880	Boeing 747
$C_{D_\alpha}(-C_{X_w})$	0.33	0.45/ 0.38	0.30/0.038	0.75/0.6	0.27/0.15	0.66/0.47
$C_{L_\alpha}(-C_{Z_w})$	4.44	3.44/2.0	3.45/4.0	5.0/6.5	4.52/4.8	5.7/5.5
$C_{L_q}(-C_{Z_q})$	3.8	0.0	0.0	0.0	7.72/7.5	5.4/6.58
$C_{L_{\delta e}}(-C_{Z_{\delta e}})$	0.355	0.68/0.52	0.36/0.4	0.4/0.44	0.213/0.19	0.338/0.3
C_{m_α}	-0.683	-0.64/-1.3	-0.38/-0.41	-0.8/-0.72	-0.90/-0.65	-1.26/-1.6
C_{m_q}	-9.96	-5.8/-4.8	-3.6/-4.3	-8.0/-0.92	-12.1/-4.5	-20.8/-25
$C_{m_{\delta e}}$	0.923	-1.46/-0.1	-0.5/-0.6	-0.81/-0.88	-0.64/-0.57	-1.34/-1.2

In Table 7.8, the numbers are derivative values of different types of aircraft. In some cells there are two numbers, which corresponding to different aircraft mass situations. Comparing the identified derivatives with the ones shown in Table 7.7 and Table 7.8, it is seen that most of them are fairly close. This further validates the reliability of the derivatives identified by the two methods.

7.2 Identification of a delta-wing UAV

Figure 7.51 A delta-wing UAV (From uas.trimble.com)

Figure 7.51 shows a typical delta-wing aircraft. The main goal of system identification for the delta-wing UAV is to identify the longitudinal channel transfer function (δ_e-q). Pitch rate q is the only state variable that is required. The delta-wing UAV's input excitation for elevator is a pilot generated Chirp signal. The output collected is body pitch rate q. The input-output pair is shown by Figure 7.52 and Figure 7.53.

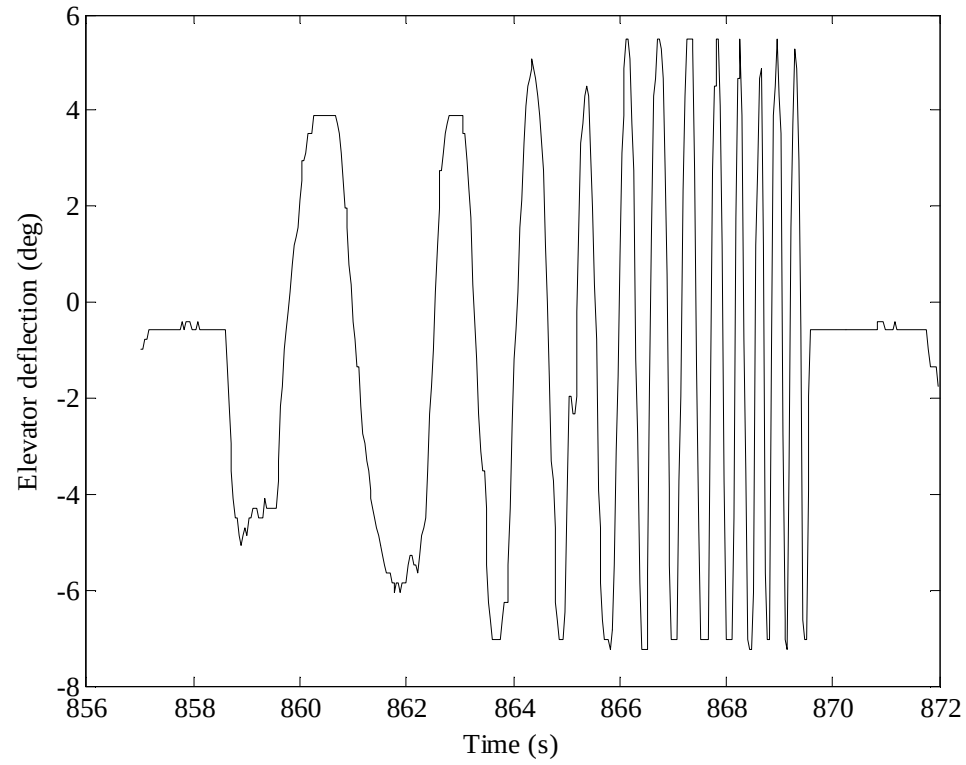

Figure 7.52 Input excitation for delta-wing aircraft

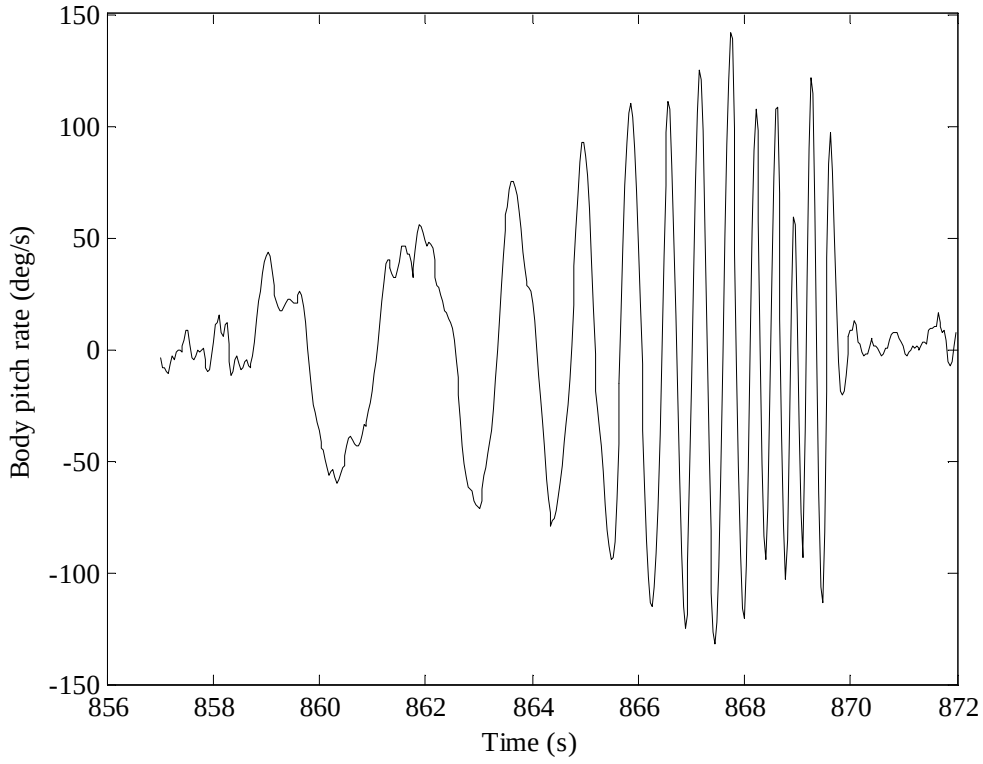

Figure 7.53 Measured output of the delta-wing aircraft

Figure 7.54 is the FFT plot of the manually generated Chirp input excitation.

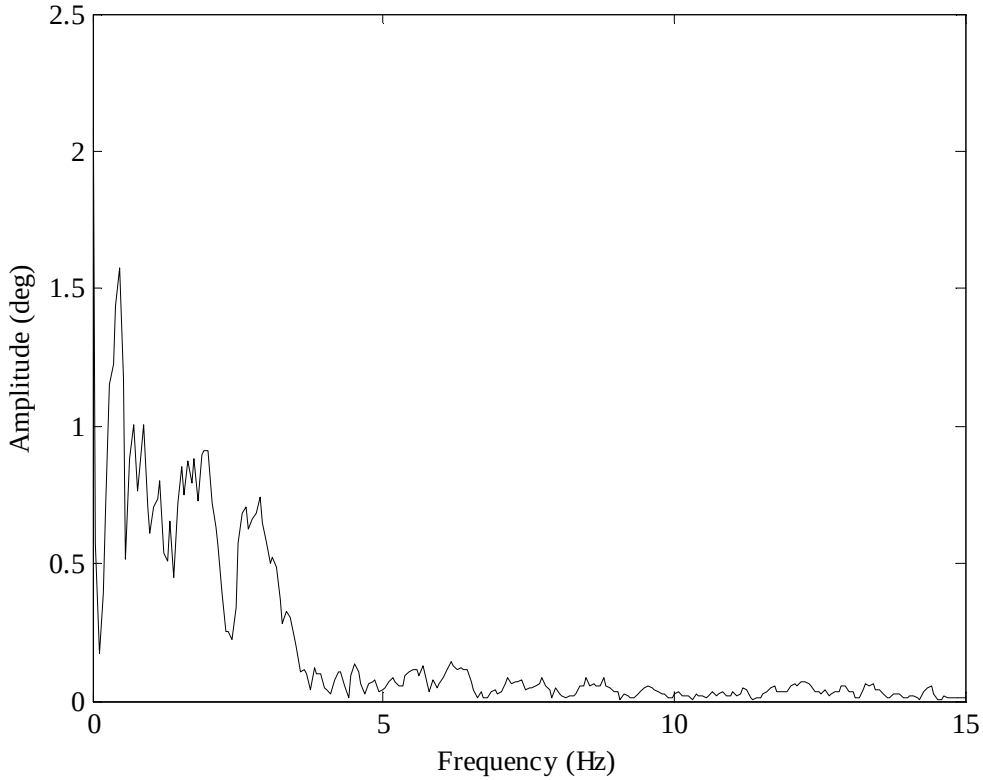

Figure 7.54 Finite Fourier transform plot of input excitation

From the FFT plot, it is seen that the frequency range of the input excitation is 0.47 ~ 3.7 Hz, which indicates that the signal is very suitable for identification of the system, from the frequency range point of view. For the system identification with flight test data, some data pre-processing work needs to be done. Sampling time inconsistency is one of the typical problems which need to be resolved by regulating the data sample times. The actual sampling time of the gathered data is shown by Figure 7.55.

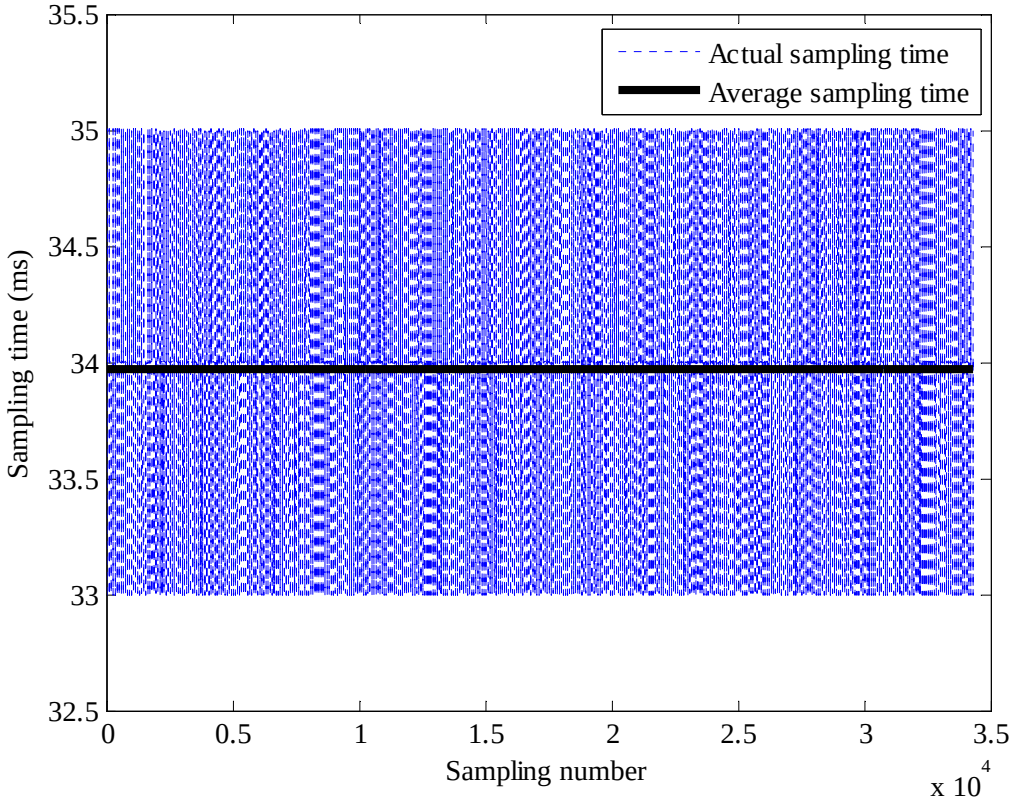

Figure 7.55 Sampling time

From Figure 7.55, it is seen that average sampling time is around 34 ms, and the actual sampling is between 33 and 35 ms. Since CIFER is sensitive to the deviation of the sampling time in data processing, it is recommended that the data points are evenly distributed on the time axis first. This is done by interpolating the original data read by the autopilot. After pre-processing and performing the required unit conversions, the data are fed to CIFER for system identification processing. The method that CIFER uses to obtain frequency response is the Power Spectra method which was discussed in Section 6.1.1. The frequency response (Bode plot) of δ_e- q obtained from CIFER is shown in Figure 7.56.

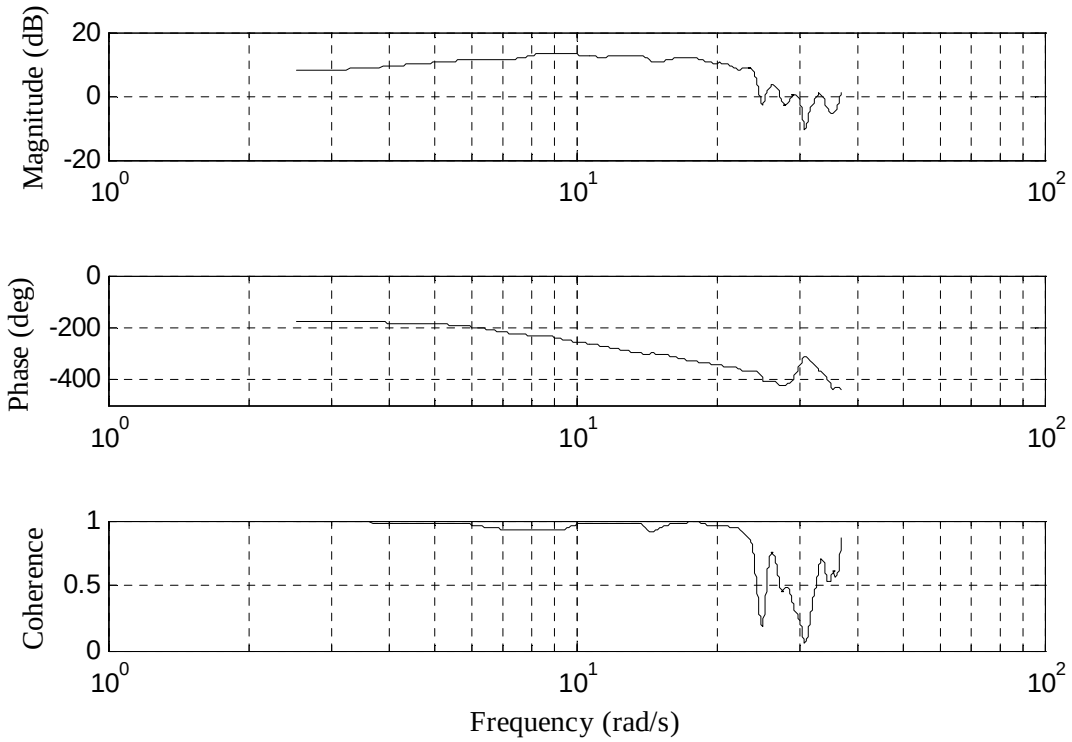

Figure 7.56 Bode plot of δ_e-q

From the coherence graph it is seen that the optimum frequency range for obtaining the transfer function is 2.53 ~ 23 rad/s, which has the coherence over 0.89. The transfer function is obtained by using the FRESPID and NAVFIT utilities of CIFER, which is acquired as,

$$\frac{q(s)}{\delta_e(s)} = \frac{-64.95(s+3.23)e^{-0.1022s}}{s^2 + 2 \times 0.74 \times 10.54s + 10.54^2} \tag{7.23}$$

where U_e = 20 m/s = 65.62 ft/s. The transfer function cost is 39.7, which is well below the maximum acceptable value of 100. The comparisons of identified Bode plots (one is plotted from identified transfer function, the other one is identified from flight test data) are shown in Figure 7.57 and Figure 7.58.

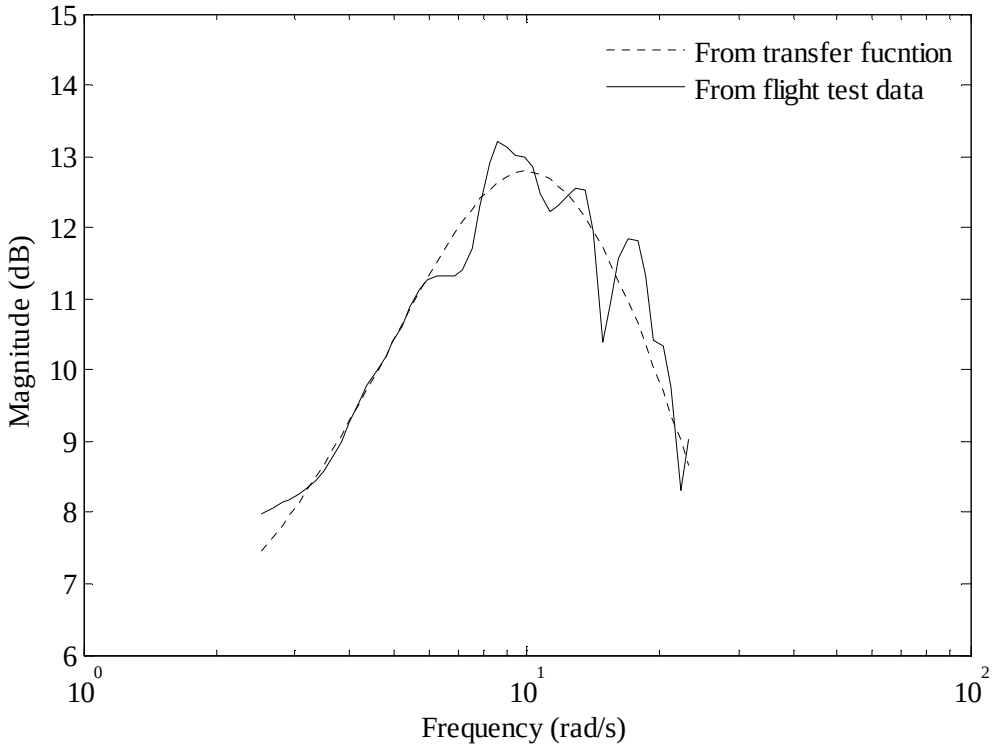

Figure 7.57 Comparison of magnitudes

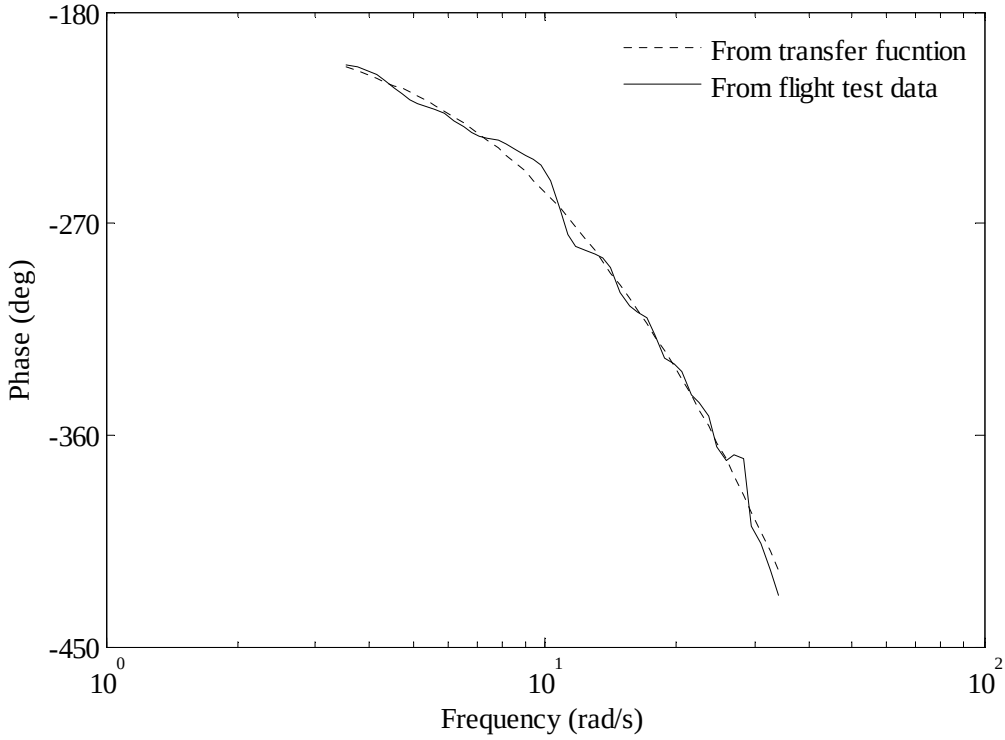

Figure 7.58 Comparison of phases

From Figure 7.57 and Figure 7.58, it can be seen that the magnitudes and phases are matching fairly well, which means that the transfer function meets the frequency domain verification requirement. The next step is to verify it in time domain. By feeding the transfer function with the same input excitation used in the flight test, the output from the transfer function can be calculated (simulated). Figure 7.59 shows the comparison of simulated output (pitch rate) with flight test measured output.

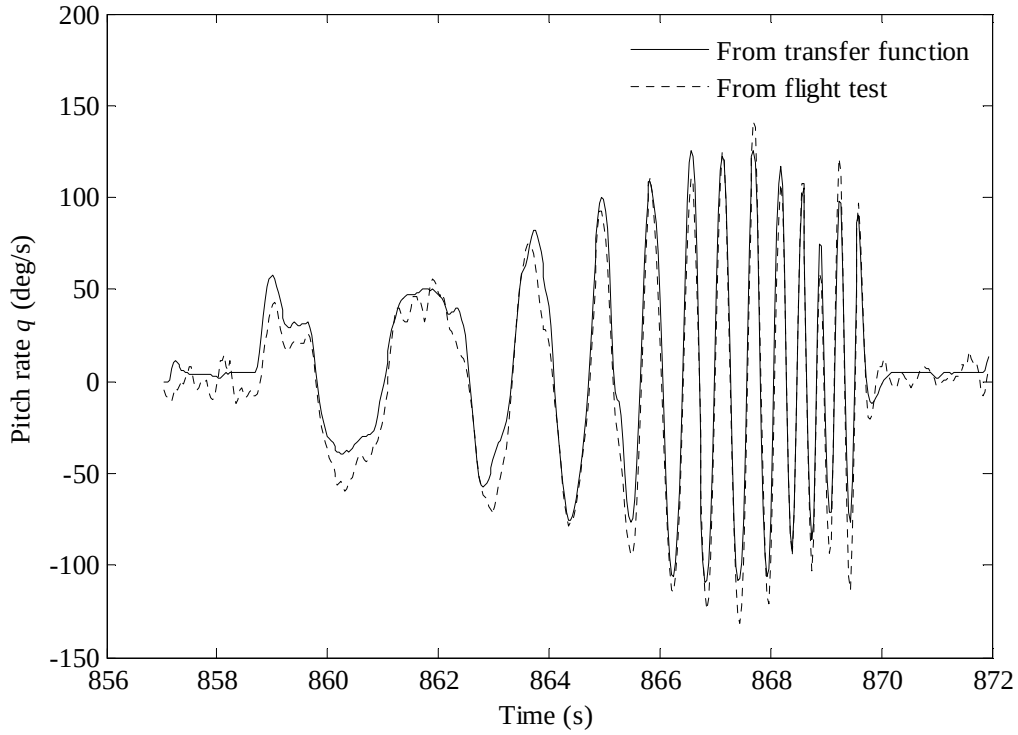

Figure 7.59 Comparison of simulated output and measured output

From Figure 7.59, it can be seen that the transfer function simulated output can track the flight test measured response very well. This means that the transfer function describes the system characteristics precisely. For examining the applicability for other flight scenarios of the transfer function, an unseen signal is used. The unseen input signal used is shown in Figure 7.60. Figure 7.61 shows the comparison of the flight test response and the transfer function simulated output.

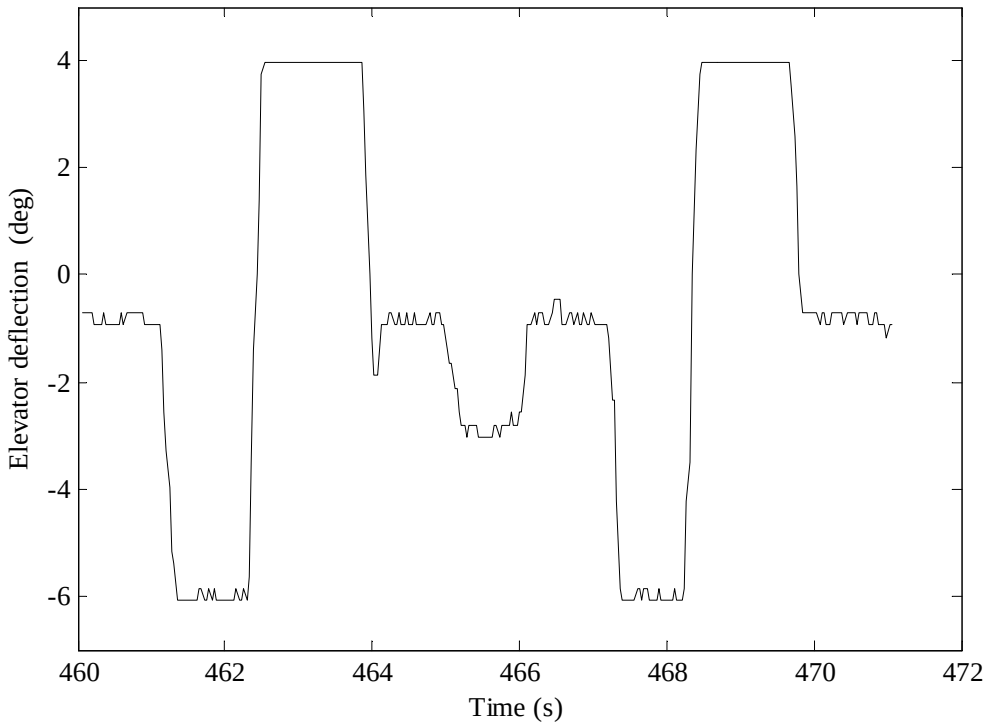

Figure 7.60 Unseen input excitation used for transfer function verification

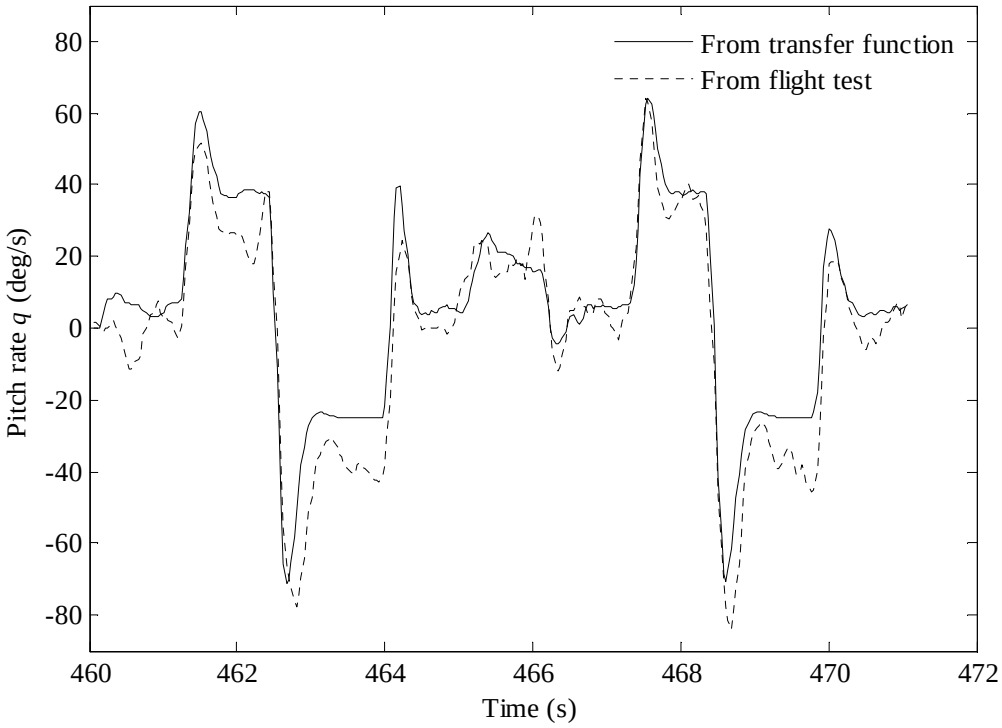

Figure 7.61 Comparison of simulated and measured outputs with unseen input signal

From Figure 7.61, it is seen that the simulated output obtained by the transfer function, can track the flight test measured output fairly well, which further demonstrate that the identified transfer function is accurate. The time domain responses comparison demonstrates that the identified transfer function can predict the aircraft's longitudinal mode responses reasonably accurately. Next, the unknown longitudinal channel aerodynamic derivatives are extracted from the identified transfer function.

$$\frac{q(s)}{\delta_e(s)} = \frac{m_{\delta_e}(s - z_w)}{s^2 - (m_q + z_w)s + (m_q z_w - m_w U_e)} = \frac{-64.95(s + 3.23)}{s^2 + 15.5s + 111.1} \tag{7.24}$$

As the following equality holds,

$$s^2 + 2\omega_s \xi_s s + \omega_s^2 = s^2 + 15.5s + 111.1$$

Therefore, the natural frequency ω_s is

$$\omega_s = \sqrt{111.1} = 10.54 \text{ rad/s}$$

And the damping ratio ξ_s is

$$\xi_s = \frac{15.5}{2\omega_s} = 0.74$$

In addition, by solving Equation (7.24), the following have:

$$\begin{cases} m_{\delta_e} = -64.95 \\ z_w = -3.23 \\ m_q = -12.27 \\ m_w = -1.09 \end{cases}$$

Following the conversion procedures used on Cropcam, the above concise notated derivatives can be converted to the North American dimensionless derivatives which are given as:

$$\begin{cases} C_{m_{\delta e}} = -0.04 \\ C_{z_w} = -3.18 \\ C_{m_q} = -0.83 \\ C_{m_w} = -0.044 \end{cases}$$

Since the identified transfer function is validated as quite accurately, and the TF method is proven reliable in identifying aerodynamic derivatives of the Cropcam, it is expected that the identified delta-wing aircraft aerodynamic derivatives are reliable.

7.3 Summary

This chapter presented the experimental results, which comprised of the identification of two classes of UAVs: a Cropcam and a delta-wing aircraft. The identification results were examined and validated in various ways. Before the two identification methods were applied to identify the actual system, they were examined and proven effective using a simulation model of a UAV.

For the identification of the Cropcam system, the transfer function method was applied first, and the system Bode plots and transfer functions were obtained accordingly. The accuracy of the obtained transfer functions was validated next. Based on the validated transfer functions, some aerodynamic derivatives were extracted and converted into the dimensionless format. Equation error method was then used to directly identify the aerodynamic derivatives. The identification results were verified by various ways. From the verification, it was seen that the EE method identified derivatives are more accurate than the AVL program estimated ones.

For the identification of the delta-wing aircraft, only TF method was applied, since the purpose of identification of the delta-wing aircraft was to obtain the system transfer function. The accuracy of the identified transfer function was also examined. Certain aerodynamic derivatives of this UAV were also calculated from validated transfer function.

8 Conclusions

8.1 Contributions made by this thesis

In this thesis, the following research questions were addressed: *i*) design and implementation of appropriate identification algorithms, which satisfy the need for low computational complexity and limited measurements while maintaining high accuracy of parameters estimation; *ii*) design and implementation of proper input excitations that can adequately stimulate different modes of aircraft behaviour and provide rich information in the output measurements in both time and frequency-domain; *iii*) poor sensory information of the vehicle variables.

For frequency domain system identification, the design of input excitation is an essential step which can affect the quality of the identification. A sweep input excitation generating program was developed in this research. Two types of input excitation were executed in the flight test: Chirp and Doublet. Chirp was proved to be more appropriate for frequency domain system identification due to its rich frequency components. Doublet was selected for result verification.

The main aim of this research was to identify the longitudinal channel transfer functions of UAVs, as well as the corresponding aerodynamic derivatives. Two approaches were developed for identifying the derivatives: one is the Transfer Function (TF) method; the other one is the Equation Error (EE) method. The EE method was considered as the main approach for identifying aerodynamic derivatives, because it can identify more derivatives with better accuracy as compared to the TF method. The TF method, however, has some unique positive characteristics. In particular, it requires fewer measurements. The TF method is also demonstrated as an alternative approach for identification of aerodynamic derivatives. In order to

check the feasibility, both identification methods were first tested with a simulation scenario, before they were applied to the real aircraft data. The identification for the simulation model system demonstrated that both of the methods are applicable and effective.

For identification of the Cropcam, both transfer function and EE methods were applied. Using the transfer function method, the longitudinal transfer functions of the aircraft were obtained. Based on the identified transfer functions, some of the aerodynamic derivatives were extracted. By applying the EE method, an entire set of longitudinal channel aerodynamic derivatives were identified. The derivatives identified by the two methods were compared and verified in multiple ways. To further verify the reliability of identification results, the identified derivatives were compared with the derivatives from two other sources, namely AVL estimated derivatives and derivatives of some conventional aircrafts published by the aircraft manufacturer. The verification showed that most of the identified derivatives are fairly reliable, especially for pitching moment derivatives. For some axial force related derivatives, the simulation responses do not match very well with the flight responses. It is mainly due to the deficiency of the data measurements, such as the coupling between the longitudinal and lateral channels, and nonlinearities or data recording deficiencies. The mismatch may also be attributed to the built in models of the identification algorithm (EE method) are not accurate or have too many unknowns.

For identification of the delta-wing aircraft system, the transfer function method was applied. As a result, the longitudinal transfer function of the aircraft was obtained, and some corresponding aerodynamic derivatives were extracted from the identified transfer function. Since the objective of the delta-wing aircraft identification is to obtain the system transfer function, the transfer function method is the only method used rather than the EE method.

The TF and EE methods were first implemented and used on the simulation model to examine and analyze the efficiency of each method. By verifying the derivatives based on computer simulation, the EE method identified derivatives showed a better ability to track the actual flight responses than the AVL estimated derivatives. Therefore, it is expected that the EE method is more capable of calculating aerodynamic derivatives than the AVL software. By comparing the derivatives identified by the TF and EE methods, it is seen that their results are close. Therefore, the transfer function method is believed to be an effective alternative for aerodynamic derivatives identification. The identification results are expected to improve the simulation program developed by MicroPilot Inc.

8.2 Future research

For the future research, the following issues need to be addressed: *i*) poor flight test data; *ii*) data delay; *iii*) applicability validation.

i. Some of the identified derivatives have high parameter standard errors indicating that they are not accurate. This could be due to the poor flight test, improper data delay processing, or even the algorithm deficiency. Therefore, more work is required to focus on the data pre-processing and the identification program optimizing. Also, ways need to be found to solve the problem of poor parameter accuracy.

ii. Since the EE identification method was found highly sensitive to the delay (identified as shifting between the input and output), the delay problem should be resolved. The delay is caused by the control servos response delay, as well as the delay inherently associated

with the system's dynamics. Other sources of delay and method(s) to rectify their effects on the identification must be investigated in the future.

iii. To validate the applicability of the identification results in practice, the identified derivatives should be applied to further enhance the simulation model. Currently the values of derivatives used by 'Horizon' (a simulation software developed by MicroPilot Inc.) are taken from the open-source AVL program. The degree on enhancement that can be achieved using the newly obtained derivatives should be tested on Horizon.

References

AVL — Aerodynamic Analysis, Trim Calculation, dynamic Stability Analysis, Aircraft Configuration Development: http://web.mit.edu/drela/Public/web/avl/.

Bischoff, D. E, and Palmer, R. E. (1982), "Investigation of Low Order Lateral Directional, Transfer Function Models for Augmented Aircraft", AIAA Guidance and Control Conference, Paper 82-1610, Aug., pp. 579-586.

Bischoff, D. E (1983), "The Definition of Short-Period Flying Qualities Characteristics via Equivalent Systems', *Journal of Aircraft*, vol. 20. No. 6, pp.494-499.

Bodson, M. (1995), An adaptive algorithm with information- dependent data forgetting, *American Control Conference* **5**, 3485-3489.

Carnduff, Stephen (2008), System Identificaion of Unmanned Aerial Vehicles, Ph. D thesis, Cranfield University.

Chandler, P. R., Patchter, M., and Mears, M. (1995), System identification for adaptive and reconfigurable control, *Journal of Guidance, Control, and Dynamics* **18**, 516-524.

Chen, R. T. N. (1975), Input design for aircraft parameter identification: Using time- optimal control formulation, AGARD Methods for Aircraft State and Parameter Identification 15p (SEE N 75-29997 21-01).

Chowdhary, G. and Jategaonkar, R. (2006). "Aerodynamic Parameter Estimation from Flight Data Applying Extended and Unscented Kalman Filter". *AIAA Atmospheric Flight Mechanics Conference and Exhibit*, Keystone, Colorado.

Chowdhary, G. and Jategaonkar, R., (2010), Aerodynamic Parameter Estimation from Flight Data Applying Extended and Unscented Kalman Filter, *Aerospace Science and Technology* **14(2)**, 106-117.

Cook, M. V. (2012), *Flight dynamics principles: a linear systems approach to aircraft stability and control*, Butterworth-Heinemann.

Crassidis, J. L. and Junkins, J. L. (2001), *Optimal Estimation of Dynamic Systems*. CRC press.

DeBusk, W. M., Chowdhary, G., and Johnson, E. (2009), Real-Time system identification of a small multi-engine aircraft, *In Proceedings of the AIAA Atmospheric Flight Mechanics Conference*, 1-15.

Dorobantu, A., Murch, A., Mettler, B., and Balas, G. (2011, August), Frequency domain system identification for a small, low-cost, fixed-wing UAV", *InProceedings of the 2011 AIAA Guidance, Navigation, and Control Conference.*

Dorobantu, A., Murch, A. M., Mettler, B., and Balas, G. (2013), System identification for a small, low-cost, fixed-wing unmanned aircraft", *Journal of Aircraft* **50**, 1117-1130.

Fahimi. F. (2008), Autonomous Robots: Modeling, Path Planning, and Control **107**, Springer.

Hamel, P.G. (1991), Rotorcraft system identification, *AGARD Lecture Series LS 178*, NORTH ATLANTIC TREATY ORGANIZATION.

Hodgkinson, J., LaManna, W. J., and Heyde, J. L. (1976), "Handling Qualities of Aircraft with Stability and Control Augmentation Systems-A Fundamental Approach", *Aeronautical Journal*, Vol. 80, No. 782, pp. 75-81.

Hodgkinson, J. (1998), *Aircraft Handling Qualities*, AIAA Educational Series, AIAA, Reston, VA.

Hodgkinson, J., Boland, J. R., Brandt, M. Q., Lavretsky, E., Rossito, K. F., Stephens, A. T., Stevenson, S. W. and Thompson, T. L. (1998). "An Aircraft Manufacturer's View of Parameter Identification". *Proceedings of*

the Nato/Research and Technology Organisation Symposium on System Identification for Integrated Aircraft Development and Flight Testing. Madrid, Spain.

Hoh, R.H., Myers, T. T., Ashkenas, I. L., Ringland, R. R. and Craig, S. (1981), Development of handling quality criteria for aircraft with independent control of six degrees of freedom (No. STI-TR-1135-1). SYSTEMS TECHNOLOGY INC HAWTHORNE CA.

Jang, J. S. and Tomlin, C. J. (2003). "Longitudinal Stability Augmentation System Design for the DragonFly UAV Using a Single GPS Receiver". *AIAA Guidance, Navigation and Control Conference and Exhibit*, Austin, Texas.

Jategaokar, R. V. and Monnich, W. (1997, August), Identification of Do-328 aerodynamic database for a level D flight simulator, *In AIAA Atmospheric Flight Mechanics Conference*, 248-258.

Jategaonkar, R. V. (2006), Flight vehicle system identification (a time domain methodology), *Progress in astronautics and aeronautics*.

Karpenko, M.and Sepehri, N. (2008), Equivalent time-invariant modeling of electrohydraulic actuators with application to robust control synthesis, *International Journal of Fluid Power* **9**(3), 7-18.

Karpenko, M. and Sepehri, N. (2009), Hardware-in-the-loop simulator for research on fault tolerant control of electrohydraulic actuators in a flight control application, *Mechatronics* **19**(7), 1067-1077.

Karpenko, M. and Sepehri, N. (2012), Electrohydraulic force control design of a hardware-in-the-loop load emulator using a nonlinear QFT technique, *Control Engineering Practice* **20**(6), 598-609.

Keesman, Karel J. (2001), *System Identification*, Springer.

Khan, M. E. and Khan, F. (2012), A comparative study of white box, black box and grey box testing techniques", *International Journal of Advanced Computer Science and Applications* **3**(6), 12-15.

Klein, V. , Ratvasky, T. R. and Cobleigh, B. R.(1990), "Aerodynamic Parameters of High-Angleof-Attack-Research-Vehicle (HARV) Estimated from Flight Data". NASA TM-102692.Klein, V. and Morelli, E. A. (2006), Aircraft System Identification: Theory and Practice, American Institute of Aeronautics and Astronautics.

Lawler, M. A., Ivler C. M., Tischler, M. B. and Shtessel, Y. B. (2006, August), System identification of the longitudinal/ heave dynamics for a tandem- rotor helicopter including higher- order dynamics, In *AIAA Atmospheric Flight Mechanics Conference*, 21-24.

Lee, S. H., and Park, Y. M. (2009), System Identification of Dragon Fly UAV via Bayesian Estimation, Stanford University.

Marchand, M. and Koehler, R. (1975), Determination of aircraft derivatives by automatic parameter adjustment and frequency response methods, *AGARD Methods for Aircraft State and Parameter Identification* 18 *p*(*SEE N* 75-29997 21-01).

Mehra, R. K. and Gupta, N. K. (1975), *Status of input design for aircraft parameter identification*, In AGARD Methods for Aircraft State and Parameter Identification 21 *p* (*SEE N*75-29997 21-01).

Morelli. E. A. (1993), *Practical Input Optimization for Aircraft Parameter Estimation Experiments*, National Aeronautics and Space Administration, Langley Research Center.

Morelli. E. A. (1997, August), Flight test validation of optimal input design and comparison to conventional inputs", In *AIAA Atmospheric Flight Mechanics Conference* **1**, 11-13.

Morelli. E. A. (2000), Real- time parameter estimation in the frequency domain, *Journal of Guidance, Control, and Dynamics*, **23**(5), 812-818.

Morelli. E. A. (2003), Multiple input design for real-time parameter estimation in the frequency domain, *13th IFAC Conference on System Identification*.

Morelli, E. A. (2003b). "Low-Order Equivalent System Identification for Tu-144LL Supersonic Transport Aircraft". *Journal of Guidance, Control and Dynamics*, Vol. 26, No. 2, pp 354-362.

Morelli. E. A. and Smith, M. S. (2009), Real-time dynamic modeling: Data information requirements and flight-test results, *Journal of Aircraft*, **46**(6), 1894-1905.

Newsom, H. G., Gorell, J., Achadjian and K., Anderson.J (2013), *Civilian Applications of UAVs – A California Perspective, a Policy Symposium*, American Institute of Aeronautics and Astronautics.

Nonami, K. (2010), *Autonomous Flying Robots: Unmanned Aerial Vehicles and Micro Aerial Vehicles*, Springer.

Paris, A. C. and Bonner, M. (2004), "Nonlinear Model Development from Flight Test Data for F/A-18E Super Hornet". Journal of Aircraft. Vol. 41, No. 4, pp 692-702.

Pintelon, R. and Schoukens, J. (2012), *System Identification: A Frequency Domain Approach*, John Wiley & Sons.

Ryan, A., Zennaro, M., Howell, A., Sengupta, R., and Hedrick, J.K. (2004), An overview of emerging results in cooperative UAV control, In *Decision and Control, 2004. CDC. 43rd IEEE Conference* **1**, 602-607.

Simon, D. (2006), *Optimal State Estimation: Kalman, H Infinity, and Nonlinear Approaches*, John Wiley & Sons.

Theodore, C. R., Tischler, M. B., and Colbourne, J. D. (2004), Rapid frequency-domain modeling methods for unmanned aerial vehicle flight control applications, *Journal of Aircraft*, **41**(4), 735-743.

Tischler, M. B. (1982), "Aerodynamic Model for Piloted V/STOL Simulation', Systems Technology, Inc., WP 1171-2, Hawthorne, CA, May.

Tischler, M. B. (1987), " Digital Control of Highly Augmented Combat Rotorcraft", NASA TM 88346, ARMY TR 87-A-5, May.

Tischler, M. B. (1987b), "Freqeuncy-Response Identification of XV-15 Tilt-Rotor Aircraft Dynamics", NASA TM 89428, ARMY TM 87-A-2, Ph.D. Dissertation, Stanford Univ., Stanford, CA, May.

Tischler, M. B. (1996), System identification methods for aircraft flight control development and validation, *Advances in Aircraft Flight Control*, 35-69.

Tischler, M. B. and Remple, R. K. (2006), *Aircraft and Rotorcraft System Identification*, American Institute of Aeronautics and Astronautics, New York.

Tischler, M. B., Remple, R. K. (2012), *Aircraft and Rotorcraft System Identification*, Second Edition, American Institute of Aeronautics and Astronautics, New York.

Ward, D. G., Monaco, J. F., Barron, R. L. and Bird, R. A., Viring, J. and Landers, T. (1996), Self-designing controller-design, simulation, and flight test evaluation, *BAI, Lockheed Martin, Calspan AFRL Final Report*, WL-TR-97-3095.

Young, P. (1989), An Assessment of Techniques for Frequency-Domain Identification of Helicopter Dynamics, Ph.D. dissertation, Dept. of Electronics, Univ. of York, UK.

Young, P., and Patton R. J. (1990), Comparison of test signals for aircraft frequency domain identification, *Journal of Guidance, Control and Dynamics*, **13**(3), 430-438.

Zaloga, S. and Rockwell, D. (2011), UAV market set for 10 years of growth, *Earth Imaging Journal*.

Appendix 1 Derivatives Conversion

Tables A 1 to A 4 show the conversions of longitudinal aerodynamic stability and control derivatives.

Table A 1 British notation longitudinal derivatives conversion (Cook, 2012)

	Dimensionless	Multiplier	Dimensional
Axial force related stability derivatives	X_u	$\frac{1}{2}\rho V_0 S$	$\mathring{X}_u$
	X_w	$\frac{1}{2}\rho V_0 S$	$\mathring{X}_w$
	$X_{\dot{w}}$	$\frac{1}{2}\rho S\bar{\bar{c}}$	$\mathring{X}_{\dot{w}}$
	X_q	$\frac{1}{2}\rho V_0 S\bar{\bar{c}}$	$\mathring{X}_q$
Lift force related stability derivatives	Z_u	$\frac{1}{2}\rho V_0 S$	$\mathring{Z}_u$
	Z_w	$\frac{1}{2}\rho V_0 S$	$\mathring{Z}_w$
	$Z_{\dot{w}}$	$\frac{1}{2}\rho S\bar{\bar{c}}$	$\mathring{Z}_{\dot{w}}$
	Z_q	$\frac{1}{2}\rho V_0 S\bar{\bar{c}}$	$\mathring{Z}_q$
Pitch moment related stability derivatives	M_u	$\frac{1}{2}\rho V_0 S\bar{\bar{c}}$	$\mathring{M}_u$
	M_w	$\frac{1}{2}\rho V_0 S\bar{\bar{c}}$	$\mathring{M}_w$
	$M_{\dot{w}}$	$\frac{1}{2}\rho S\bar{\bar{c}}^2$	$\mathring{M}_{\dot{w}}$
	M_q	$\frac{1}{2}\rho V_0 S\bar{\bar{c}}^2$	$\mathring{M}_q$

Control derivatives	X_η	$\frac{1}{2}\rho {V_0}^2 S$	$\mathring{X}_\eta$
	Z_η	$\frac{1}{2}\rho {V_0}^2 S$	$\mathring{Z}_\eta$
	M_η	$\frac{1}{2}\rho {V_0}^2 S\bar{\bar{c}}$	$\mathring{M}_\eta$

Table A 2 North American notation longitudinal derivatives conversion (Cook, 2012)

	Dimensionless	Multiplier	Dimensional
Axial force related aerodynamic derivatives	C_{x_u}	$\rho V_0 S/2m$	X_u
	C_{x_w}	$\rho V_0 S/2m$	X_w
	$C_{x_{\dot{w}}} = C_{x_{\dot{\alpha}}}$	$\rho S\bar{\bar{c}}/4m$	$\mathrm{X}_{\dot{w}}$
	C_{x_q}	$\rho V_0 S\bar{\bar{c}}/4m$	X_q
	$C_{x_{\delta_e}}$	$\rho {V_0}^2 S/2m$	X_{δ_e}
Lift force related aerodynamic derivatives	C_{z_u}	$\rho V_0 S/2m$	Z_u
	C_{z_w}	$\rho V_0 S/2m$	Z_w
	$C_{z_{\dot{w}}}$	$\rho S\bar{\bar{c}}/4m$	$\mathrm{Z}_{\dot{w}}$
	C_{z_q}	$\rho V_0 S\bar{\bar{c}}/4m$	Z_q
	$C_{z_{\delta_e}}$	$\rho {V_0}^2 S/2m$	Z_{δ_e}
Pitch moment related aerodynamic derivatives	C_{m_u}	$\rho V_0 S\bar{\bar{c}}/2I_y$	M_u
	$C_{m_w} = C_{m_\alpha}$	$\rho V_0 S\bar{\bar{c}}/2I_y$	M_w
	$C_{m_{\dot{w}}} = C_{m_{\dot{\alpha}}}$	$\rho S\bar{\bar{c}}^2/4I_y$	$\mathrm{M}_{\dot{w}}$
	C_{m_q}	$\rho V_0 S\bar{\bar{c}}^2/4I_y$	M_q
	$C_{m_{\delta_e}}$	$\rho {V_0}^2 S\bar{\bar{c}}/2I_y$	M_{δ_e}

Table A 3 British and North American notation longitudinal dimensionless derivatives conversion (Cook, 2012)

North American	British	North American	British
C_{x_u}	X_u	C_{z_q}	$2Z_q$
C_{x_α}	X_w	$C_{z_{\delta_e}}$	Z_η
$C_{x_{\dot{w}}}$	$2X_{\dot{w}}$	C_{m_u}	M_u
C_{x_q}	$2X_q$	C_{m_w}	M_w
$C_{x_{\delta_e}}$	X_η	$C_{m_{\dot{w}}}$	$2M_{\dot{w}}$
C_{z_u}	Z_u	C_{m_q}	$2M_q$
C_{z_α}	Z_w	$C_{m_{\delta_e}}$	M_η
$C_{z_{\dot{w}}}$	$2Z_{\dot{w}}$		

Table A 4 Longitudinal concise and dimensional derivatives conversion (Cook, 2012)

Concise Derivative	Dimensional Derivative	Concise Derivative	Dimensional Derivative
x_u	$\frac{\mathring{X}_u}{m} + \frac{\mathring{X}_{\dot{w}}\mathring{Z}_u}{m(m-\mathring{Z}_{\dot{w}})}$	x_q	$\frac{\mathring{X}_q - mW_e}{m} + \frac{(\mathring{Z}_q + mU_e)\mathring{X}_{\dot{w}}}{m(m-\mathring{Z}_{\dot{w}})}$
z_u	$\frac{\mathring{Z}_u}{m-\mathring{Z}_{\dot{w}}}$	z_q	$\frac{\mathring{Z}_q + mU_e}{m-\mathring{Z}_{\dot{w}}}$
m_u	$\frac{\mathring{M}_u}{I_y} + \frac{\mathring{M}_{\dot{w}}\mathring{Z}_u}{I_y(m-\mathring{Z}_{\dot{w}})}$	m_q	$\frac{\mathring{M}_q}{I_y} + \frac{(\mathring{Z}_q + mU_e)\mathring{X}_{\dot{w}}}{I_y(m-\mathring{Z}_{\dot{w}})}$
x_w	$\frac{\mathring{X}_w}{m} + \frac{\mathring{X}_{\dot{w}}\mathring{Z}_w}{m(m-\mathring{Z}_{\dot{w}})}$	x_η	$\frac{\mathring{X}_\eta}{m} + \frac{\mathring{X}_{\dot{w}}\mathring{Z}_\eta}{m(m-\mathring{Z}_{\dot{w}})}$
z_w	$\frac{\mathring{Z}_w}{m-\mathring{Z}_{\dot{w}}}$	z_η	$\frac{\mathring{Z}_\eta}{m-\mathring{Z}_{\dot{w}}}$
m_w	$\frac{\mathring{M}_w}{I_y} + \frac{\mathring{M}_{\dot{w}}\mathring{Z}_w}{I_y(m-\mathring{Z}_{\dot{w}})}$	m_η	$\frac{\mathring{M}_\eta}{I_y} + \frac{\mathring{M}_{\dot{w}}\mathring{Z}_\eta}{I_y(m-\mathring{Z}_{\dot{w}})}$

Appendix 2 Simulation Results

In this appendix, an aircraft simulation model is introduced first. Then, by using the computer simulation data, both the TF and EE methods are applied to the identification of longitudinal channel aerodynamic derivatives. Additionally, the transfer function method will be used to identify the longitudinal channel system transfer functions, and the EE method will be used to identify the lateral channel aerodynamic derivatives.

A2.1 Simulation responses

Based on the aerodynamic motion equations presented in Chapter 4, a model of Cropcam is built. The geometric parameters such as mass, wing span and wing area are physically measured for Cropcam. The initial aerodynamic derivatives are then obtained by AVL. Input excitations, such as Chirp and Doublet, are implemented and employed in the simulation model to test the accuracy of the aircraft model response.

Since the Doublet signal is easy to generate and its corresponding responses are simple to analyse, it is used to test and excite the model first. The model is revised based on the analysis of simulation responses. After the reliability of the model is validated with Doublet, it is excited with the Chirp input signal. Meanwhile, the aircraft behaviour is studied. Figure A 1 shows the Chirp input used.

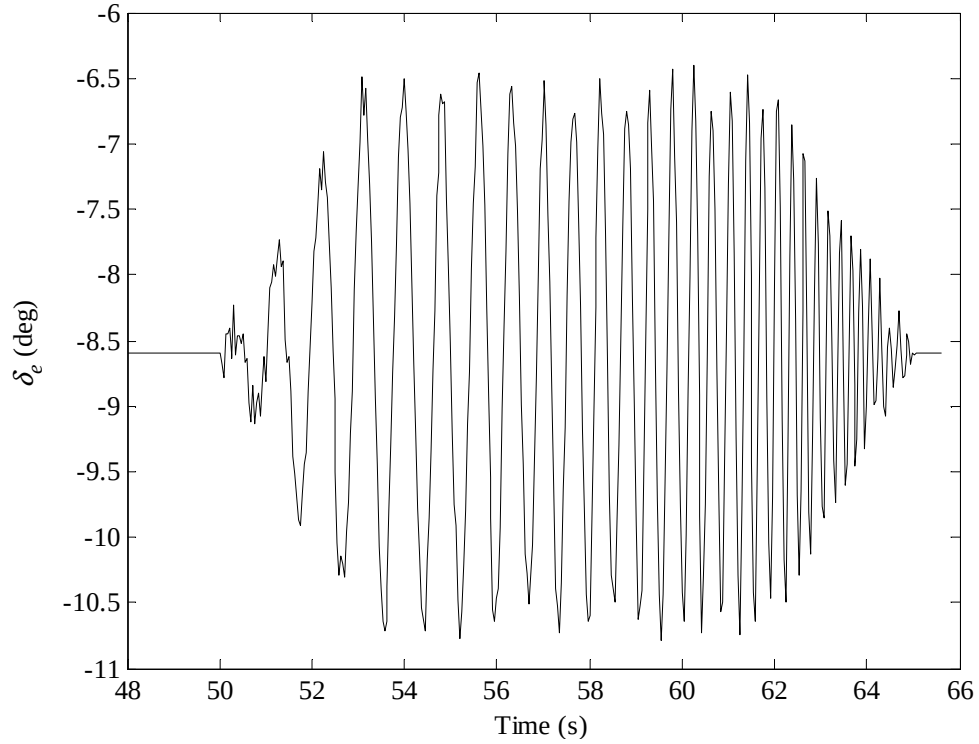

Figure A 1 Input excitation

The input excitation design obeys the criteria discussed in Section 5.1. In Figure A 1, it is seen that the aircraft is flying under trim condition before deploying significant elevator perturbation. And the input excitation ends up with the trim state as well. Figure A 2 to Figure A 13 display the aircraft corresponding responses.

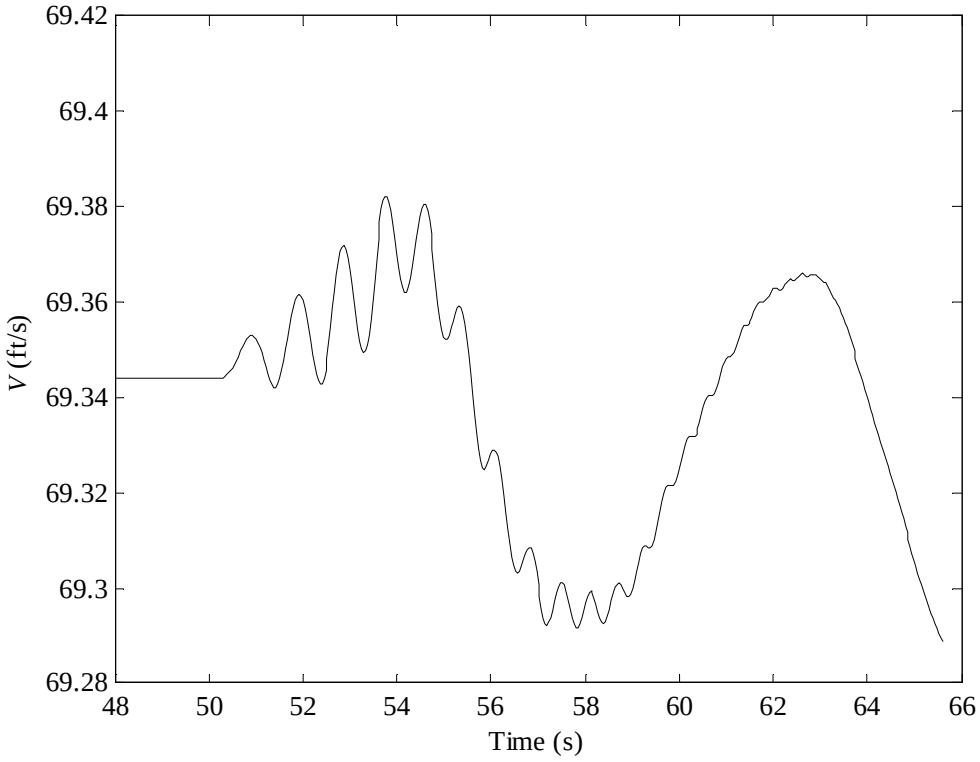

Figure A 2 Total velocity *V*

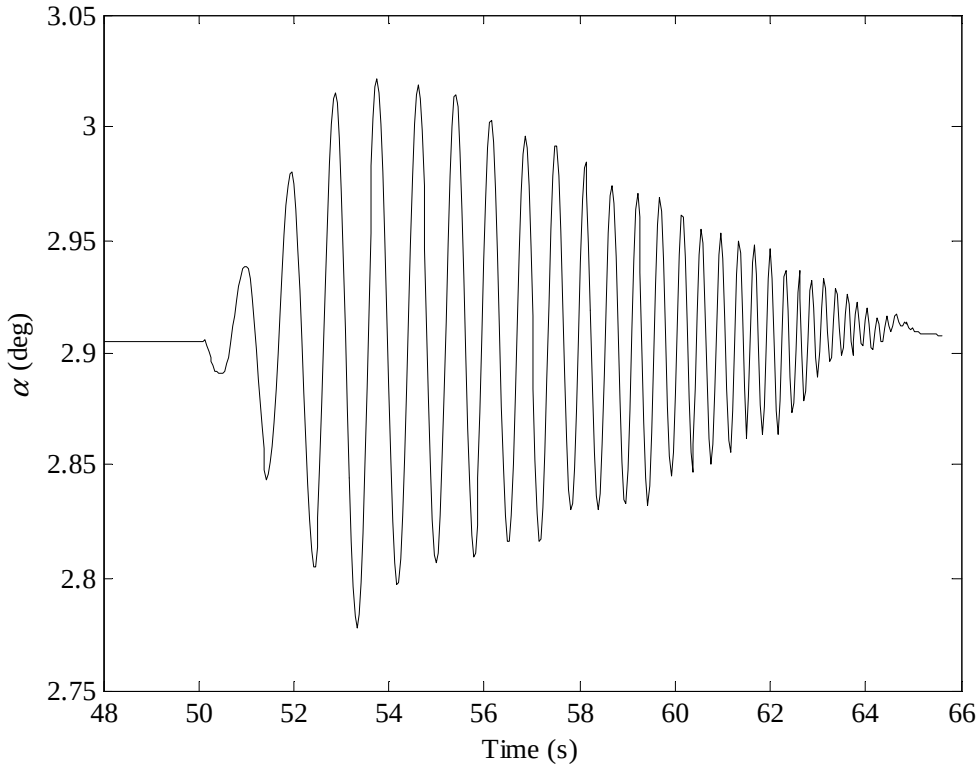

Figure A 3 Angle of attack *α*

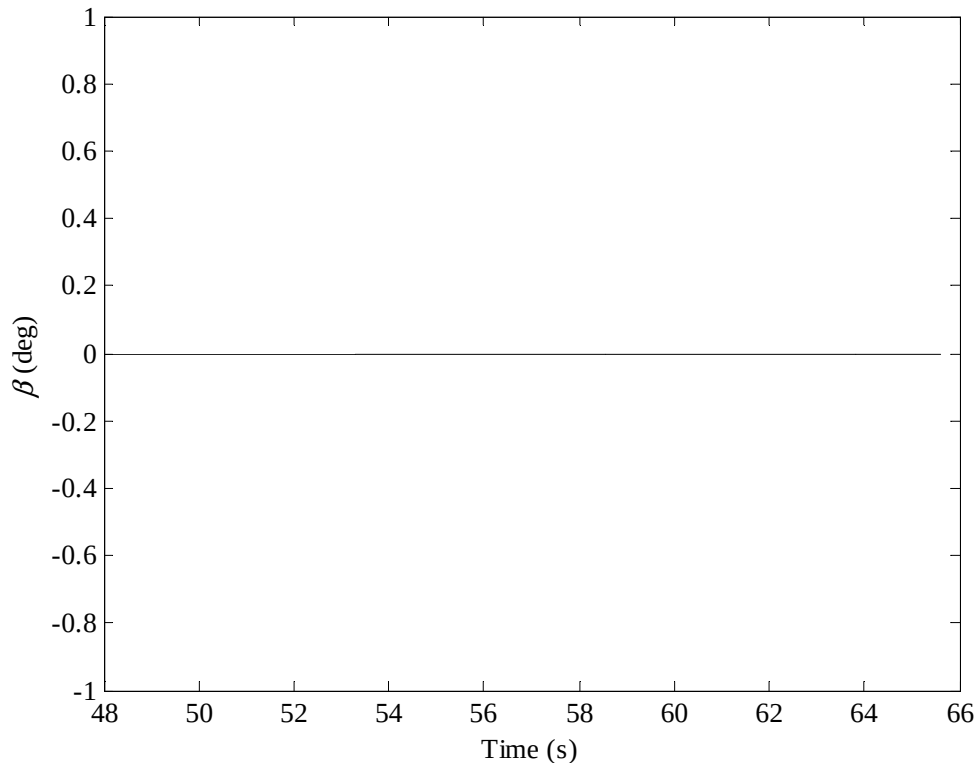

Figure A 4 Sideslip angle β

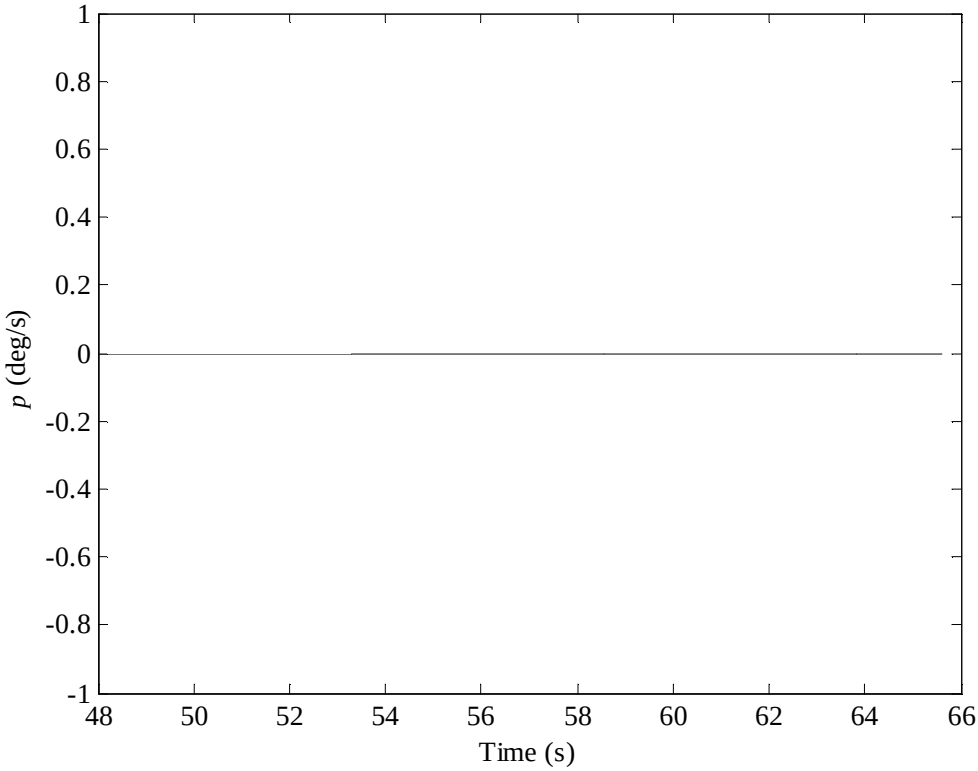

Figure A 5 Roll rate *p*

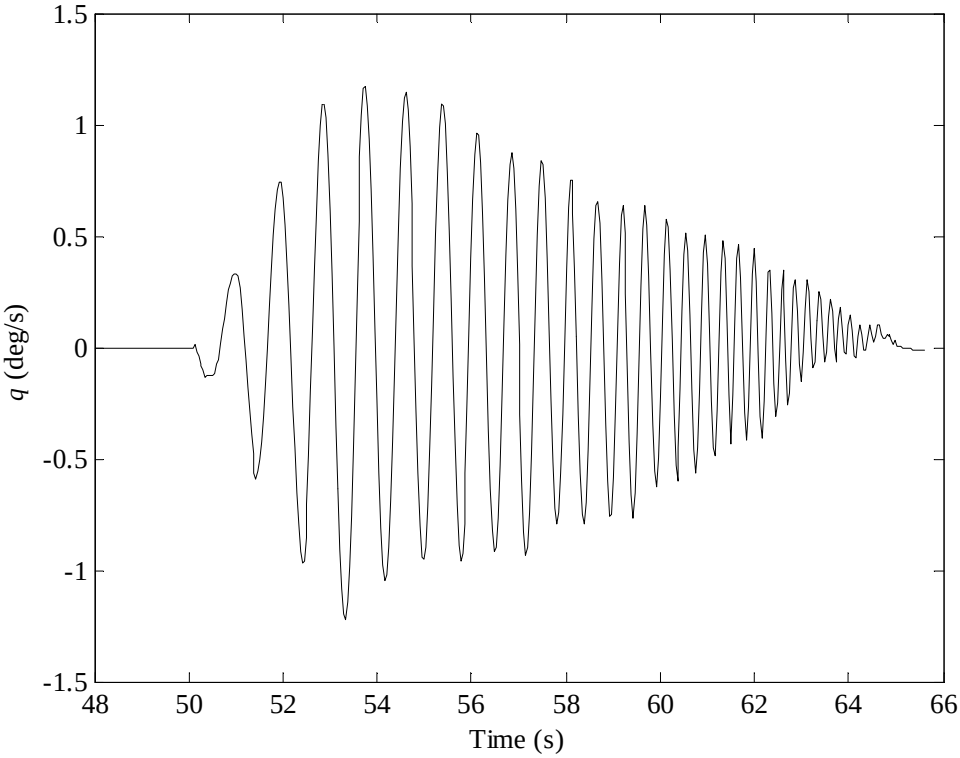

Figure A 6 Pitch rate *q*

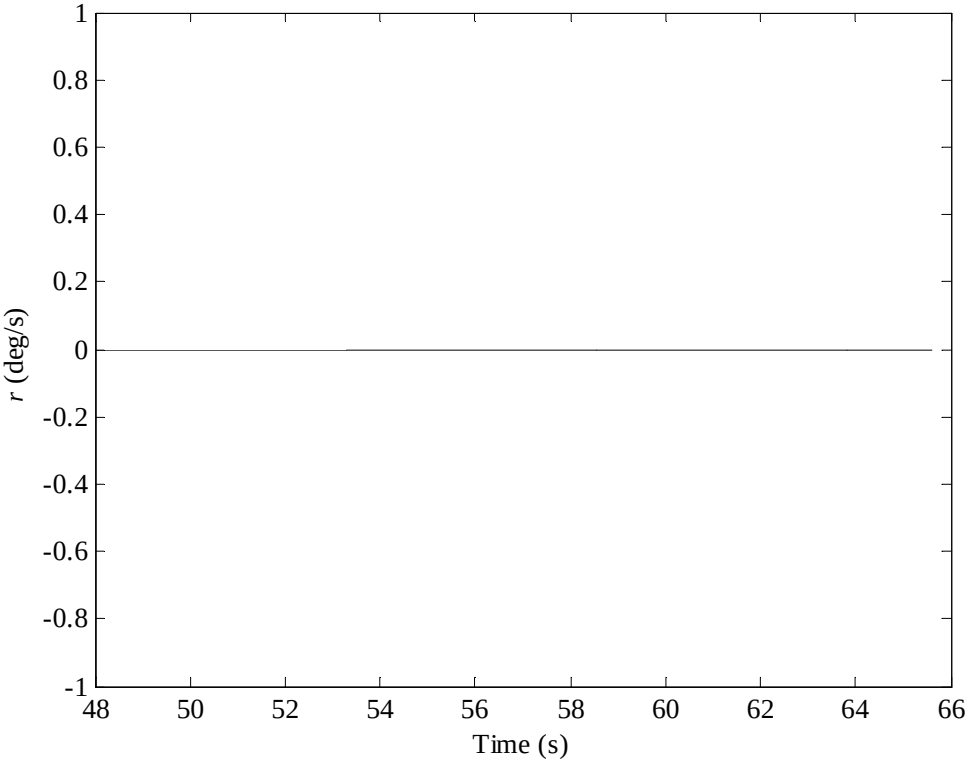

Figure A 7 Yaw rate *r*

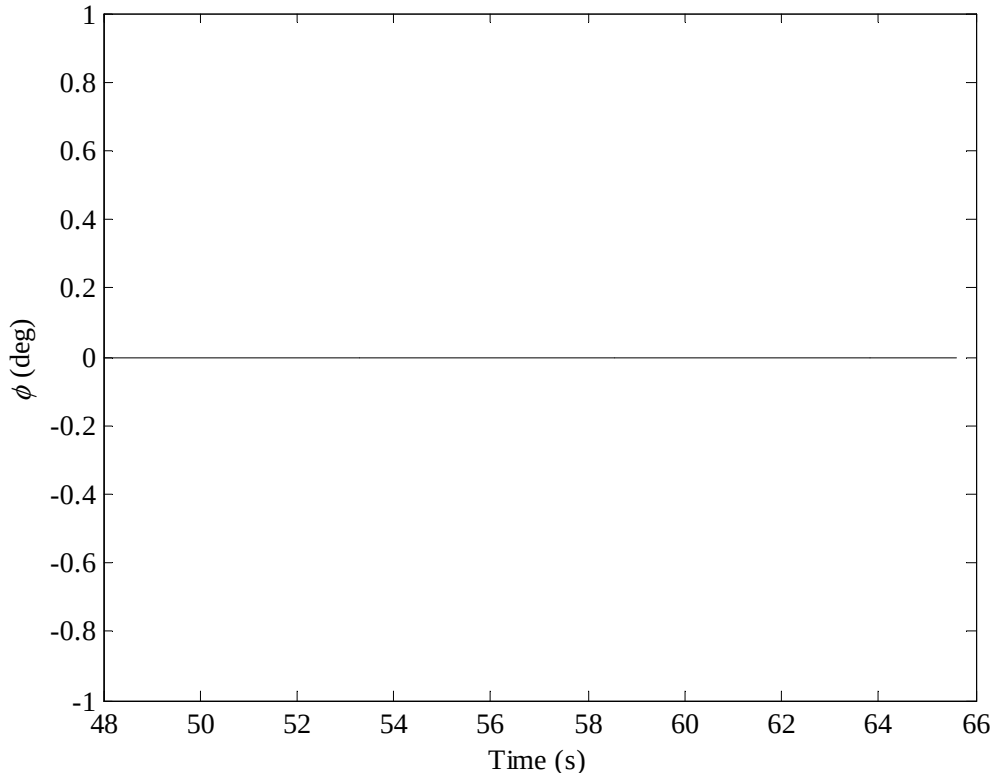

Figure A 8 Roll angle φ

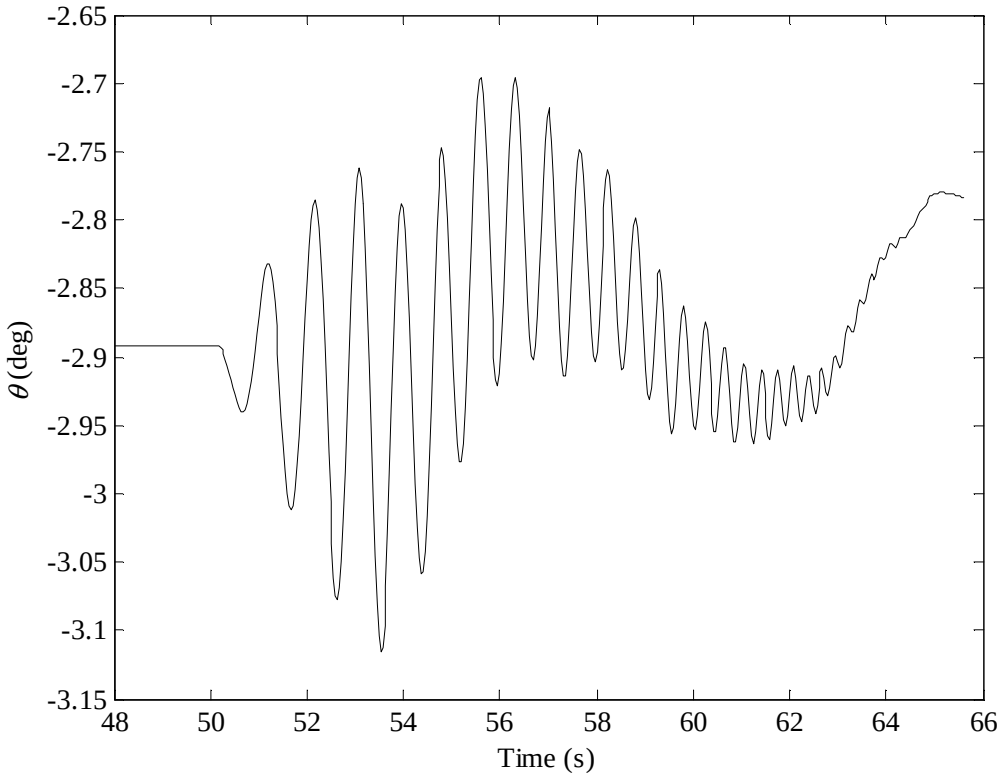

Figure A 9 Pitch angle θ

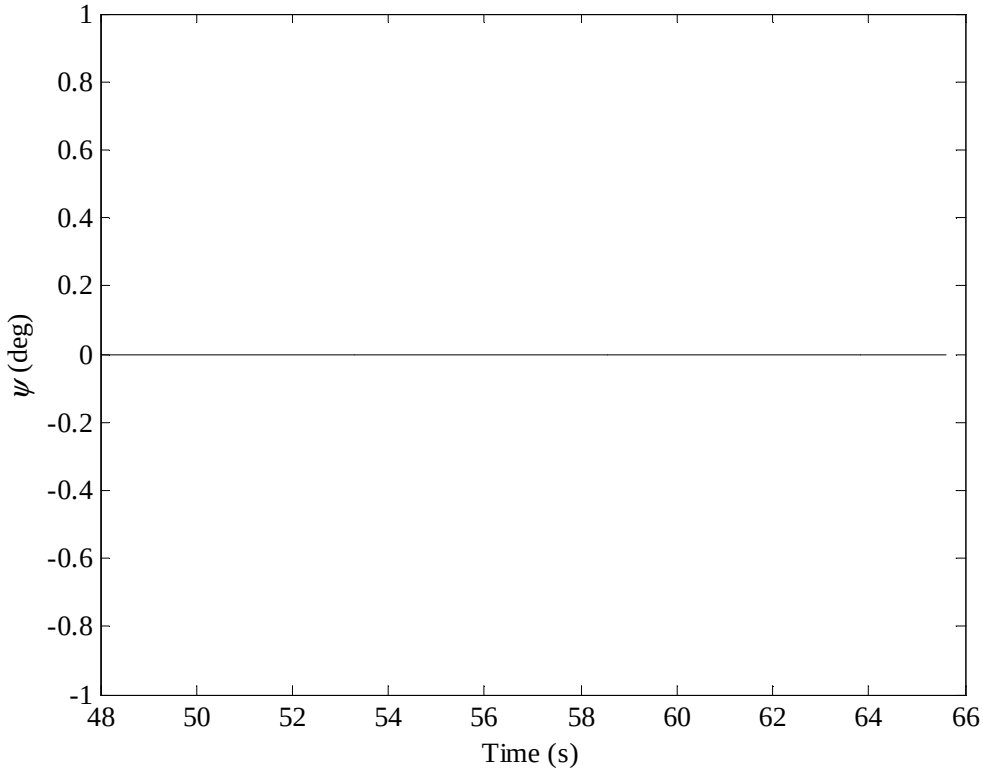

Figure A 10 Yaw angle ψ

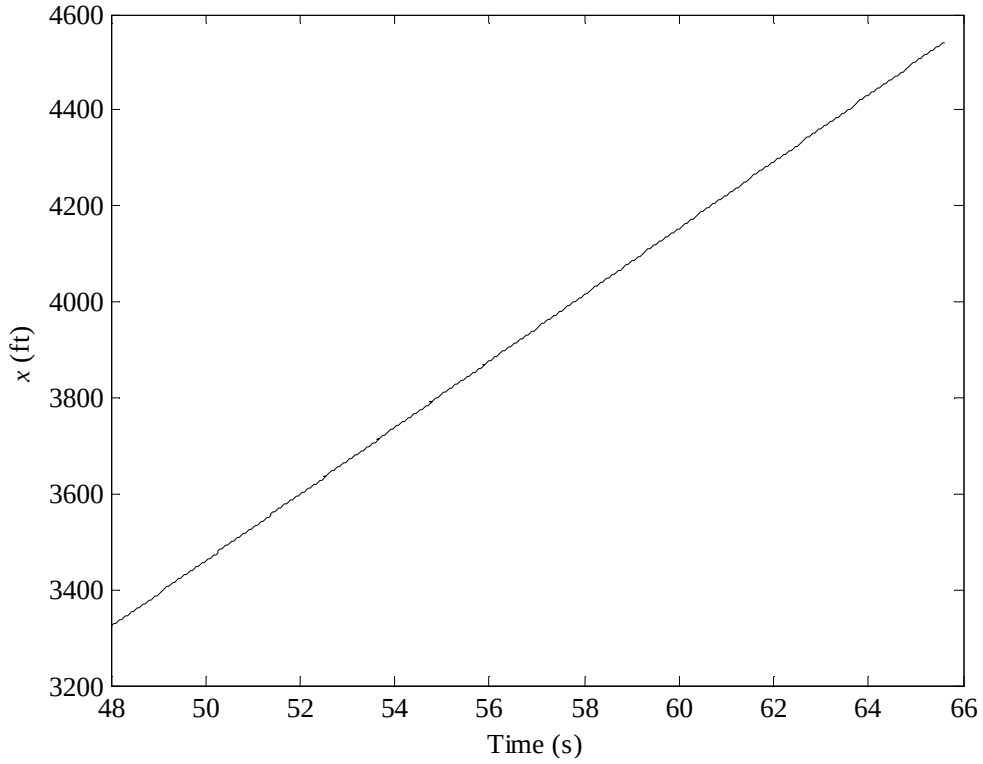

Figure A 11 Axial position x

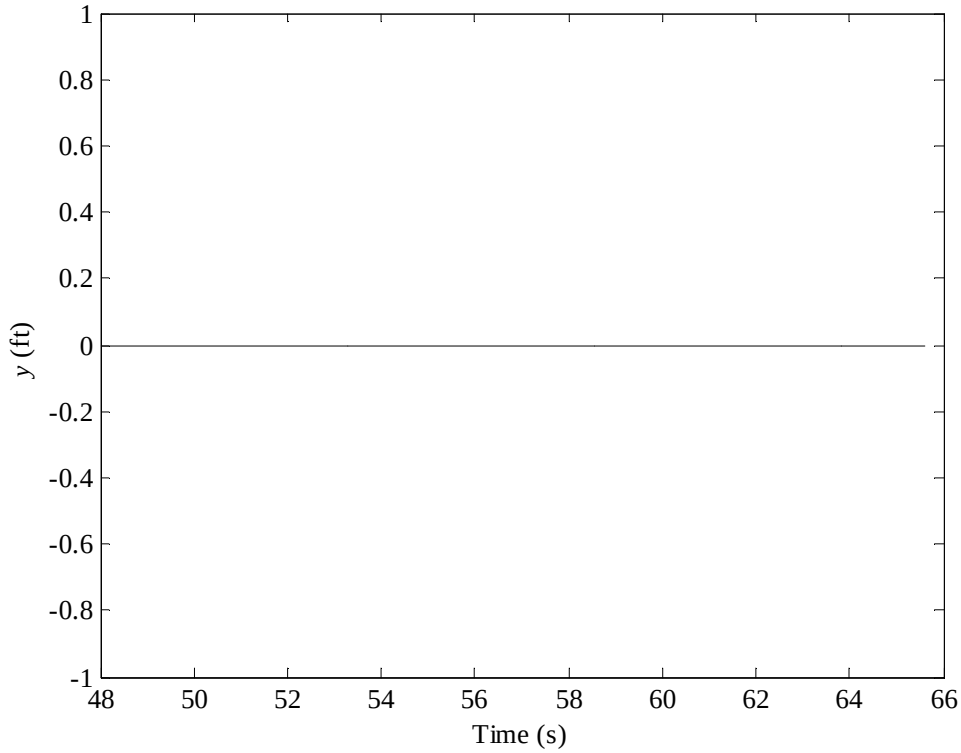

Figure A 12 Lateral position *y*

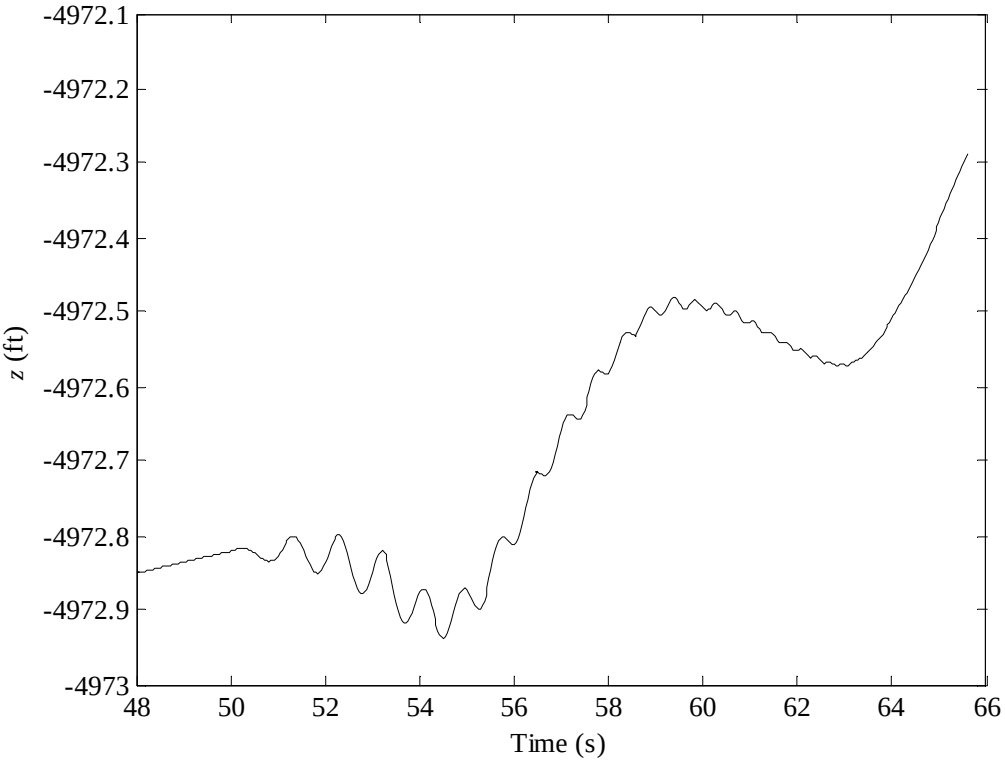

Figure A 13 Altitude *z*

The responses are examined and demonstrated make sense to a certain extent. For example, positive elevator deflection causes negative *w* and *q* responses. So far, the signs (phases) of the responses are make sense, however, their magnitudes are not that convincing. It seems that some of the states' magnitudes are incredibly high, while some of them are too low. It is believed that this is caused by the inaccurate estimation of aerodynamic derivatives, since when modifying the model, some of the derivatives are tuned. This demonstrates that the AVL is deficient in estimating the aerodynamic derivatives precisely. That is why the system identification is given wide attention.

A2.2 Identification using transfer function based method

For the longitudinal channel system identification, the chirp input signal is used to excite the simulation model. The main parameters used by the Chirp are: time duration, 15 seconds; maximum elevator deflection, 2 degrees; and frequency range, 0.1 ~ 5 Hz. The computer generated input excitation is shown as Figure A 14.

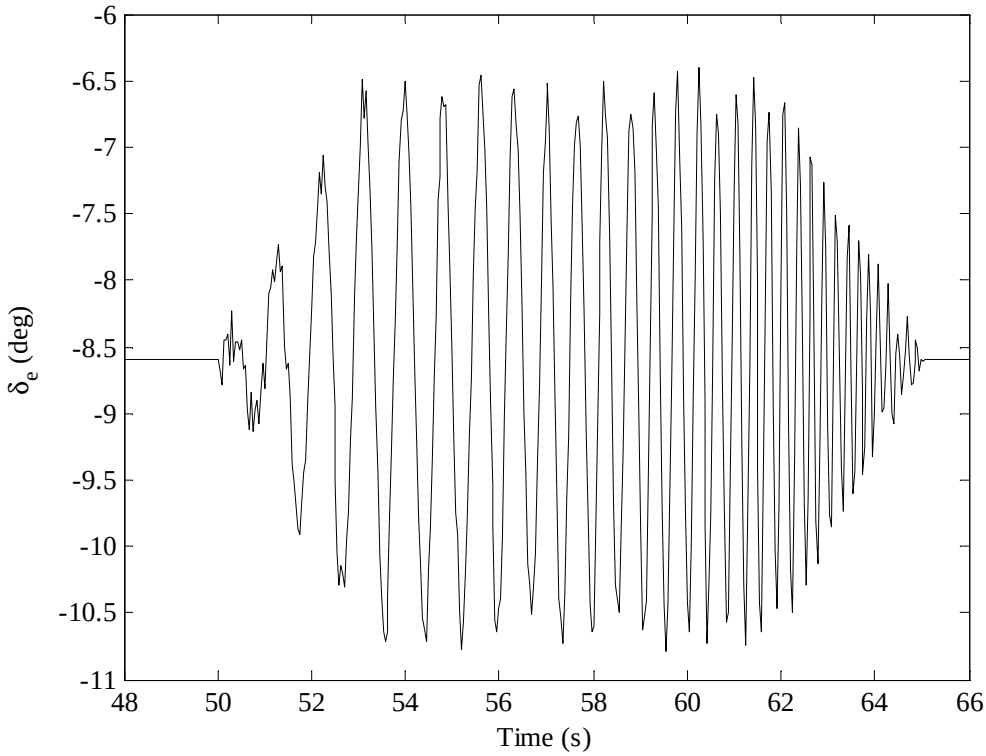

Figure A 14 Chirp input excitation

The Chirp input excitation's frequency range is shown by the FFT plot in Figure A 15.

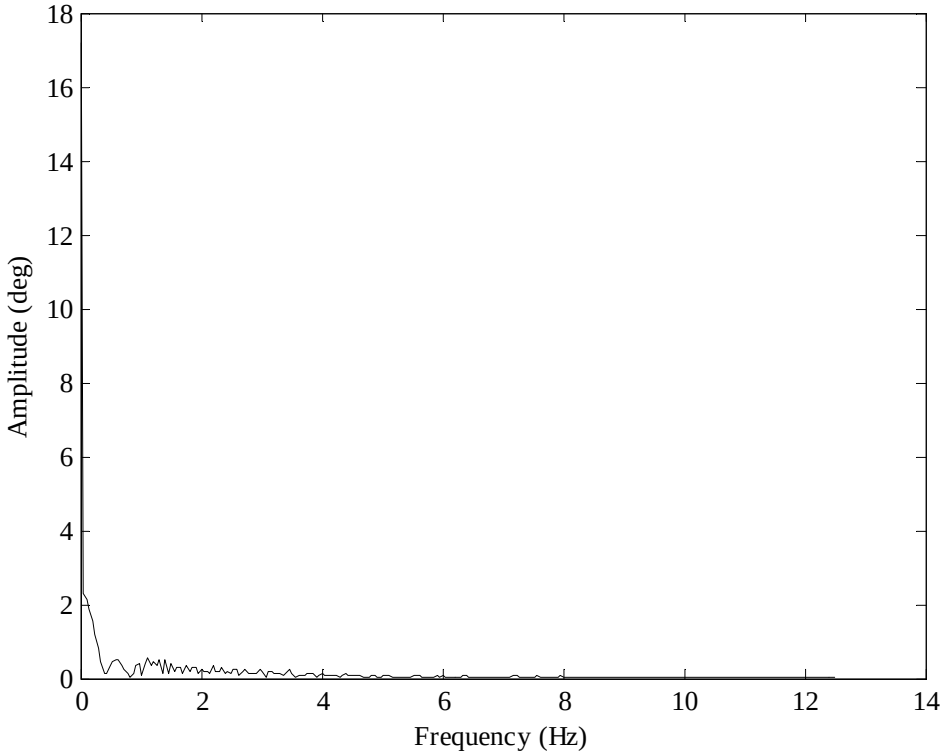

Figure A 15 FFT of input excitation

From Figure A 15, it is seen the Chirp frequency range is 0.1 to 5 Hz, which is exactly as set. And also it is seen that the frequency component of the signal is rich, which is ideal for frequency domain system identification. The transfer function based algorithm is mainly based on Equations (6.24) and (6.25) for longitudinal channel system identification. The output responses needed are vertical body velocity *w* and pitch rate *q*. For data processing, the variables' units should be normalized. Here the input δ_e's unit is set as rad, output *w*'s unit is set as ft/s, and *q*'s unit is rad/s. By using the CIFER batch work utility, the Bode plots of δ_e-*w* and δ_e-*q* can be obtained, and are shown in Figure A 16 and Figure A 17.

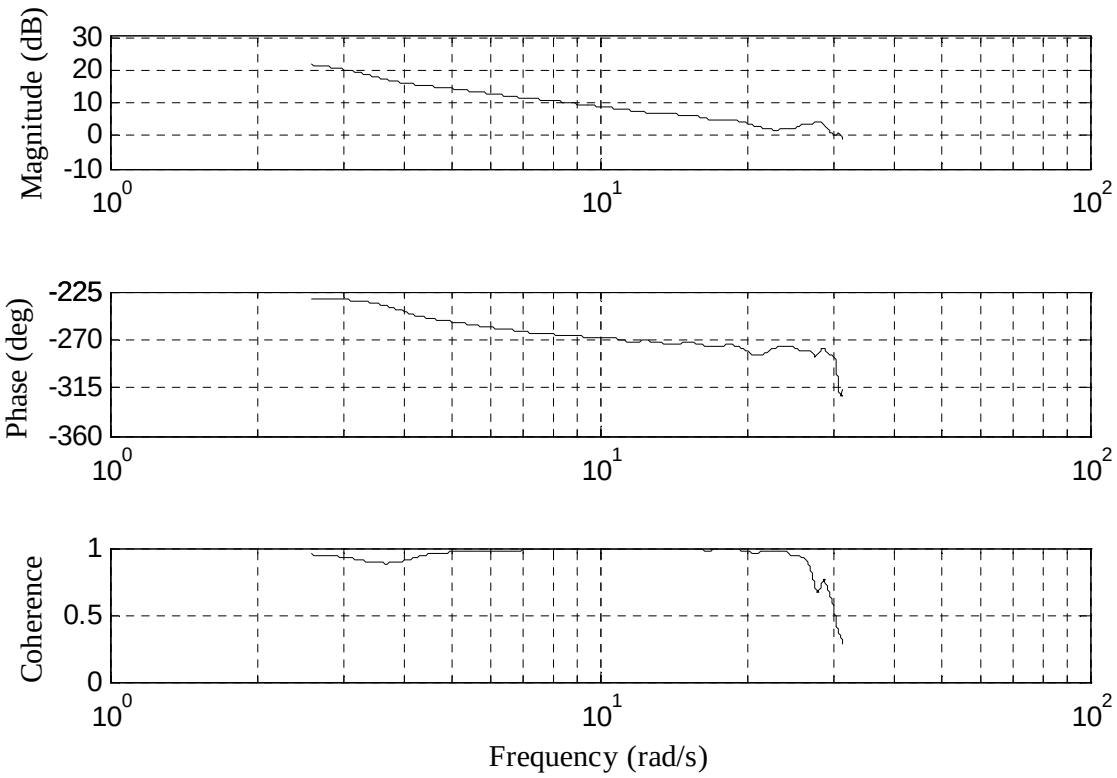

Figure A 16 Bode plot of δ_e-w

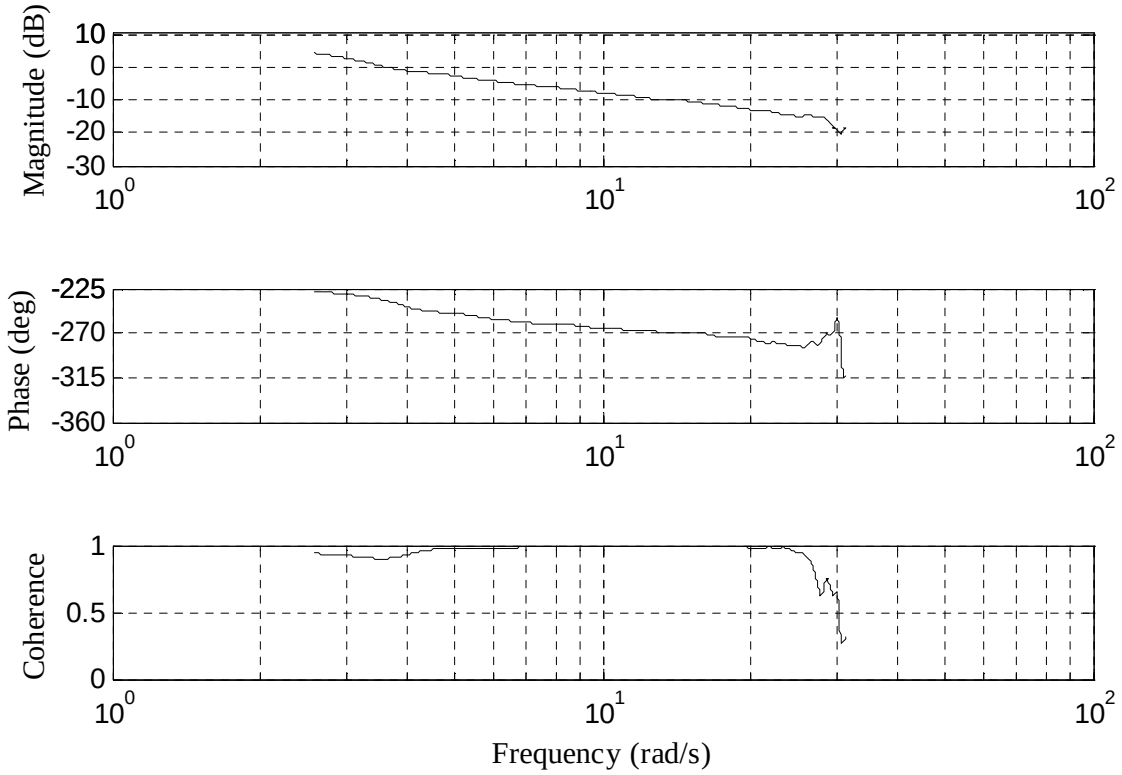

Figure A 17 Bode plot of δ_e-q

The two plots show that both δ_e-w and δ_e-q's coherences are good (coherence over 0.8) or acceptably high (above 0.6) between 2.58 and 30 rad/s. To guarantee good linearity, a frequency range of 2.58 ~ 27 rad/s is picked for the identification of transfer functions. This maintains the coherence over 0.8. By using the CIFER NAVFIT module, the transfer functions of δ_e-w and δ_e-q are acquired and are shown as:

$$\frac{w(s)}{\delta_e(s)} = \frac{-26.37(s+8.95)e^{-0.0086s}}{s^2+8.81s+20.9} \quad \text{(A 1)}$$

$$\frac{q(s)}{\delta_e(s)} = \frac{-3.91(s+8.14)e^{-0.0085s}}{s^2+8.81s+20.9} \quad \text{(A 2)}$$

The cost of the δ_e-w transfer function is 36.9, and 28.2 for δ_e-q. These are all satisfactorily under the guideline of 100.

Figure A 18 to Figure A 21 show the verification of two transfer functions' accuracy by comparing the identified Bode plots (from the flight data) with the ones plotted from the transfer functions.

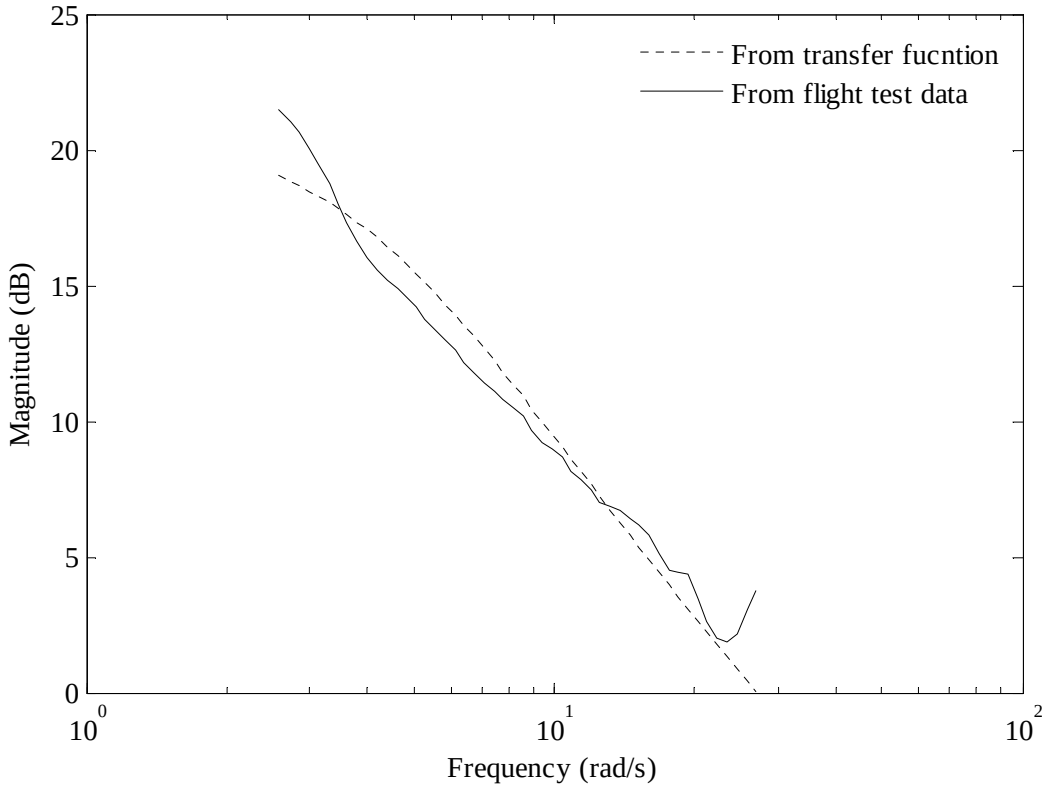

Figure A 18 Magnitude of δ_e-w

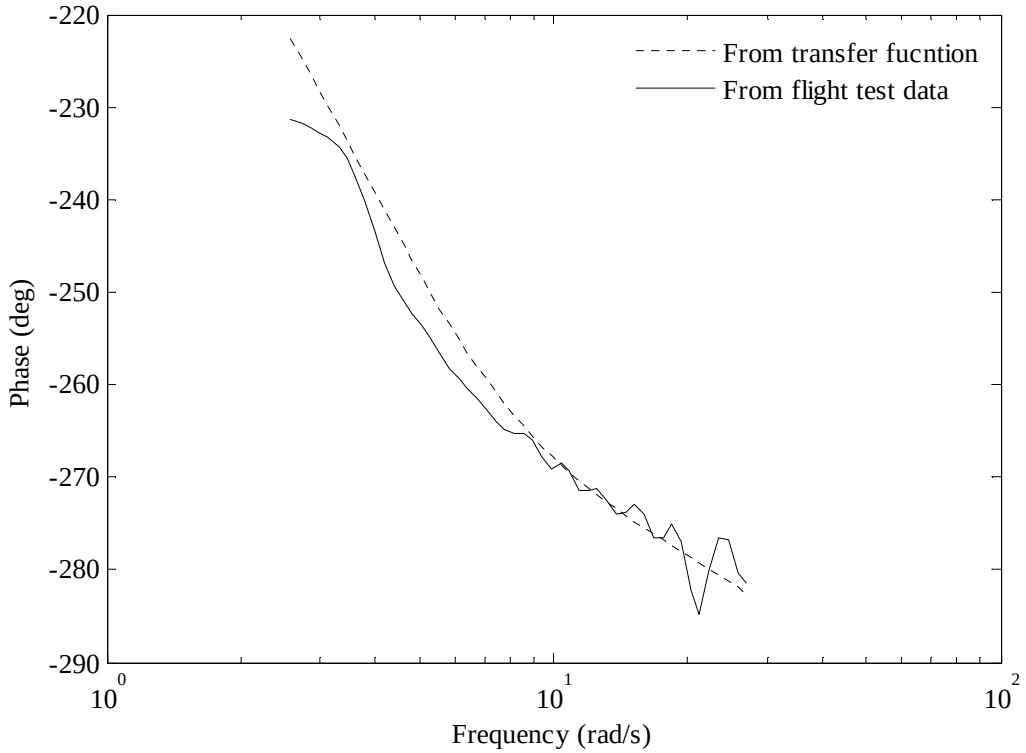

Figure A 19 Phase of δ_e-w

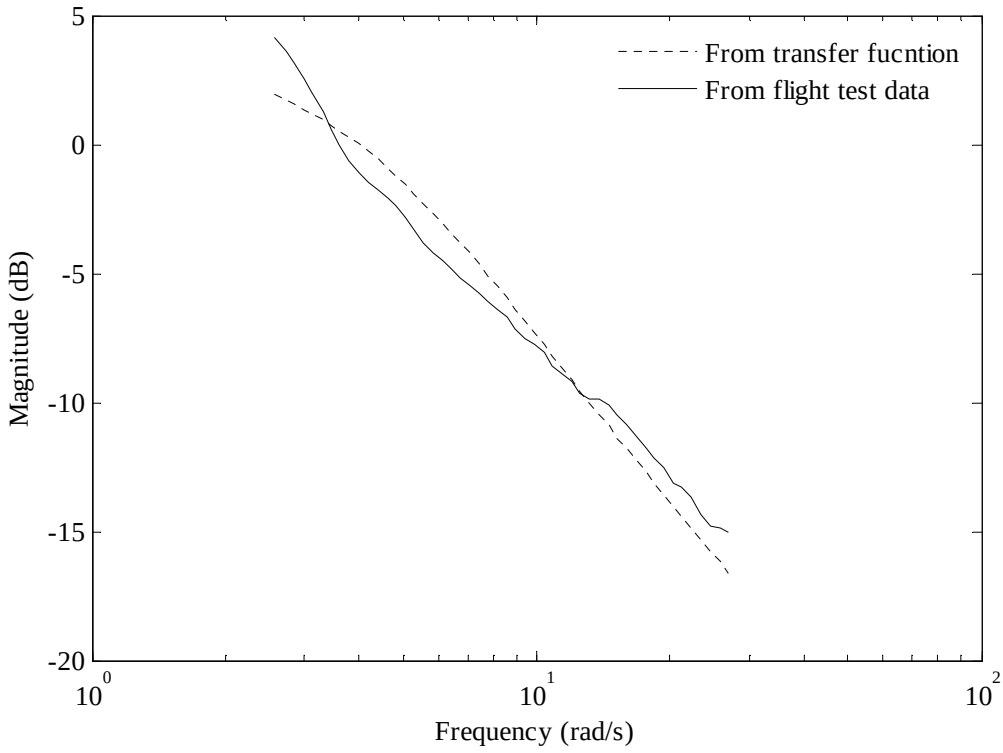

Figure A 20 Magnitude of δ_e-q

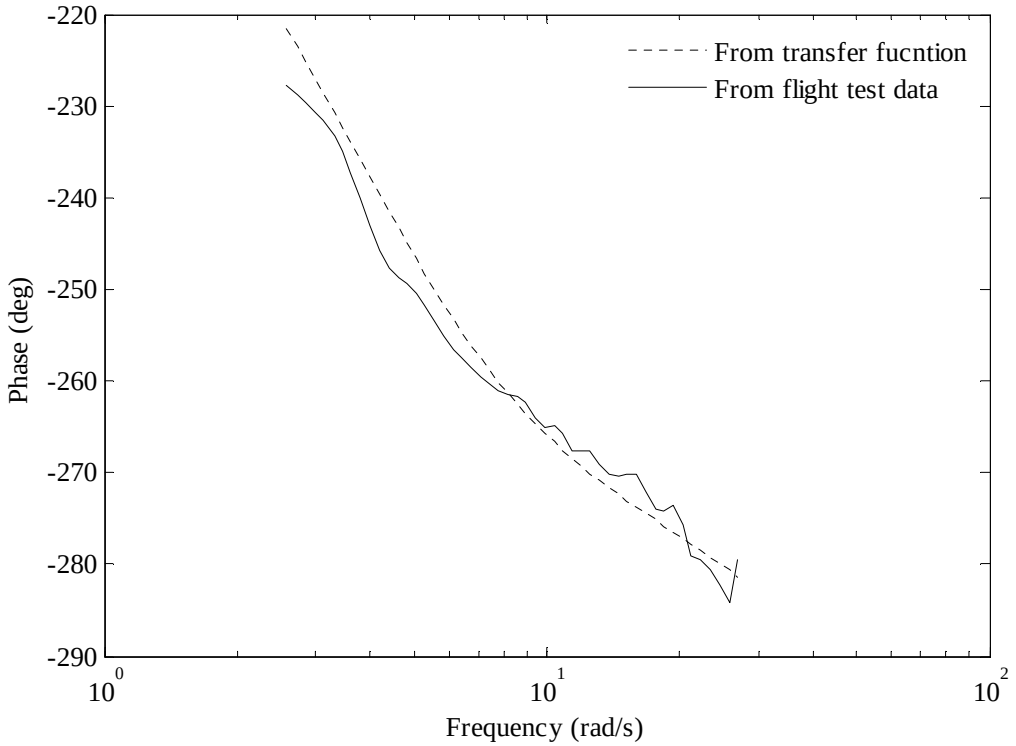

Figure A 21 Phase of δ_e-q

From Figure A 18 to Figure A 21, it can be seen that both of the magnitude and phase plots of the δ_e-w and δ_e-q's transfer functions match fairly well with the data identified ones. To further examine the accuracy of the transfer functions, they are fed with the simulation input δ_e (refer to Figure A 14) to get the simulated outputs $\widehat{w}$ and $\widehat{q}$, which are compared with the flight measured outputs w and q. The simulated outputs $\widehat{w}$ and $\widehat{q}$ are calculated and the comparisons are shown as Figure A 22 and Figure A 23.

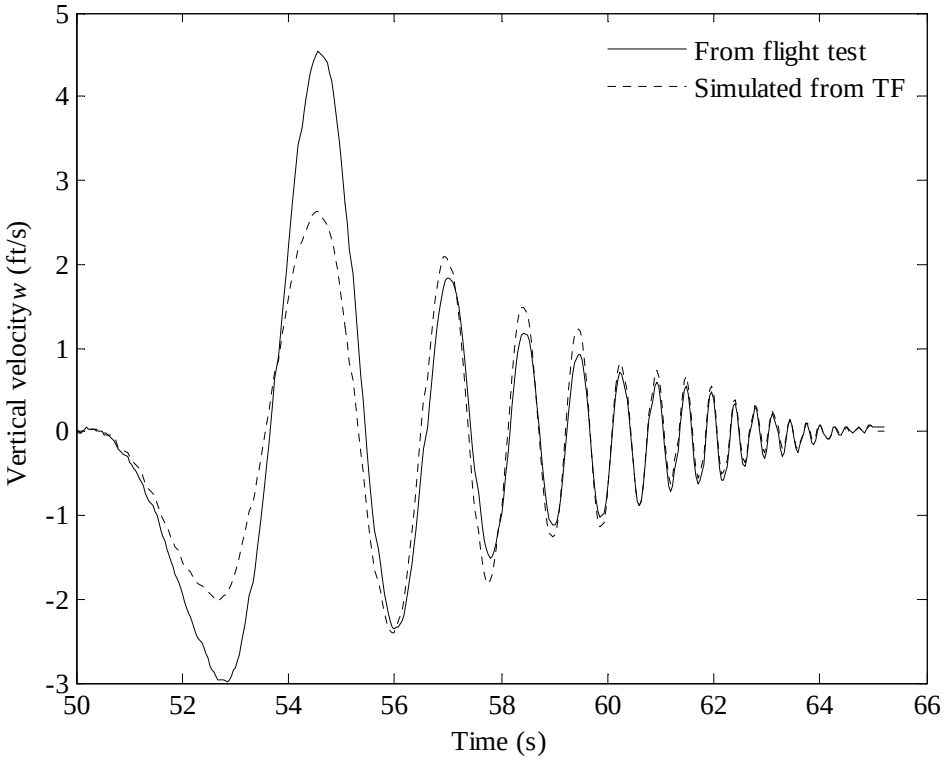

Figure A 22 Verification of vertical velocity *w*

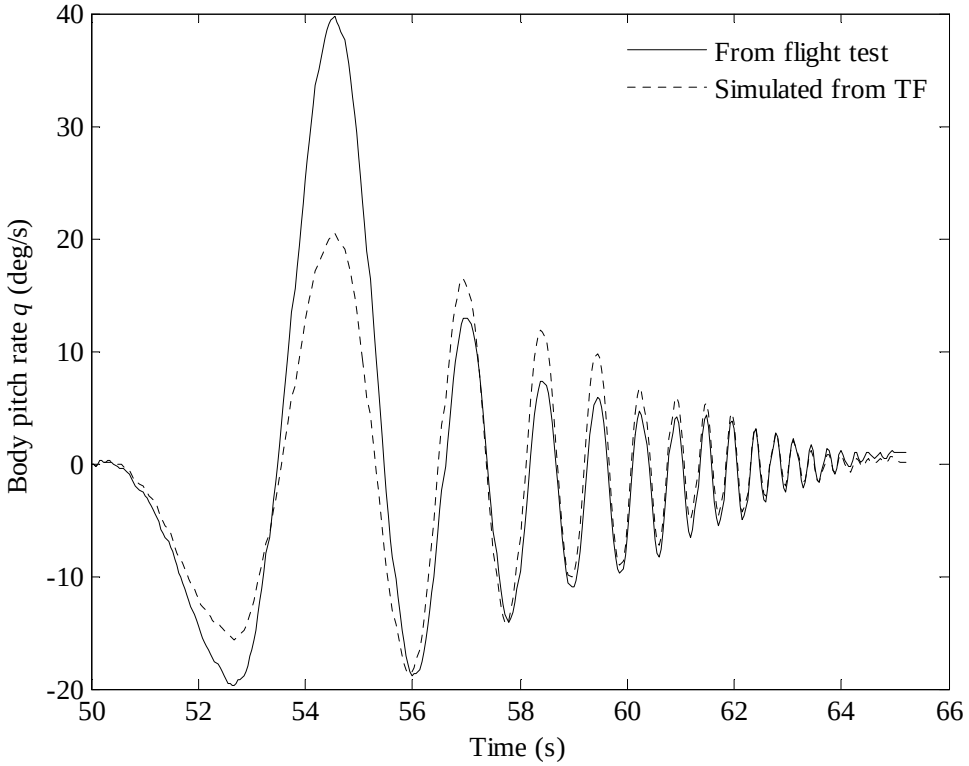

Figure A 23 Verification of pitch rate *q*

The comparison plots show that the transfer function simulated outputs can track the aircraft responses quite well. This indicates that the transfer functions are fairly accurate in describing the system characteristics. Thus, next, the transfer function method discussed in Chapter 6 can be applied to extract the aerodynamic derivatives.

$$\frac{w(s)}{\delta_e(s)} = \frac{z_{\delta_e}(s + U_e\frac{m_{\delta_e}}{z_{\delta_e}})}{s^2 - (m_q + z_w)s + (m_q z_w - m_w U_e)} = \frac{-26.37(s + 8.95)}{s^2 + 8.81s + 20.9} \quad \text{(A 3)}$$

$$\frac{q(s)}{\delta_e(s)} = \frac{m_{\delta_e}(s - z_w)}{s^2 - (m_q + z_w)s + (m_q z_w - m_w U_e)} = \frac{-3.91(s + 8.14)}{s^2 + 8.81s + 20.9} \quad \text{(A 4)}$$

To extract the derivatives, the homologous terms in the transfer functions are set as equal:

$$\begin{cases} z_{\delta_e} = -26.37 \\ m_{\delta_e} = -3.91 \\ -z_w = 8.14 \\ -(m_q + z_w) = 8.81 \\ m_q z_w - m_w U_e = 20.9 \end{cases} \quad \text{(A 5)}$$

where U_e = 69.34 ft/s. Therefore the concise aerodynamic derivatives are solved:

$$\begin{cases} z_{\delta_e} = -26.37 \\ m_{\delta_e} = -3.91 \\ z_w = -8.14 \\ m_q = -0.67 \\ m_w = -0.22 \end{cases}$$

Note the derivatives here are neither dimensional nor dimensionless. They are notated concisely. The way of converting them to North American dimensionless notated derivatives can refer to Section 7.1.1. Some parameters used in the conversions are: ρ = 0.002286 slug/ft^3, S = 5.31 ft^2, $\bar{\bar{c}}$ = 0.77 ft, V_0 = 69.34 ft/s, I_y= 3.04 lb·ft^2.

By converting them to dimensionless North American derivatives, they can be compared with the ones that will be identified by the EE method. The dimensionless derivatives identified by the transfer function method can then be summarized as:

$$\begin{cases} C_{z_w} = -4.6083 \\ C_{z_{\delta e}} = -0.0094 \\ C_{m_w} = -2.0861 \\ C_{m_q} = -16.4153 \\ C_{m_{\delta e}} = -0.0294 \end{cases}$$

A2.3 Identification using equation error method

For the identification of the simulation model, all the derivatives used in this research are non-dimensional. The prior model equations used for longitudinal channel system identification are summarized as (adapted from Equations (4.108) to (4.110)):

$$\dot{u} = \mathrm{X}_u u + \mathrm{X}_{\dot{w}}\dot{w} + \mathrm{X}_w w + \left(\mathrm{X}_q - W_e\right)q - g\theta cos\theta_e + \mathrm{X}_{\delta_e}\delta_e \quad \text{(A 6)}$$

$$\dot{w} = \mathrm{Z}_u u + \mathrm{Z}_{\dot{w}}\dot{w} + \mathrm{Z}_w w + \left(\mathrm{Z}_q + U_e\right)q - g\theta sin\theta_e + \mathrm{Z}_{\delta_e}\delta_e \quad \text{(A 7)}$$

$$\dot{q} = \mathrm{M}_u u + \mathrm{M}_{\dot{w}}\dot{w} + \mathrm{M}_w w + \mathrm{M}_q q + \mathrm{M}_{\delta_e}\delta_e \quad \text{(A 8)}$$

Equations (A 6) to (A 8) can be further written as,

$$\dot{u} + qW_e + g\theta cos\theta_e = \mathrm{X}_u u + \mathrm{X}_w w + \mathrm{X}_q q + \mathrm{X}_{\delta_e}\delta_e + \mathrm{X}_{\dot{w}}\dot{w} \quad \text{(A 9)}$$

$$\dot{w} - qU_e + g\theta sin\theta_e = \mathrm{Z}_u u + \mathrm{Z}_w w + \mathrm{Z}_q q + \mathrm{Z}_{\delta_e}\delta_e + \mathrm{Z}_{\dot{w}}\dot{w} \quad \text{(A 10)}$$

$$\dot{q} = \mathrm{M}_u u + \mathrm{M}_w w + \mathrm{M}_q q + \mathrm{M}_{\delta_e}\delta_e + \mathrm{M}_{\dot{w}}\dot{w} \quad \text{(A 11)}$$

By combining the Equations (4.35) to (4.111), Equations (A 9) to (A 11) can be rewritten in dimensionless case, and shown as,

$$C_X = m(\dot{u} + qW_e + g\theta cos\theta_e)/\bar{q}S = C_{X_u}\hat{u} + C_{X_w}\hat{w} + C_{X_q}\hat{q} + C_{X_{\delta e}}\delta_e + C_{X_{\dot{w}}}\dot{\hat{w}} \quad \text{(A 12)}$$

$$C_Z = m(\dot{w} - qU_e + g\theta sin\theta_e)/\bar{q}S = C_{Z_u}\hat{u} + C_{Z_w}\hat{w} + C_{Z_q}\hat{q} + C_{Z_{\delta e}}\delta_e + C_{Z_{\dot{w}}}\dot{\hat{w}} \quad \text{(A 13)}$$

$$C_m = \dot{q} * I_y/\bar{q}S\bar{c} = C_{m_u}\hat{u} + C_{m_w}\hat{w} + C_{m_q}\hat{q} + C_{m_{\delta e}}\delta_e + C_{m_{\dot{w}}}\dot{\hat{w}} \quad \text{(A 14)}$$

where, the quantities with dressing "^" denote the non-dimensionalized variables.

For the Equation Error method identification, all the time domain parameters and variables C_X, C_Z, C_m, $\hat{u}$, $\hat{w}$, $\hat{q}$, δ_e and $\dot{\hat{w}}$ are converted into the frequency domain by applying the finite Fourier transform. The frequency domain variables can be written in vector form as follows by referring to Equations (6.50) and (6.51):

For the axial force C_X case,

$$\boldsymbol{Y} \equiv \begin{bmatrix} \widetilde{\boldsymbol{C}_X}(1) \\ \widetilde{\boldsymbol{C}_X}(2) \\ \cdot \\ \cdot \\ \cdot \\ \widetilde{\boldsymbol{C}_X}(m) \end{bmatrix} \quad \text{(A 15)}$$

For the lift force C_Z case,

$$\boldsymbol{Y} \equiv \begin{bmatrix} \widetilde{\boldsymbol{C}_Z}(1) \\ \widetilde{\boldsymbol{C}_Z}(2) \\ \cdot \\ \cdot \\ \cdot \\ \widetilde{\boldsymbol{C}_Z}(m) \end{bmatrix} \quad \text{(A 16)}$$

For the pitching moment C_m case,

$$\boldsymbol{Y} \equiv \begin{bmatrix} \widetilde{\boldsymbol{C}_m}(1) \\ \widetilde{\boldsymbol{C}_m}(2) \\ \cdot \\ \cdot \\ \cdot \\ \widetilde{\boldsymbol{C}_m}(m) \end{bmatrix} \tag{A 17}$$

For C_X, C_Z and C_m, matrix $\boldsymbol{X}$ is the same, which is,

$$\boldsymbol{X} \equiv \begin{bmatrix} \widetilde{\boldsymbol{u}}(1) & \widetilde{\boldsymbol{w}}(1) & \widetilde{\boldsymbol{q}}(1) & \widetilde{\boldsymbol{\delta_e}}(1) & \dot{\widetilde{\boldsymbol{w}}}(1) \\ \widetilde{\boldsymbol{u}}(2) & \widetilde{\boldsymbol{w}}(2) & \widetilde{\boldsymbol{q}}(2) & \widetilde{\boldsymbol{\delta_e}}(2) & \dot{\widetilde{\boldsymbol{w}}}(2) \\ \cdot & \cdot & \cdot & \cdot & \cdot \\ \cdot & \cdot & \cdot & \cdot & \cdot \\ \cdot & \cdot & \cdot & \cdot & \cdot \\ \widetilde{\boldsymbol{u}}(m) & \widetilde{\boldsymbol{w}}(m) & \widetilde{\boldsymbol{q}}(m) & \widetilde{\boldsymbol{\delta_e}}(m) & \dot{\widetilde{\boldsymbol{w}}}(m) \end{bmatrix} \tag{A 18}$$

where m is the total number of frequency components. Since the model quantities in Equations (A 15) to (A 18) are all determined, the EE method discussed in Chapter 6 can be applied. Equation (6.58) can be executed to obtain axial force, lift force and pitching moment related derivatives by substituting $\boldsymbol{Y}$ matrix. Also, the parameter standard errors can be computed according to Equations (6.59) to (6.61). Table A 5 tabulates the longitudinal channel system identification results identified by the EE method. The derivatives estimated by AVL and extracted by transfer function method are also listed in Table A 5 for comparison.

Table A 5 Derivatives of simulation model

	Derivative	EE method	Parameter Standard Error	TF Result	AVL software
Pitch moment related derivatives	C_{m_u}	0.0543	0.0125	N/A	-0.032~ 0.015
	C_{m_w}	-1.7914	0.1848	-2.0861	-1.9219~ -1.15
	C_{m_q}	-10.4704	3.7187	-16.4153	-14.43~ -12.6
	$C_{m_{\delta e}}$	-0.0310	0.0004	-0.0294	-0.032~ -0.027
	$C_{m_{\dot{w}}}$	0.0002	0.0066	N/A	N/A
Lift force related derivatives	C_{Z_u}	0.0918	0.0269	N/A	-2.5~ 0.2
	C_{Z_w}	-4.7180	0.3972	-4.6083	-5.47~ -5.73
	C_{Z_q}	-8.3151	7.9937	N/A	-9.1~ -8.4
	$C_{Z_{\delta e}}$	-0.0100	0.0006	-0.0094	-0.0091~ -0.0099
	$C_{Z_{\dot{w}}}$	0.0025	0.0141	N/A	N/A
Axial force related derivatives	C_{X_u}	-0.1591	0.0075	N/A	-0.15~ 0.07
	C_{X_w}	2.0796	0.1113	N/A	-2~ 2.85
	C_{X_q}	-40.3759	2.2394	N/A	-2.1~ 1.67
	$C_{X_{\delta e}}$	0.0002	0.0002	N/A	-0.00198~ 0.0018
	$C_{X_{\dot{w}}}$	-0.0002	0.0039	N/A	N/A

By comparing the EE identified derivatives with the ones estimated by AVL, it can be seen that most of the values are identical or fairly close. The only defect is that C_{X_q} which seems to be inaccurate. The deviation needs to be explored in the future. Beyond this, the identified parameter results are in good agreement. By comparing the derivatives' values acquired by using two identification methods, it can also be seen that they are reasonably close. This further proves

that the two methods are effective and valid for identifying aerodynamic derivatives. In addition, the low Parameter Standard Error also indicates that the identified derivatives are fairly reliable.

To summarize, in this appendix, an aircraft simulation model was introduced first. Then, both the TF and EE methods were applied to identify the longitudinal mode aerodynamic derivatives, using the simulation data. The TF method was used to identify the system transfer functions; some longitudinal mode aerodynamic derivatives were extracted from the identified transfer functions. The EE method was used to directly calculate the aerodynamic derivatives from the simulation data. The identification results demonstrated that both the TF and EE methods are reliable in identifying aerodynamic derivatives. Therefore, they can be used for identification of the actual aircraft system.